Using atomic force microscopy to measure the nanomechanical properties of cell nuclei and clathrin cages

An odyssey towards the nano-world

Michael Lherbette

Submitted for the degree of Doctor of Philosophy

Heriot Watt University
School of Engineering and Physical Sciences

February 2019

Abstract

This thesis presents how mechanical measurements with atomic force microscopy in combination with finite element analysis were used to increase our understanding of the functioning of sub-cellular biological assemblies.

Clathrin proteins are known for their ability to form curved lattices that play an essential role in the bending of, and transport across, the cell membrane. Force spectroscopy experiments on isolated and reconstituted model systems revealed that the lattice mechanics can be regulated by several binding factors. This finding suggests that besides chemical signals, mechanical regulation can play an important role in biological processes.

The cell nucleus is a complex structure consisting of DNA and various proteins enclosed in the nuclear membrane. Although there is evidence that mechanical stimuli affect gene expression it remains largely unclear how forces are transduced through the nucleus. Micro-rheology measurements showed a non-homogeneous distribution of elasticity and viscosity in the nucleus which provides an explanation why some nuclear regions are more active in gene transcription than others.

Besides the biological findings, this work describes multiple technological advances that were essential to perform the measurements. These include methods to calibrate the stiffness of atomic force microscopy cantilevers with interferometry, to perform high-bandwidth micro-rheology while staining the nucleus, and to perform 3D image reconstruction with optical microscopy during mechanical measurements.

To my thirst for knowledge

ACADEMIC REGISTRY
Research Thesis Submission

Name*:*	MICHAEL LHERBETTE		
School:	Engineering and Physical Sciences		
Version: *(i.e. First, Resubmission, Final)*	Final	Degree Sought:	Doctor of Philosophy

Declaration

In accordance with the appropriate regulations I hereby submit my thesis and I declare that:

1) the thesis embodies the results of my own work and has been composed by myself
2) where appropriate, I have made acknowledgement of the work of others and have made reference to work carried out in collaboration with other persons
3) the thesis is the correct version of the thesis for submission and is the same version as any electronic versions submitted*.
4) my thesis for the award referred to, deposited in the Heriot-Watt University Library, should be made available for loan or photocopying and be available via the Institutional Repository, subject to such conditions as the Librarian may require
5) I understand that as a student of the University I am required to abide by the Regulations of the University and to conform to its discipline.
6) I confirm that the thesis has been verified against plagiarism via an approved plagiarism detection application e.g. Turnitin.

* *Please note that it is the responsibility of the candidate to ensure that the correct version of the thesis is submitted.*

Signature of Candidate*:*		Date:	8 February 2019

Submission

Submitted By *(name in capitals):*	MICHAEL LHERBETTE
Signature of Individual Submitting:	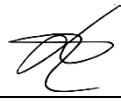
Date Submitted:	8 February 2019

For Completion in the Student Service Centre (SSC)

Received in the SSC by *(name in capitals):*			
Method of Submission *(Handed in to SSC; posted through internal/external mail):*			
*E-thesis Submitted (**mandatory for final theses**)*			
Signature:		Date:	

Please note this form should be bound into the submitted thesis.
Academic Registry/Version (1) August 2016

Contents

Conferences and publications

Poster presentations

1. Groningen (Netherlands, 2016) at the 26^{th} Conference of the Condensed Matter Division,
   Mechanics of polyhedra with AFM and finite element analysis.
2. Geneva (Switzerland, 2016) at the Euro AFM Forum,
   Mechanics of polyhedra with AFM and finite element analysis (updated version).
3. Cambridge (United-Kingdom, 2016) at Bruker's Annual SPM conference,
   Combining AFM with single molecule fluorescence and finite element analysis.
4. London (United-Kingdom, 2017) for STEM for Britain competition,
   Beyond the microscale: touching the nano-mechanics that regulate the entry pathway of cells.

Publications

1. **M. Lherbette**[*], Á dos Santos[*], Y. Hari-Gupta, N. Fili, C.P. Toseland, I.A.T. Schaap
   Atomic Force Microscopy micro-rheology reveals large structural inhomogeneities in single cell-nuclei.
   Scientific Reports 7, Article number: 8116 (2017)
   — Chapter 6
2. **M. Lherbette**[*], L. Redlingshöfer[*], F.M. Brodsky, I.A.T Schaap, P.N. Dannhauser
   The AP2 adaptor enhances clathrin coat stiffness.
   Submitted to Federation of European Biochemical Societies Journal (2018)
   — Chapter 4

[*] Joint first authors.

1

General introduction

"Defining is more complex than we think, if not more complex than we can believe. Moreover, it turns out that any complex problem - if it is treated with the utmost scruple - continues to gain in complexity", Elgozy [1].

1.1 Biomechanics: a mechanical approach to biology

The experimental research presented in this thesis is best defined by biomechanics on a small length-scale. Now, what does biomechanics refer to? Its two elements, "bio" and "mechanics" accurately point towards the investigation of mechanical properties of biological systems. In a nutshell, nanoscale biomechanics borrows bottom-up strategies from physics which implies dissecting complex biological entities into simple sub-ones and adding complexities along the way to understand the initial phenomenon. In biology, *a contrario*, top-down approaches are generally favoured and the complete system is observed for changes while altering one single component at a time.

Although biomechanics is certainly not a new avocation as to some extend it can be dated back to the beginning of the 20^{th} century [2], the recent advent of specific and powerful tools to study the role of mechanics on a single cell level has triggered a boom in the field. Since 1975 the number of articles including "biomechanics" or "biomechanical" has grown exponentially [2] and the emergence of scanning probe microscopy (SPM) techniques is one of the responsible breakthroughs. For example, atomic force microscopy (AFM), a SPM technique that uses mechanical interaction with the sample as feedback signal and developed in the 1980s [3], was successfully implicated ten years later in the discovery of porosome [4], a small structure in the membrane of eukaryotic cells responsible for its secretory properties. Previously, the porosome was invisible by conventional microscopy techniques because of its tininess and thus left completely unknown. Eventually, such events lead to the birth of a new research field, the nano cell biology [5].

1.2 Introducing clathrin and the cell nucleus

The biological building block of all living organisms is the cell. It provides their structure, produces the energy required for their good functioning and contains all machinery and the genetic code to allow their own replication.
This complex system is not a hermetic enclosure. Indeed, it massively relies on external inputs to survive but also needs to export materials and to generate signals to its surroundings. In fact, the membrane of a cell is a very active area where tons of exchanges between the outside world and the inside are settled simultaneously. Many of these exchanges are regulated by clathrin, a customs officer at the entry pathway of cells.

1.2.1 Clathrin

The invagination of foreign bodies into the cell is called endocytosis [6]. In 1964, Rosenbluth and Wissig [7] discovered that it involves the formation of coated vesicles, decorated lipid bilayers rolled-up into spherical shells, that encapsulate the external cargoes. This discovery was possible thanks to the scanning electron microscopy (SEM) study of the uptake into neurons of ferrite nanoparticles, which were found to be contained by baskets. It initiated much other research as a tremendous number of questions arose: "How can ferrite be coated?", "Do different coatings exist?", "Do all cargoes have to be coated?".
Work done by Pearse [8] in 1976 presented the clathrin-mediated endocytosis (CME) as the main pathway to bring cargo into a cell, see Figure 1.1.

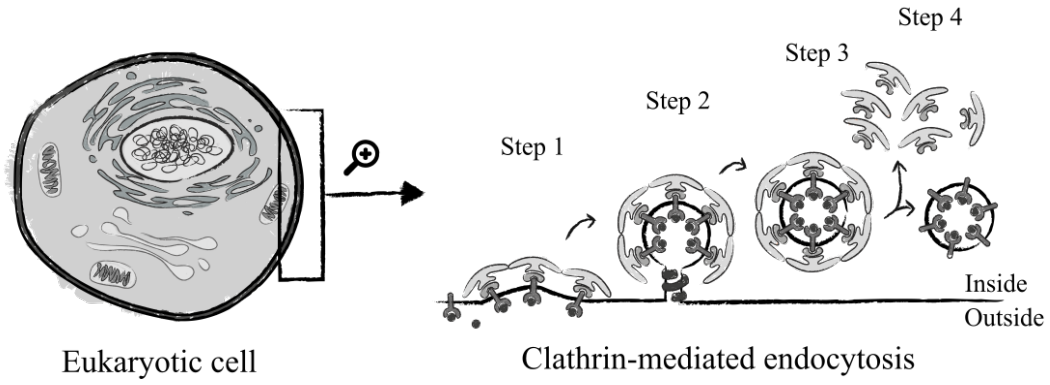

Figure 1.1: Schematic of the clathrin-mediated endocytosis: the uptake of external cargoes into a eukaryotic cell using clathrin polyhedra. *Step 1: External cargo binds the cell membrane while clathrin is recruited. Step 2: Creation of clathrin-coat. Step 3: Scission and liberation of the clathrin-coat. Step 4: Disassembly of the clathrin-coat.*

She found that cargoes are coated by a cage made of clathrin proteins that were characterised by electrophoresis. These natural baskets consist of regular pentagons and hexagons that form an almost perfect natural polyhedron. Their basic sub-unit is called a triskelion because of its trimer conformation: three clathrin heavy chains (one chain being approximately 190 kDa) each associated with a light chain (approximately 25 kDa) [9], as shown in Figure 1.2a. A clathrin leg is divided in three main domains: the proximal domain, where the light chains bind and which forms the rib of a pentagon or hexagon, the distal domain that is flexible and extends in the interior of the basket, and the terminal domain that serves as binding site for accessory proteins such as Epsin or AP180 [10].
More recently, the architecture of clathrin-coated-vesicles (CCVs) was investigated with subnanometre resolution via cryo-electron microscopy. Fotin et al. [11] identified in their structure, the position of bound proteins as well as their binding site, and reconstructed three main assemblies of different sizes (the cage diameter is believed to be cargo dependent [12]). The last are made of at least 12 regular pentagons and multiple hexagons all having approximately 17.5 nm rib length (measured by AFM [13]), see Figure 1.2b:

- the truncated triakis tetrahedron of approximately 62 nm diameter and 4 hexagons,
- the hexagonal barrel of approximately 70 nm diameter and 8 hexagons,
- the truncated icosahedron of approximately 80 nm diameter and 20 hexagons.

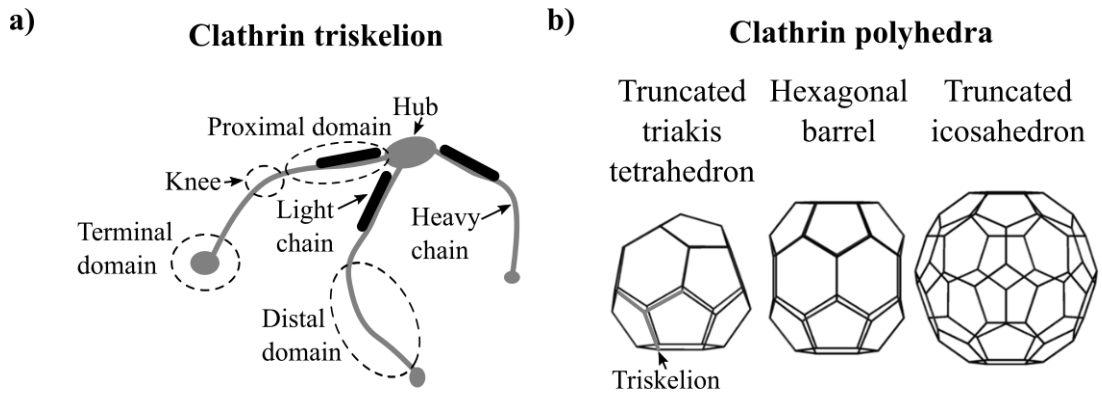

Figure 1.2: Clathrin triskelion and polyhedron architecture. *(a) A clathrin triskelion is composed of 3 heavy chains (CHCs) connected by a hub. Each CHC can be divided into three parts: the proximal domain, the distal domain and the terminal domain. "Distal" and "proximal" refer to the distance from the threefold centre (knee) of the triskelion. A light chain is bound to each CHC proximal domain. (b) In physiological conditions, the triskelia are bound together to form hexagons and pentagons which compose a complete and almost perfect biological polyhedron.*

Proteins of the Epsin protein family belong to the so-called adaptor proteins connecting the clathrin structure to the cell membrane and have been shown to be a notable promoter of the CCV formation. Strictly speaking, if Espin function is disrupted the polymerisation of clathrin-trimers is blocked and no CCVs are formed. Furthermore, Epsin has been found to induce membrane curvature thanks to its insertion in the cell membrane and the forced rearrangement of the lipid heads [14]. These insertions reduce the required energy to induce vesicle formation, which facilitates the formation of CCV. The clathrin cage is then thought to be a structure that does not have a strong mechanical impact on the bending of the membrane. Hypothesis which is further confirmed by Nossal [15] who showed that clathrin cages should lack the ability to bend the membrane due to their softness. However, this is challenged by the work of Dannhauser and Ungewickell [16] who proved that also without this adaptor clathrin alone is capable of bending the cell membrane.
This controversial role of clathrin in bending the membrane is difficult to study as CCVs are less than 120 nm in height and their assembly and disassembly is a very dynamic process [17]. The answer should also ideally come from a direct measurement of their mechanical properties *in vivo* but from my knowledge no microscopy/spectroscopy techniques exist that would allow researchers to investigate such properties under these conditions. Eventually, I have initiated the settlement of this debate by investigating CCV and its derivatives *in vitro* using AFM force spectroscopy and finite element analysis.

1.2.2 Cell nucleus

Besides my interest for the CME mechanics, I have also focused on quantifying how the hereditary genetic code of single cell nuclei responds to external forces. In eukaryotic cells, cells with a nucleus which differ from prokaryotic cells like bacteria that do not possess one, the nucleus houses the hereditary genetic code in the form of DNA-protein complexes named chromatin. It also stocks the necessary machinery for the replication of the chromosomes, chromatin packaged into thread-like structures, and the expression of the information contained in the genes. It is, by far, the largest organelle of a eukaryotic cell, around 10 µm in diameter, 2 orders of magnitude bigger than clathrin polyhedra. Figure 1.3 shows a typical representation of a nucleus.
The nucleus is surrounded by a double membrane called nuclear envelope. The inner membrane is covered by the lamina, a dense fibrillary network that mechanically supports the nucleus structure. The external surface, on the other hand, is connected to the

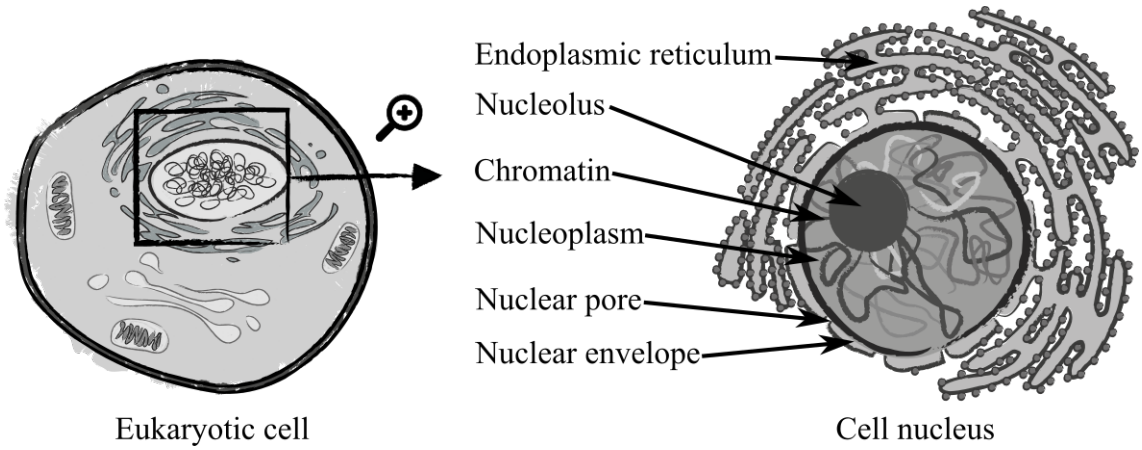

Figure 1.3: Representation of a nucleus. *A nucleus encloses the chromatin inside a nuclear envelope containing nuclear pores. The ribosomes are synthesised in the nucleolus and routed later towards the endoplasmic reticulum.*

endoplasmic reticulum where ribosomes, one of the most complex molecular machineries, synthesise proteins. The ribosomes are assembled in the nucleolus which is a compact region of the nucleus rich of condensed chromatin. The internal and external membranes are fused in a regular manner leading to the formation of nuclear pores that, despite their littleness, approximately 120 nm in diameter and approximately 50 nm in height, allow vital exchanges between the nucleus and the cell. Similarly to clathrin, nuclear pores are considered as gatekeepers.

The nucleus' size and shape get modified during growth, differentiation and migration of the cell while experiencing forces from the cell itself and the surrounding environment [18]. Even though there is evidence that such mechanical signals are used to control gene expression [19, 20, 21, 22], it remains ambiguous how mechanics are transduced through the nucleus. To better understand its behaviour under stress, I have employed AFM micro-rheology, finite element analysis and fluorescence microscopy to accurately quantify the mechanical properties of individual isolated cell nuclei.

1.3 Biophysical techniques in this thesis

In this section, I will succinctly present the different biophysical techniques that I have employed to characterise the mechanical properties of clathrin cages and cell nuclei. Since AFM plays a crucial role in all investigations and is a rather complex technique, it also has a dedicated chapter, see chapter 2. Most of the other techniques described here are standard but they were often modified and adapted to my needs.

1.3.1 Michelson interferometer

During my second year, I had the opportunity to join SmarAct GmbH, a German company based in Oldenburg, to work on a novel system for the calibration of AFM cantilevers. To this end, I have developed with Dr. Iwan A.T Schaap a raster-scanning vibrometer based on an existing compact Michelson interferometer (http://www.smaract.com/picoline/picoscan/, patent pending).

A Michelson interferometer, invented in 1887 by Michelson and Morley [23], is an optical system capable of quantifying the changes in distance separating two surfaces. In a minimalist configuration, it only consists of a light source, a beam splitter, a reference mirror and a detector, a simplified version being displayed in Figure 1.4. The incident light goes through a beam splitter which divides the incoming beam into two new ones that are either reflected off a reference mirror or off the sample. Both reflected beams pass back through the beam splitter which combines their intensity and where interference (constructive or destructive) takes place. In an aligned set up, the combined intensity measured, I, is related to the distance the light had travelled, Δd, by $I \propto \cos(2 \cdot \pi \cdot \Delta d / \lambda)$ with λ the wavelength of the incident beam.

An interferometer can also be used to precisely measure the amplitude of oscillations of a mechanical system down to the picometre range. To this end, many commercial instruments use a Fourier transformation of the changes in distance measured while the system

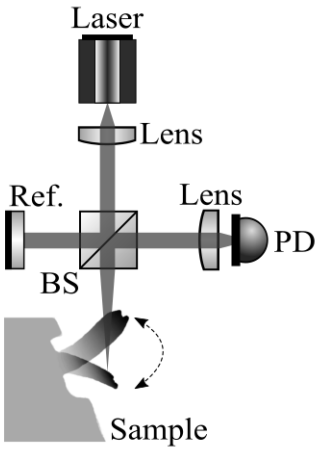

Figure 1.4: Compact Michelson interferometer. *The system includes laser source, a beam splitter (BS) which is used to divide the incident beam into two beams that are reflected off the reference mirror (Ref.) and off the sample. The reflected beam that combines the intensities is routed to a photodetector (PD).*

is thermally or actively excited. In our case we have chosen to benefit from a digital lock-in amplifier which is a component capable of extracting a signal with a known carrier from a noisy environment [24]. It consists of a demodulator that multiplies the input signal with a reference carrier followed by a combination of low-pass filters to isolate a specific frequency component and thus to extract the amplitude and phase of vibrations on-the-fly.

1.3.2 Atomic force microscopy

Atomic force microscopy, developed in 1986 by Binnig et al. [3], is a powerful but rather complex technique that employs a probe to scan a surface. It reveals topography far beyond the maximum resolution of optical microscopy techniques while being also capable to extract other physical properties of a sample without altering its integrity.
A meaningful metaphor to explain this technique is to compare its working principle with how blind people "feel" their environment. Both use a probe, a micrometre lever or a white cane, that is put in motion in a raster fashion to sense the surrounding. If no obstacles are felt, the probe is moved towards the unknown. However, if the displacement is blocked, which indicates that an object had been found, adjustments are done in consequence to overcome this barrier while keeping the probe at vicinity of the surface. Knowing constantly the position of the probe during the scan meshes precisely the world the probe had been put in. In the case of AFM single atom resolution can be achieved [25, 26].
In practise, the motion of the AFM probe is monitored with optics, see Figure 1.5.

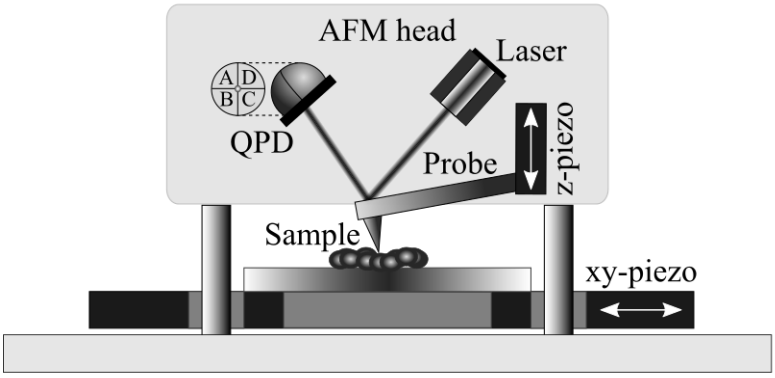

Figure 1.5: Working principle of an AFM. *A laser is focused on the probe, then reflected on a quadrant photodiode (QPD) to measure the deflection of the lever. In dynamic imaging mode, the probe is actively oscillated and raster-scanned thanks to the xy-piezo stage. The signal from the QPD is fed to a lock-in amplifier that extracts the amplitude and the phase. It also controls the feedback loop operating the z-piezo.*

A laser is focused on the free end of the probe and reflected on a four-section segmented photodiode. The latter converts the bending (lateral and normal) of the cantilever into an electrical potential. This signal can be used as feedback input to allow an active adjustment of the position of the probe with respect to the surface while scanning.
Besides its obvious advantage over optics regarding sensitivity and achievable resolution, AFM can also be used to reveal electrical, magnetic and mechanical properties of a sample in air, vacuum and liquid. Aqueous media allow to investigate biological systems in a native-like environment which, in the case of this thesis, has been intensively used.

1.3.3 AFM combined with fluorescence microscopy

Fluorescence is a property of certain molecules to emit light after absorption of photons of higher energy/shorter wavelength. This red-shift, also called Stokes shift, is caused by a partial loss of the original energy during inelastic collisions between incident photons and surrounding molecules [27]. In fluorescence microscopy, the Stokes shift is exploited to selectively collect the emitted light from the sample while blocking the excitation light with optical filters. If the sample itself is not fluorescent by nature, as for clathrin and the cell nucleus, chemical dyes are bound to allow fluorescence investigations.
Special fluorescence microscopy techniques can be employed to overcome the theoretical maximum resolution limits of conventional optical microscopy, on the order of the wavelength of the incident beam (usually between 350 and 800 nm), such as TIRF [28], FRET [29, 30], PALM [31], STORM [32], STED [33] and fPALM [34]. These techniques allow resolution down to the nanometre-scale. Nonetheless, none of them competes yet with the atomic resolution of AFM.
For this thesis work, fluorescence was used to identify molecules and boundaries by selective staining which allowed me to properly quantify the initial contact area between the nuclei and the supporting surface prior to the AFM experiments. This is one among multiple corrections that was applied to the common Hertz contact mechanics model [35] to improve the accuracy of the extracted nuclei mechanics, see chapter 6. Here, I combined AFM with a fluorescence microscope which allowed me to align precisely the position of the AFM probe with the centre of the camera field of view and conduct AFM measurements while recording fluorescence images. However, simply mounting an AFM on top of a conventional inverted optical microscope leads to unacceptable high noises (from camera, which has an integrated fan to cool the CCD chip) and temperature gradients

levels (from laser source) that would limit the resolution of AFM imaging. To overcome this, the AFM and scanner were affixed on a custom made inverted microscope that can be operated in epifluorescence [36] or total internal reflection fluorescence [28] (not used) and to prevent transmission from mechanical and thermal noise, the cooled EM-CCD camera and the laser source were decoupled from the AFM, as shown in Figure 1.6.
The excitation of the fluorescent dyes was performed by laser light coupled into the optical path. Focusing took place with an objective z–piezo element operated in open-loop to avoid vibrations caused by a close-loop operation. A galvo mirror, used to select the angle of illumination, was placed in a conjugate plane of the focal plane of the objective. To properly select the emitted light from the fluorescent dyes, an optical band pass filter specific to the chemical dye in used was integrated within the optical path of the camera. The image acquisition of the camera also triggered the galvo mirror to switch off the illumination between frames which helped to reduce the photobleaching of the fluorescent dyes.

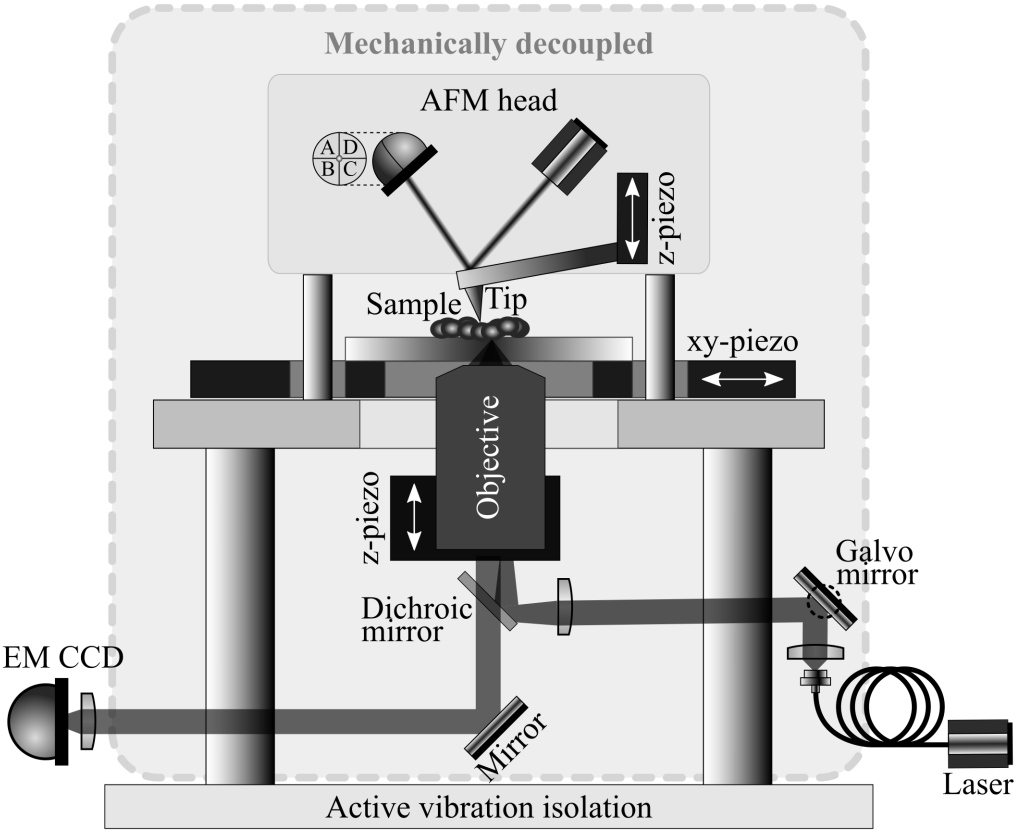

Figure 1.6: Combined atomic force microscopy and fluorescence microscopy. *The AFM is affixed on top of a custom inverted optical microscope. The laser source and EM CCD camera are mechanically decoupled from the microscopes to reduce parasitic noise.*

1.3.4 Finite element analysis

Finite element analysis (FEA) is a method for the modelling of physical systems in a virtual environment in order to numerically solve complex physical models. Nowadays, computer performances are such that computation time has drastically reduced, from several days [37] to a couple of hours for similar models, which allows scientists to easily perform preliminary simulation experiments before actually testing a set-up and/or to compute analytical models to describe multiphysics problems with complex constrains.

Previously, FEA has been successfully implemented to extract valuable information regarding the behaviour of microtubules, tubular structures present in cells, under stresses [37]. In the case of this thesis, it was employed to mimic AFM mechanical measurements on clathrin cages and nuclei, as discussed in chapter 4, chapter 5 and chapter 6. During FEA, polyhedral meshes of the tip and the samples were generated and the non-linear load from the modelled probe was calculated at each of the nodes.

Examples of FEA on a clathrin cage, in 3D, and on a nucleus, in 2D, are shown in Figure 1.7a and Figure 1.7b respectively. In Figure 1.7a, the modelled parabolic tip is lowered to deform the polyhedron while the resulting stress is monitored (colour gradient). In Figure 1.7b, symmetries such as mirror symmetry and radial symmetry are used to reduce the size of the model and thus the computation time. The tipless cantilever modelled as a plate is lowered to compress the sphere. The triangular mesh is optimised to increase the accuracy at the boundary of the sphere while keeping a computation time low by reducing the mesh resolution at the sphere core.

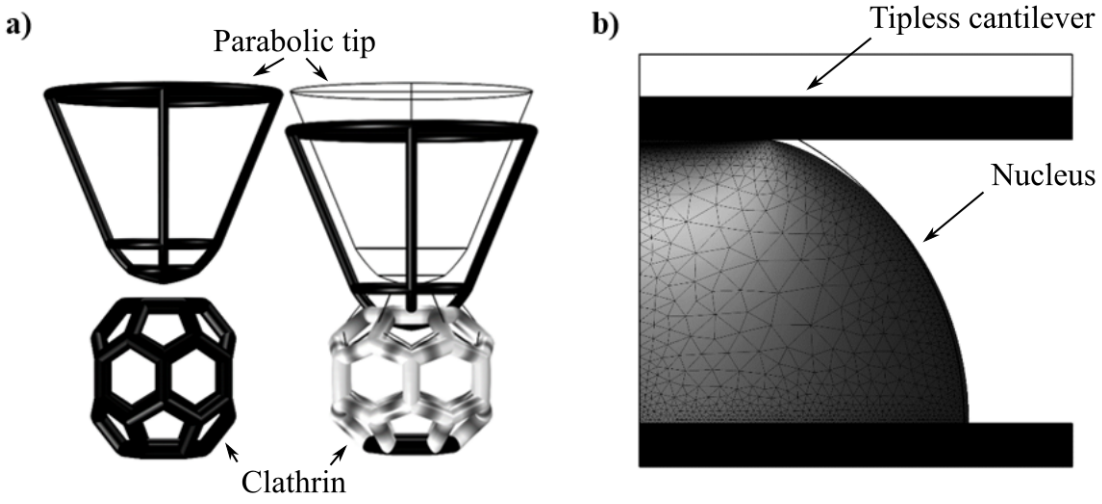

Figure 1.7: Example of finite element models. *3D FEA on clathrin hexagonal barrel and 2D FEA on cell nucleus shown in (a) and (b) respectively.*

1.4 Thesis motivation

My research has been aimed at the successful application of atomic force microscopy and the development of new AFM-based biomechanical methods to measure the mechanical properties of soft biological samples.

More specifically, I chose to investigate clathrin and the cell nucleus not only because these two samples are closely related to the work of the hosting laboratory [13, 38] but also because important questions regarding their mechanics are still pending, as stated in subsection 1.2.1 and subsection 1.2.2, due to the complexity they offer but also because of the lack of proper methods and models to accurately measure and describe their behaviour under stress.

On one hand, a deeper understanding of the entry pathway of a cell is of prime interest to get a better insight of the process itself and thus its potential malfunctioning. For instance, viruses such as Ebola can hijack this pathway to infect the cell [39]. As a result, having a clearer description of the CME could potentially lead to the development of new drugs and bio-inspired delivery vehicles to inhibit or enhance the invagination of foreign bodies.

On the other hand, a comprehensive description of how forces are transduced into single cell nuclei from various cell lines would conceivably give rise to new techniques to identify defective cells. Indeed, being able to establish a common behaviour among nuclei mechanics would allow to use them as mechano-sensor while investigating whole cells: by simply looking at (and quantifying) the deformation of the nucleus, the forces that act on it can be deduced. Finally, the quantification of the response under stress of various nuclei may lead to the development of new medicines based on the nucleus mechanical alteration.

1.5 Outline of this thesis

This thesis is organised as follow:

In **chapter 2**, the working principle of atomic force microscopy briefly presented in subsection 1.3.2 is described in more details. First I will focus on the van der Waals interactions that affect the AFM probe behaviour while being close to a surface. Then, the tapping imaging mode, which was exclusively used during all experimental works, is detailed. Finally, AFM force spectroscopy that allowed me to extract the mechanical properties of clathrin polyhedra and cell nuclei is explained.

In **chapter 3**, a new technique to calibrate the force constants of AFM cantilevers is introduced. It is based on a novel raster-scanning interferometer as described in subsection 1.3.1. Unlike the common calibration method described in chapter 2 that requires to perform a force curve on a hard surface to calibrate the sensitivity of the system and thus possibly affect the tip geometry, this approach does not need any physical contact. Furthermore, besides being used for calibration, raster-scanning interferometry can be employed to study the bending modes of cantilevers that have more complex shapes than that of a common and well-theorised rectangular one. Without taking into account the development of the instrument itself, this chapter represents a 3 months project.

In **chapter 4**, AFM in liquid is used to study the mechanical properties of clathrin polyhedra. The amplitude modulated imaging mode as described in chapter 2 is now employed to generate topographies of various types of clathrin assemblies at unprecedented resolution. While local force spectroscopy is performed in a raster-scan fashion to allow the mapping of the mechanical properties of the cages, FEA is used in parallel to overcome the current lack of physical models to characterise inhomogeneous polyhedral structures. This 1.5 year project was performed as a collaboration between the groups of Dr. Iwan A.T Schaap and Dr. Philip Dannhauser from University College of London (London, United-Kingdom).

In **chapter 5**, additional experiments on clathrin using low-force AFM in liquid are presented. I investigate the effect of light chain isoforms, with and without neuronal inserts, and accessory proteins (Epsin, AP180 and Auxilin) on the mechanical properties of reconstituted clathrin cages. In addition, I measure the impact of calcium, a promising agent in altering the structural property of the clathrin triskelion hub, on the cages mechanics. This 3 months project is the outcome of a collaboration between the groups of Dr. Iwan A.T Schaap and Dr. Philip Dannhauser from University College of London (London, United-Kingdom).

In **chapter 6**, I combine AFM spectroscopy and fluorescence microscopy to extract the complex viscoelastic properties of nuclei from different cell lines. Tricks to overcome the limitations of the AFM Z-scanner are employed to perform localised AFM force measurement at the apex of the nuclei, which heights exceed the scanner range, using tipless cantilevers. The force spectroscopy includes a dwell time integrating multiple sinusoids

with increasing oscillatory frequency to measure the frequency dependency of the mechanical response of the nuclei. The measurements are performed at multiple indentation depths to map structural differences within the nuclei. FEA is also used to support the measurements. This 9 months project arises from a collaboration between the groups of Dr. Iwan A.T Schaap group and Dr. Chris Toseland from the University of Kent (Canterbury, United-Kingdom).

Due to the variety of biological constructs that are addressed in this thesis each chapter contains an individual conclusion to put the biomechanical findings in the correct context.

2

Atomic Force Microscopy

This chapter aims to provide sufficient physical understanding of amplitude modulated (tapping) imaging mode and force spectroscopy techniques which were used in this experimental work. For a detailed derivation of each of the equations presented and an extended description of the AFM itself, the relevant references are included.

2.1 Introduction

In atomic force microscopy, all things that matter are the interactions between the tip, located at the free end of a flexible cantilever, and the sample. Depending on the distance separating them, the material of the tip as well as the one of the sample, and the surrounding medium, multiple forces can be felt that will affect the cantilever behaviour. The list includes magnetic and electrostatic forces, chemical bonding, surface charge screening and many more but I will only introduce the van der Waals interactions which often dominate the response [40].

Van der Waals forces are weak electrical interactions that become prevalent when the AFM probe is relatively close to the sample surface ($1 < z < 10\,\text{nm}$, with z the distance tip-surface) [41, 42]. They are included in the Buckingham potential [43] which states that the tip will first be sensitive to the van der Waals long-range attractive forces and then short-range repulsive ones caused by the Pauli repulsion. The latter is the necessary condition to overcome possible overlapping of electronic orbitals between atoms from the tip and the sample. Analytically, the Buckingham potential, $U_B(z)$, as function of the tip-sample distance, z, is proportional to [43]:

$$U_B(z) \propto e^{-\frac{z}{z_0}} - \left(\frac{z_0}{z}\right)^6 \tag{2.1}$$

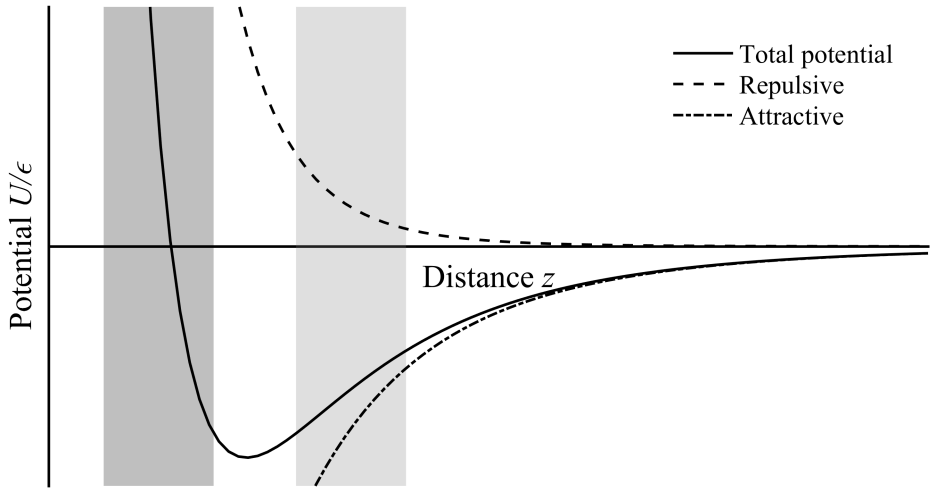

Figure 2.1: Electrostatic interactions arising when the probe of an atomic force microscope is in vicinity of a surface. *They are described by the Buckingham potential, solid line, which is the combination of long-range attractive forces, dashed-dotted line, and short-range repulsive forces, dashed line, due to van der Waals' interactions and Pauli's repulsion respectively. The potential is normalised, with ϵ the depth of minimum energy.*

where z_0 is the interatomic distance at equilibrium, z^{-6} denotes the van der Waals attraction while the exponential term reflects the Pauli repulsion, shown in Figure 2.1.
In fact, besides defining the tip-sample interaction, this potential can also be used to describe the different AFM imaging modes in air [44, 45]. Static modes are employed in the Pauli region ($dU_B(z)/dz < 0$, in dark grey in Figure 2.1) while dynamic modes refer to the van der Waals region ($dU_B(z)/dz > 0$, bright grey in Figure 2.1).

2.2 Amplitude modulated (tapping) imaging mode

In static imaging mode the tip is permanently in contact while being raster-scanned. Eventually, this may lead to a deterioration of the sample due to high lateral forces and/or possible detachment and drag of the sample if these lateral forces exceed the attractive forces that keep the sample in a steady state. This makes the static imaging mode unsuitable for the study of biological nano-objects that are fragile and not firmly attached to the substrate.
In dynamic imaging mode, on the other hand, the cantilever is actively oscillated and the probe either only intermittently touches the sample (tapping mode, repulsive interactions)

or remains far enough to avoid any possible contact (non-contact amplitude modulated mode, attractive interactions) [46]. This greatly reduces the applied forces and the above-mentioned consequences. Because of this feature, it is usually preferred in biomechanics. Among the different dynamic techniques, I exclusively employed tapping mode. The latter requires to monitor the motion of the cantilever while having a feedback routine that keeps the oscillation amplitude constant during imaging. This feedback routine controls the z-piezo scanner that adjusts the distance between the cantilever and the sample.

2.2.1 Cantilever motion in air

- **Bending modes of AFM cantilevers**

In tapping mode, and actually in all dynamic imaging modes, the cantilever is actively excited. The induced vibrations cause the lever to deflect with a shape that depends on its geometry and the input frequency of excitation [47]. Usually the first resonance frequency mode is favoured because it often has the sharpest resonance thus higher sensitivity when compared to higher resonance modes as well as a lower effective spring constant which helps to minimise sample damage. However, it is possible to drive the cantilever at higher harmonics and since the cantilever has an infinite number of resonance modes, it also has multiple ways to deflect, called bending modes, which gain in complexity when the resonance mode increases [48].

The shapes of the bending modes, $s_n(x)$ with x the distance from the base of the cantilever and n the n^{th} bending mode, are analytically derived from the Euler-Bernoulli beam theory [49] and, in the case of rectangular cantilever of length, L, are proportional to:

$$s_n(x) \propto \cosh(\beta_n \cdot x) - \cos(\beta_n \cdot x) + \frac{(\cos(\beta_n \cdot L) + \cosh(\beta_n \cdot L)) \cdot (\sin(\beta_n \cdot x) - \sinh(\beta_n \cdot x))}{\sin(\beta_n \cdot L) + \sinh(\beta_n \cdot L)} \tag{2.2}$$

where $\beta_n = \left(\rho \cdot w_n^2 / E \cdot I\right)^{1/4}$ with E the cantilever's elastic modulus, I the second moment of area of the cantilever's cross section, ρ the cantilever's mass per unit length and w_n the natural frequencies of the cantilever.

Eq.(2.2) has only non-trivial solutions if $\cosh(\beta_n \cdot L) \cdot \cos(\beta_n \cdot L) = 0$. The roots of this non-linear equation allow to express the natural frequencies with respect to the first natural frequency w_0. For example, the second natural frequency, w_1, is defined as $w_1 \approx 6.27 \cdot w_0$, the third one as $w_2 \approx 15.56 \cdot w_0$, etc.

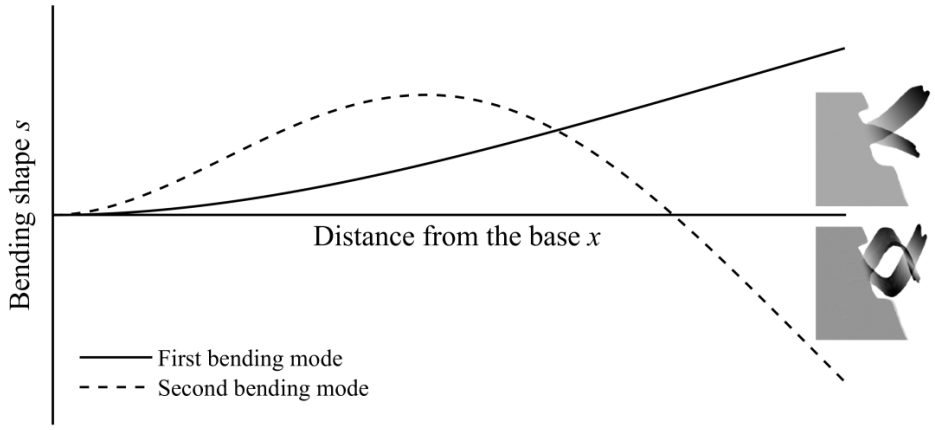

Figure 2.2: First two bending modes of a rectangular cantilever. *2D representation of the deflection of a cantilever if driven at its first and second resonance frequencies as derived from the Euler-Bernoulli beam theory. Insets: 3D deflection images of the first bending mode and second bending modes of a RC150 biolever from Olympus (Tokyo, Japan). Each image shows the maximum deflection with a phase shift of π. The images were recorded by raster-scanning interferometry.*

Figure 2.2 shows the shape of the induced first two bending modes calculated with Eq.(2.2). To facilitate the visualisation of the motion of the cantilever 3D images of its deflection are included. The latter were measured using our novel raster-scanning interferometer, described in chapter 3. In this thesis, I exclusively employed tapping mode using the first resonance frequency of the cantilevers.

- **Influence of the Buckingham potential on the cantilever oscillation**

The movement of a cantilever is commonly described by a driven damped harmonic oscillator. It is characterised by a non-linear second order differential equation of motion that, when the probe is far from sample, is written as [50]:

$$far \Rightarrow \ddot{z(t)} + \frac{w_0}{Q} \cdot \dot{z(t)} + \frac{k_c}{m_c} \cdot z(t) = \frac{F_{drive}(t)}{m_c} \tag{2.3}$$

where $z(t)$ is the tip-sample distance, the dots denote the differentiation with respect to the time t, w_0 is the undamped resonance frequency of the cantilever, Q the quality factor that characterises the cantilever's bandwidth relative to its centre frequency, k_c the cantilever force constant, m_c its mass and $F_{drive}(t)$ the driving force of excitation. A schematic of a harmonic oscillator is depicted in Figure 2.3.

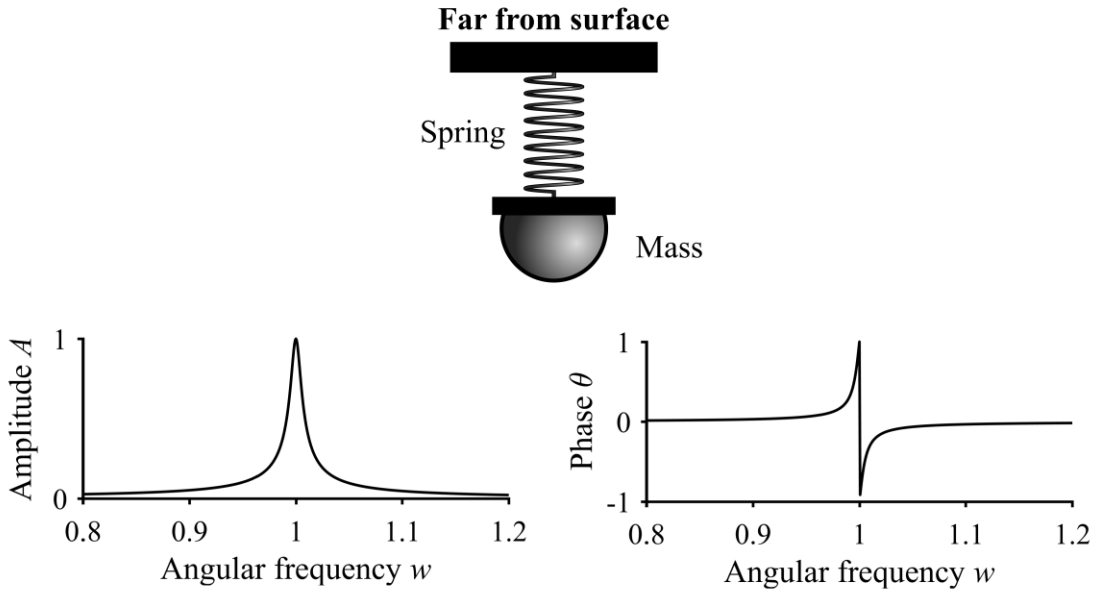

Figure 2.3: Cantilever nominal response. *The cantilever can be seen as an almost perfect harmonic oscillator described by a mass and an ideal spring. The amplitude, A, and the phase, θ, of the oscillations are induced by the intrinsic properties of the cantilever. The amplitude, phase and angular frequency are normalised.*

When the tip is close to the surface of the sample, during scanning for example, it also encounters the Buckingham potential described earlier. Eq.(2.3) gains then an additional term, $k_{ts}(z) = -\partial F_{ts}/\partial z|_{z=z_0}$ (which is positive in the van der Waals region and negative in the Pauli region), describing the tip-surface force and treated as an additional damper:

$$close \Rightarrow \ddot{z(t)} + \frac{w_0}{Q} \cdot \dot{z(t)} + \frac{(k_c - k_{ts})}{m_c} \cdot z(t) = \frac{F_{drive}(t)}{m_c} \tag{2.4}$$

Eq.(2.4) has a similar form as Eq.(2.3). The only difference arises from that the effective force constant of the cantilever, $k = k_c - k_{ts}$, depends now on the tip-sample interaction, thus the distance separating them. The general solutions have the sinusoidal oscillation form of:

$$z(t) = A \cdot \cos(w \cdot t - \theta) \tag{2.5}$$

where

$$A = A_{drive} \cdot \frac{w'^2}{\sqrt{(w'^2 - w^2)^2 + (w \cdot \frac{w'}{Q})^2}} \tag{2.6}$$

and

$$\theta = \arctan\left(\frac{w \cdot \frac{w'}{Q}}{w'^2 - w^2}\right) \tag{2.7}$$

with A_{drive} the driving amplitude and w' the damped angular resonance frequency. Assuming that $|k_{ts}| \ll k_c$, then $w' = w_0 \cdot (1 - k_{ts}/(2 \cdot k_c))$ with $w_0 = 2 \cdot \pi \cdot f_0$ the undamped angular resonance frequency. The resonance frequency of the cantilever while in vicinity of a surface is then shifted by:

$$\Delta f = \frac{w' - w_0}{2 \cdot \pi} = -\frac{f_0 \cdot k_{ts}(z)}{2 \cdot k_c} \tag{2.8}$$

In the case of van der Waals' forces, $k_{ts} > 0$ and thus $\Delta f < 0$ while for repulsive potential, $k_{ts} < 0$ and $\Delta f > 0$. In other words, the resonance curve of the cantilever at equilibrium is either shifted to the left or to the right of its resonance frequency, as shown in Figure 2.4. Thus, when the probe is close to a surface, the interaction tip-sample induces a reduction of the oscillation amplitude of the AFM lever which can be monitored and used as feedback parameter. In a different imaging mode, namely the frequency modulation AFM, the frequency shift is used as feedback parameter instead [51].

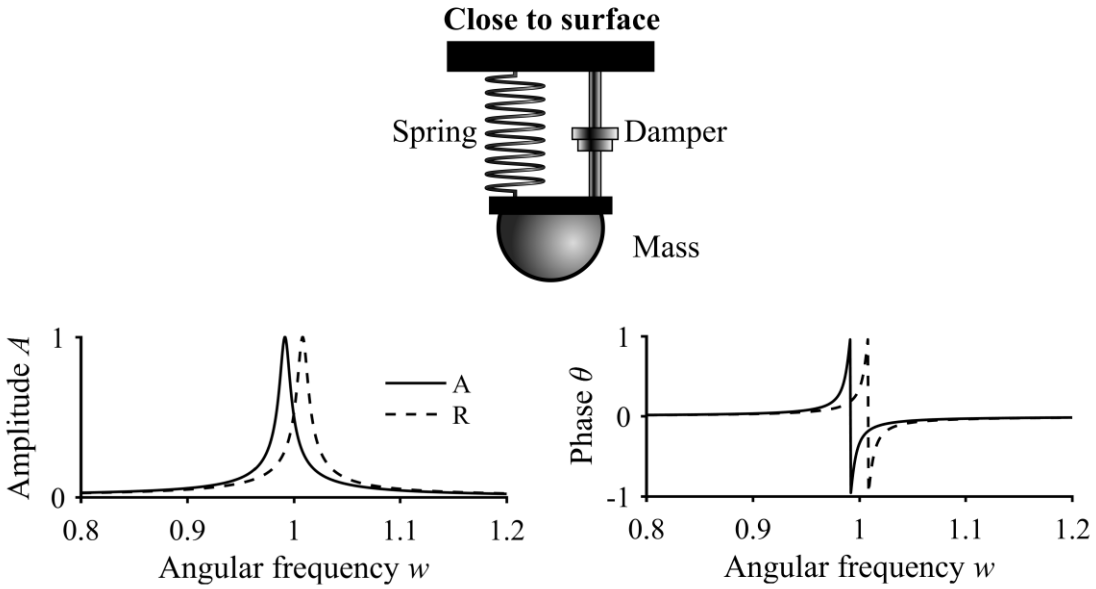

Figure 2.4: Influence of the Buckingham potential on the oscillations of the cantilever. *The amplitude and the phase are influenced by the type of interactions, whether attractive from the van der Waals forces (A, plain line), or repulsive from the Pauli repulsion (R, dashed line). The amplitude, phase and angular frequency are normalised.*

2.2.2 Cantilever immersed in liquid

In liquid the cantilever is also affected by hydrodynamic forces. These forces are related to the viscous behaviour of the fluid as well as squeeze forces, which are drag forces occurring when the cantilever is oscillating close to a surface, when imaging in tapping mode for example. They have a significant impact on the effective mechanical properties of the cantilever and thus its general behaviour.

- **Mechanical properties**

The resonance frequency of a cantilever in air, f_{air}, is written as:

$$f_{air} \propto \sqrt{\frac{E \cdot I}{b \cdot \rho_c \cdot h}} \tag{2.9}$$

with E the Young's modulus of the cantilever, I the second moment of area of the cantilever's cross section, b the width of the cantilever, h its thickness and ρ_c its density. In liquid however, the resonance frequency, f_f, is expressed as [52]:

$$f_f \propto \sqrt{\frac{E \cdot I}{b \cdot \rho_c \cdot h + \rho_a}} \tag{2.10}$$

Here, ρ_a is an additional mass density due to the fact that when the cantilever oscillates, a fraction of the surrounding liquid moves as well, increasing the effective mass of the system. Since ρ_a is positive and non-zero when the cantilever is immersed in liquid, the resonance of the cantilever unavoidably decreases.
Additionally, the total quality factor Q_{total} equals [52]:

$$Q_{total}^{-1} = Q_c^{-1} + Q_f^{-1} \tag{2.11}$$

Generally, the quality factor of cantilevers, Q_c, is much higher than the one of the surrounding fluid, Q_f, and the above equation can be reduced to:

$$Q_{tot} \approx Q_f \tag{2.12}$$

The surrounding liquid broadens the resonance peak of the cantilever up to two orders of magnitude. It results in an effective cantilever that has a lower quality factor which makes the AFM imaging in liquid less sensitive to a change in amplitude than in air. On the other hand, it suggests that the stored energy of the cantilever is rather small and allows

to gently touch the sample instead of hammering it. A fact which is obviously welcomed when imaging soft biological samples such as clathrin.

However, while both the resonance frequency and the quality factor are affected by the liquid environment, it should be noted that the stiffness of an immersed cantilever is nearly identical to the one in air [53].

- **Cantilever motion**

The hydrodynamic force consists of the viscous friction of the liquid, $F_v(t)$, and the squeeze force mentioned earlier, $F_s(t)$, such as [54]:

$$F_h(t) = F_v(t) + F_s(t) \tag{2.13}$$

with

$$F_v(t) = -\rho_a \cdot \ddot{z(t)} \tag{2.14}$$

$$F_s(t) = -c_a \cdot \dot{z(t)} \tag{2.15}$$

where $z(t)$ is the tip-sample distance over time, the dots denote the differentiation with respect to the time t, ρ_a is the additional mass density previously introduced and c_a an additional damping coefficient due to the presence of the liquid.

The additional damping coefficient, c_a, has two components: one when the tip is far from the surface and thus the squeeze force is small but homogenous along the cantilever, c_∞, and an other which depends on the transient distance between the cantilever and the surface, c_s, such as $c_a = c_\infty + c_s$. Far from the surface, c_s can be neglected and the total force exerted on the tip, $F_{total}(t)$, can be written as:

$$far \Rightarrow F_{total}(t) = F_{drive}(t) + F_v(t) + F_s(t) = F_{drive}(t) - \rho_a \cdot \ddot{z(t)} - c_\infty \cdot \dot{z(t)} \tag{2.16}$$

with $F_{drive}(t)$ the drive force bringing the cantilever holding the tip into oscillation.

When the tip is close to a surface, c_s is no longer negligible and must be included. In addition, and as previously mentioned in subsection 2.2.1, the tip is now sensitive to the tip-sample interaction, $F_{ts}(t)$. Thus, Eq.(2.16) when close to a surface gains in complexity and is now written as:

$$close \Rightarrow F_{total}(t) = F_{drive}(t) - \rho_a \cdot \ddot{z(t)} - (c_s + c_\infty) \cdot \dot{z(t)} + F_{ts}(t) \tag{2.17}$$

Despite their simple appearance, both Eq.(2.16) and Eq.(2.17) are rather complex, especially because I reduced their definition to the force exerted on the tip, omitting the overall behaviour of the whole cantilever, but analytical solutions of the Bernouilli-Euler equation taking into account the hydrodynamic forces can be derived using the modal analysis for a continuous beam model [55].
In chapter 6, I directly measured the hydrodynamic forces exerted on a cantilever prior to investigate the mechanical properties of the cell nuclei. This was an important step as this damping depends on the driving frequency of oscillations and influences the accurate extraction of the cell nucleus mechanics.

2.2.3 Optical read-out system

The deflection of the cantilever is commonly measured with optics with a laser beam being focused on the reflective back side of the free end of the cantilever [56]. The reflected laser beam is mirrored onto a segmented quadrant photodiode that translates the laser spot into normal and lateral signals corresponding to the bending and the torsion of the cantilever respectively, see Figure 2.5. The electrical potential measured is then converted into length units with the photodiode sensitivity, see chapter 3 for more details.
In dynamic imaging mode, the cantilever is actively excited and the oscillation amplitude and phase are extracted after feeding the deflection signal into a dual-phase lock-in amplifier [57]. In tapping imaging, the amplitude is used as feedback input [58] to keep the amplitude constant. The feedback loop adjusts the position of the z-piezo scanner in consequence.

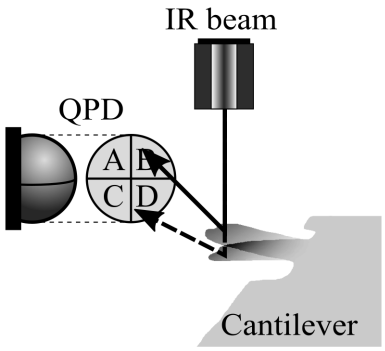

Figure 2.5: Optical read-out system principle. *A laser is focused on the free end of the cantilever. It is reflected onto a quadrant photodiode (QPD) that converts the reflection angle into an electrical signal. The QPD sensitivity is used to convert the potential measured into length units.*

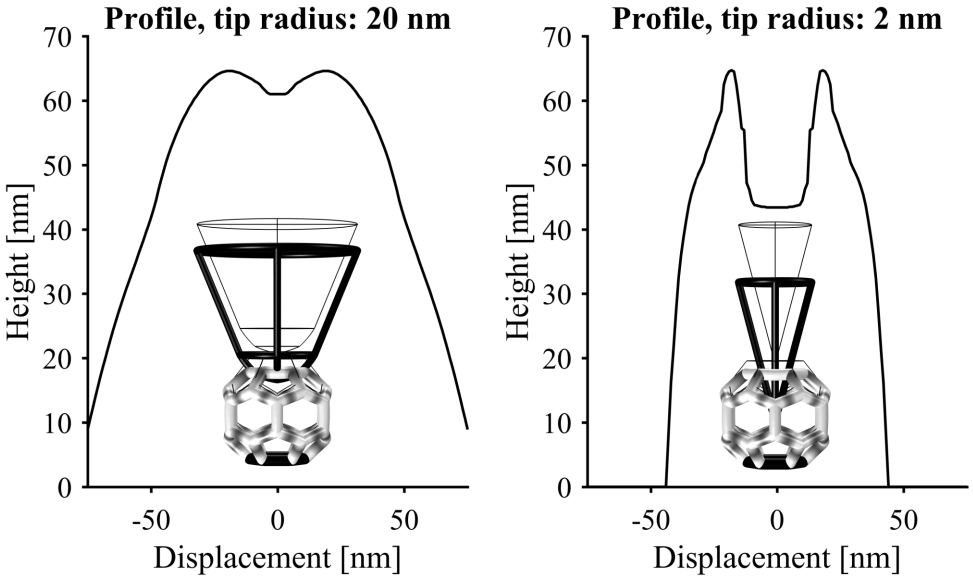

Figure 2.6: Case study of AFM resolution on modelled clathrin hexagonal barrel. *The cage is* 42 nm *wide but appears bigger when probed:* 75 nm *and* 45 nm *with a probe radius of* 20 nm *and* 2 nm *respectively.*

2.2.4 Lateral resolution

In AFM, the maximum achievable lateral resolution depends heavily on the radius of the probe [59] rather than on the scanner efficiency which has nowadays picometre resolution. As a rule of thumb, the sharper the tip is the more details the AFM can resolve and less pronounced are the tip-sample convolution [60], as shown in Figure 2.6.

2.3 Force spectroscopy

An AFM is not only capable of imaging, it can also be used as spectroscope to extract valuable information such as mechanical, electrical and magnetic properties of a sample. In this thesis I exclusively focus on the mechanical properties.

In AFM, when referring to mechanical properties, we mostly speak about the way a system is deformed under normal load and usually employ the terms stiffness and Young's modulus:

- The stiffness of an object is its capacity of handling deformation. This is a structural property which is described by Hooke's law and written as:

$$F = k \cdot \vec{x} \tag{2.18}$$

where F is the applied force on the object, k the stiffness or spring constant and $\vec{x}$ the displacement induced by the force.

- The Young's modulus, E, corresponds to the elastic resistance to extension/compression under an applied load of an object. This is a material property that be described by:

$$E = \frac{F/A}{\Delta L/L_0} \tag{2.19}$$

where A is the area of the cross-section perpendicular to the applied force F, ΔL is the deformation normalised by the original length of the sample L_0.

2.3.1 Calibration of the cantilever

To measure the mechanics of a sample, the deflection in length unit of the cantilever has to be converted into forces. The last are deduced from Hooke's law via $F = -k_c \cdot d$ where k_c is the spring constant of the cantilever and d the measured deflection. The spring constant of a cantilever is provided by the cantilevers' manufacturers. In practise however, the actual value can differ significantly from the one given and for an accurate conversion, each cantilever has to be calibrated. To this end, the Sader method [61] and the thermal noise method [62] are usually applied, both providing a relative error less than 10 % [63]. I will focus on the thermal noise method developed by Hutter and Bechhoefer [62] which is again based on the study of a harmonic oscillator in equilibrium.

The haphazard motion of the molecules from the surrounding medium, called Brownian motion, imparts random impulses to the cantilever which in turn starts to resonate. Based on the equipartition theorem, the potential energy equals the thermal energy and the spring constant of the cantilever can be written as:

$$k_c = \frac{k_B \cdot T}{\langle d^2 \rangle} \tag{2.20}$$

where k_B is the Boltzmann constant, T the temperature and $\langle d^2 \rangle$ the mean square thermal deflection of the cantilever.

The thermal deflection is usually deduced from the Fourier transformation of the sampled thermal oscillations and the integration of the resonance peak of the first bending mode. An example is given in Figure 2.7 where the thermal deflection of a cantilever is experimentally measured using interferometry, see chapter 3 for more details.

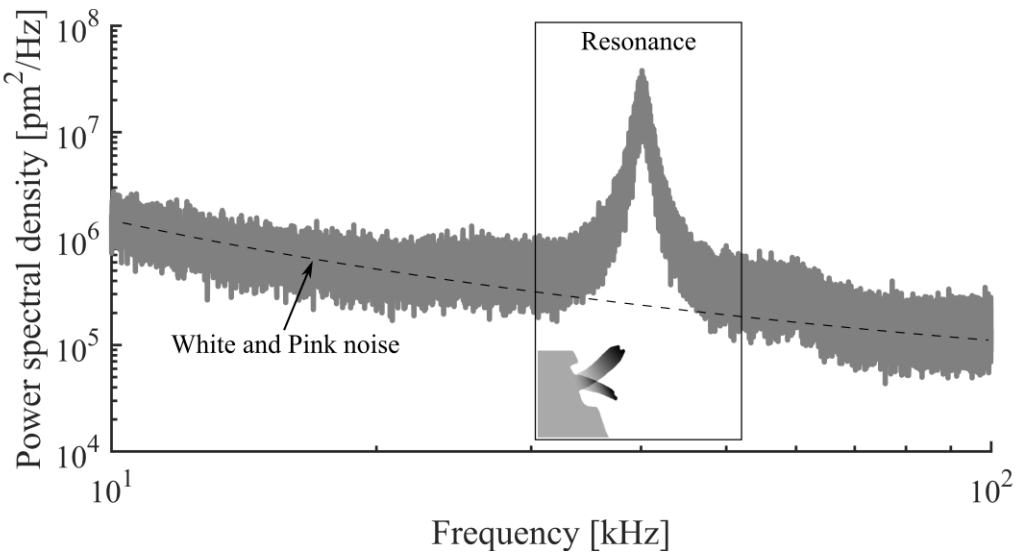

Figure 2.7: Calibration of a cantilever spring constant using the thermal noise method. *The Brownian motion of a RC150VB cantilever measured by interferometry. The stiffness of the cantilever is calculated after integrating the resonance peak. The visible slope from the background noise represents the contribution of white and pink noise.*

2.3.2 Indentation of a sample

Once the cantilever spring constant is known, the mechanical properties of the sample can be obtained by analysing force *versus* z-piezo curves, also called "force curves", [64, 65] that relate the localised deformation of the sample and the forces exerted on the cantilever. In practice, force curves result from the lowering of the tip until it reaches a specific indentation depth. Then the probe is lifted from the surface and brought back to its original position. The indentation is obtained by subtracting the bending of the cantilever from the z-piezo displacement.

Force curves are divided into three parts [66]: the trace, which corresponds to the downward movement of the probe towards the surface of the sample, an optional dwell and finally the retrace, the upward movement of the tip. In most basic AFM force spectroscopy, no dwell time is set and the tip is instantly retracted as in Figure 2.8. However, it is possible to perform more complex force curves that incorporate a specific dwell function to reveal time-depend mechanical properties of the sample, as discussed in chapter 6.

Force curves provide thus a local measurement of the mechanical properties of a sample but similarly to imaging, they can be performed in a raster-scanned fashion to spatially map the sample response to stimuli. This specific scan mode is called force mapping and generates forcemaps.

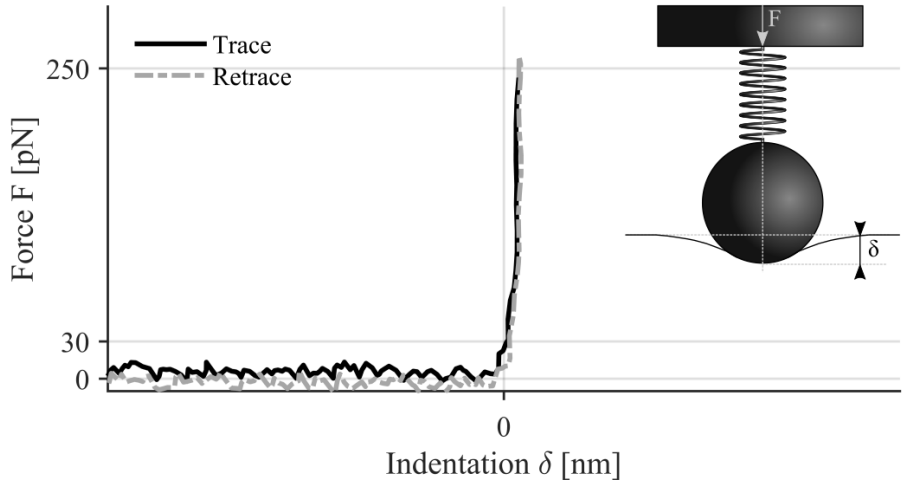

Figure 2.8: Typical force curve obtained after indenting a sample. *Monitoring the force while lowering and retracting the AFM probe results in a force versus indentation curve. In this example, the probe was indenting a very stiff reference substrate such that the force increases very rapidly at minimal indentation. Inset: the sphere represents the AFM probe that is penetrating the material with an applied force, F, up to an indentation depth of δ.*

2.3.3 Mechanical analysis

- **Deducing the stiffness.**

The clathrin cages investigated in chapter 4 and in chapter 5 are considered as hollow spheres indented with a point force. Since the contact area between tip and sample remains constant during the measurement, the sample deformation scales linearly with the applied force. This simplifies the analysis of the force curve because the system (tip and sample) can be seen as two springs in series [67] and the resulting spring constant is:

$$k_{system}^{-1} = k_c^{-1} + k_{sample}^{-1} \tag{2.21}$$

In this scenario, the force felt by the cantilever while indenting clathrin, $F(\delta)$, is:

$$F(\delta) = k_{system} \cdot \delta \tag{2.22}$$

with δ the indentation depth.

Thus the stiffness of the sample can be easily extracted from the slope of the indentation region (region above the 30 pN AFM noise threshold for bio-cantilever [68]) since k_{system} and the stiffness of the cantilever k_c are measured.

- **Deducing the Young's modulus.**

Multiple contact mechanics models can be applied to extract the mechanical properties of a sample if the aforementioned conditions are not met or if the material property of the sample instead of its structural property is of interest. Among the mechanics models, Hertz's one is widely used.

Hertz [35] described the elastic and frictionless contact mechanics between two spheres in interaction that can be extended to a sphere, such as the AFM tip, indenting a half-space, a given sample. The force applied, $F(\delta)$, by a sphere of radius R onto a half-space can be written as:

$$F(\delta) = K \cdot \sqrt{R \cdot \delta^3} \tag{2.23}$$

with δ the indentation depth, and K the effective elastic modulus:

$$K^{-1} = \frac{3}{4} \cdot \left(\frac{1 - \nu_s^2}{E_s} + \frac{1 - \nu_t^2}{E_t} \right) \tag{2.24}$$

where ν_t, ν_s and E_t, E_s are the Poisson's ratios and the Young's moduli of the sphere and the half-space respectively.

Similarly to deducing the stiffness, the Young's modulus from a sample is extracted by fitting the indentation region of a force curve with Eq.(2.23). However, Hertz's model is an over simplified model when describing the mechanical properties of cell nuclei. Indeed, the latter are not purely elastic and the contact boundary conditions during the experiments do not match the above-mentioned requirements. Thus, a more complex model has to be applied as explained in chapter 6.

3

Direct calibration of atomic force microscopy cantilevers using a raster-scanning Michelson interferometer

3.1 Abstract

Calibration of the stiffness of atomic force microscopy cantilevers is of great importance to accurately determine the mechanical properties of a sample. While common methods provide an accurate measurement of the cantilevers force constant, they require to either define precisely the dimensions of the cantilevers or to perform a spectroscopy curve on a stiff reference surface to evaluate the sensitivity of the detection system. However, uncertainties on the cantilevers geometry will induce calibration errors while the spectroscopy curve will potentially damage and contaminate the tip.

Here, Dr. Iwan A.T. Schaap and I have developed a raster-scanning interferometer based on the Michelson principle to measure the thermal vibrations of cantilevers down to several hundreds of femtometre. Because the interferometric measurements provide an output that depends on the wavelength of the used laser source, the measurements show directly the cantilever vibrations in length units and the thermal noise method can straightforwardly be applied. This removes the need to calibrate the sensitivity of the photodetector which is required in conventional AFM optical beam deflection measurement schemes and thus greatly reduces the potential damage and contamination of the AFM probe.

3.2 Introduction

The working principle of AFM force spectroscopy is based on knowing the mechanical properties of the probe, the AFM cantilever, to extract the mechanics of a sample. However, the properties of a given cantilever are usually not constant among members of the same family as disparities caused by the manufacturing process are unavoidable. Each cantilever is unique. This is the reason why manufacturers only provide an average value of the cantilever spring constant and its resonance frequency as these can vary up to a factor of 2 [69]. As a consequence, every cantilever has to be calibrated prior to any AFM force spectroscopy measurement. To this end, two methods are widely used: the Sader method [61] and the thermal noise method [62].

According to Sader's method [61], the spring constant of a rectangular cantilever, k_{Sader}, is defined as:

$$k_{Sader} = 0.1906 \cdot L \cdot b^2 \cdot \rho_{air} \cdot Q_{air} \cdot \Gamma_i \cdot (2 \cdot \pi \cdot f_{air})^2 \tag{3.1}$$

where L and b are the length and width of the cantilever respectively, ρ_{air} is the density of the air, Q_{air} is the quality factor of the resonance peak in air, Γ_i relates to the imaginary component of the hydrodynamic function of the surrounding medium (which depends on the cantilever cross section shape and the Reynold number [70]), and f_{air} the resonance frequency in air. In practice f_{air} and Q_{air} are found by analysing the power spectral density in $[V^2]$ of the vibrations. Corrections on Eq.(3.1) for more complex cantilever shapes were derived [71].

As shown in Eq.(3.1), the Sader method relies on knowing precisely the dimensions, length and width, of the cantilever. Manufacturers usually record them after imaging the cantilevers with a scanning electron microscopy (SEM) that offers nanometre resolution. However, since every cantilever is unique, this routine should ideally be repeated for each individual probe. Because this is time consuming and this would potentially either contaminate or in the worst case deteriorate the tip, both manufacturers and AFM users stick to the average values from a given set of reference cantilevers. These geometrical uncertainties lead to an error of approximately 10 % in the calibration [63, 72].

The alternative approach is the thermal noise method. According to the analysis of an ideal simple harmonic oscillator, which is only excited by the Brownian motion of the surrounding medium and thermal motion from within the cantilever [50, 62], the spring

constant of cantilever, $k_{thermal}$, can be written as:

$$k_{thermal} = \frac{0.97 \cdot k_B \cdot T}{\langle d^2(m) \rangle} = \frac{0.97 \cdot k_B \cdot T}{invOLS \cdot \langle d^2(V) \rangle} \tag{3.2}$$

where the prefactor 0.97 corrects from the fact that the cantilever cannot be regarded as an ideal simple harmonic oscillator [50], k_B is the Boltzmann constant (in [Nm/K]), T the temperature (in [K]), $\langle d^2(m) \rangle$ and $\langle d^2(V) \rangle$ the power spectral densities of the resonance peak in [m^2] and [V^2] respectively, and $invOLS$ the sensitivity of the photodetector that measures the cantilever deflection (in [V/m]). The term "$invOLS$" stands for inverse optical lever sensitivity [73, 74]. The combination "optical lever sensitivity" is the result of using optical read-out to measure the vibration of the cantilever (IR laser beam reflected off the free end of the cantilever and mirrored onto a photodiode [56]) while "inverse" is the consequence of defining the actual cantilever sensitivity in [m/V].

As shown in Eq.(3.2), the thermal noise method preliminary requires to define the photodetector sensitivity in order to convert the measured potential from the read-out system into displacement. It is done by pushing the cantilever against a stiff reference surface using a pre-calibrated z-piezo. From the slope of the curve, corresponding to the $invOLS$, the measured deflection in volt can be directly converted into meter [74]. However, AFM tips are fragile and easily contaminated/damaged [75] and performing such a calibration procedure may negatively affect the following experiments. Indeed, a damaged tip, its apex being flattened for example, reduces the image quality and the achievable resolution while a contaminated tip drags artefacts and instabilities all along the measurements. These aspects are particularly pronounced when investigating biological samples in physiological environments. In the case of this thesis where the thermal noise method was chosen for calibration, multiple AFM cantilevers were binned right after the calibration routine as the tips appeared contaminated. Besides a waste of time it is also a waste of money with a single cantilever costing 10 to 30 GBP. Nonetheless, since the thermal method does not require a precise knowledge of the cantilever dimension, it is usually favoured.

Here, to optimise the calibration process of AFM cantilevers, I was involved in the development of a raster-scanning interferometer based on the Michelson principle, also called "vibrometer". This instrument allows to directly measure vibrations in meter thus removing the need of pre-calibration of the $invOLS$ of the photodetector. The performance of this device was estimated by comparing the calibration results according to both of the above-mentioned methods with vibrometry.

3.3 Methods

3.3.1 Power spectral density analysis

All analysis were done in LabVIEW 2015 (National Instruments, Austin, USA).
The power spectral density peaks were fitted with [76]:

$$\langle d^2(m)\rangle = \frac{a_0}{f} + a_1 + \frac{a_2}{(f-a_3)^2 + a_4} \tag{3.3}$$

where f is the frequency, a_0 is the pink noise coefficient, a_1 the white noise floor, and a_2, a_3 and a_4 coefficients describing the shape of the Lorentzian peak.
I used non-linear regression based on the Levenberg–Marquardt algorithm with iterative least square minimisation to estimate the coefficients. The goodness of fit parameter was computed as the adjusted chi-square value. The initial guesses for the different coefficients were calculated for each cantilever according to:

$$a0 = \frac{d\,PSD(f)}{df} \tag{3.4}$$

$$a1 = \overline{PSD(f)} \tag{3.5}$$

$$a2 = df^2 \cdot \left(max\left(PSD(f)\right) - \overline{PSD(f)}\right) \tag{3.6}$$

$$a3 = f\left(max\left(PSD(f)\right)\right) \tag{3.7}$$

$$a4 = a3 - f\left(\frac{max\left(PSD(f)\right)}{\sqrt{2}}\right) \tag{3.8}$$

where $PSD(f)$ is the power spectral density, $\overline{PSD(f)}$ the mean value of the $PSD(f)$ and df is the frequency step.
The coefficients are related to the mechanical properties of the cantilever following:

$$f_0 = a_3 \tag{3.9}$$

$$Q_0 = \frac{a_3}{2 \cdot \sqrt{a_4}} \tag{3.10}$$

$$k = \frac{k_B \cdot T \cdot \sqrt{a_4}}{\pi \cdot a_2} \tag{3.11}$$

where Q_0 is the quality factor of the resonance peak centred at f_0, k_B is the Boltzmann constant and T is the temperature (20 °C during experiments).

3.3.2 Calibration methods

- **Vibrometer method**

The cantilevers were initially imaged in their packaging using the interferometric IR beam of the instrument. The IR beam was then moved onto the free end of the cantilevers and the thermal vibrations were recorded and averaged (minimum of 10 time series, each lasting 1 sec with 10 MHz sampling frequency) to reduce the noise level. The resulting thermal spectra were fitted with Eq.(3.3) and the force constants determined from Eq.(3.11).
It should be noted that the vibrometer method is actually the thermal noise method, only the way how the displacements are measured is different.

I thank Dr. Florian Rehfeldt from Goettingen University (Goettingen, Germany) for calibrating the cantilevers using the standard Sader method and thermal noise method.

- **Sader's method**

I preliminary measured the cantilever dimensions using scanning electron microscopy, see below. Then the cantilevers were successively mounted on a MFP-3D AFM (Asylum Research, Santa Barbara, USA) and the power spectral densities of the vibrations at their free end were recorded. The thermal peaks of the first bending mode were fitted with Eq.(3.3) to extract the quality factors and resonance frequencies. Finally, these fitting results were incorporated in Eq.(3.1) to extract the spring constants, Γ_i being determined by a look-up table [61].

- **Thermal noise method**

In the case of the thermal noise method, the $invOLS$ was determined after performing a spectroscopy curve on a glass substrate. It was used to convert the measured power spectrum recorded in $[V^2]$ into $[m^2]$. The thermal peaks of the first bending mode were fitted with Eq.(3.3) to extract the quality factors and resonance frequencies. Then, Eq.(3.2) was further corrected to take into account the tilt of the cantilever (10°) (due to the AFM cantilever holder) [77] and the fact that the AFM optical read-out measures in reality the cantilever inclination rather than the deflection [78]:

$$k_{thermal_{corrected}} = 0.82 \cdot \cos(10) \cdot k_{thermal} \tag{3.12}$$

These corrections do not apply to the vibrometry method, since the last measures directly the deflection, but also because the cantilever is not titled during the measurements.

3.3.3 Scanning electron microscopy imaging

The cantilevers were fixed on a scanning electron microscopy sample holder with vacuum grease (Apiezon H, Neuss, Germany). This allowed me to easily unfix the cantilevers. They were imaged with a Vega3 electron microscope (Tescan, Brno, Czech Republic) at 30 kV. SEM pictures were analysed using the open source software *ImageJ*.

3.3.4 Atomic force microscopy

All experiments were performed on an MFP-3D AFM (Asylum Research, CA, USA) at room temperature. The reference substrate for the calibration of the *invOLS* was a glass coverslip.

3.4 Results and discussion

3.4.1 Raster-scanning interferometer

The raster-scanning interferometer developed combines two distinct sub-instruments: an interferometer, to measure the displacements of the cantilever and to extract the amplitude and the phase of the vibrations, and a scanning unit, to move an interferometric sensor head over the sample as depicted in Figure 3.1.

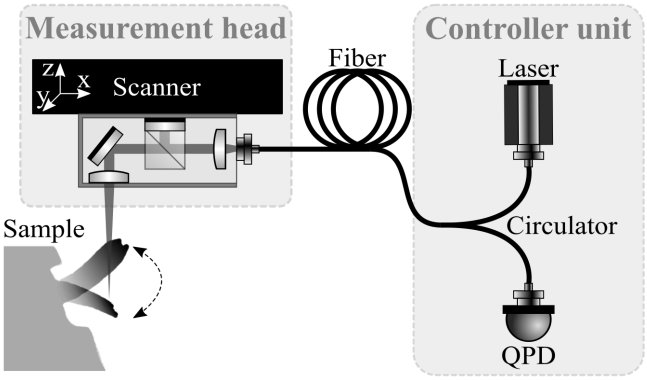

Figure 3.1: Raster-scanning Michelson interferometer working principle. *The system includes a controller unit and a measurement head connected to each other by an optical fibre. In the measurement head, a beam splitter is used to divide the incident beam into two beams. In the controller unit, a circulator routes the reflected beam to a photodetector (QPD). A complete XYZ scanner unit holds the measurement head.*

- **Interferometer**

The vibrometer is based on an existing interferometer with picometre resolution. It contains i) a controller unit that hosts a 1550 nm laser source, a detector as well as a powerful Field-Programmable-Gate-Array (FPGA), and ii) an interferometric sensor head which is connected to the controller via a single mode optical fibre. The wavelength of the laser source is deliberately chosen to allow the investigation of cantilevers through various packaging materials (plastic, silicon etc).

The interferometric sensor head is made very compact by combining all optical components directly at the end of the fibre: a primary lens that collimates the emitted laser beam followed by a beam splitter to split the collimated beam in a measurement and a reference arm. One of the beams is reflected off the reference mirror which is directly attached to the beam splitter while the other goes through an additional lens that focuses the beam on the sample (the beam radius at focus is 5 µm with the current optics). Then, the reflected beam passes back through the beam splitter where it is combined with the reflected reference light, thus forming an interferometric signal. This combined beam is routed back through the optical fibre and coupled out in the controller using an optical circulator after which it reaches a photodetector.

The signal received by the detector is digitised at 10 MHz and analysed in the FPGA. At first the changes in distance separating the surface from the reference mirror are calculated. Then the distance signal is sent to a digital dual phase lock-in amplifier that extracts the amplitude and phase of the vibrations [79]. It should be noted that the FPGA sampling rate allows the investigation of oscillations up to 5 MHz (Nyquist frequency) which is high enough to precisely study most AFM cantilevers.

- **Scanning unit**

The IR laser is invisible for human eyes and complicates the positioning of the beam on the sample (cantilevers are only a few tens of micrometres wide). To overcome this limitation, the interferometric head is scanned over the region of interest in a raster fashion and the intensity of the reflected beam is recorded at the same time as the amplitude and phase of the vibrations. Thus by creating an intensity map it is possible to precisely move the IR beam to a specific location as both are intrinsically aligned. The head is put in motion thanks to 3 closed loop linear positioners forming a complete XYZ scanner with nanometre accuracy and a working range of 20 mm. The XYZ scanner is controlled by an additional controller that is synchronised with the data acquisition of the interferometer.

3.4.2 Calibration comparison

In this experimental work, I characterised 10 BL-RC150VB biolevers (Olympus, Tokyo, Japan) by vibrometry while 5 of them were additionally calibrated using the Sader method and the thermal noise method on a commercial AFM. These cantilevers have a nominal resonance frequency of 37 kHz and 0.03 N/m nominal spring constant.

At first, I calibrated the cantilevers using raster-scanning interferometry because this method is non-invasive. To do so, I initially performed a 5×5 mm with 1 megapixel scan over the whole chip to clearly identify the location of the cantilevers. Then, I centred the scan on top of them and reduced the area by a factor of 10 with 500×500 pixels, minimising thus the recording time from approximately 20 min to approximately 4 min. Figure 3.2 shows an example of reflection images acquired by vibrometry.

Taking advantage of the closed loop positioner accuracy, I positioned the laser beam at the free end of the cantilever, near the tip location, and recorded multiple time series of the local thermal vibrations. The Fourier transformation of the averaged time series revealed the resonance, as shown in Figure 3.3, which is then analysed to extract the mechanical properties of the cantilever. The first chip allowed me to optimise the technique. Afterwards, the other cantilevers were investigated with a much faster routine by directly centring the scan on top of the cantilevers and reducing the scan resolution. All vibrometry images, raw amplitude spectra along with the fitting coefficients and goodness of fits, can be found in Appendix I.

Then, I measured the dimensions of each cantilever using scanning electron microscopy for their calibrations according to Sader's method.

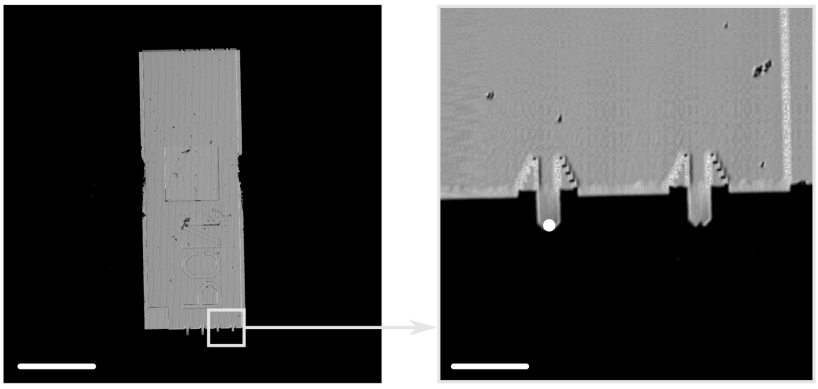

Figure 3.2: Vibrometry images. *After locating the cantilevers, the laser beam is moved to one of them (dot). Scale bars:* 1 mm *and* 100 nm *left and right respectively.*

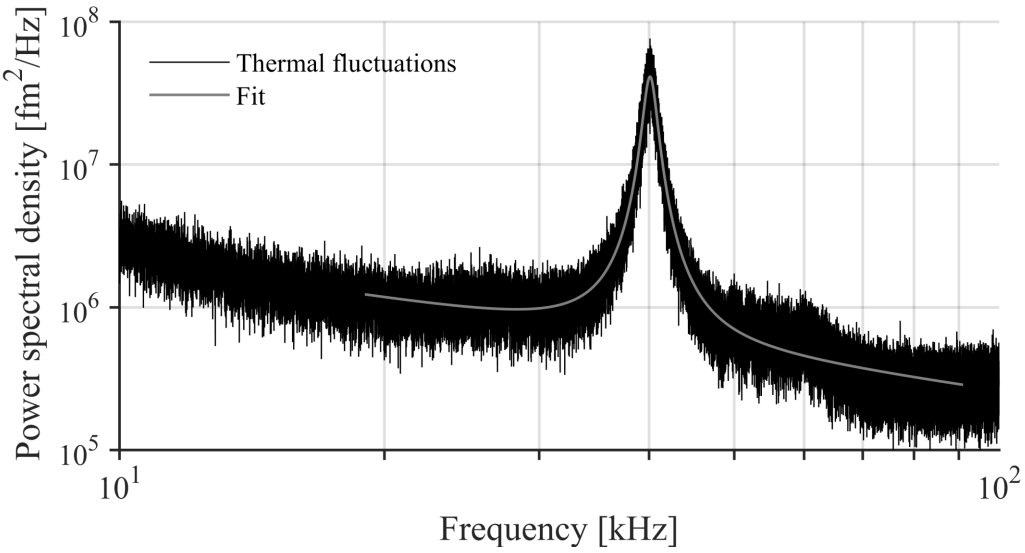

Figure 3.3: Vibrometry calibration. *The measured noise is shown in black while the theoretical Brownian noise, plus its pink and white noises, is displayed in grey. Fitting the peak of the first resonance frequency allows the extraction of the cantilever spring constant.*

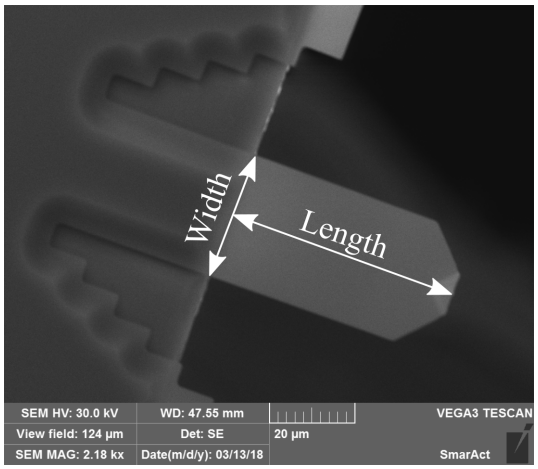

Figure 3.4: Dimensions definition. *The width and the length, important parameters for Sader's method, of each cantilever were defined after their imaging with SEM. In this example, the cantilever is* 29.39 µm *wide and* 57.70 µm *long.*

Figure 3.4 shows how the dimensions were extracted from the SEM images. All SEM images can be found in Appendix II. The thermal noise method was applied last as it requires to perform a force curve on a stiff surface and potentially alters the mechanical properties of the cantilever. For these two methods, a Lorentzian fit near the resonances from the AFM power spectral densities allowed me to extract the parameters needed for the calibrations.

Table 3.1: Mechanical properties of various bioLevers. *Each chip (A to E) contains two identical cantilevers (1 and 2). The resonance frequency, f_0, the quality factor, Q_0, and the spring constant according to the method chosen, k_{method}, are displayed. The average value, mean, as well as the standard deviation, std, are added.*

	AFM				**Vibrometer**		
Cantilever	f_0 [kHz]	Q_0	k_{Sader} [pN/nm]	$k_{thermal}$ [pN/nm]	f_0 [kHz]	Q_0	$k_{vibrometer}$ [pN/nm]
A1	/	/	/	/	37.35	27.16	31.50
A2	40.67	27.85	32.4	30.3	38.15	26.59	38.99
B1	/	/	/	/	37.96	19.27	37.33
B2	39.02	24.46	39.0	31.4	37.46	19.01	35.01
C1	/	/	/	/	40.27	27.18	33.90
C2	42.04	27.39	32.5	33.5	42.47	28.66	30.36
D1	/	/	/	/	38.40	26.26	32.76
D2	36.97	24.79	35.1	29.4	37.32	26.28	27.16
E1	/	/	/	/	40.10	26.73	42.17
E2	39.48	26.69	35.2	32.1	39.51	26.11	28.49
mean	39.64	26.24	34.9	31.4	38.90	25.32	33.77
std	1.69	1.34	2.4	1.4	1.58	3.02	4.28

The calibration results of the cantilevers are summarised in Table 3.1. The biolevers were found to be 34.9 ± 2.4 pN/nm (mean ± std, n = 5), 31.4 ± 1.4 pN/nm (mean ± std, n = 5) and 33.8 ± 4.3 pN/nm (mean ± std, n = 10) according to Sader's method, thermal noise method and vibrometery respectively. A Student's t test assuming equal variance lead to a p value of 0.50 and 0.78 when comparing the stiffness extracted from vibrometery analysis to the one of either the Sader method or the thermal noise one respectively. The agreement between the three methods shows that all methods yield comparable results.

3.5 Conclusion

I have determined the force constants of multiple AFM cantilevers using either the Sader method, the thermal noise method or with a raster-scanning vibrometer. While the first two are now standard methods in the field, they have drawbacks that affect the accuracy of the AFM measurements and the post-analysis of the acquired data.

In the case of the Sader method, the $invOLS$ is not important for the calibration of the cantilever but is later necessary for the conversion of the quadrant photodiode potential into proper displacement. Thus, in both thermal noise and Sader's method, a force

spectroscopy curve on a stiff surface is unavoidable. It potentially leads to damages and contaminations of the AFM probe. Nowadays, researchers combine Sader's method and the thermal noise method to first determine the spring constant of the cantilever and then estimate the $invOLS$ from the thermal noise [80]. It represents an appealing strategy but suffers from geometrical uncertainties. Alternatively, raster-scanning interferometry can be employed instead of the Sader method to first define the $invOLS$ and reduce the calibration errors. However, because the vibrometer method reports the spring constant at the exact position of the laser spot it is important to position the beam exactly where the AFM tip is mounted.

Appendix I: Vibrometry data

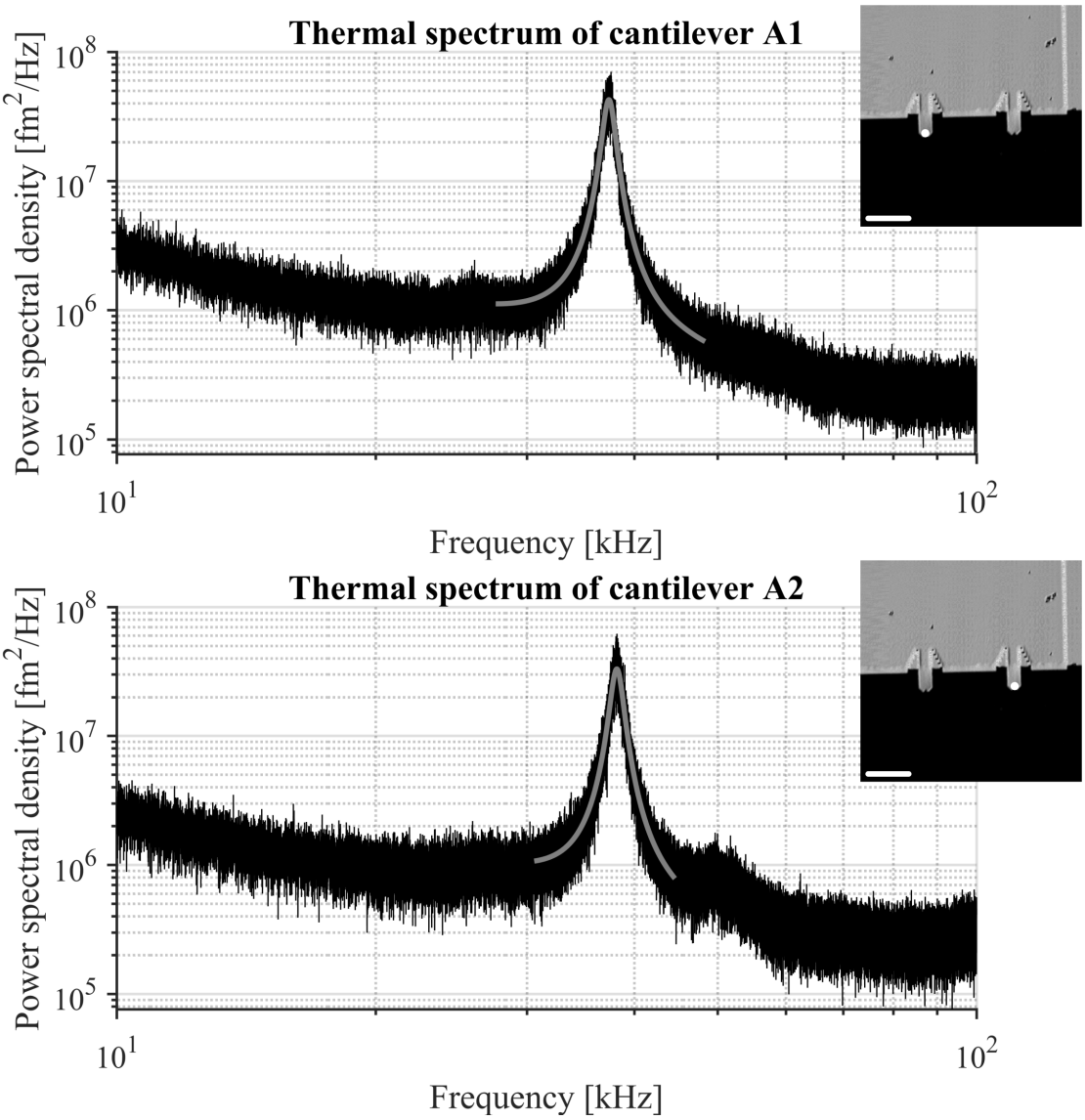

Figure 3.5: Brownian noise fitting. *The resonance peak from the thermal noise (black) measured by interferometry is fitted with a Lorentzian function (grey). Insets: Vibrometry images, scale bars:* 100 nm. *The dots indicate the beam position during the recording.*

Table 3.2: Fitting results. *The spring constant, $k_{vibrometer}$, quality factor, Q_0, resonance frequency, f_0, and adjusted chi-square, χ^2, are displayed along with their standard deviation calculated from the non linear regression.*

Cantilever	$k_{vibrometer} \pm$ **std** [pN/m]	$Q_0 \pm$ **std**	$f_0 \pm$ **std** [kHz]	χ^2
A1	31.50 ± 2.46	27.16 ± 0.06	37.35 ± 0.85	0.94
A2	38.99 ± 2.81	26.59 ± 0.07	38.15 ± 1.13	0.91

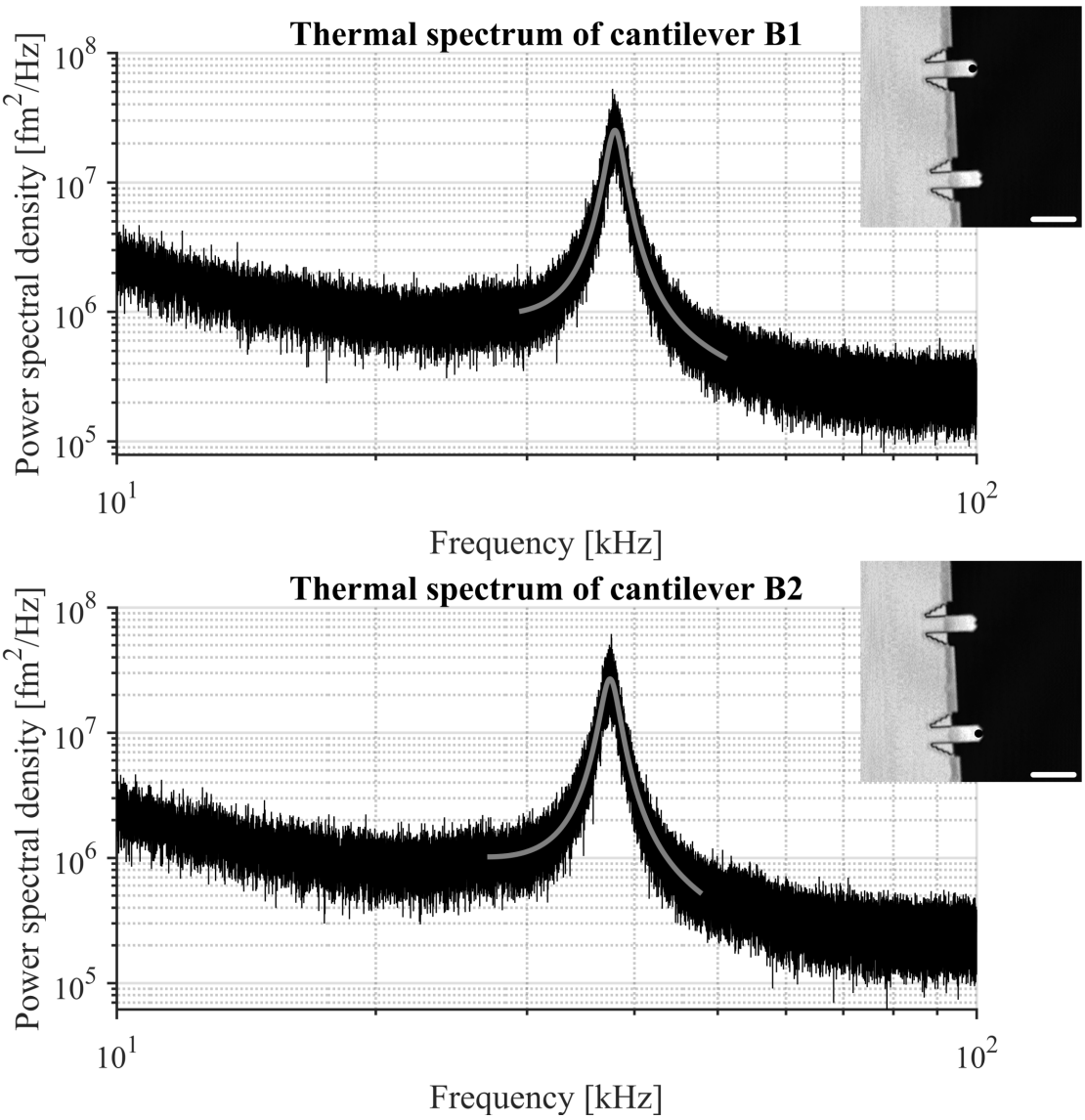

Figure 3.6: Brownian noise fitting. *The resonance peak from the thermal noise (black) measured by interferometry is fitted with a Lorentzian function (grey). Insets: Vibrometry images, scale bars:* 100 nm. *The dots indicate the beam position during the recording.*

Table 3.3: Fitting results. *The spring constant, $k_{vibrometer}$, quality factor, Q_0, resonance frequency, f_0, and adjusted chi-square, χ^2, are displayed along with their standard deviation calculated from the non linear regression.*

Cantilever	$k_{vibrometer} \pm$ **std** [pN/m]	$Q_0 \pm$ **std**	$f_0 \pm$ **std** [kHz]	χ^2
B1	37.33 ± 1.16	19.27 ± 0.05	37.96 ± 1.52	0.92
B2	35.01 ± 1.15	19.01 ± 0.05	37.46 ± 1.51	0.91

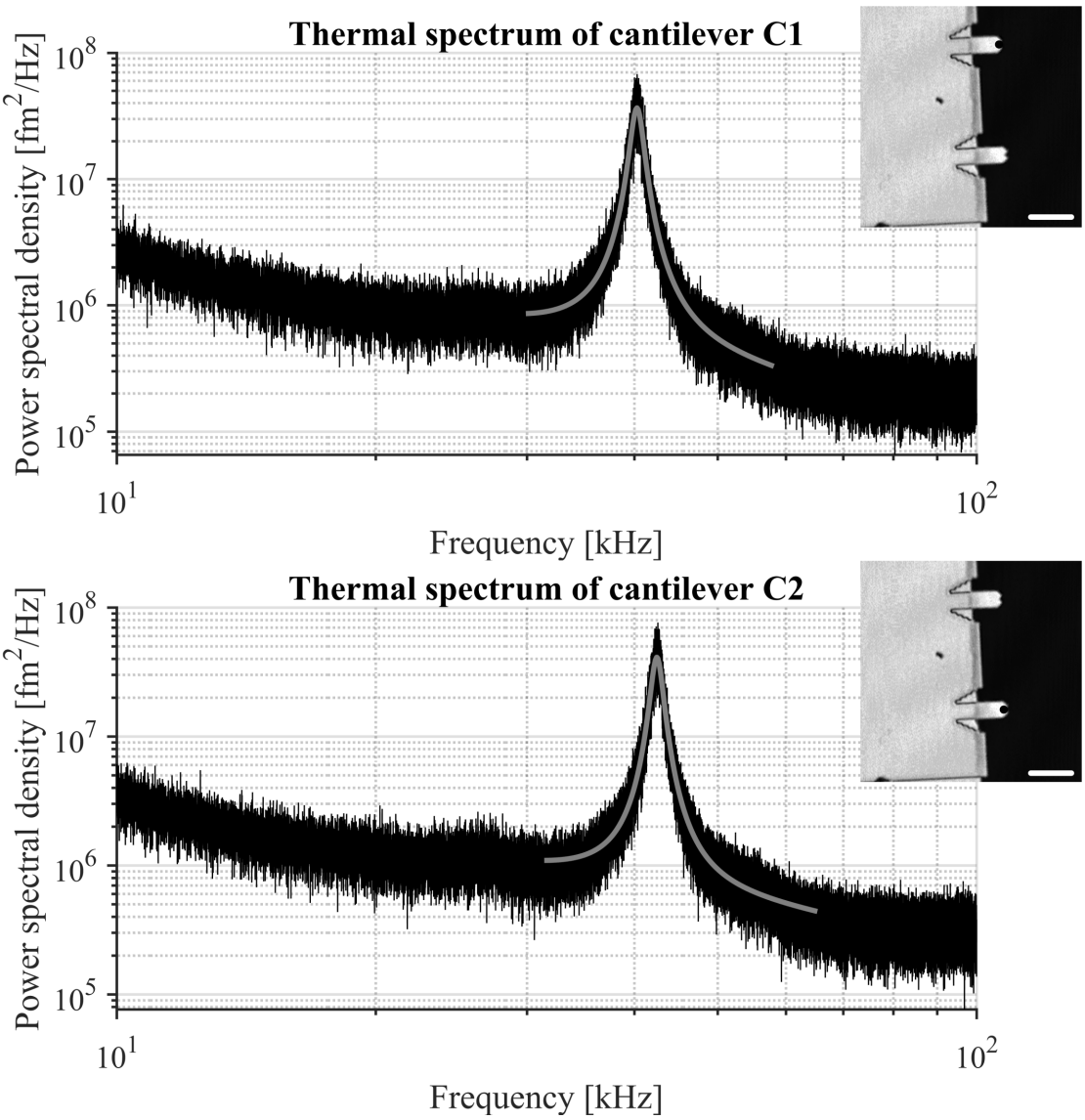

Figure 3.7: Brownian noise fitting. *The resonance peak from the thermal noise (black) measured by interferometry is fitted with a Lorentzian function (grey). Insets: Vibrometry images, scale bars:* 100 nm. *The dots indicate the beam position during the recording.*

Table 3.4: Fitting results. *The spring constant, $k_{vibrometer}$, quality factor, Q_0, resonance frequency, f_0, and adjusted chi-square, χ^2, are displayed along with their standard deviation calculated from the non linear regression.*

Cantilever	$k_{vibrometer} \pm$ **std** [pN/m]	$Q_0 \pm$ **std**	$f_0 \pm$ **std** [kHz]	χ^2
C1	33.90 ± 2.18	27.18 ± 0.06	40.27 ± 1.05	0.92
C2	30.36 ± 2.35	28.66 ± 0.07	42.47 ± 1.06	0.93

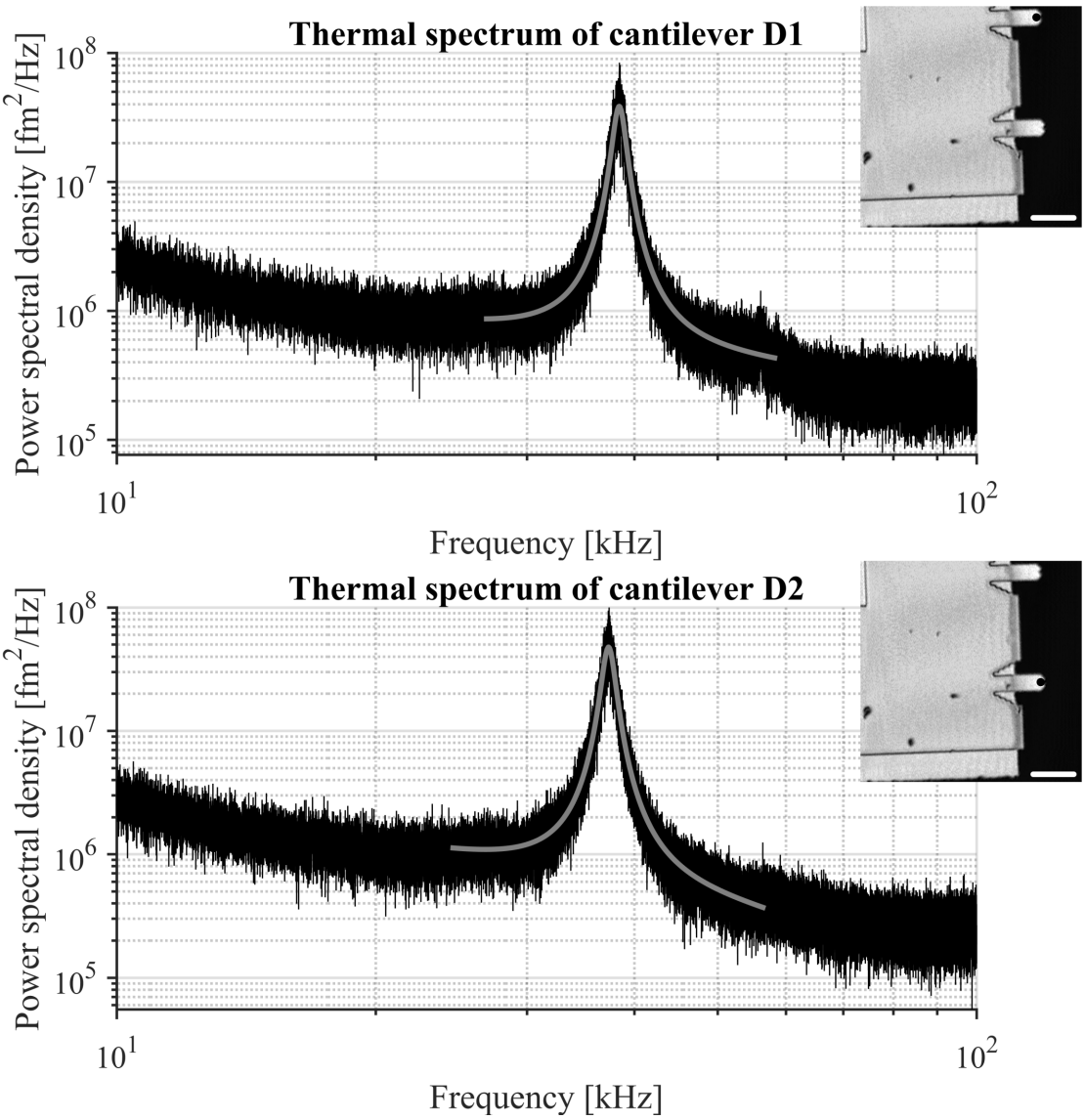

Figure 3.8: Brownian noise fitting. *The resonance peak from the thermal noise (black) measured by interferometry is fitted with a Lorentzian function (grey). Insets: Vibrometry images, scale bars:* 100 nm. *The dots indicate the beam position during the recording.*

Table 3.5: Fitting results. *The spring constant, $k_{vibrometer}$, quality factor, Q_0, resonance frequency, f_0, and adjusted chi-square, χ^2, are displayed along with their standard deviation calculated from the non linear regression.*

Cantilever	$k_{vibrometer} \pm$ **std** [pN/m]	$Q_0 \pm$ **std**	$f_0 \pm$ **std** [kHz]	χ^2
D1	32.76 ± 2.68	26.26 ± 0.07	38.40 ± 1.17	0.92
D2	27.16 ± 2.69	26.28 ± 0.07	37.32 ± 1.06	0.92

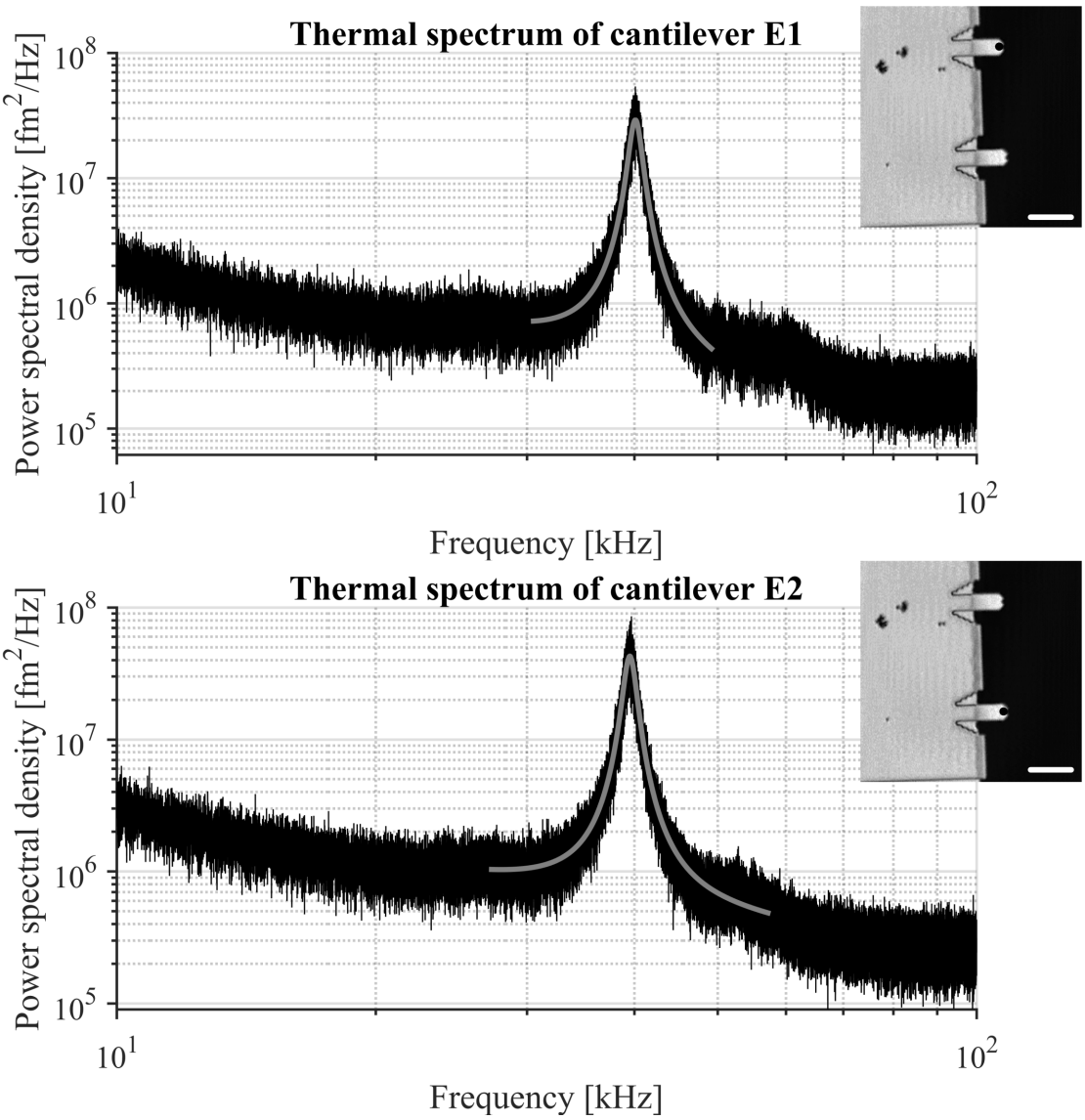

Figure 3.9: Brownian noise fitting. *The resonance peak from the thermal noise (black) measured by interferometry is fitted with a Lorentzian function (grey). Insets: Vibrometry images, scale bars:* 100 nm. *The dots indicate the beam position during the recording.*

Table 3.6: Fitting results. *The spring constant, $k_{vibrometer}$, quality factor, Q_0, resonance frequency, f_0, and adjusted chi-square, χ^2, are displayed along with their standard deviation calculated from the non linear regression.*

Cantilever	$k_{vibrometer} \pm$ **std** [pN/m]	$Q_0 \pm$ **std**	$f_0 \pm$ **std** [kHz]	χ^2
E1	42.17 ± 2.19	26.73 ± 0.06	40.10 ± 1.08	0.92
E2	28.49 ± 2.33	26.11 ± 0.07	39.51 ± 1.15	0.93

Appendix II: SEM images

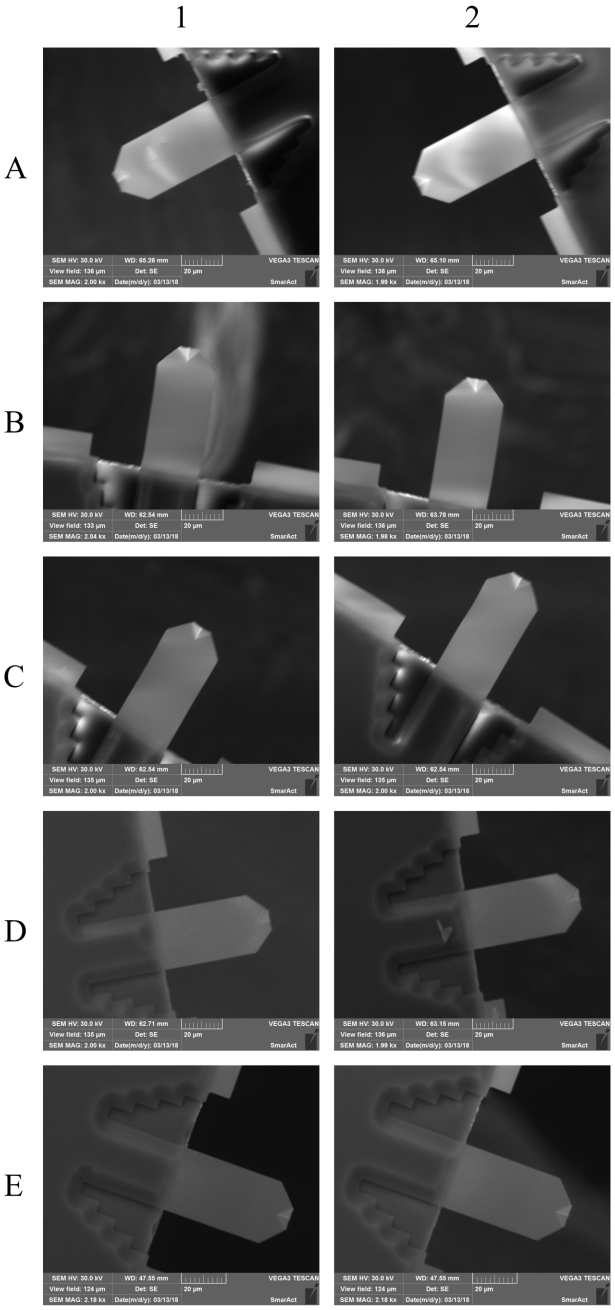

Figure 3.10: SEM images. *They were used to determine the dimensions of each cantilever.*

Table 3.7: Cantilevers dimensions by SEM. *The dimensions, width (W) and length (L), are given in* µm.

	A1	**A2**	**B1**	**B2**	**C1**	**C2**	**D1**	**D2**	**E1**	**E2**
W	28.73	29.08	28.76	27.80	28.64	28.89	28.92	28.79	29.39	29.16
L	57.86	57.82	58.25	58.08	57.21	57.27	57.97	57.25	57.70	57.15

4

Clathrin coat rigidity is dynamically regulated

4.1 Abstract

Half a century after the discovery of clathrin, a cage forming protein complex, its roles in mitosis, uptake of pathogens, and vesicle formation in eukaryotic cells, have been intensively investigated. The majority of experiments addressing membrane bending during clathrin-mediated vesicle formation are based on imaging techniques. However, still remarkably little is known about the actual mechanics of the clathrin-coat which represent a key aspect in understanding how molecular forces drive this conserved eukaryotic process. Here, I have employed atomic force microscopy to probe the structure and nano-mechanics of native clathrin vesicle coats. Variants of well-defined compositions were also reconstructed and studied. I found that clathrin coats are surprisingly compliant and have a similar softness as the vesicles they enclose. In addition, I present evidence that the coat properties can be regulated through the clathrin light chains and I show a novel role of the major membrane adaptor protein AP2 in modulating the coat rigidity during its formation. My results depict a mechanically dynamic structure that undergoes distinct phases to achieve vesicle formation.

4.2 Introduction

Membrane trafficking regulates extracellular uptake and facilitates transport between cellular compartments. As such, packaging of cargo into transport vesicles enables nutrient uptake, regulation of receptor signalling as well as the uptake of pathogens [81]. A major pathway for vesicular trafficking in eukaryotes is clathrin-mediated endocytosis [82]. During this process, see Figure 4.1, clathrin-coated vesicles (CCVs) are formed, usually triggered by the binding of cargo molecules to trans-membrane receptor proteins that are recognised on the cytosolic side of the membrane by so-called adaptor proteins.
These adaptors recruit clathrin, a trimeric complex (the triskelion) composed of three clathrin heavy chains (CHCs) and three associated clathrin light chains (CLCs), to the plasma membrane. The triskelia self-assemble into polyhedral coats upon adaptor recruit-

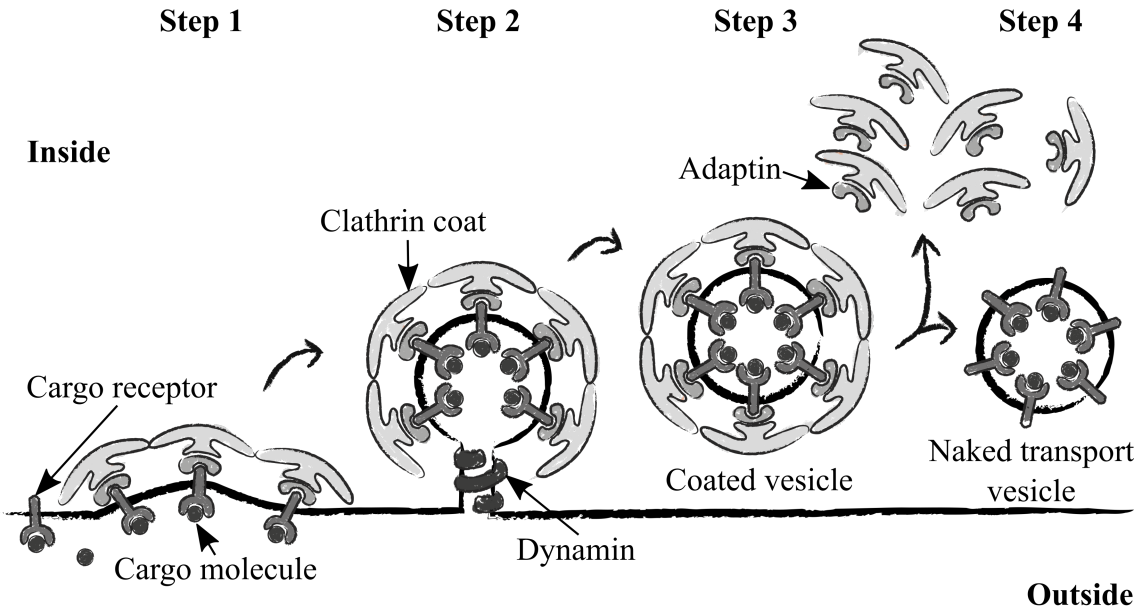

Figure 4.1: Clahtrin mediated endocytosis schematic. *Clathrin is recruited to the plasma membrane by adaptor protein 2 (AP2), which in turn is bound and activated by phosphoinositides and cargo receptors. Continuous recruitment of clathrin to the membrane leads to its deformation of the membrane as well as the formation a clathrin-coated pit (step 1) and finally to the formation of a deeply invaginated clathrin-coated bud (step 2). The narrow membrane neck of the bud is cleaved by the mechano-GTPase dynamin, yielding a clathrin-coated vesicle (CCV) (step 3) which in the next step will shed its clathrin/ adaptor coat aided by the ATPase Hsc70 and it co-chaperone Auxilin (step 4).*

ment, thereby inducing local membrane curvature and trapping cargo molecules into a clathrin-coated pit that maturates into a clathrin-coated bud. Finally, CCVs are released from the donor membrane via scission of the buds by the mechano-GTPase dynamin [82, 83]. After release, the chaperone Hsc70 in conjunction with its co-chaperone Auxilin binds the vesicle in an ATP dependent process, removing the clathrin coat so that the vesicles can be routed to, and fused with, target organelles within the cell [82, 84].

Clathrin-mediated vesicle formation is a clear example of a mechanically driven biological process. Essentially planar membranes are deformed into vesicle shape, requiring approximately $400\,k_BT$ [85]. In comparison, the hydrolysis of one ATP molecule, consumed for example by the uncoating reaction, will produce just approximately $20\,k_BT$ per ATP, showing that bud formation is an energetically costly process.

Previously, the rigidity of clathrin coat has been estimated to be similar to the rigidity of the vesicle it encloses [86]. Nevertheless, it was found that also other proteins, such as Epsin, can produce membrane curvature even in absence of clathrin [87, 88]. As result clathrin's function in CCV formation has also been discussed as merely helping to organise and concentrate protein factors on the membrane to drive its curvature by protein crowding [13].

On the other hand, the structural design of the coats suggests a mechanical role for the coats. Their pronounced polyhedral cage-like structure, as observed in electron micrographs, shows similarities with the tensegrity-based Buckminster Fuller architecture [89, 90] which is able to holds up heavy loads with a minimal amount of material. This implies that clathrin may play an important mechanical role in the formation of membrane vesicles. Previous investigations have shown that membranes can also be bent by the mechanical action of the clathrin coat alone [83] and that the membrane bending ability of clathrin lattices is dependent on their rigidity [91]. Additional experiments have shown that clathrin assembly is essential for membrane bending and can drive vesicle formation directly, probably by acting as scaffold and/or Brownian ratchet [83, 92, 93].

As throughout its life cycle the functionality of the clathrin coat is continuously adjusted, it is conceivable that its mechanical properties change as well. The stiffening or softening of the clathrin lattice at the right moments could facilitate membrane bud formation and coat disassembly. A similar phenomenon has been observed in protein coats of enveloped viruses that soften before fusion with the target membrane can occur [94]. Indeed, several observations point to the possibility of mechanical modulation of the clathrin lattice. For example, cryo-electron microscopy reconstruction has shown that the structure of the

clathrin triskelion can be altered by CLCs that modify the CHC knee conformation [95]. The finding that CLCs affect clathrin lattice assembly and enhance Auxilin activity implies that CLCs may play a role in clathrin coat rigidity [96, 97]. Further support for the mechanical effect of CLC on the clathrin lattice comes from a recent observation that CLC stiffens planar lattices against flattening [91] which is consistent with an alteration of CHC knee conformation by CLCs [95].

Because of the small size and the transient nature of CCVs, it is impossible to directly characterise their mechanics within the living cell. However, testing of isolated CCVs, reconstituted coats and membrane vesicles is in principle possible with atomic force microscopy (AFM) operated in liquid. AFM imaging has been employed to study the mechanical structure of CCVs in an indirect fashion [15]. From imaging at different forces the stiffness could be estimated and compared with the values of the bending rigidity of lipid bilayers from the literature, which gave a first clue that clathrin coats might actually be fairly soft [15, 98]. Beyond imaging, AFM can be used to measure localised nano-mechanics of biological protein shells via force spectroscopy [99, 100].

Here, this strategy was further refined to measure the mechanical response of individual clathrin coats that represented different stages in the clathrin life-cycle. In addition, I modelled the different polyhedra with finite element method [100] to identify the mechanical function of the different cage constituents. To elucidate possible regulation of the clathrin coat rigidity I compared native coats that were purified from tissue with coats that were reconstructed from purified components. The native coats were chosen as the reference whereas the reconstituted coats allowed me to evaluate the influence of CLCs and adaptor proteins.

4.3 Methods

The clathrin coats were prepared at University College of London (London, United-Kingdom) by Dr. Dannhauser's group while I conducted the AFM measurements, their analysis and the mechanical modelling at Heriot-Watt University. To make this distinction clear, this method section is divided into two subsections.

4.3.1 Biochemical sample preparation (Dannhauser's group)

- **Protein purification**

The various clathrin-coated vesicles (CCVs) are extracted from pig brains. They were purified following previously published protocols on clathrin purification [16, 101, 102]. Triton-treated clathrin-coated vesicles (T-CCVs) were produced out of the CCVs by incubating them in a solution containing 1 % Triton in buffer A (100 mM 2-(N-morpholino)-ethanesulfonic acid (MES), 1 mM ethylenediaminetetraacetic acid, 0.5 mM $MgCl_2$ and 2 mM $CaCl_2$, 0.02 % (w/v) NaN_3, pH 6.4) during 2 h while kept on ice. The T-CCVs were collected by centrifugation (109 g for 30 min at 4 °C). Finally they were resuspended in buffer A for storage. Figure 4.2 confirms that the treatment did not modify the coat composition.

Clathrin proteins and the adaptor proteins AP2 were purified from pig brain as described earlier [102, 103]. The clathrin was stored as reconstructed cages, see the subsequent section, in buffer A and kept on ice. AP2 was stored in 0.5 M Tris, 20 % (w/v) glycerol pH 7.4 at −80 °C. Light chain-free clathrin coats (CHCs) were purified as described previously [97, 104].

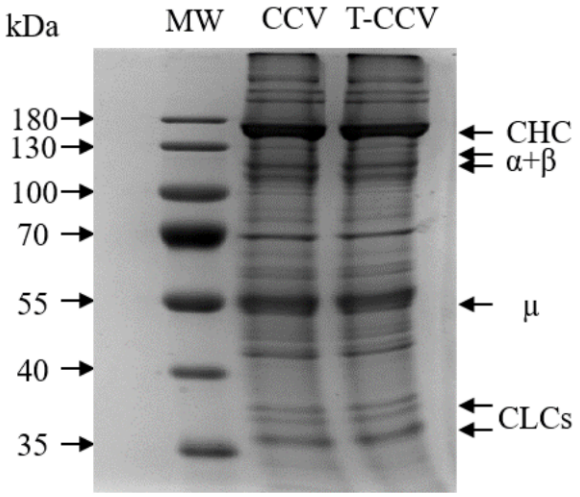

Figure 4.2: SDS-PAGE identification of CCVs and T-CCVs (Dannhauser's group). *The protein composition of both CCV and T-CCV is largely the same. No clathrin or adaptor proteins are lost. Ratio CHC/AP: approximately* 3.3 *(CCV) and* 3.5 *(T-CCV).* μ*,* α*,* β *are AP2 adaptins.*

- **Clathrin assembly**

Clathrin coats were assembled from isolated clathrin or clathrin heavy chains at 0.5 – 1 mg/mL in 0.5 M Tris, 2 mM Ethyleneditetracetetic acid (EDTA) at pH 8 and dialysed

into buffer A (100 mM 2-(N-morpholino)-ethanesulfonic acid, 1 mM ethylenediaminetetraacetic acid, 0.5 mM $MgCl_2$ and 2 mM $CaCl_2$, 0.02 % (w/v) NaN_3, pH 6.4) over night.

- **Adapator binding**

In order to coassemble adaptor protein AP2 and CHC+CLCs / CHCs coats, clathrin triskelia and AP2 were mixed in a ratio of 3:1 (w/w) (molar ratio 1.5:1) prior to dialysis in 1 L buffer A.

The binding of AP2 to pre-assembled CHC+CLCs or CHCs coats was performed by mixing the components in a ratio of 3:1 (w/w) in buffer A followed incubation on ice during 1 h. The AP2+CHC+CLCs and AP2+CLCs coats were recovered by centrifugation (109 *g* for 30 min at 4 °C) and again suspended in buffer A.

- **Electron microscopy sample preparation**

Freshly glow-discharged carbon-coated formvar grids were used for negative staining of the cages investigated with SEM. To this end, 5 to 10 µL were deposited onto to the grids and left for 1 min to allow adsorption of the cages. The remaining mobile cages from the solution were removed by rincing the surface with buffer A. Then, the cages were fixed with 3 % (w/v) of glutaraldehyde (diluted in buffer A) for 5 min, after which they were washed with 100 mM MES, 1 mM EDTA and 0.5 mM $MgCl_2$, at pH 6.4. Finally the cages were stained with 2 % (w/v) uranyl acetate for 1 min.

For the ultrathin sectioning of the cages, they were pelleted at 109 g , immobilised with 3 % (w/v) glutaraldehyde (diluted in buffer A) and further processed for embedding in Epon and staining as described previously [16]. The samples were imaged with a Tecnai spirit (FEI, Waltham, USA) electron microscope at 120 kV.

4.3.2 AFM, modelling and data analysis (my contribution)

- **Atomic force microscopy sample preparation**

The substrate used during all experiments was Highly Oriented Pyrolytic Graphite (HOPG, Micromasch, Sofia, Bulgaria). It was plasma cleaned for 2 min and a solution of 0.02 M cages in 20 µL of buffer A was left for 1 min for absorption. The surface was then washed with 100 µL of buffer A to remove any unbound cages. Next, 0.05 % (w/v) of glutaraldehyde (diluted in buffer A) was added for 10 min after which the surface was rinsed again with buffer A. For experiments with AP2 attached to the cages, I added the protein at 1:1 ratio (AP2:heavy chains) to the cages solution for 10 min before the cages were adsorped to the HOPG.

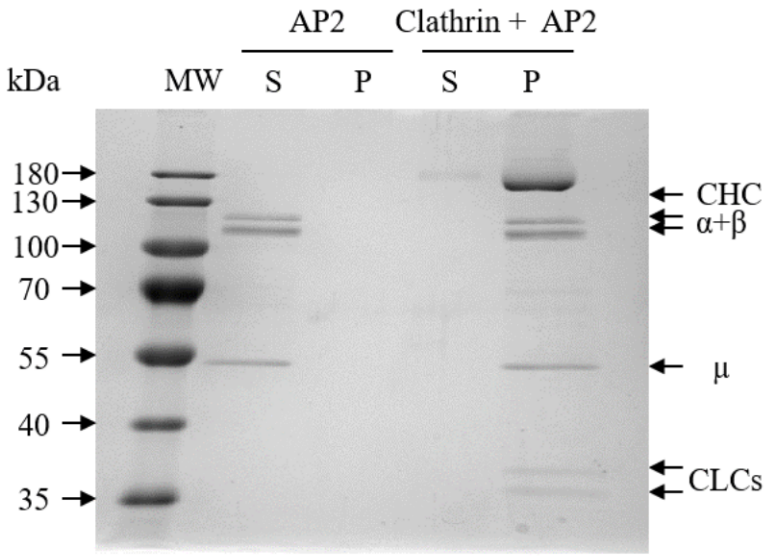

Figure 4.3: SDS-PAGE identification of co-assembly of AP2 and clathrin (Dannhauser's group). *The cage complexes are present in the pellet (P) while AP2 remain in the supernatant (S). Ratio CHC/AP2: approximately* 2.9 *(in pellet Clathrin + AP2).*

This incubation time allowed AP2 to bind onto the cages, see Figure 4.3.

- **Atomic force microscopy operation**

All experiments were performed on a MFP-3D AFM (Asylum Research, Santa Barbara, USA) at room temperature. I used RC150VB cantilevers (Olympus, Tokyo, Japan) which resonate in liquid at approximately 4 kHz. Their force constant was calibrated with the built-in thermal noise method [62] (0.031 ± 0.001 N/m, mean ± sem, $n = 42$). The AFM images presented were taken in amplitude modulation (tapping) mode (approximately 7 nm amplitude) at a scan rate of 1 Hz. In this configuration the images were recorded in 5 min approximately. The forcemaps were recorded over a 300×300 nm area divided in 24×24 individual curves (500 nm displacement; 2 μm/s velocity, approximately 5 min total recording time per forcemap).

- **Estimation of the size of clathrin-coats via AFM and SEM**

The geometrical dimensions of the coats probed by AFM were extracted from the forcemaps. Height maps were calculated at 30 pN which is the AFM noise threshold in aqueous environment for low force constant cantilevers [68]. On the other hand, I manually measured the diameter of the cages with *ImageJ* from SEM images for comparison.

- **Force curves analysis**

The force curves analysis is based on the routine described in [105]. The only difference

is that the program was rewritten and optimised in MATLAB 2016 (MathWorks, Natick, USA). In a nutshell, the spectroscopy curves from a forcemap belonging to a 20 nm radius circle and centred on the apex of the cage were first interpolated and then aligned before they were averaged. The slope of the indentation region, which gives the local stiffness of the sample according to Hooke's law, of the average force curve was extracted with a linear fit and the standard error of the fit was computed. An exhaustive example of the fitting routine is shown in Appendix I. All fits with a Pearson's chi-squared test result below 0.95 were rejected. The measurements were not considered satisfying enough to accurately describe the mechanical properties of the sample. In some scenarios, up to 40 % of the total population was rejected which is explained by substantial tip contamination that softened the measured response and removed the linear behaviour of the indentation. I found that the stiffness and the height of clathrin samples are sometimes related. In this situation, calculating an average stiffness and performing common statistical analysis such as a t-test would be influenced by the height distribution of the cages, which I found to differ between different cage types. To overcome this problem, all stiffness *versus* height curves were fitted with a power law function inspired by the thin shell theory and defined as $k(r) \propto r^{\alpha}$ where r denotes the cage radius and α a dimensionless exponent describing the correlation between the height and the stiffness [106]. I used a non-linear regression method where the coefficients were estimated using iterative least squares minimisation. Finally, the stiffness of a 80 nm shell was chosen to allow comparison among the various coats investigated. The errors due to the regression provided the mean absolute error (MAE). I also computed the adjusted χ^2 for each stiffness *versus* height fit.

- **Finite Element Analysis**

I employed Comsol 5.2a (Comsol, Stockholm, Sweden) to model the different clathrin polyhedra. The ribs of the cages were modelled as circular beam objects which were rigidly connected at the nodes. In order to mimic AFM experiments and the fact that the clathrin cages were kept immobile by electrostatic forces thanks to the plasma cleaning of the substrate, the edges in contact with the supporting surface were constrained in all 3 directions. The applied load from the tip was exerted normal to the polyhedron surface and computed with the contact-penalty method [107]. All mechanical properties of the modelled structures were kept constant for proper comparison of their responses: Poisson's ratio of 0.45, rib diameter of 7 nm, rib length of 17.5 nm [13] and Young's modulus of 100 MPa which is a common value for proteins albeit at the low side (100*s* of MPa [37, 106]). The parabolic tip was positioned 10 nm above the apex of the polyhedra

and then lowered by steps between 0.1 to 0.25 nm during the simulation until the force felt by the cages reached 150 pN. For more details, see Appendix II.

- **Averaging of EM clathrin lattices**

The EM reconstruction was performed with data acquired and presented in previous experimental research [13]. In a nutshell, EM images of 2D clathrin lattice were divided in multiple sub-images each containing a central hexagon encircled by 6 adjacent hexagons. Then, these fragments were aligned according to a random sub-picture reference by translation and rotation until the cross-correlation was maximised. This procedure was iterated with respect to the obtained averaged image until the cross-correlation did not further increase.

- **Estimation of the bending rigidity of clathrin coats**

To give a rough estimate of the bending rigidity of the cages I assumed that they could be described to some extend by the thin shell theory [108]. This theory relates the stiffness, k, of a shell to the inverse of its radius, r, following:

$$k = b \cdot E \cdot \frac{t^2}{r} \tag{4.1}$$

with b is a prescaler, E the Young's modulus and t the thickness of the shell.
On the other hand, the bending rigidity, k_b, is defined as:

$$k_b = \frac{E \cdot t^3}{\alpha \cdot (1 - \nu^2)} \tag{4.2}$$

where ν is the Poisson's ratio and α a prescaler.
Incorporating Eq.(4.1) into Eq.(4.2) gives:

$$k_b = r \cdot k \cdot t \cdot c \tag{4.3}$$

where c is equal to $(b \cdot \alpha \cdot (1 - \nu^2))^{-1}$ and thus constant. I deduced $c = 0.0598$ from earlier measurements on Egg PC liposomes [105]. Finally the bending rigidity of an 80 nm cage can be simplified, assuming clathrin has a similar thickness than liposome, $t = 4.5$ nm [105], to:

$$k_{b_{80nm}} = 10.764 \cdot 10^{-18} \cdot k_{80nm} \tag{4.4}$$

4.4 Results and discussions

4.4.1 Probing clathrin coats with AFM

In order to precisely measure the clathrin-coat mechanics, I first had to ensure that the process of imaging by AFM, necessary to locate the sample at first due to their small dimensions, preserved the integrity of the samples. To minimise the forces exerted by the AFM tip, the samples were imaged in buffer using soft cantilevers ($k \approx 0.03\,\mathrm{N/m}$) at an oscillation amplitude of approximately 7 nm. As a result, the applied forces were only several tens of pN, close to the lowest force limit of AFM [109]. As preliminary test I imaged native CCVs isolated from pig brain. Figure 4.4 shows that successive scans on the same CCVs did not lead to changes in their structure. Indeed, the typical pentagon/hexagon pattern as well as the dimensions of the coats remained identical.

In addition, to validate that the clathrin coats withstand the AFM sample preparation without major deformation I compared the heights measured with AFM with the diameter as measured from standard electron microscopy (SEM) images of clathrin structures [37, 68]. For this comparison clathrin coats were reconstituted *in vitro* from purified components, either from clathrin composed of clathrin heavy chains and light chains (CHC + CLCs) or from clathrin heavy chains alone (CHCs). The electron micrographs of the CHC + CLCs and CHCs revealing the typical polyhedral structure are shown in Figure 4.5a and Figure 4.5b.

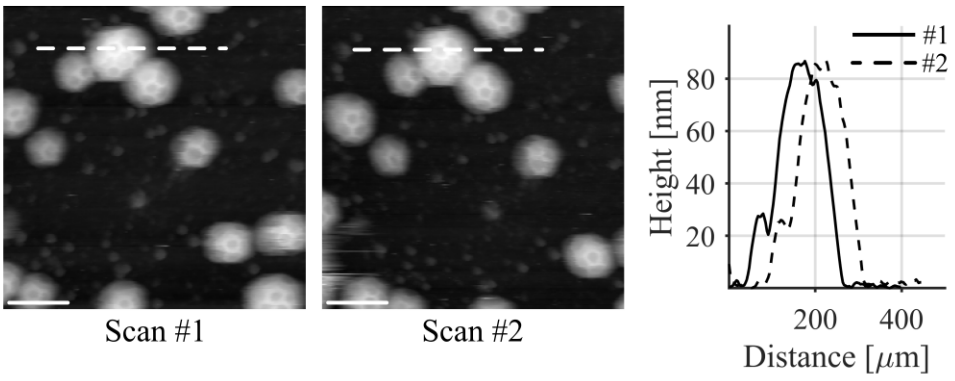

Figure 4.4: Imaging of clathrin cages by AFM: validating the technique. *Successive imaging scans on clathrin coats show no changes in their appearance, scale bar:* 150 nm. *The dashed lines show the location of the height profiles shown at the right. The height remains nearly constant with a reduction of only* $1.3 \pm 0.5\,\%$ *(*$n = 8$*).*

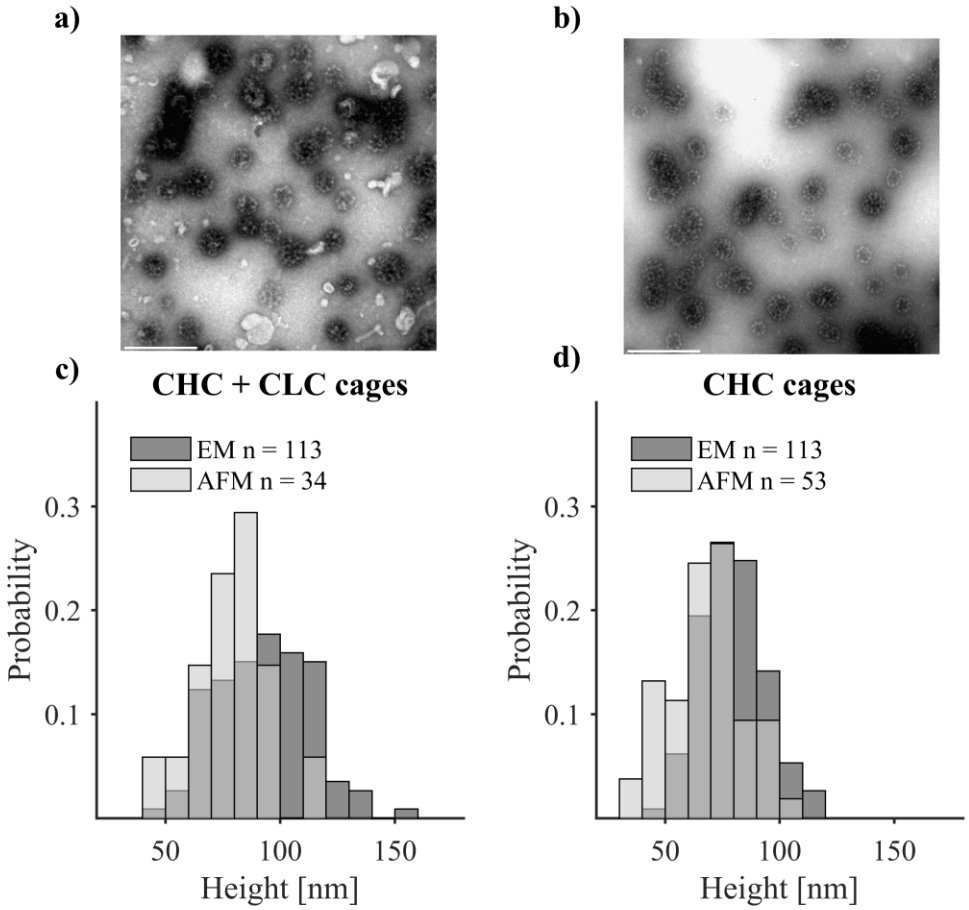

Figure 4.5: Electron microscopy images from reconstituted clathrin coats. *(a) Full clathrin coats (CHC+CLCs) and (b) clathrin heavy-chains (CHCs), from Dannhauser's group, scale bar:* 200 nm. *(c) For clathrin cages the mean size ± std is* 78.4 ± 2.7 nm *(bright grey) for AFM and* 92.6 ± 2.0 nm *for EM (dark grey) whereas in (d) CHC cages are* 67.9 ± 2.1 nm *for AFM (bright grey) and* 79.3 ± 1.4 nm *for EM (dark grey). The number of bins for each histogram is chosen according to Sturges's rule [110].*

I found that for both sample preparations the heights measured by AFM were on average about 15 % smaller than the diameter measured in EM, see Figure 4.5c and Figure 4.5d. This variation is coherent with previous research [101] and can be explained by the different imaging techniques. EM staining also visualised exposed peptide loops on the cage exterior that may remain invisible in AFM scans due to their mobile nature. Furthermore, the immobilisation of the coats on a substrate and the application of low forces, approximately 30 pN, during imaging may lead to some initial flattening of the coats.

After a clathrin coat was imaged with AFM, identified by its characteristic polyhedral pattern, as shown in Figure 4.6a, I probed its mechanical properties by performing AFM force spectroscopy measurements, Figure 4.6b: an array of force spectroscopy curves,

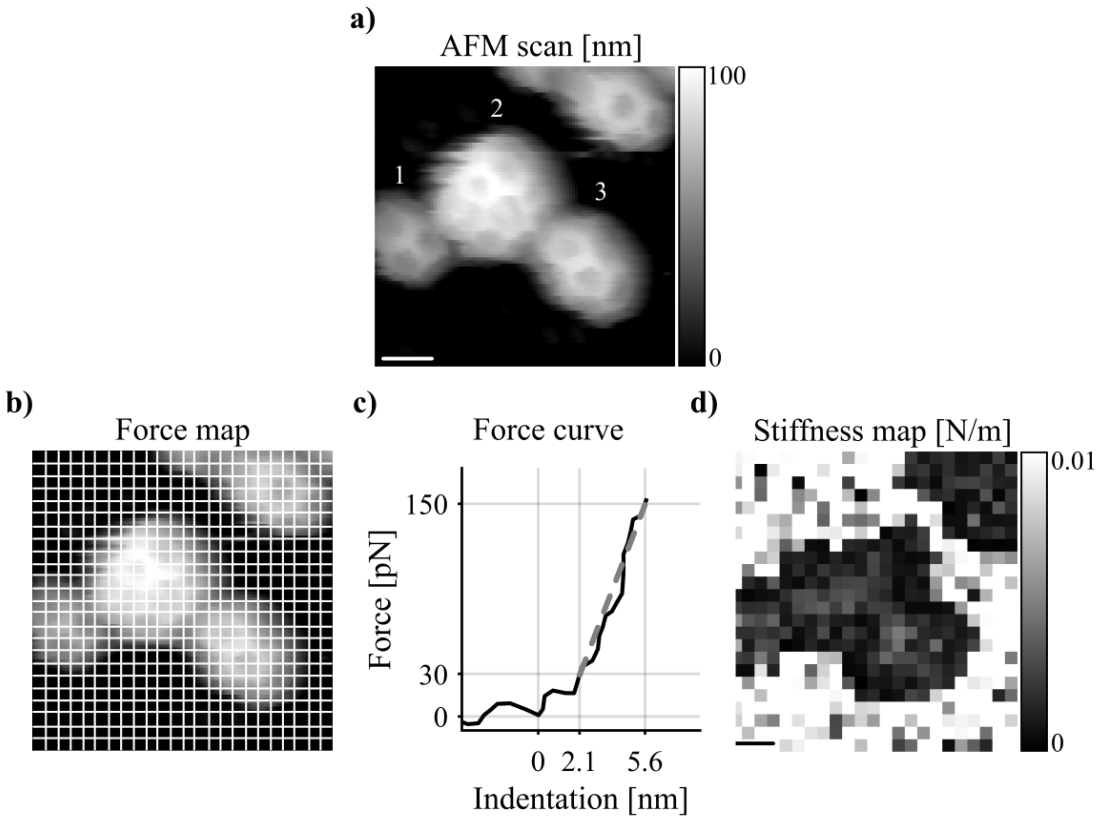

Figure 4.6: Imaging and force measurements of clathrin cages by AFM. *(a) AFM scan over multiple clathrin coats. It shows three clearly distinguishable structures: (1) a triakis tetrahedron, (2) a truncated icosahedron and (3) a hexagonal barrel, scale bar:* 50 nm. *(b) The scan area is downsampled and a single force versus indentation curve is performed at each pixel, (c). The indentation region* $[2.1 : 5.6]$ *is linearly fitted (grey dashed line) to extract its slope, the stiffness. (d) Example of a stiffness map, scale bar:* 50 nm. *Each pixel of the map represents a slope of a single force versus indentation curve.*

Figure 4.6c, over the complete coat. From each force curve I defined the contact point and measured the slope of the indentation region to compute height and stiffness maps respectively, that spatially described the mechanical properties of the sample, Figure 4.6d. All the measurements were performed within the elastic deformation regime of the coats. As a control, I carried out three successive force measurements with increasing forces (150 pN, 200 pN and 250 pN) and extracted the corresponding height maps, see Figure 4.7a. The profile and the mechanical response of the cage, shown in Figure 4.7b and Figure 4.7c, remained similar after the force measurements proving that the AFM investigations did not lead to any alteration of the structures.

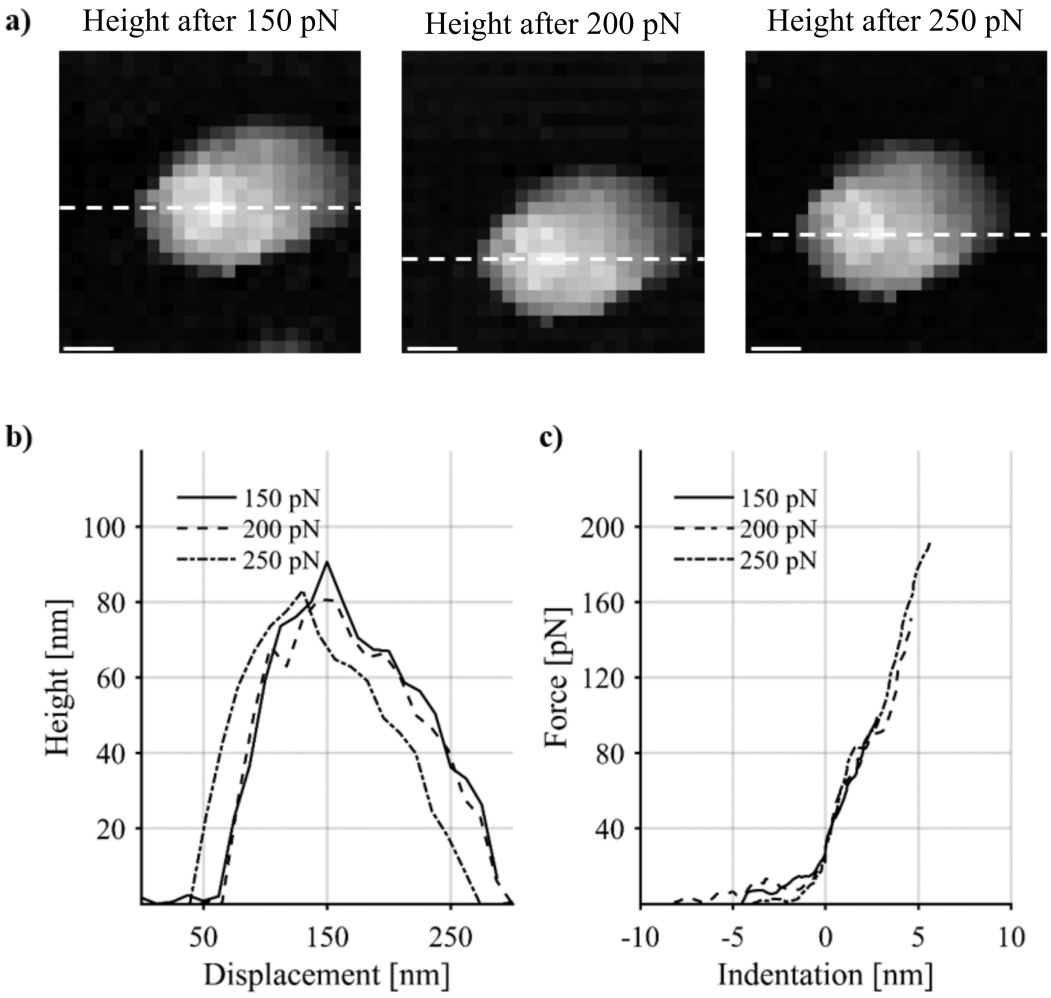

Figure 4.7: Force measurements of clathrin cages by AFM: validating the technique. *(a) Height maps extracted after three successive mechanical measurements with increasing force on the same CHC-CLC cage, scale bar:* 50 nm*. Profiles at* 30 pN*, shown in a), after performing a force map at* 150 pN*, at* 200 pN *and at* 250 pN *are plotted in plain, dashed and semi-dashed respectively in (b). The averaged force curves of each forcemap are shown in (c).*

To chemically stabilise the samples against depolymerisation during the AFM measurements that could last 1 h, I added to all samples the same low concentration, 0.05 % (w/v), of glutaraldehyde, a cross-linking reagent. To determine the effect of glutaraldehyde on my measurements I tested the change in stiffness of clathrin coats when treated with increasing concentrations of the cross-linker. For each individual cage the stiffness was measured and plotted versus its height and the resulting stiffness *versus* height curve was fitted with a power law function inspired by the thin shell theory, see section 4.3. The stiffness of the coats were $0.017 \pm 0.004\,\mathrm{N/m}$ ($n = 23$), $0.025 \pm 0.004\,\mathrm{N/m}$ ($n = 28$), and $0.028 \pm 0.007\,\mathrm{N/m}$ ($n = 22$), at 0.00 % (w/v), 0.05 % (w/v) and 0.80 % (w/v) respectively.

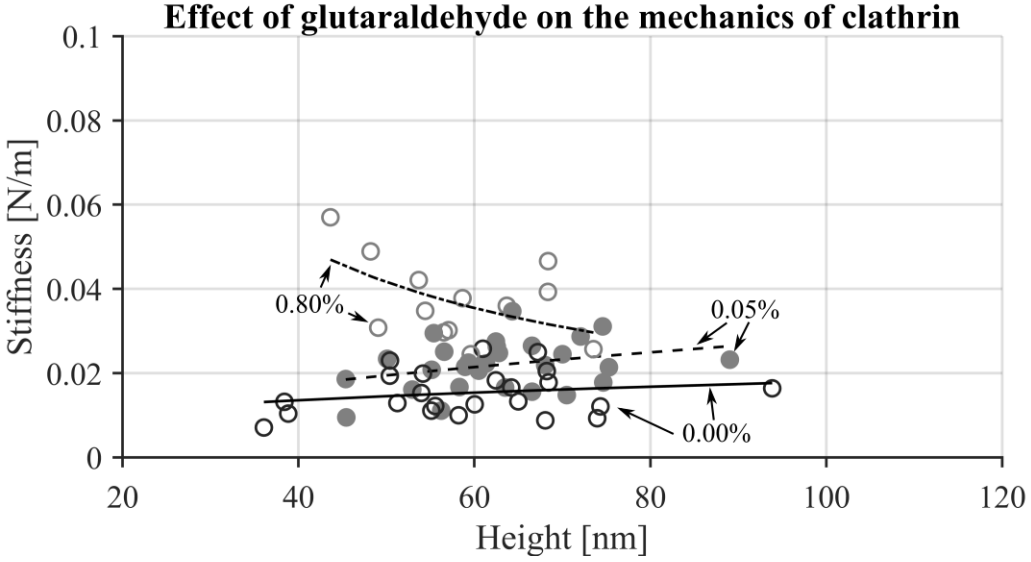

Figure 4.8: Effect of the glutaraldehyde on the mechanical properties of clathrin coats. *Three different concentrations had been investigated:* 0.00 % *(w/v) in empty black circles,* 0.05 % *(w/v) in grey filled circles, and* 0.80 % *(w/v) in grey empty circles.*

Table 4.1: Statistical analysis of the stiffness measurements. *The probabilities were calculated after performing a Student's t test assuming equal variance on the fitted mean stiffness after log-transformation (*$5e-2$ *level), see Appendix IV.*

Samples compared	p **value**
Clathrin + 0.05 % glutaraldehyde *versus* Clathrin + 0.00 % glutaraldehyde	$7.20e-5$
Clathrin + 0.05 % glutaraldehyde *versus* Clathrin + 0.80 % glutaraldehyde	$6.07e-7$

I found that the coats are only moderately affected, see Figure 4.8 and Table 4.1. At a glutaraldehyde concentration of 0.05 % (w/v) the stiffness increases by 47 %, which is less than the stiffness variations that result from the different cage compositions that are reported in the next sections. Even at 0.80 % (w/v) glutaraldehyde concentration the stiffness of the coats increases by just 65 %.

All clathrin were investigated in pH 6.4. At this pH, clathrin triskelia self-assemble into clathrin coats but, on the other hand, this pH is non physiological. As a result, I verified that the pH itself did not influence the mechanical properties of the coats. Figure 4.9 shows that a change of pH from 6.4 to 7.2 did not affect the measured stiffness: the Student's t test gave a p value of $5.58e-1$ when comparing the two populations.

Having established that I can study the clathrin coats with AFM at minimal deformation I continued with a systematic investigation of their mechanical properties.

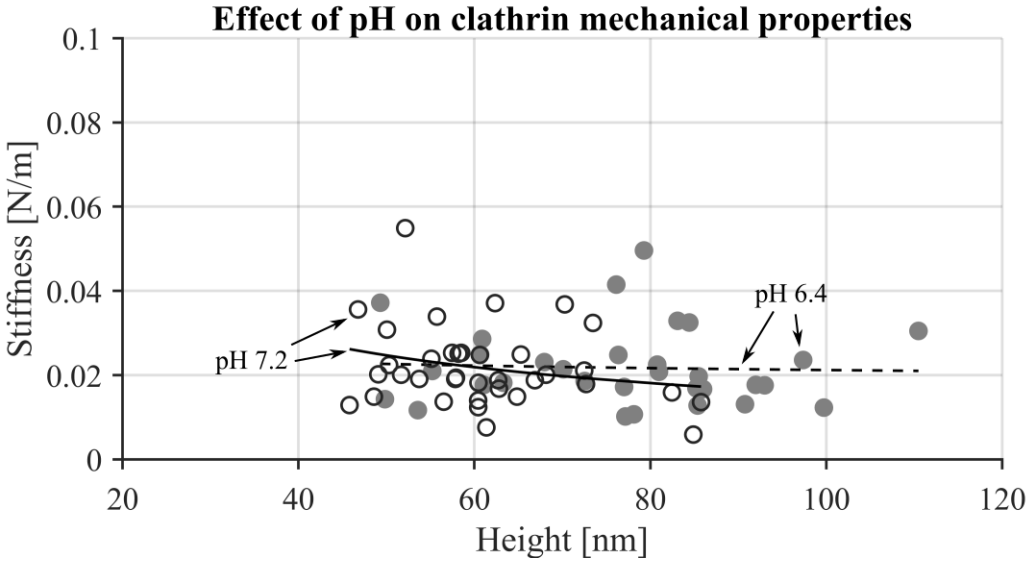

Figure 4.9: Effect of the buffer pH on the mechanical properties of the clathrin coats. *The stiffness of the cages at pH 6.4 (grey, filled) is* $0.022 \pm 0.009\,\mathrm{N/m}$ *(*$n = 32$*), and at pH 7.2 (black, empty)* $0.018 \pm 0.007\,\mathrm{N/m}$ *(*$n = 36$*).*

4.4.2 Coupling between clathrin coat and lipid bilayer vesicle

First, I investigated the stiffness of tissue extracted CCVs composed mainly of CHCs and CLCs, adaptor proteins, membrane vesicles and cargo proteins. Electron micrographs confirming the presence of the membrane vesicles are displayed in Figure 4.10.

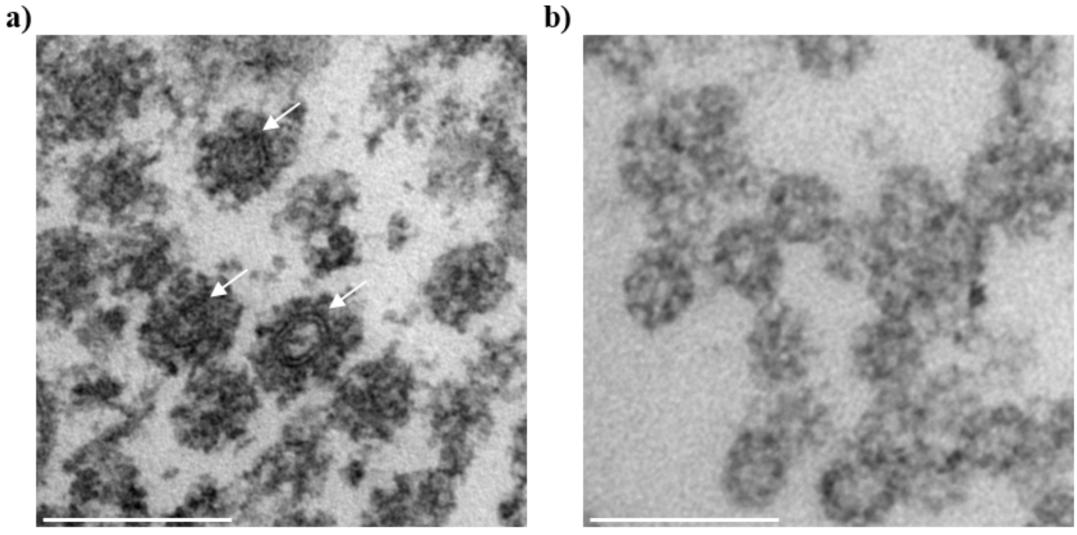

Figure 4.10: Electron micrographs of CCVs and reconstituted cages (Dannhauser's group). *EM of ultra-thin sections from (a) Clathrin-coated vesicles (CCV), purified from porcine brain containing membrane vesicles (arrows) and (b) Clathrin cages reassembled from isolated clathrin triskelia, lacking membrane. Scale bars:* 200 nm.

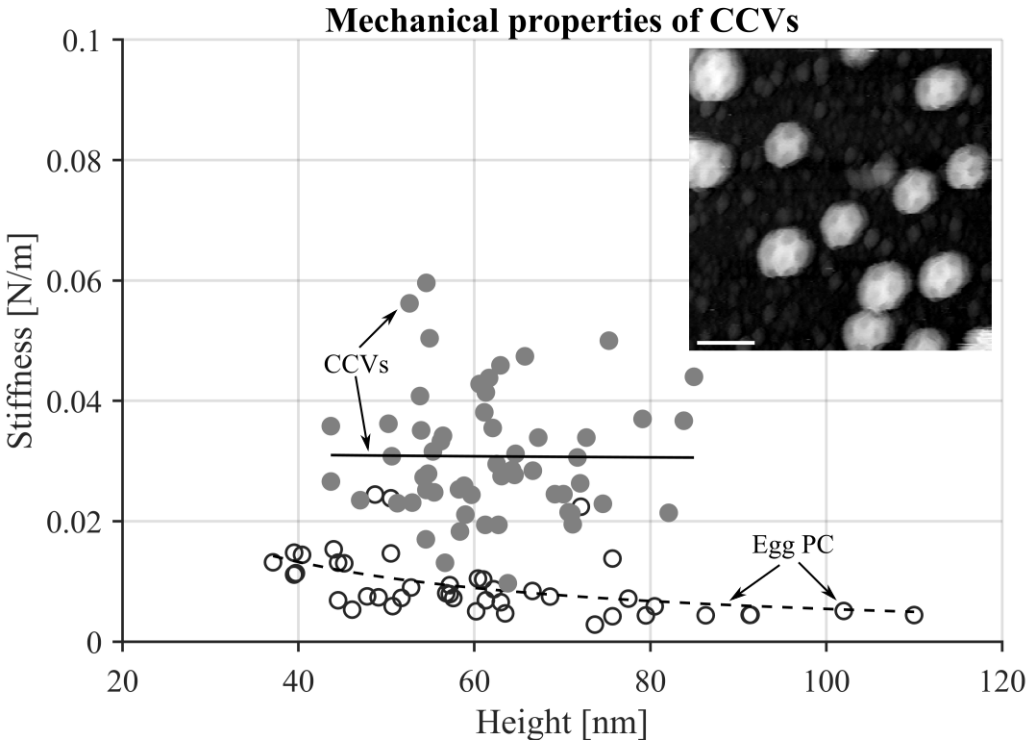

Figure 4.11: Mechanical properties of clathrin-coated vesicles. *Stiffness versus height plot to compare the mechanics of EggPC liposome (black, empty) and CCVs (grey, filled). Inset: AFM image of CCVs, scale bar:* 150 nm. *The cages are well defined and the polyhedral structure is visible.*

While scanning in tapping mode, I found well-defined polyhedra with heights between 40 and 90 nm as display in the inset of Figure 4.11. I could resolve different coat structures such as the truncated triakis tetrahedra and truncated icosahedra. For each individual cage the stiffness was measured and plotted versus its height, see Figure 4.11. Details regarding the fits can be found in Appendix III. For comparison, I have added the stiffness of small liposomes reconstituted from egg PC (data from [105] but reanalysed by myself).
Although the lipid composition of egg PC may vary from that of the vesicles enclosed by CCV, the effects of a different composition on the stiffness will be within a factor of two [111]. The CCVs were found to be $0.031 \pm 0.008\,\mathrm{N/m}$ ($n = 57$) stiff, approximately 4 times stiffer than the liposomes ($0.007 \pm 0.001\,\mathrm{N/m}$; $n = 43$). The Student's t test gave a p value of $6.10e-25$ when comparing the two populations, so they are statistically different. For both samples the smaller objects are slightly stiffer than the larger ones, which is a predicted trend of thin shells of which the stiffness is a function of the inverse of the radius [105]. Even though CCVs are clearly stiffer than the liposomes it is interesting to compare their stiffness with that of proteinaceous viruses as both are protein coats of

similar dimensions. Typical stiffness of viral protein capsids is approximately 0.4 N/m [112] - an order of magnitude higher than that of CCV. This is a first indicator that clathrin coats have not evolved to reach maximum rigidity as their stiffness is much closer to that of the liposomes than to that of viral protein capsids.

In order to dissect the contribution of the clathrin coat and the enclosed membrane vesicle to the measured stiffness of the CCV, I measured the stiffness of clathrin coats free from vesicles. To this end, the purified CCVs were triton-treated to remove the hosted vesicles. The resulting empty coats, shown in the inset of Figure 4.12, are referred to as T-CCVs (in literature also referred to as "TCV" [106]). Their shapes and sizes were similar to complete CCVs indicating that their integrity is preserved by triton extraction, as previously reported [106]. Figure 4.12 shows a stiffness for T-CCVs of 0.025 ± 0.004 N/m ($n = 28$). Interestingly, the CCV stiffness is almost the sum of the T-CCV and the liposome stiffness, which means that they can be treated as a mechanical system of two springs in parallel. This directly shows the absence of a strong coupling between the clathrin coat and vesicle, which would have been visible as a stiffness that is much more than the sum of clathrin coat and vesicle, about an order of magnitude stiffer.

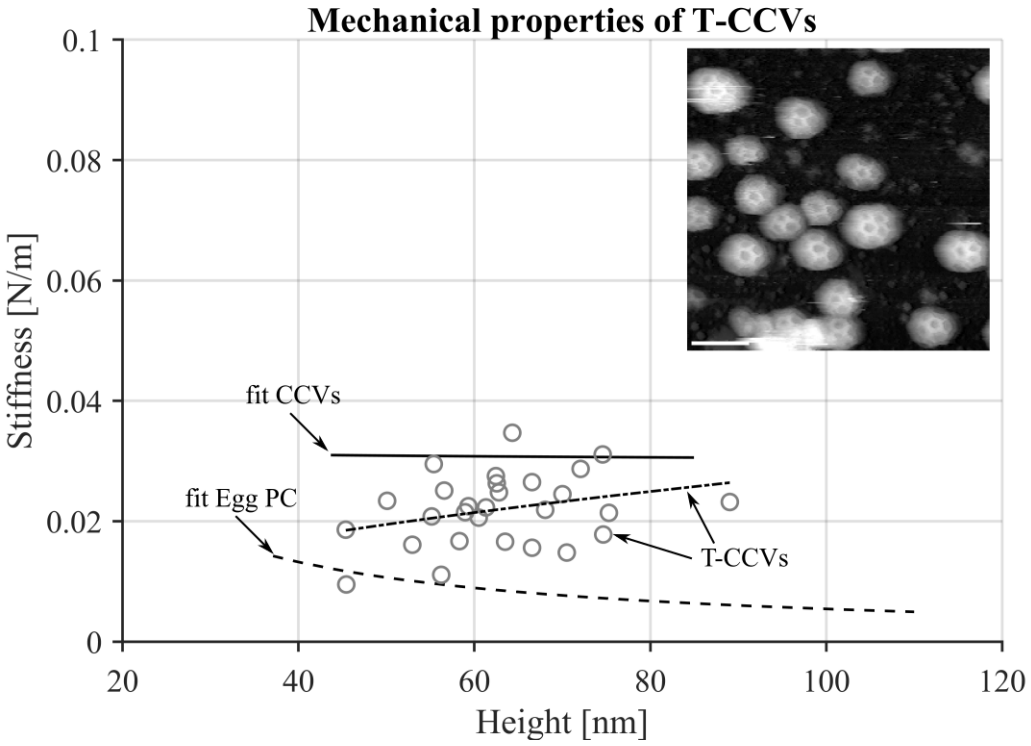

Figure 4.12: Mechanical properties of triton treated clathrin-coated vesicles. *Stiffness versus height plot of T-CCVs (grey, empty). The fits of the liposome data (dashed) and CCVs (plain) are added for comparison. Inset: AFM image of T-CCVs, scale bar:* 150 nm.

Table 4.2: Statistical analysis of the stiffness measurements. *The probabilities were calculated after performing a Student's t test assuming equal variance on the fitted mean stiffness after log-transformation ($5e-2$ level), see Appendix IV.*

Samples compared	p **value**
CCV *versus* Liposome	$6.10e-25$
CCV *versus* T-CCV	$1.16e-8$
T-CCV *versus* Liposome	$3.24e-14$

Table 4.2 resumes the different p values when comparing the populations. From a statistic point of view, all the samples are clearly different.

I have converted the measured stiffness of clathrin coats into bending rigidities to allow comparison with reported values from lipid bilayers. However, this conversion is only a rough estimation since the precise coupling between the vesicle and the clathrin coat as well as the thickness of each of the layers, including the intermediate layer, is unknown. Furthermore, the clathrin coat is a polyhedral structure which is not a continuous shell. It was previously estimated that the bending rigidity of egg-PC lipid bilayers is approximately $12\,k_BT$ [101]. If I assume a similar effective thickness for a clathrin coat, as stated before [98], this results in $44\,k_BT$ for the T-CCVs. On the other hand, assuming that the effective thickness is only doubled in the case of the CCVs, thus not considering any intermediate layer, their bending rigidity is estimated to be $112\,k_BT$. The question remains however to which extend the intermediate layer contributes to the bending rigidity of the coat.

4.4.3 Regulating the stiffness of clathrin coats

- **Effect of the light chains**

I hypothesised that the stiffness of the clathrin coat is variable during its life-cycle to regulate the formation of the lipid bilayer vesicle: from a high bending rigidity during the budding-off stage when the lipid bilayer needs to be bent to a lower rigidity after the vesicle is formed and the clathrin coat can be recycled. To test this hypothesis, I compared the stiffness of T-CCV, which still contains various adaptor proteins, with the stiffness of reconstituted clathrin coats, only made of CHCs and CLCs (CHC+CLC cages). Figure 4.13 shows that the stiffness of reconstituted clathrin coats is with $0.022 \pm 0.007\,\mathrm{N/m}$ ($n = 32$) identical to that of T-CCV (p value of $6.84e-1$). This finding suggests that the clathrin coat rigidity is mainly defined by the clathrin cage and the additional proteins attached to the clathrin coat, as on T-CCV, do not significantly affect the mechanics of the coat.

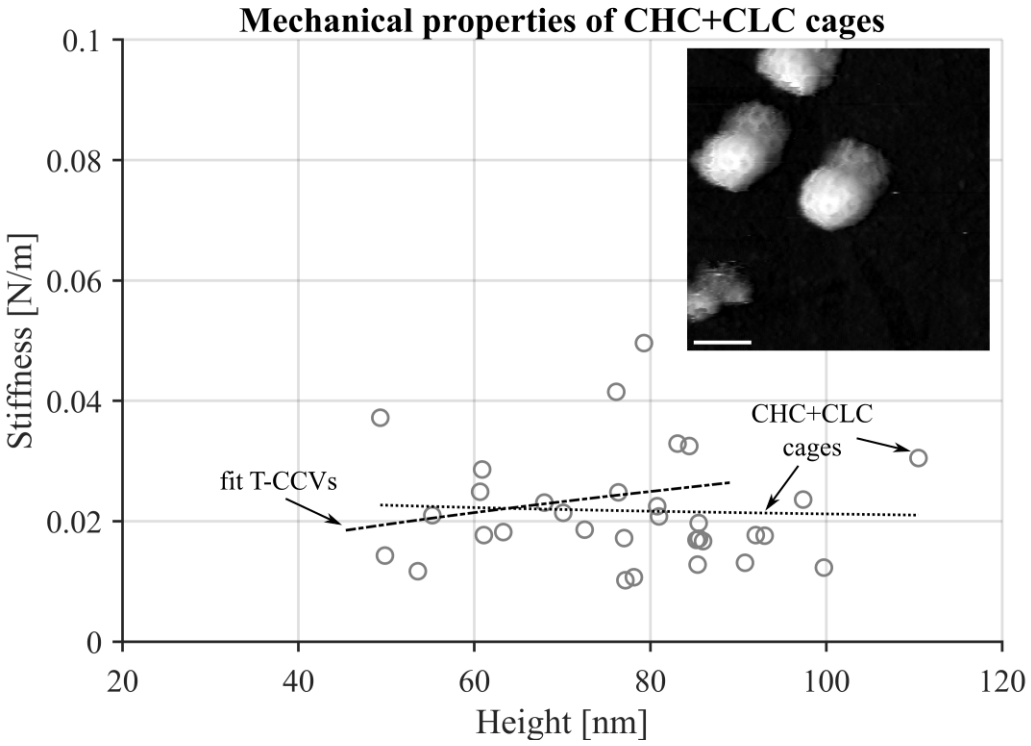

Figure 4.13: Mechanical properties of reconstituted clathrin cages. *The stiffness of the CHC+CLC cages (grey, filled) is identical to that of T-CCVs. The fit of the T-CCVs (semi dashed) is added for comparison. Inset: AFM image of reconstituted clathrin cages (CHC+CLCs cages), scale bar:* 150 nm. *The average height of the measured CHC+CLC cages is approximately* 1.25 *higher than that of the CCVs. In the inset image a double tip effect is visible, which however did not affect the mechanical measurements.*

It was previously shown, that the presence of CLCs increases the stiffness of planar clathrin lattices against flattening as compared to planar CHC lattices [91]. By averaging EM images [91] of such planar clathrin lattices and CHC lattices (lacking CLCs) it becomes apparent that the structure of the lattice nodes, corresponding to clathrin trimerisation domains, is indeed different in the presence of CLC, Figure 4.14a. To demonstrate the importance of the node rigidity for the mechanical stiffness of a clathrin cage I modelled the various polyhedral clathrin coats being compressed by the AFM tip with finite element analysis (FEA, see also Appendix II). As example, Figure 4.14b shows the deformation of a hexagonal barrel [113], a structure which had been probed many times in the AFM images. The highest structural stress, indicated by bright colours, is always concentrated in the nodes. In line with the previous statement, I have modelled a polyhedron with low rigidity nodes which resulted in a very soft structure (data not shown). It confirms that the structural rigidity of the nodes is strongly related to the stiffness of the clathrin coats.

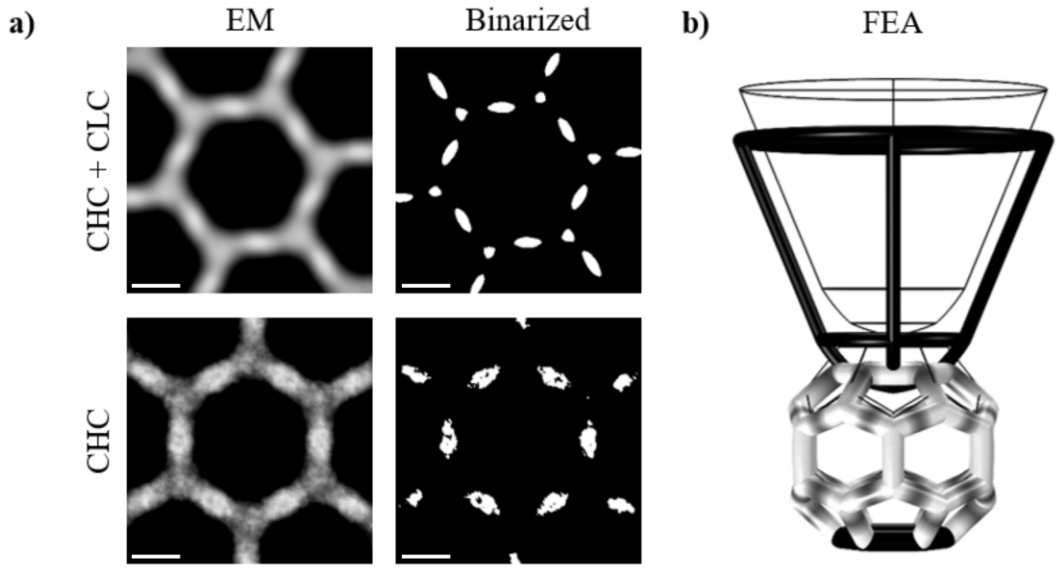

Figure 4.14: Light chains affect structure and mechanics of clathrin-coats. *(a) Left: Average pictures of 2D clathrin lattice imaged by EM. Right: Average pictures after binary transformation to enhance the visualisation of the distribution of electron density which is a measure for the protein density. Scale bars:* 10 nm. *(b) FEA simulation of a hexagonal barrel being indented by a parabolic tip. The stress within the structure is described by the colour gradient, dark is low and white is high.*

If the light chains affect the structure of the nodes this is expected to have a large influence on the stiffness of the clathrin coats.

To test this simulation result, CHC coats were reconstituted on which I performed AFM imaging and force measurements. Figure 4.15 shows that the CHC coats are with $0.040 \pm 0.013\,\mathrm{N/m}$ ($n = 44$) almost 2 times stiffer than the earlier tested clathrin coats. Furthermore, I found that the effect of CLC absence is reversible: if CLC is added to pre-assembled CHC cage (CHC coats + CLCs), these coats recover the low stiffness that was found for the clathrin coats, $0.023 \pm 0.006\,\mathrm{N/m}$ ($n = 18$). This shows that CLC can directly change the cage stiffness but does not lead to irreversible structural changes during assembly. Table 4.3 resumes the p values from the Student's t tests.

Yet, it was previously reported that CLC increases the rigidity of planar clathrin lattices [91]. This apparent contradiction with my findings that the stiffness of coats decreases in the presence of CLC can be explained by the different modes of deformation of the planar and spherical clathrin assemblies. For the coats I identified the rigidity of the nodes as key factor for their rigidity. The planar lattices on the other hand, owe their resistance against flattening largely to the rigidity of the proximal triskelion legs on which the lattice rests.

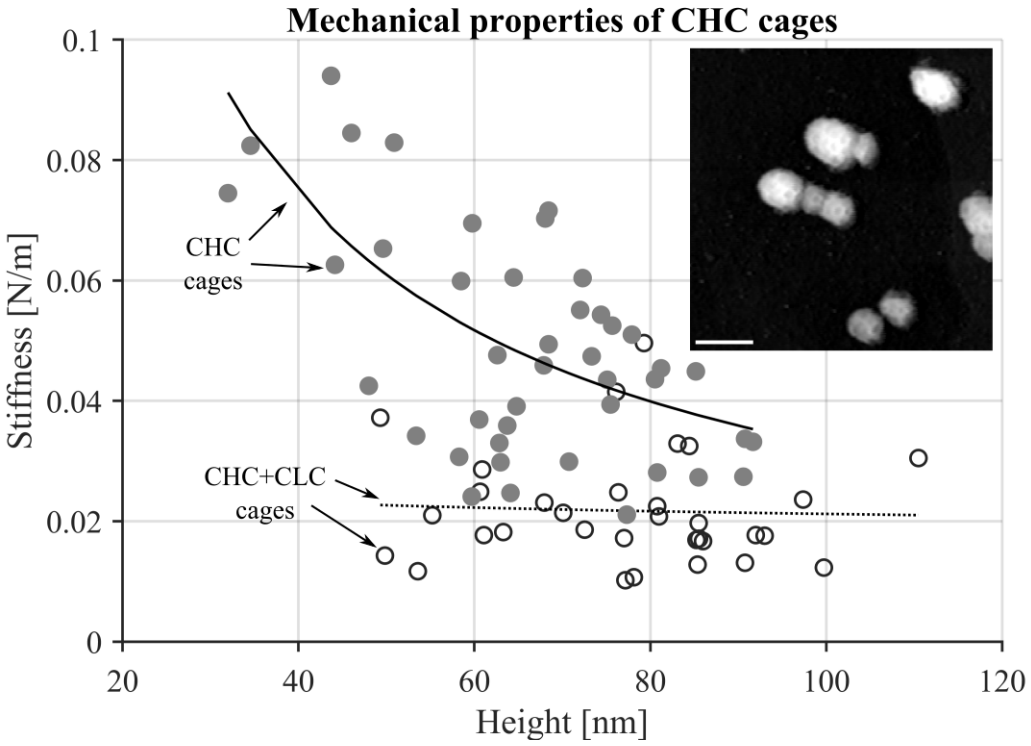

Figure 4.15: Effect of the light chains on the mechanical properties of the cages. *Stiffness versus height plot of CHC cages (grey, filled). The data of CHC+CLC cages (black, empty) is added for comparison. Inset: AFM image of CHCs, scale bar:* 150 nm. *As expected they resemble the CHC+CLC coats.*

Table 4.3: Statistical analysis of the stiffness measurements. *The probabilities were calculated after performing a Student's t test assuming equal variance on the fitted mean stiffness after log-transformation (*$5e-2$ *level), see Appendix IV.*

Samples compared	p **value**
CHC + CLC *versus* CHC	$6.96e-10$
CHC *versus* CHC cage + CLC	$1.04e-6$
CHC + CLC *versus* CHC cage + CLC	$9.50e-1$

Thus, it is possible that CLC reinforces the proximal triskelion leg but at the same time weakens the structure of the node. The observation that CLCs also chemically weaken the coats was made previously in the context of enzymatic uncoating by Hsc70 and its co-chaperon Auxilin under consumption of ATP [97]. In absence of CLCs, the CHC-CHC interaction appears to be strengthened, decreasing the efficacy of enzymatic uncoating. I therefore speculate that the softening effect as induced by CLCs may serve to enable efficient uncoating at the final stages of the clathrin coat life-cycle.

Nevertheless, in cells, CLCs are tightly bound to triskelia [114, 115] which makes it unlikely that their dissociation and association represents a regulatory process for the stiffness of clathrin coats *in vivo*. Instead, their interaction with the triskelia may be regulated by additional factors such as adaptor proteins.

- **Influence of adaptor proteins AP2**

The influence of adaptor proteins on the ability of clathrin coats to bend membranes have been discussed before and mechanisms such as crowding have been proposed and studied [13, 104]. I therefore investigated the mechanical influence of adaptor proteins on reconstituted clathrin cages. Here, I focus on the membrane-clathrin adaptor AP2 which is, after clathrin, the main constituent of clathrin coats at the plasma membrane and previously shown to be able to support clathrin-mediated membrane bending *in vitro* [16, 116]. Figure 4.16 shows that the stiffness of clathrin coats is increased when AP2 is present during assembly ($0.037 \pm 0.012\,\mathrm{N/m}$, $n = 16$) to a level similar to that of CHC coats.

Interestingly this is not the case when AP2 was added after assembly ($0.017 \pm 0.004\,\mathrm{N/m}$, $n = 16$). A control experiment in which AP2 was added during the assembly of CHC coats did not lead to a further increase in stiffness ($0.050 \pm 0.015\,\mathrm{N/m}$; $n = 26$) which suggests a common mechanism for the effects of light chains and AP2. These results show that AP2 does increase clathrin cage rigidity during coat assembly, possibly by counteracting or preventing the effect of CLC on the cage nodes. Interestingly I did not observe the same stiffness for CCVs or T-CCVs, although during the formation of these native coats AP2 was present. I speculate that during the final stage of CCV formation, the rigidity built up under influence of AP2 is released by a yet unknown mechanism, which is not present when isolated clathrin and AP2 are co-assembled.

Table 4.4: Statistical analysis of the stiffness measurements. *The probabilities were calculated after performing a Student's t test assuming equal variance on the fitted mean stiffness after log-transformation (5e − 2 level), see Appendix IV.*

Samples compared	p **value**
CHC *versus* AP2 + CHC	$5.29e-2$
CHC *versus* AP2 + CHC + CLC	$9.32e-1$
AP2 + CHC *versus* AP2 + CHC + CLC	$7.66e-2$
CHC + CLC *versus* CHC + CLC cage + AP2	$8.74e-2$

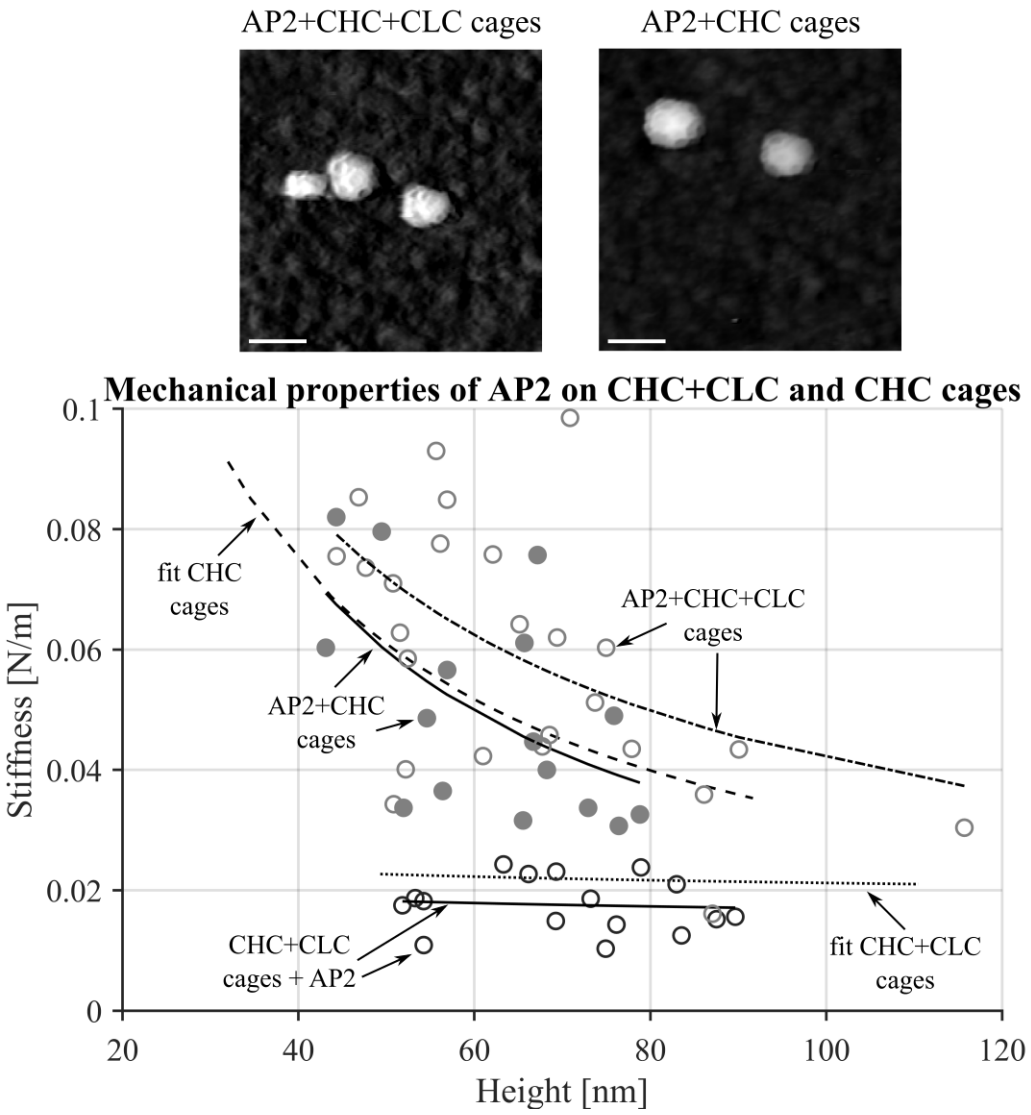

Figure 4.16: Effect of adaptor protein AP2 on the mechanical properties of the cages. *AFM images of AP2+CHC+CLC cages and AP2+CHC cages, left and right respectively. Scale bar:* 150 nm. *Stiffness versus height plot to compare the mechanical effect of the AP2 when added during assembly of the clathrin cages, AP2+CHC+CLC (grey, empty), or after assembly of the clathrin cages, CHC+CLC cages + AP2 (black, empty) and during assembly of CHC cages, AP2+CHC cages (grey, filled). The fits of the CHC+CLC (dots) and CHC cages (dashed) are added for comparison.*

4.5 Conclusion

In this experimental work, I have performed a systematic study of the mechanical properties of clathrin-coated vesicles to answer the question whether mechanical regulation could play a role during vesicle transportation in eukaryotic cells. I used low force AFM in liquid to ensure non-damaging imaging and performed direct mechanical characterisation

of single coats by localised force measurements. I discovered that CCVs and their native clathrin-coats are surprisingly soft when compared to structures like virus particles. This indicates that the final stage of the clathrin coat has not evolved towards maximum rigidity. At first sight, this seems to contradict the role of clathrin coats to bend membranes containing potentially rigid cargo into vesicle shape. However, because the clathrin coats are still about four times more rigid than the membranes they enclose, this might suffice to bend membranes into shape. Interestingly, the stiffness of the clathrin coat can be further up-regulated by the light chains. When light chains are absent or when AP2 is present the cage stiffness is doubled. Because this stiffening is reversible and because the quantitative effects of CLC absence or AP2 presence are nearly identical I speculate that the stiffness is regulated through the light chain conformation and can be used to dynamically regulate the stiffness of the clathrin lattice in order to facilitate vesicle formation.

Whether and how adaptor proteins like AP2, which lack the autonomous ability to bend membranes, contribute to membrane bending during CCV formation is a long standing question in the field of vesicle trafficking. Yet the only conceivable contribution described is the crowding effect. However, this was shown for a fragment of the adaptor Epsin when recruited in unphysiological large amounts in model membranes [117]. The ability to directly regulate the stiffness of clathrin coats is a novel role that I discovered for AP2, which is the main adaptor in all clathrin coated pits at the plasma membrane. This feature of AP2, which was speculated upon before [98], may help to generate more force on the underlying membrane. Since I did not observe an elevated stiffness in the final stage of native CCVs (T-CCVs), I hypothesise that the effect of AP2 occurs in living cells at earlier stages of CCV formation. Especially during these early stages, a high coat rigidity might be essential to be able bend the lipid bilayer into a vesicle. At the final stage, when the mature CCV prepares for uncoating, the rigidity lowers again. A possible explanation for this could be a change in CLC conformation as demonstrated in Wilbur et al. [96] mediating the release of cage stiffness built up by co-assembly with AP2. Thus, after the vesicle is formed, CLC overcome the influence of the adaptor protein weakening the nodes, preparing the coat for disassembly [97].

Appendix I: Comprehensive data analysis

To analyse the forcemaps obtained during the AFM experiments I have developed a complete MATLAB graphical user interface (GUI) that was written for the MFP3D AFM from Asylum Research, different AFMs would require an adaptation of my program. The forcemaps are stored as a folder containing all individual force curves as Igor binary waves, Igor being the platform used by Asylum Research to operate the AFM.

At first, each force curve is converted in a MATLAB readable format, thanks to the function *IBWread* provided by Jakub Bialek, and stored in a matrix of cells (this part is not ideal as it suggests storing a huge number of data, making the loading process rather slow, but it makes the future analysis and the corresponding code simpler). A cell contains two vectors: the z-piezo displacement, z, in meter and the deflection of the cantilever, d, in meter as well. Both vectors need to be converted into indentation, δ, and force, F, thanks to:

$$\delta = z - d \tag{4.5}$$

$$F = d \cdot k_c \tag{4.6}$$

with k_c the spring constant of the cantilever preliminary calibrated and which value is stored in the headers of the binary wave files.

As soon as all files are loaded and converted, I calculate for each curve:

- the contact point, defined as the position at which the force reaches 30 pN, and
- the local stiffness, defined as the slope from the indentation region and extracted using the function *polyfit* which performs a linear fit.

From the contact points and the different stiffness, it is possible to compute a preliminary height map (height at 30 pN) and stiffness map respectively. The initial height map is shown in Figure 4.17a.

This height map however suffers at that point from artefacts such as: thermal drift of the z-piezo scanner (the upward movement of the scanner does not necessarily match the downward movement), that the position of the scanner is not set to 0 prior force mapping (there is thus an offset in the height map) and potential real tilt of the substrate. I have written two functions to correct for these artefacts. At first, I performed a custom *planefit* on the height image by selecting manually 3 pixels from the substrate which positions are used to calculate the equation of plane that is later subtracted from the image, Fig-

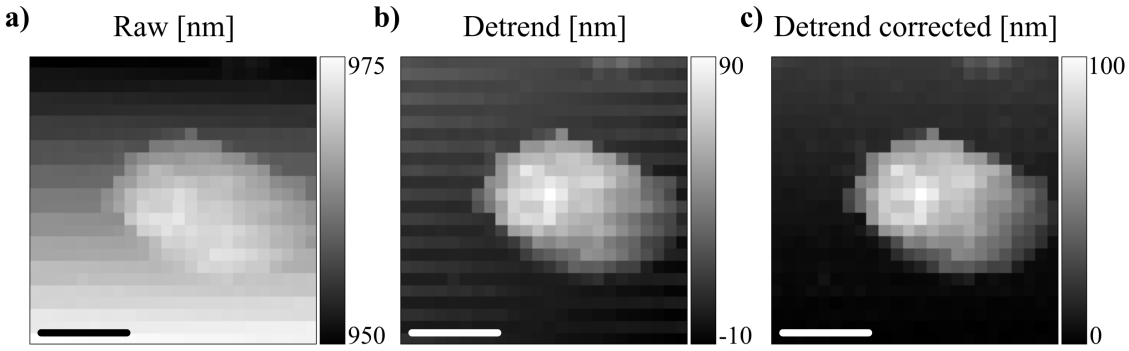

Figure 4.17: Height maps of a clathrin cage, more likely a truncated icosahedron. *(a) raw image: the cage is visible but the image needs further processing to extract the real height. (b) Detrend image of the cage after fitting a plane on the raw image. (c) Final height map after the correction of the AFM scan mode. The cage is found to be* 83.75 ± 6.61 nm *(mean ± standard deviation). Scale bars:* 100 nm.

ure 4.17b. Then, I further correct the image from the thermal drift of the piezo scanner. I select successively two even substrate lines and two odd substrate lines and averaged each set. The two averaged even and odd lines are subtracted from the even and odd lines of the height map respectively, Figure 4.17c. Such procedure allows me to significantly enhance the quality of the height map and facilitates the finding of the apex of the sample, defined as the centre of mass of the positions from the 6 highest points of the height map.

When the apex is found, all curves belonging to a 20 nm radius circle are automatically selected (based on the force map resolution, it results in a maximum of 9 curves). The selected curves are checked individually and corrupted curves are manually removed. Curves are considered corrupted when they clearly show a different behaviour than the other curves, due to local tip contamination for example. In the meantime, 9 curves from the substrate are also stored. These curves are automatically selected by finding the position of maximum stiffness from the initial stiffness map. Each set of curves (one for the sample, one for the substrate) is averaged: since the individual curves do not necessarily have the same number of points, they are linearly interpolated using a newly defined indentation vector with 0.1 nm step size. From there, the curves are aligned thanks to a custom subroutine which minimises the least square error between the distances from a fixed reference curve (randomly chosen). The curves are averaged, aligned according to the mean curve and averaged again, see Figure 4.18a and Figure 4.18b. This step is crucial to optimise the alignment procedure and is inspired by particle averaging routines from cryo-EM.

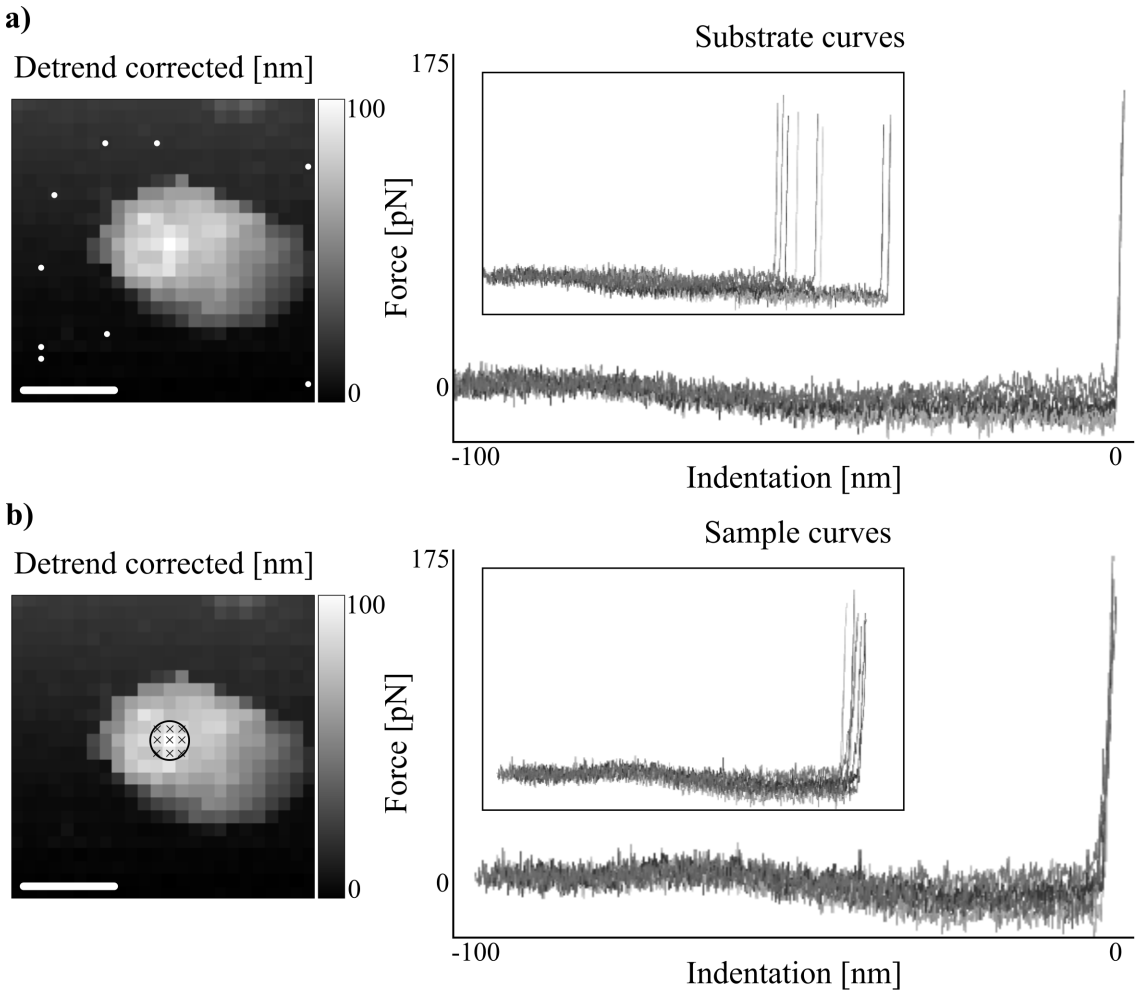

Figure 4.18: Selection and average of characteristic sample and substrate curves. *(a) Left: height map showing the location of the 9 selected curves from the substrate (white dots). Scale bar:* 100 nm. *Right: the 9 selected curves are shown in the inset while the result of the alignment procedure is shown in the main graph. (b) Left: height map showing the location of 9 selected curves from the sample (black crosses) within a* 20 nm *radius circle centred on the centre of mass of the 6 highest point. Scale bar:* 100 nm. *Right: the 9 selected curves are shown in the inset while the result of the alignment procedure is shown in the main graph.*

The final averaged curves are displayed in Figure 4.19a. Then, the averaged curve from the sample is further corrected from potential contaminations of the tip. A contamination is visible when the indentation region of the averaged substrate curve is not almost perfectly straight (the substrate being very stiff as compared to the stiffness of the cantilever, the last should not be able to indent the substrate) as shown in Figure 4.19b. This final correction is done by removing the slope of the indentation region of the averaged substrate curve from the averaged curve from the sample.

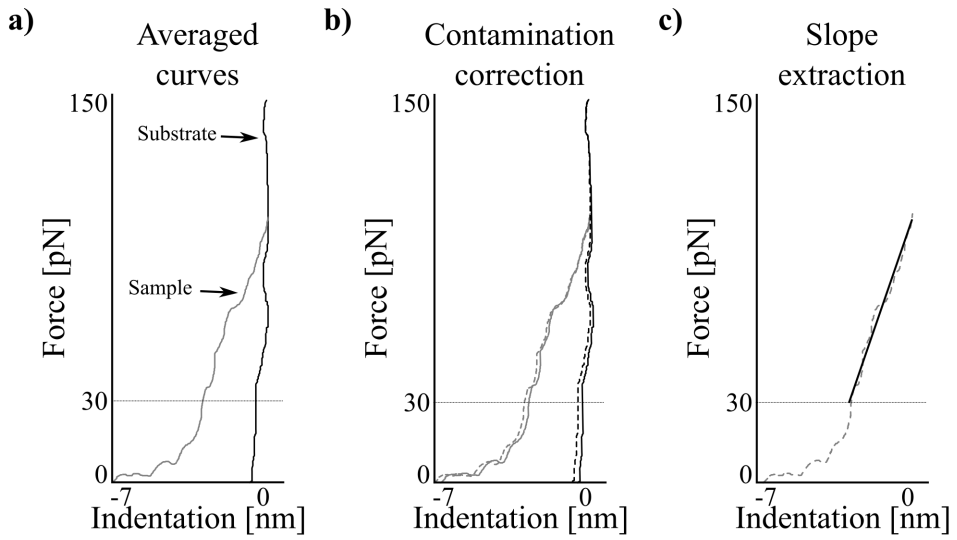

Figure 4.19: Final results. *(a) The average curves of the substrate and the cage as well as their standard deviation are presented in blue and grey respectively. (b) Correction of the slope to remove any corrupted calibration. The corrected curves are in plain. (c) The linear fit of the indentation region from the corrected averaged sample curve is displayed in black. The deduced stiffness is* $0.02012 \pm 0.00034\,\mathrm{N/m}$ *(value ± standard error of the fit). The* χ^2 *equals* 0.98767.

Finally, the indentation region of the sample averaged curve is linearly fitted using the *polyfit* function from MATLAB, Figure 4.19c. The standard error of the fit, as well as the Pearson's chi-squared test are computed, which concludes the analysis.
Time wise, a complete analysis takes approximately 10 min per cage.

Appendix II: Finite element analysis on clathrin cages

The main motivation of using finite element analysis (FEA) in this experimental work was to confirm i) the observed absence of a clear relationship between the height of the clathrin coats and their stiffness and ii) to explain their softness. To address this issue I developed 3D mechanical models of each polyhedron seen during AFM imaging with COMSOL Multiphysics (Comsol, Stockholm, Sweden), see Figure 4.20. In these models, the cages were modelled with circular cross-section beams that can be bent, stretched and compressed. The radial compression of the ribs was not included.

In earlier work, the rib length of the building pentagons and hexagons of the coats was found to be approximately 17.5 nm (measured by AFM [13]). This value was used as a reference in all generated geometries. However, the rib diameter and the exact Young's modulus are still unknown. I thus tested multiple combinations of these two parameters until the results best matched the experimental data. The rib diameter was set to 7 nm while the Young's modulus was 100 MPa which is a common value for proteins albeit at the low side (100*s* MPa – 1 GPa [37, 106]). Their Poisson's ratio was arbitrarily set to 0.45.

Both the dodecahedron and the truncated icosahedron were made of regular pentagons and hexagons of 17.5 nm rib length. However it is geometrically impossible to generate a truncated triakis tetrahedron and a hexagonal barrel with such regular polygons. Indeed,

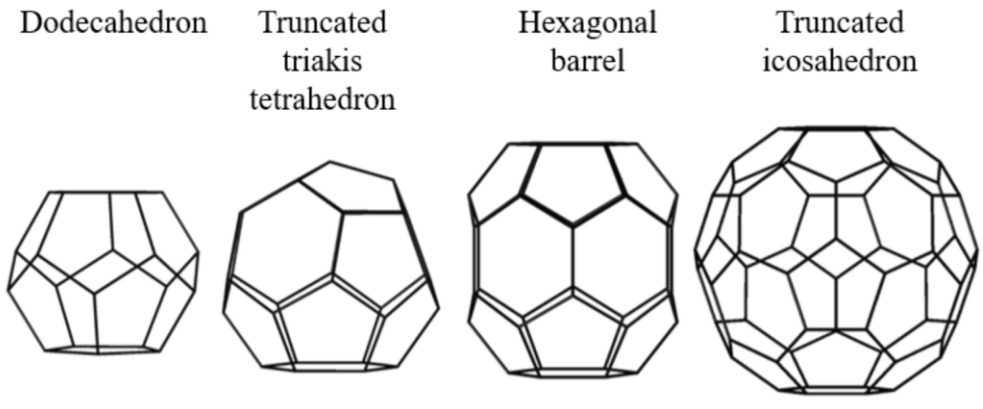

Figure 4.20: 3D models of clathrin coat. *From left to right: dodecahedron,* 48 nm *high; truncated triakis tetrahedron also called minicoat,* 62 nm *high; hexagon barrel,* 70 nm *high; truncated icosahedron also called soccer ball,* 85 nm *high. The beam radius was reduced to better visualise the structures.*

while the truncated triakis tetrahedron needed planar irregular pentagons (edges of different length), the hexagonal barrel required the 6 side-hexagons to be non-planar (vertices not in the same plane). Mechanically speaking, it infers that the legs of their building clathrin triskelia are initially bent or slightly stretched. This can probably lead to some difficulties in generating such coats *in vivo*. Yet, this is a point which was not seen in my investigation and suggests that the necessary forces to pre-deform the triskelion are rather low and not energetically demanding. This also goes in line with the fact that clathrin cages are fairly soft and thus easily deformed.

To simulate the adhesion of the clathrin coats onto the HOPG substrate by electrostatic forces, which is the result of the plasma cleaning prior investigation, the edges of a complete hexagon (or a complete pentagon, depending on the polyhedron) in contact with the supporting plane were constrained in all three directions. The AFM probe was modelled as a parabolic tip that was compressing the upper boundary of the polyhedron and linearly lowered in small steps that did not exceed 1 nm. The loads applied, P, were described by a custom contact-penalty method [107] which can be resumed as follow: at each new position of the tip, the gap between its surface and the one of the polyhedron was calculated and a specific force was exerted accordingly:

- if the gap was large, the force applied was null,
- if the gap was small but positive, the force applied was described by an exponential function to mimic the Pauli repulsion,
- if the gap was negative, a much higher force was applied that scales linearly with the gap-value.

The above-mentioned statement was written using an *if* case:

$$P(\Delta d) = if\left(\Delta d < 0,\ \Delta d \cdot (t_n - e_n),\ t_n \cdot e^{\frac{-\Delta d \cdot e_n}{t_n}}\right) \tag{4.7}$$

where Δd is the gap distance, t_n and e_n are the contact penalty method parameters chosen to be $3.25 \cdot 10^5$ Pa and $5.00 \cdot 10^{15}$ Pa/m respectively to best match the AFM experiments and to provide high enough stability during the computation of the FEA.

Since the tip was considered as a full 3D object, the lateral distance, Γ, from the loading centre had to be defined to calculate the forces applied by its edges:

$$\Gamma = \sqrt{(y + v - y_{tip})^2 + (x + u - x_{tip})^2} \tag{4.8}$$

where y and x are the original coordinates of the cage, u and v the deformation in the x and y direction respectively, and x_{tip} and y_{tip} are the tip original positions.

The direction of the applied force was perpendicular to the surface of the parabolic tip and was derived from the derivative, υ, of the parametric equation that describes the tip shape and the above-mentioned lateral distance:

$$\upsilon = z|_{\delta=0} - \delta + \frac{\Gamma^2}{2 \cdot r_{tip}} \tag{4.9}$$

where $z|_{\delta=0}$ is the original tip position in the z axis, δ the parametric variable that was used to lower the tip and r_{tip} the tip radius.

The contribution of the applied force was divided in the x, y and z components according to:

$$z_{load} = -P \cdot \cos\left(atan(\upsilon)\right) \tag{4.10}$$

$$y_{load} = -P \cdot \sin\left(atan(\upsilon)\right) \cdot \frac{(y + v - y_{tip})^2}{\Gamma^2} \cdot sign(y + v - y_{tip}) \tag{4.11}$$

$$x_{load} = -P \cdot \sin\left(atan(\upsilon)\right) \cdot \frac{(x + u - x_{tip})^2}{\Gamma^2} \cdot sign(x + u - x_{tip}) \tag{4.12}$$

where $sign$ is a function to determine the sign of its argument.

In AFM, the normal force exerted by the probe onto the sample is measured. To reproduce such condition, it was calculated by integrating the z-component of the total applied load over the whole structure at each new position of the tip with:

$$F_n = \sum z_{load} \cdot r_{ribs} \tag{4.13}$$

where r_{ribs} is the radius of the beams.

Two stop conditions were implemented to constrain the movement of the tip:

- the force felt by the cage should not exceed 150 pN to reproduce the AFM spectroscopy curve and reduce the computation time, and
- the tip should not be lowered below a fictive $z = 0$ nm plane. Ideally this plane should have been considered during the computation but it inferred increasing unnecessarily the mesh that describes the model and thus the computation time. For this reason, it was omitted.

Figure 4.21 shows two single spectroscopy curves on a hexagonal barrel from AFM experiments (plain) and from the FEA (dashed). A linear fit on the indentation region

reveals that the coat is 0.038 N/m and 0.024 N/m if measured by AFM or FEA respectively. While the stiffness of the cages probed differs due to different structural properties and measurement location, both curves show a similar linear response to the applied force which attested the custom contact penalty method and the parameters chosen for the FEA. The ability to reproduce single AFM spectroscopy curve also opened the way to simulate complete forcemaps. To achieve this, a region containing the complete polyhedron was spatially discretised in steps of 6.25 nm (twice the AFM experimental condition) and the above-mentioned FEA was repeated at each pixel. A MATLAB routine was developed to automatically analyse the resulting force curves and extract their height and stiffness (slope of the indentation region [30 : 150] pN). Since the simulations did not include noise sources (from thermal drift, liquid environment, electronical noise, tip contamination etc), the stiffness of the whole polyhedron was directly calculated by averaging the pixels values belonging to a 20 nm radius circle centred in the apex of the cage.

Finally, I calculated the height maps at different applied force, 30 pN to reproduce AFM images, and 100 pN, to visualise the induced deformation.

The FEA results of a dodecahedron, a mini coat and a hexagonal barrel models are shown in Figure 4.22a, Figure 4.22b and Figure 4.22c respectively. The data regarding the truncated icosahedron is not shown as the resulting images were containing many unstable force curves especially at the edges of the coat.

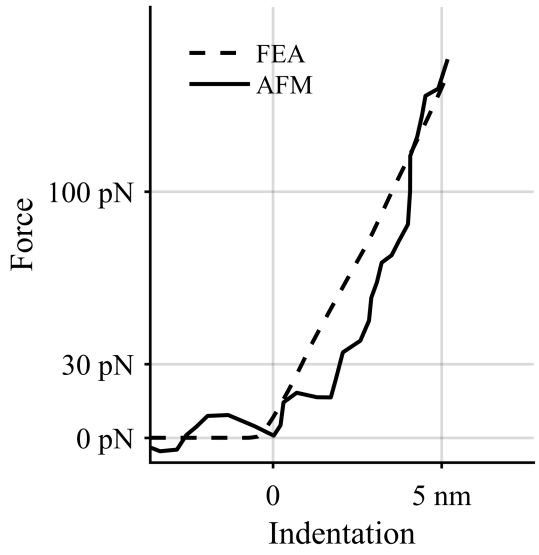

Figure 4.21: Comparison of a random single force curve from the AFM study (plain line) to one computed (dashed line). *Both curves show similar behaviour which confirms the model developed and the parameters chosen.*

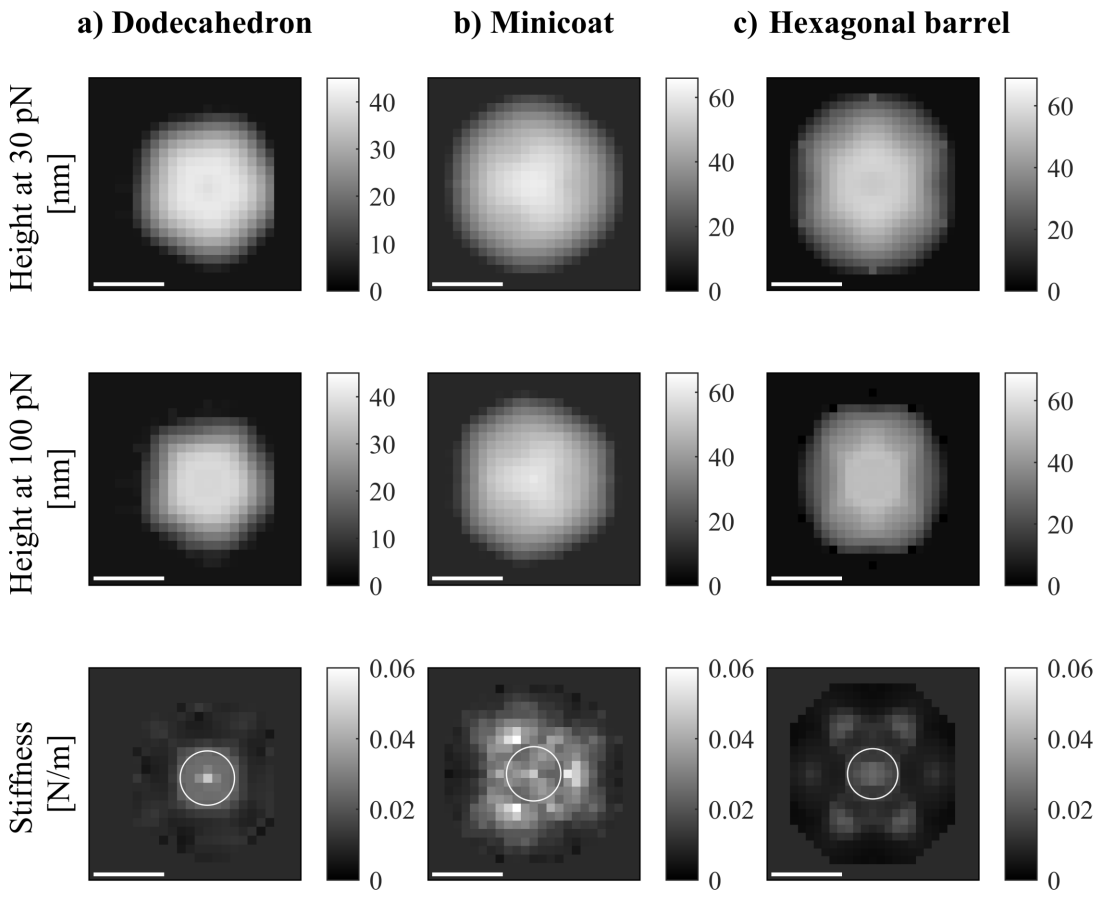

Figure 4.22: FEA of the various tested polyhedra. *A* 20 nm *radius white circle is added to the stiffness maps to emphasise the region taken to calculate the mean stiffness of each cage. The region scanned was a* 150×150 nm *area discretised in* 24×24 *pixels with* 6.25 nm *steps. Scale bars:* 50 nm.

Table 4.5: Average stiffness of the different structures scanned sorted by size from FEA. *The values are mean* ± *std. The standard deviations mentioned are from averaging the stiffness from the pixels within the centred circle.*

Polyhedron	**Height** [nm]	**Stiffness** [N/m]
Dodecahedron	40.05 ± 1.28	0.025 ± 0.006
Hexagonal barrel	55.94 ± 0.89	0.017 ± 0.003
Truncated triakis tetrahedron	58.16 ± 1.84	0.030 ± 0.006
Truncated icosahedron	77.48 ± 0.81	0.012 ± 0.002

Surprisingly, the structures appear more defined at high force as their lattices are better visible than at low force. Table 4.5 summarises the stiffness of the different geometries investigated. Interestingly, there is a weak apparent inverse relationship between the stiffness of the polyhedra and their heights. The bigger the structure is, the softer it appears. Nonetheless, the truncated triakis tetrahedron stands out from this statement as

it is the stiffest sample while being only 58 nm (not the smallest). This discovered mild correlation was not seen in the AFM data and may have been masked by experimental noise or defects in the polyhedral structures. Furthermore, the FEA assumes perfect polyhedra and omits many molecular aspects. However, the found correlation goes in line with the idea that the cages can, even if they are built from ribs, partly be described by the thin spherical shell theory.

To further validate the simulation, I calculated the apparent tip radius, r_{tip}, from the height map at 30 pN following the lateral dimension equation of a spherical sample scanned with a tip of similar radius, resulting in a tip-sample convolution, as explained in subsection 2.2.4 from chapter 2:

$$r_{tip} = \left(\frac{r_{dilated}}{2}\right)^2 \cdot \frac{1}{r} \tag{4.14}$$

with $r_{dilated}$ the dilated radius of the polyhedron, r_{tip} the radius of the probe, r the radius of the cages.

As far as the hexagonal barrel is concerned, $r_{dilated} = 78.24$ nm and $r = 60.00$ nm. The calculated tip radius was then 25.51 nm while I effectively modelled an AFM probe of 25 nm radius (RC150VB, Olympus, Tokyo, Japan) which further confirms my 3D models. To my knowledge, this is the first time that AFM force mapping experiments were simulated with FEA. Surprisingly, it also revealed that the resolution of the images increases at higher forces. This goes actually against most of the AFM imaging rules which state to image sample with the lowest exerted force possible. On the other hand, this is not devoid from logic: by applying a higher force, the AFM probe compresses or pushes aside all soft components of the sample and probes the details of its "skeleton" at the risk of damaging the sample. In addition, the high resolution mapping of the coats revealed that even in the stiffness map the pentagons and hexagons were clearly visible. This fact was not seen in the AFM forcemaps probably because of the additional noises from the experimental set up itself but also because the spatial resolution was twice the one used in the FEA. Unfortunately, these findings were not further addressed in this thesis because of experimental limitations. Reducing the resolution of the forcemaps, from 12.5 nm to 6.25 nm, would multiply the recording time by 4 (thus from approximately 5 min to 20 min). Because of the thermal drift, this would lead to artefacts that will complicate the interpretation of the acquired data.

Appendix III: Detailed fitting results

I recall that the stiffness, k, is extracted from the linear fit of the indentation region of the averaged force *versus* indentation curve over the apex of a cage. The standard error, ste, of the fit is shown. All linear fits resulting in a χ^2 value below 0.95 were rejected.
The stiffness *versus* height data is fitted using non-linear regression with $k(r) = a \cdot r^b$ where a and b are coefficients determined during iterative least square minimisation. The mean absolute error (MAE) and the adjusted χ^2 as goodness-of-fit parameters are included in all plots.

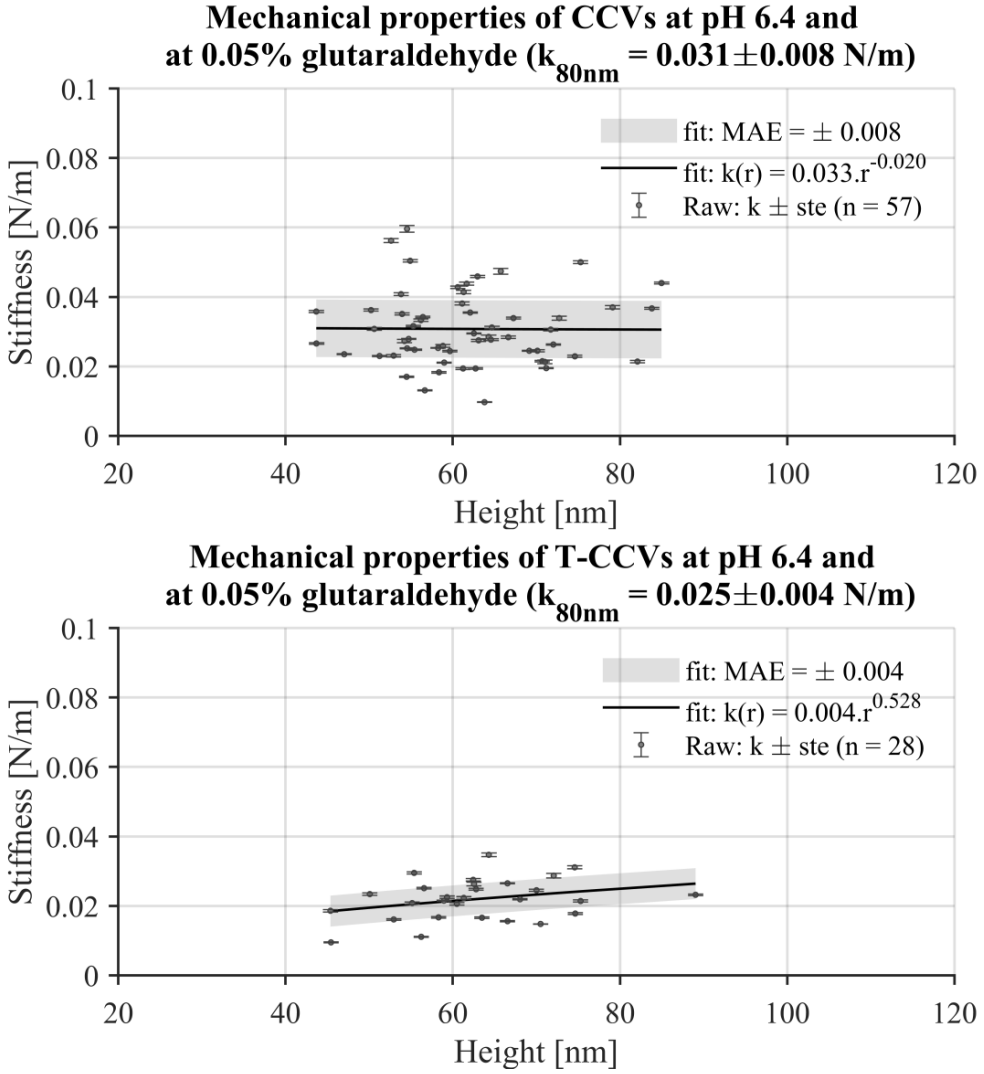

Figure 4.23: CCVs and T-CCVs comparison. *8 % of the CCVs raw stiffness were rejected ($n_{total} = 62$), adjusted $\chi^2 = 0.64$. 3 % of the T-CCVs raw stiffness were rejected ($n_{total} = 29$), adjusted $\chi^2 = 0.83$.*

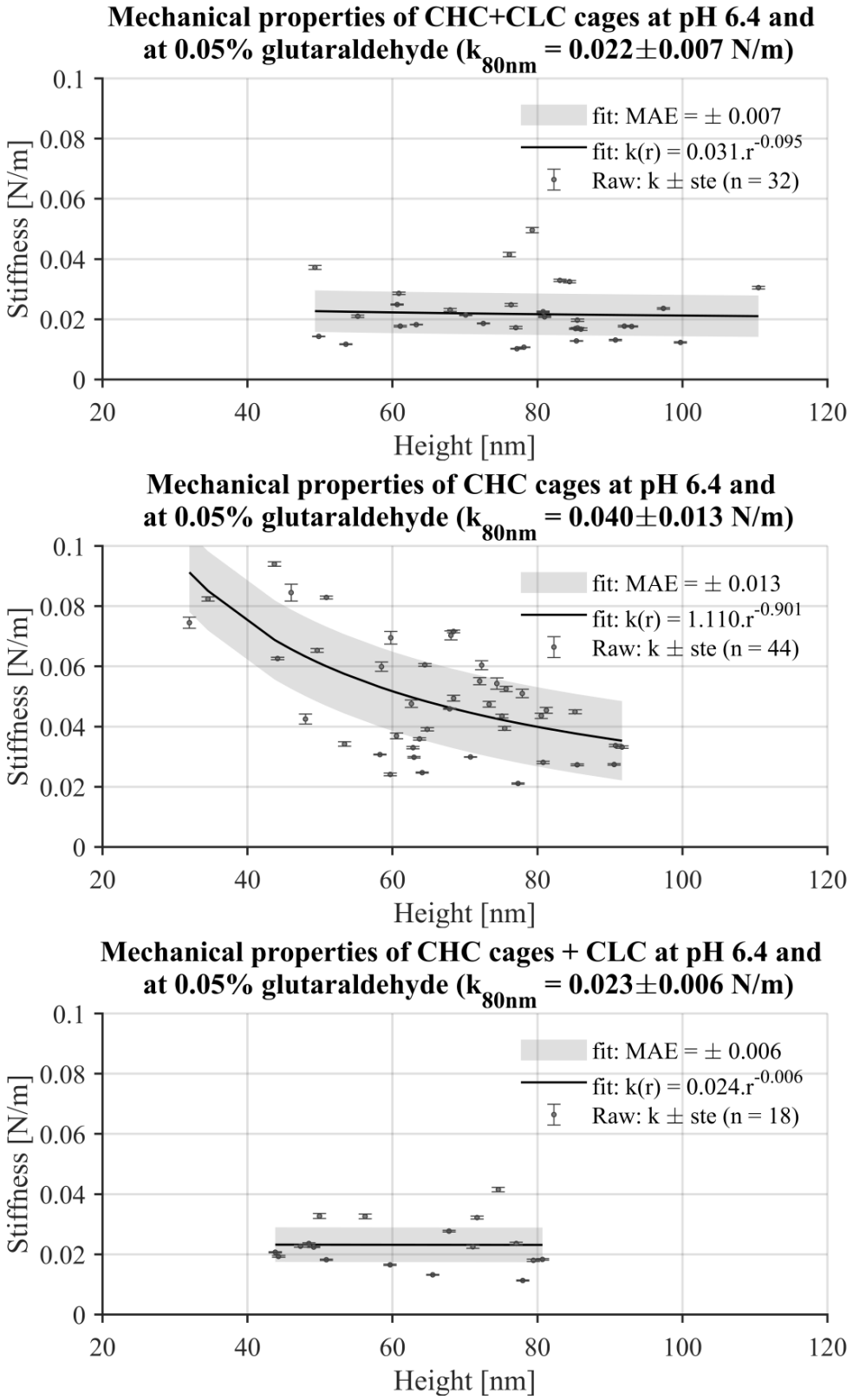

Figure 4.24: CHC+CLC cages, CHC cages and CHC cages + CLC comparison. *6% of the CHC+CLC cages raw stiffness were rejected (n_{total} = 34), adjusted χ^2 = 0.83. 17% of the CHC cages raw stiffness were rejected (n_{total} = 53), adjusted χ^2 = 0.62. No raw stiffness were rejected regarding CHC cages + CLC (n_{total} = 18), adjusted χ^2 = 0.83.*

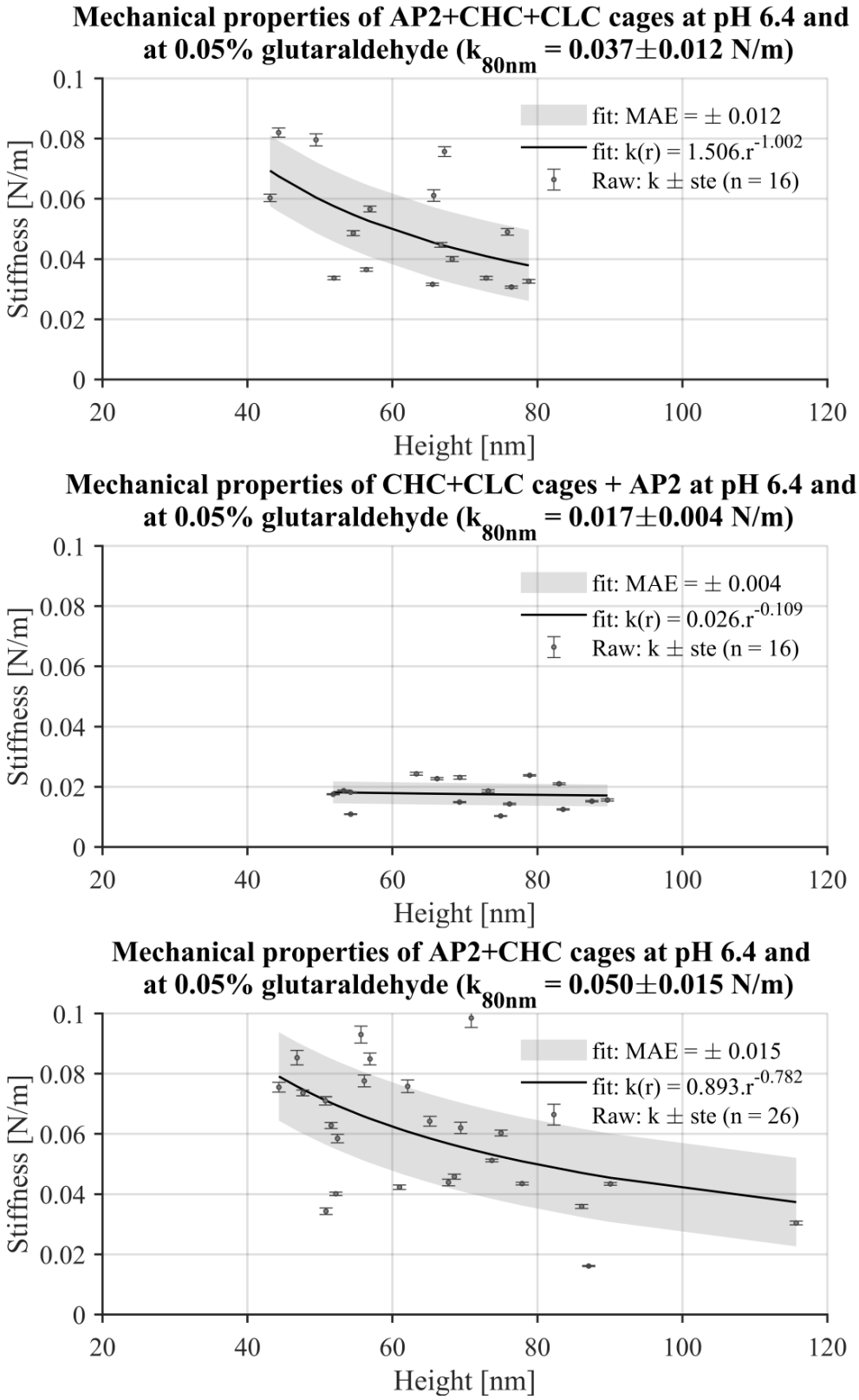

Figure 4.25: AP2+CHC+CLC cages, CHC+CLC cages + AP2 and AP2+CHC cages comparison. *40 % of the AP2+CHC+CLC cages raw stiffness were rejected (n_{total} = 27), adjusted χ^2 = 0.80. 11 % of the CHC+CLC cages + AP2 cages raw stiffness were rejected (n_{total} = 18), adjusted χ^2 = 0.89. 7 % of the CHC+CLC cages + AP2 cages raw stiffness were rejected (n_{total} = 28), adjusted χ^2 = 0.65.*

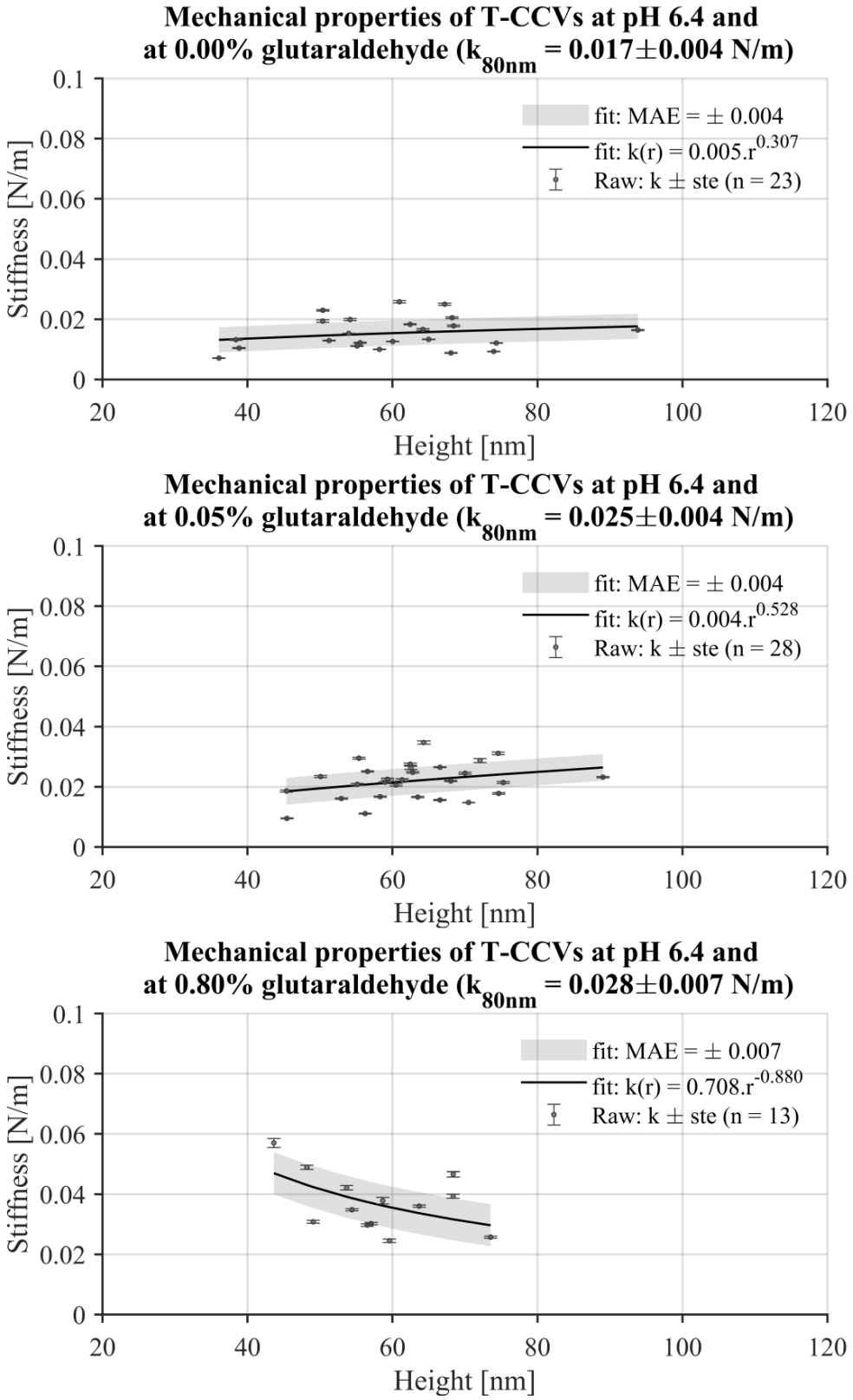

Figure 4.26: Comparison between mechanics of T-CCVs in different glutaraldehyde concentration. *No raw stiffness were rejected (n_{total} = 23) regarding T-CCVs at* 0.00 %, *adjusted* χ^2 = 0.84. 3 % *of the T-CCVs at* 0.05 % *raw stiffness were rejected (n_{total} = 29), adjusted* χ^2 = 0.83. 27 % *of the T-CCVs at* 0.80 % *raw stiffness were rejected (n_{total} = 22), adjusted* χ^2 = 0.88.

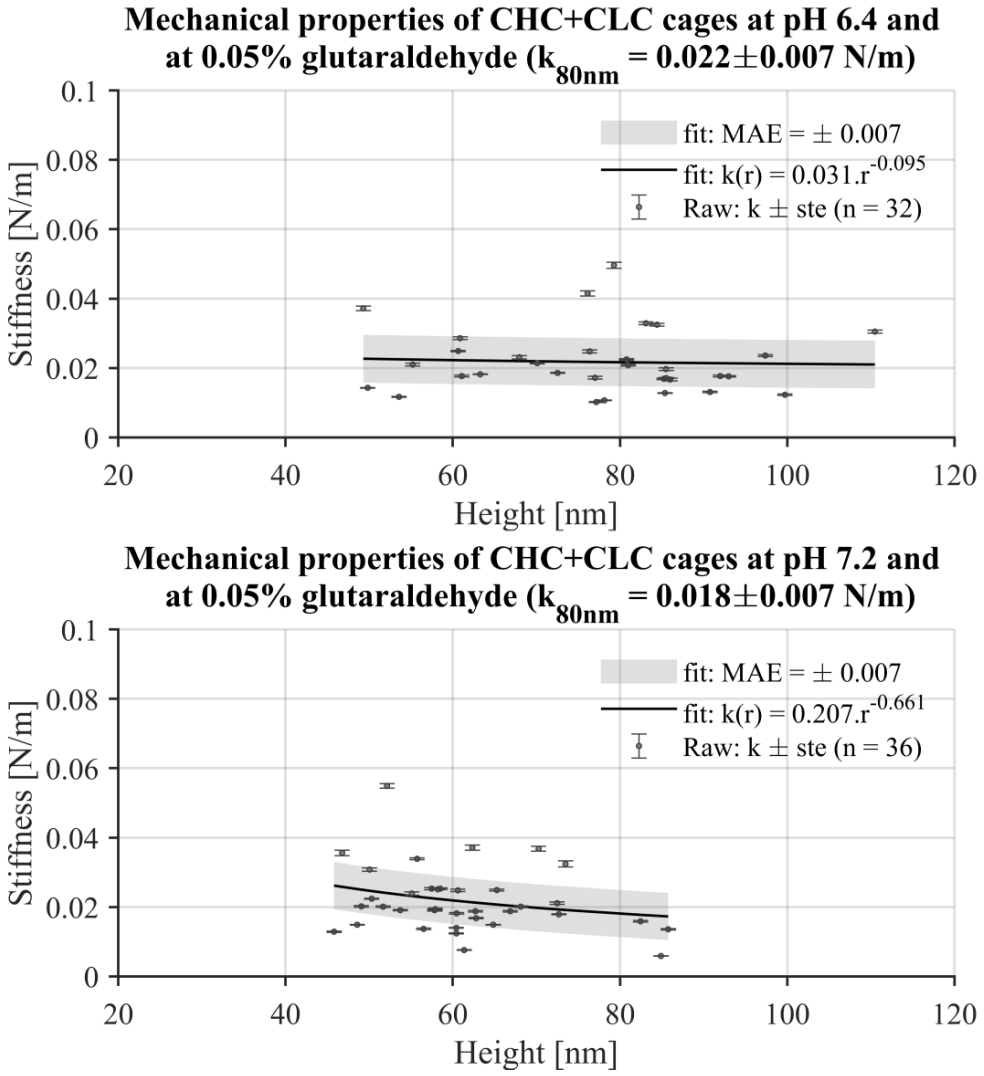

Figure 4.27: Effect of the buffer pH on the mechanical properties of the clathrin coats. *6 % of the CHC+CLC cages at pH 6.4 raw stiffness were rejected (n_{total} = 34), adjusted* $\chi^2 = 0.83$. *8 % of the CHC+CLC cages at pH 7.2 raw stiffness were rejected (n_{total} = 39), adjusted* $\chi^2 = 0.70$.

Appendix IV: Stiffness distribution

The stiffness data are log-normal distributed in most cases (data not shown), which indicates that after log-transformation they present a normal distribution. Figure 4.28 to Figure 4.32 show the log-transformed stiffness (in [mN/m]) distributions from the various clathrin assemblies. The number of bins per histogram was chosen according to Sturges's rule [110]. The histograms were tested for normality and for each test, the mean log-transformed stiffness, μ, and its standard deviation, σ, were extracted.

The normal distribution describes well the log-transformed stiffness but deviances can be seen due to a low number of cages measured for the specific population. Nonetheless, I decided to systematically apply the Student's t test, which requires normality, to evaluate whether cages from two different populations share similar mechanical properties.

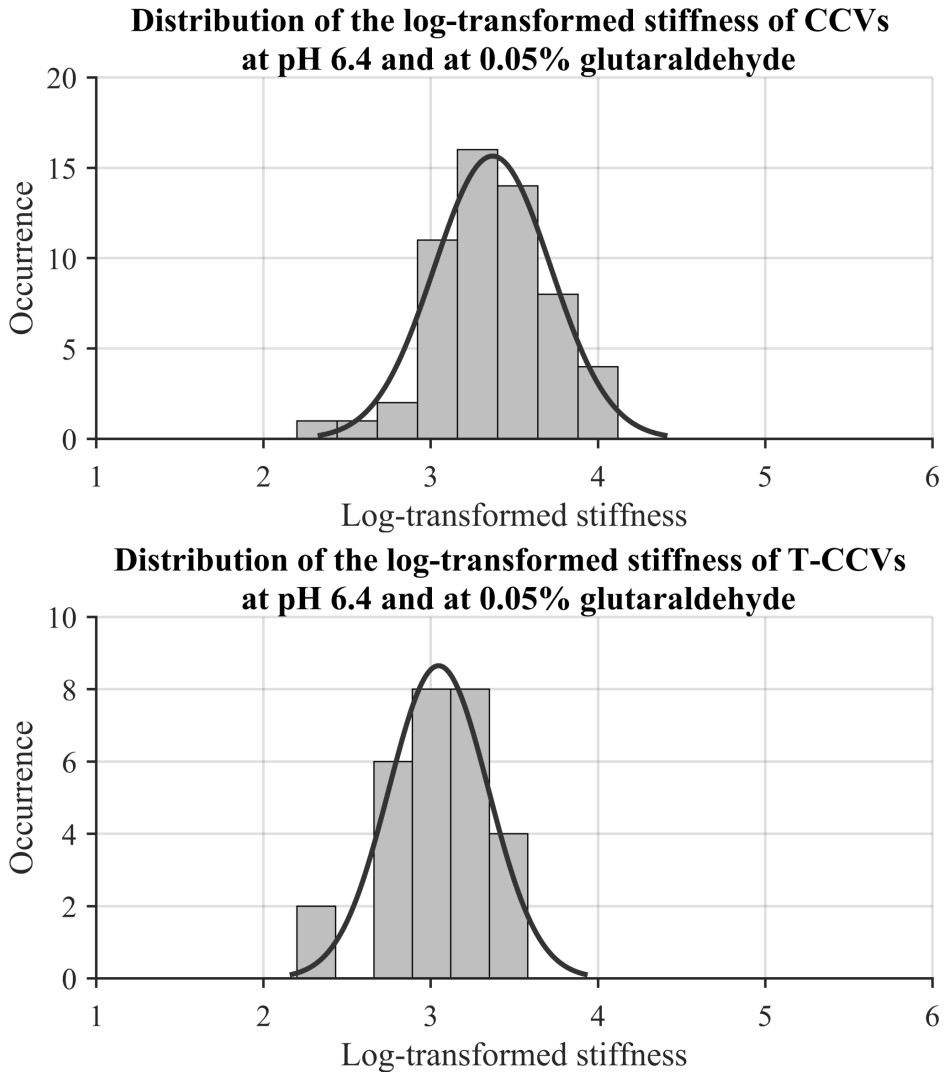

Figure 4.28: CCVs and T-CCVs stiffness distribution. *Probability density parameters:* $\mu = 3.37$ *and* $\sigma = 0.35$*;* $\mu = 3.05$ *and* $\sigma = 0.30$ *for the CCVs and the T-CCVs respectively.*

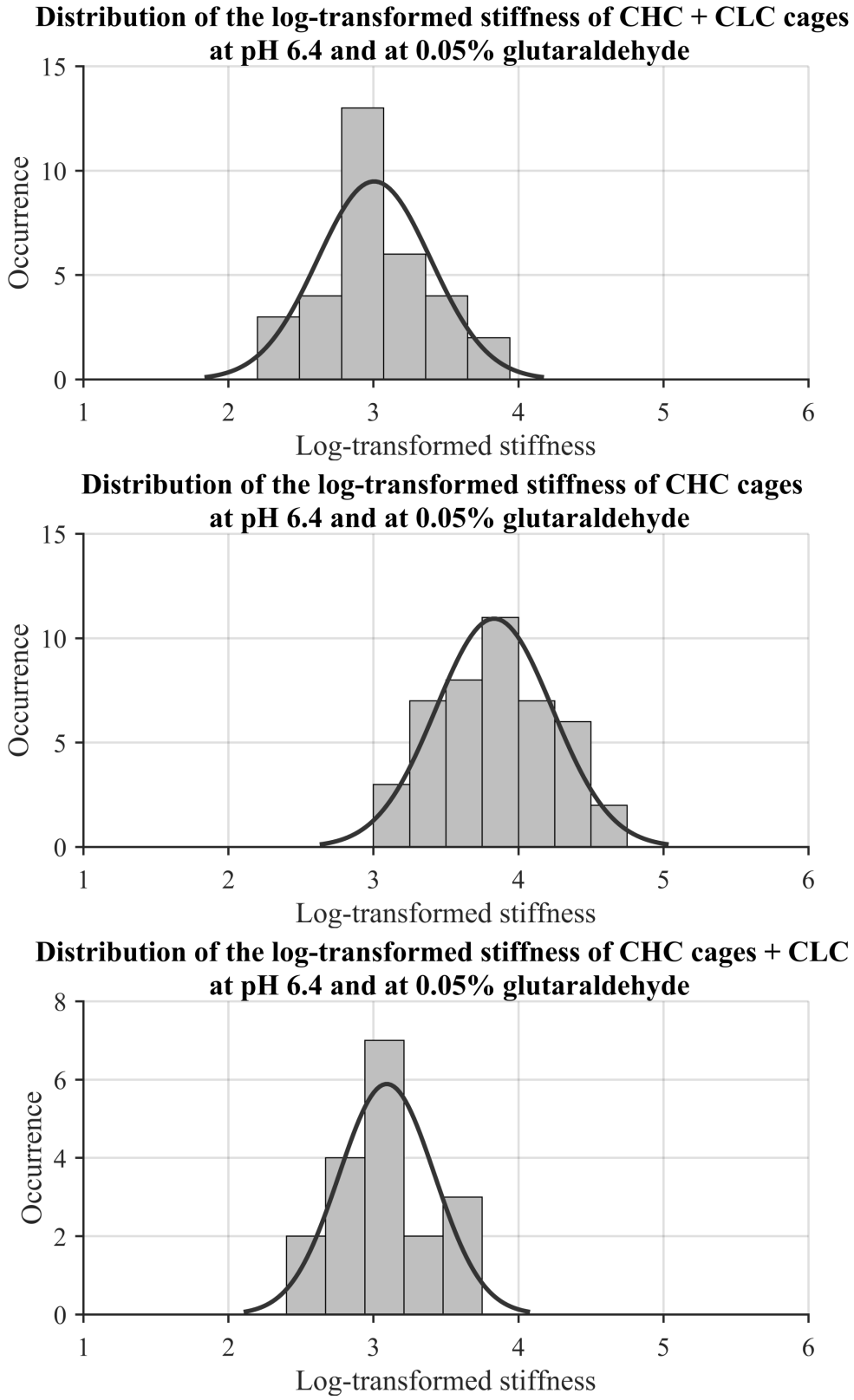

Figure 4.29: CHC+CLC cages, CHC cages and CHC cages + CLC stiffness distribution. *Probability density parameters:* $\mu = 3.00$ *and* $\sigma = 0.39$*;* $\mu = 3.83$ *and* $\sigma = 0.40$*;* $\mu = 3.09$ *and* $\sigma = 0.33$ *for the CHC+CLC cages, CHC cages and CHC cages + CLC respectively.*

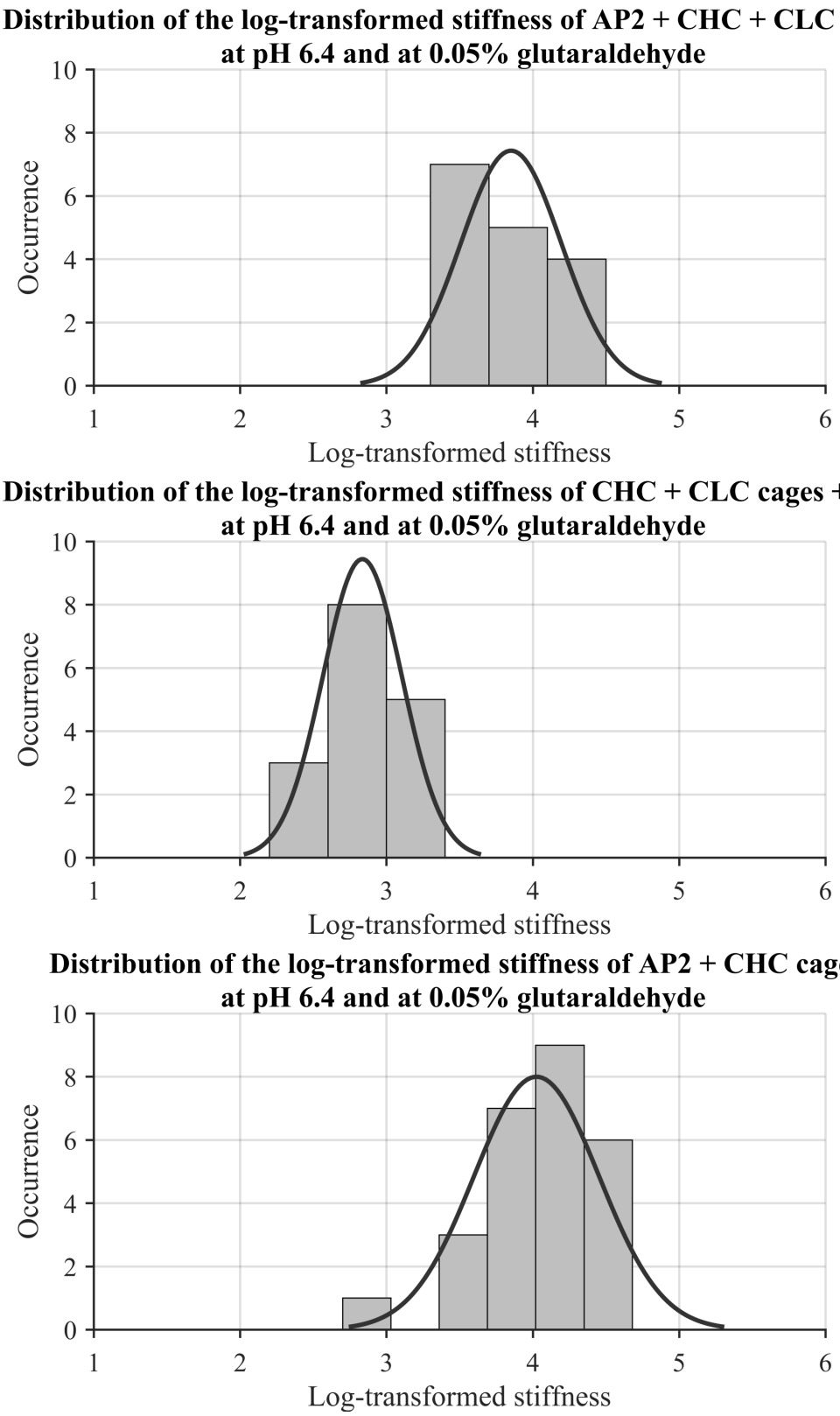

Figure 4.30: AP2+CHC+CLC cages, CHC+CLC cages + AP2 and AP2+CHC cages stiffness distribution. *Probability density parameters:* $\mu = 3.85$ *and* $\sigma = 0.34$*;* $\mu = 2.84$ *and* $\sigma = 0.27$*;* $\mu = 4.02$ *and* $\sigma = 0.43$ *for the AP2+CHC+CLC cages, CHC+CLC cages + AP2 and AP2+CHC cages respectively.*

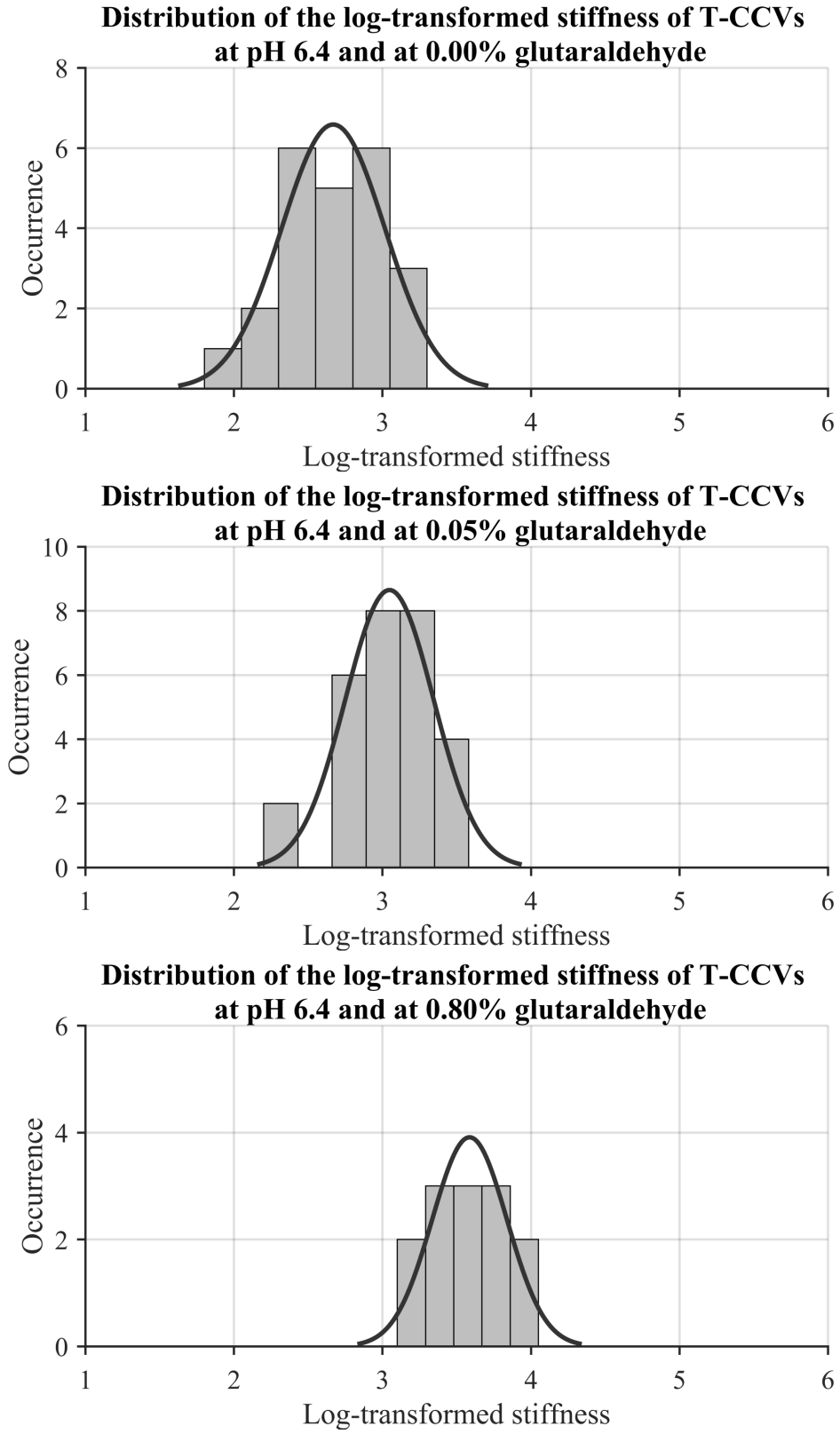

Figure 4.31: Distribution of T-CCVs stiffness in different glutaraldehyde concentration. *Probability density parameters:* $\mu = 2.67$ *and* $\sigma = 0.35$*;* $\mu = 3.05$ *and* $\sigma = 0.30$*;* $\mu = 3.59$ *and* $\sigma = 0.25$ *for the T-CCVs at* 0.00 %*,* 0.05 % *and* 0.80 % *glutaraldehyde concentration respectively.*

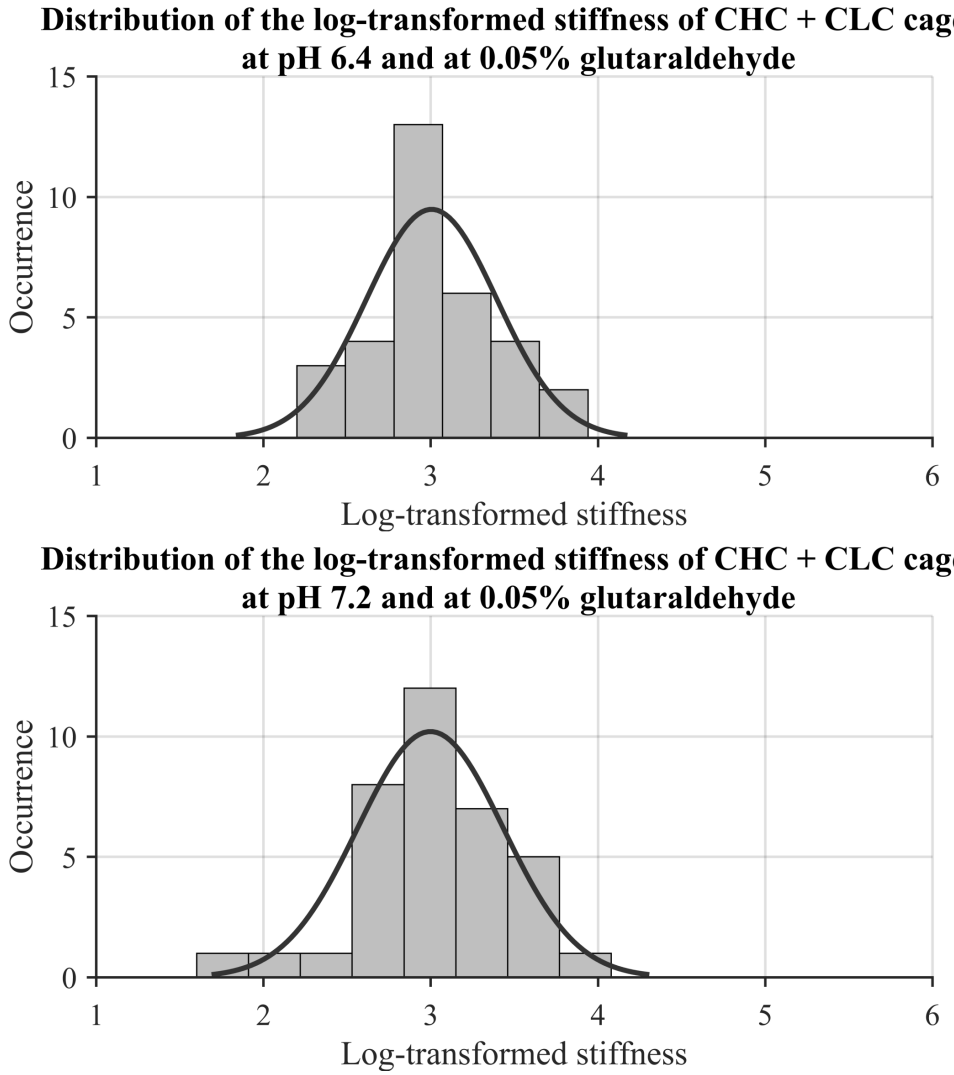

Figure 4.32: Distribution of clathrin coats stiffness in different pH. *Probability density parameters:* $\mu = 3.00$ *and* $\sigma = 0.39$*;* $\mu = 3.05$ *and* $\sigma = 0.44$ *for the CHC + CLC cages at pH* 6.4 *and pH* 7.2 *respectively.*

5

More experiments on clathrin

5.1 Motivation

In chapter 4, I found that the clathrin (CLCs) have a large effect on the mechanical properties of the clathrin coats. I also discovered that the adaptor AP2 appears to inhibit the softening effect of the CLCs.

However, there are many more proteins than only CLCs and AP2 present on the coats. One can cite the accessory proteins Epsin, Auxilin or AP180 and even CLCs have multiple isoforms. I hypothesised that they may influence the mechanics of the clathrin coats as well and perhaps in a different manner.

Furthermore, it had been previously shown that the CLCs have a specific binding site for calcium that may affect the structure of the triskelion hub [118]. Thus, calcium concentration may be the key to trigger the change of mechanical properties seen in my measurements.

5.2 Measuring the impact of light chains isoforms on the mechanical properties of the clathrin coat

In most eukaryotic cells, two different isoforms of clathrin light chains are expressed, namely the light chains a (CLCa) and light chains b (CLCb) [111, 119, 120, 121]. CLCa and CLCb are 60 % identical in sequence: they share a similar CHCs binding domain, calcium and calmodulin binding sites and binding sites for the endocytic accessory proteins Hip1 and Hip1R [122, 123, 124]. The latter can bind actin so can connect clathrin to the cytoskeleton which seems to regulate the clathrin cage dimensions [125, 126, 127]. However, CLCa has a heat shock cognate protein 70 (Hsc7) binding site [128] while CLCb has a casein kinase 2 (CK2) one [127]. In earlier work, it had been shown that

CLCa is predominant in lymphoid tissues while it coexists with CLCb in nonlymphoid ones. From this observation, it was concluded that both isoforms influence cargo selection differently, perhaps mechanically [129]. In addition, each light chain isoform exists in two higher-molecular weight forms with neuron-specific inserts in their sequences [130]. The neuronal insert introduces a short hydrophobic stretch that might be used to control clathrin polymerisation [123].

According to my previous analysis and the findings that CLCs, which consisted of a mixture of CLCa and CLCb both neuronal and non-neuronal randomly distributed, regulate the stiffness of the coats, it is plausible that these isoforms, with or without the neuronal inserts, impact the coat mechanics differently. To test this hypothesis, I have measured the stiffness of nCLCa, uCLCa, nCLCb and uCLCb cages ("n" denotes neuronal CLCs while "u" denotes the absence of neuronal inserts). Besides the AFM force spectroscopy measurements, the novelty of this study is the ability of Dannhauser's group to isolate each isoform and generate coats with a specific light chain composition, see Figure 5.1. Figure 5.2 and Figure 5.3 display the stiffness of the different cages *versus* their height.

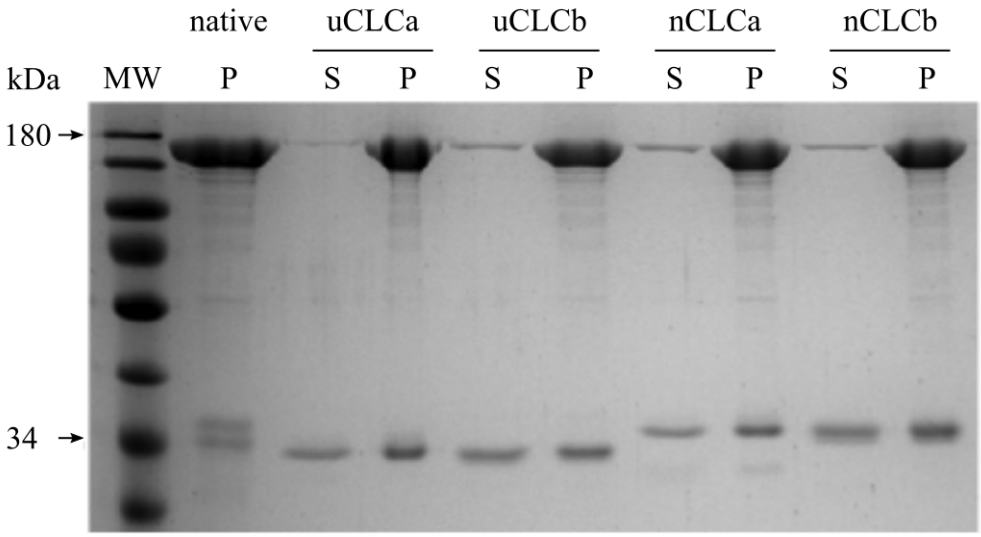

Figure 5.1: SDS-PAGE identification of clathrin light chains isoforms (Dannhauser's group). *From left to right: MW: Marker. Native P: Pelleted fraction of a native clathrin coat. The dark upper band shows the heavy chains and the two lower bands both types of light chains. uCLCa-S: supernatant fraction of the uCLCa sample, only one type of light chain is visible. uCLCa-P: the pellet shows both CHC and the CLCa. uCLCb: the supernatant and pellet fractions appear similar as the uCLCa sample. nCLCa and nCLCb: the neuronal insert leads to a slightly larger light chain which caused the shift of the band.*

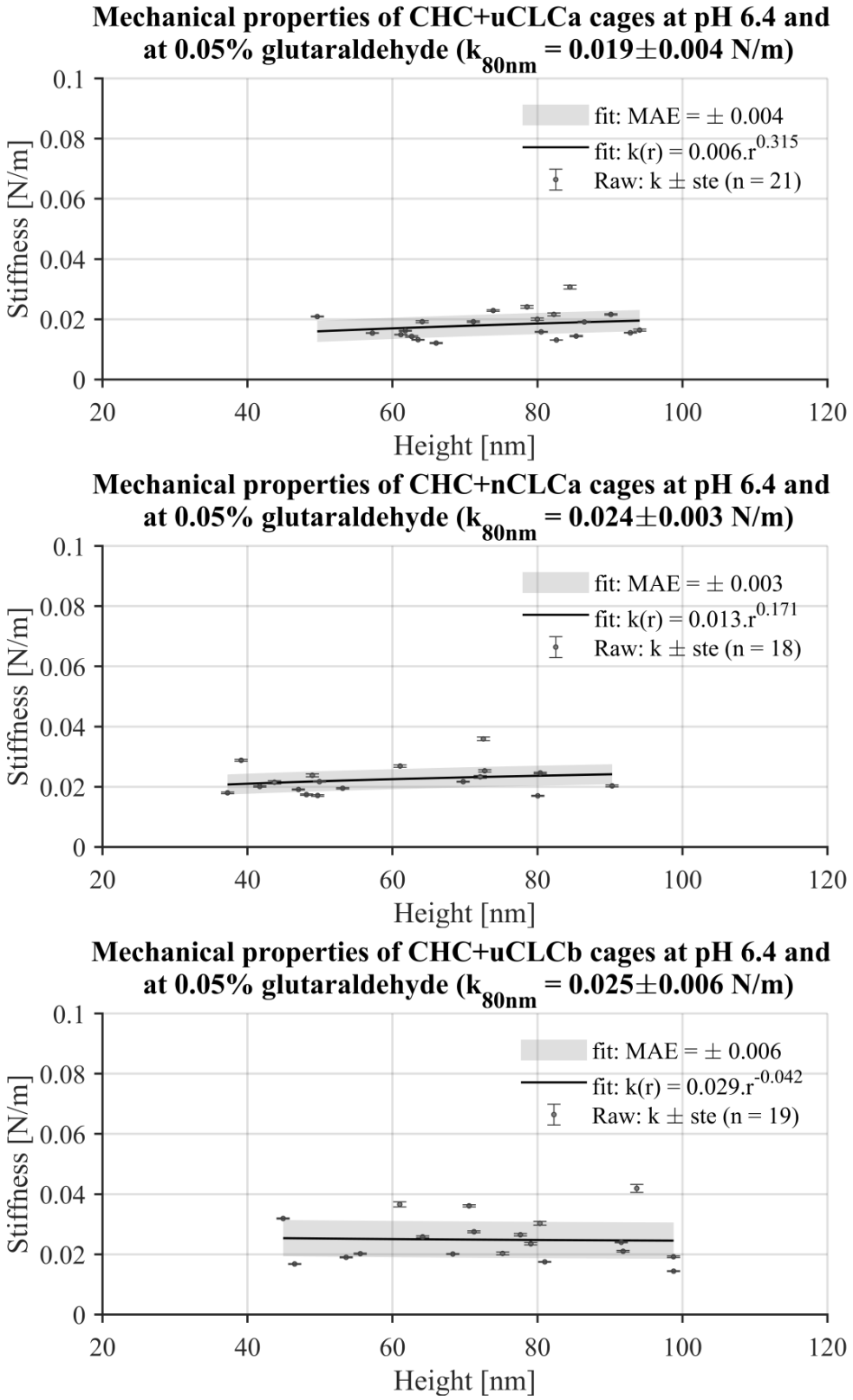

Figure 5.2: Mechanical properties of reconstituted clathrin coat from various non-neuronal and neuronal CLCa and CLCb. *8 % of the CHC+uCLCa raw stiffness were rejected (n_{total} = 23), adjusted χ^2 = 0.89. 31 % of the CHC+nCLCa cages raw stiffness were rejected (n_{total} = 26), adjusted χ^2 = 0.90. No raw stiffness were rejected (n_{total} = 19) regarding CHC+uCLCb, adjusted χ^2 = 0.84.*

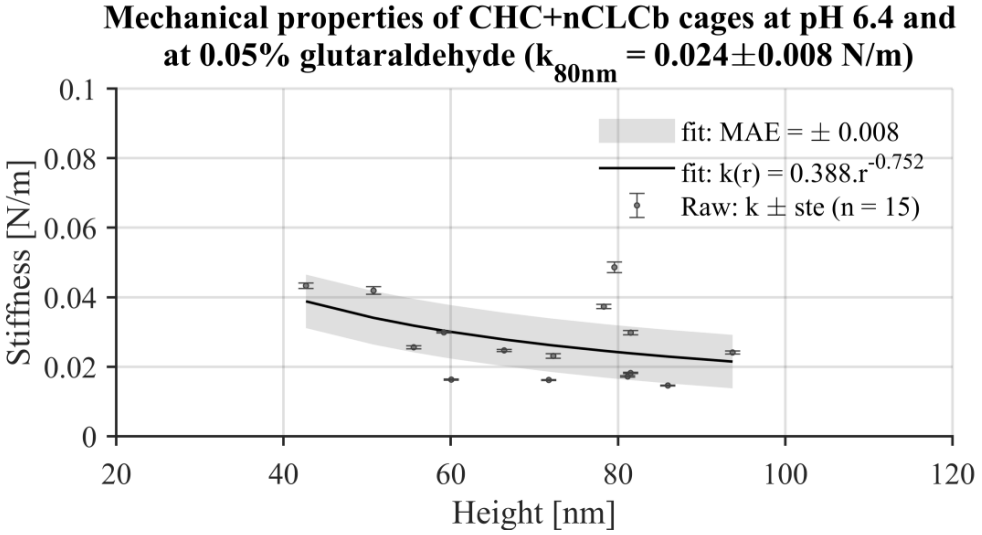

Figure 5.3: Mechanics of reconstituted clathrin coat from neuronal CLCb. *17 % of the CHC+nCLCb cages raw stiffness were rejected ($n_{total} = 18$), adjusted $\chi^2 = 0.82$.*

Table 5.1: Statistical analysis of the stiffness measurements. *The probabilities were calculated after performing a Student's t test assuming equal variance on the fitted mean stiffness after log-transformation ($5e-2$ level), see Appendix I.*

Samples compared	p **value**
CHC+uCLCa *versus* CHC+nCLCa	$2.52e-1$
CHC+uCLCb *versus* CHC+nCLCb	$8.17e-2$
CHC+uCLCa *versus* CHC+uCLCb	$1.99e-1$
CHC+nCLCa *versus* CHC+nCLCb	$1.91e-1$

Similar to the previously investigated CHC+CLCs, there is no clear relationship between height and stiffness. The CHC+uCLCa cages are $0.019 \pm 0.004\,\mathrm{N/m}$ ($n = 21$) while the CHC+nCLCa cages are $0.024 \pm 0.003\,\mathrm{N/m}$ ($n = 8$). On the other hand, CHC+uCLCb cages are $0.025 \pm 0.006\,\mathrm{N/m}$ ($n = 19$) and CHC+nCLCb cages are $0.024 \pm 0.008\,\mathrm{N/m}$ ($n = 15$).

In conclusion, while the isoforms tested have a different composition, they do not provide the coats with different mechanical properties, see Table 5.1. Although the neuronal inserts have been speculated to affect clathrin polymerisation [123], such a regulation does not rely on the alteration of the mechanical properties. Furthermore, the presence of a binding site for Hsc7 on CLCa and for CK2 on CLCb do not modify the mechanics neither. However, it cannot be excluded that binding of these or other ligands is required to mediate a conformational change of the CLCs that could trigger a mechanical transition in the coat.

5.3 Measuring the impact of accessory protein Epsin, AP180, and Auxilin on the mechanics of clathrin

During the formation of clathrin coated vesicles, clathrin mainly binds to AP2. The last controls the clathrin polymerisation into lattices [131] and, as shown previously, also influences the clathrin light chains mechanics. However, not all external entities going to be invaginated interact with AP2 [132, 133, 134]. This is for example the case of influenza viruses that interact with a different accessory protein called Epsin [135].

Although Epsin and AP2 have comparable functionality they have different structure, since Epsin is for example not a protein complex. Both bind to the terminal domain of the clathrin heavy chains (CHCs) but Epsin does not share the same clathrin binding site with AP2 [136, 137]. Furthermore, Epsin is less potent in stimulating triskelia polymerisation than AP2 [138]. A unique feature of Epsin is that it is able alone to induce membrane curvature and the formation of highly curved clathrin coats [139]. AP2 alone lacks this ability and requires the recruitment of clathrin and AP180 to achieve the same goal [140].

AP180 is an additional clathrin assembly protein which, similarly to Epsin and AP2, binds to the terminal domain of the CHCs and impacts the formation of CCVs. Indeed, AP180 has been found to regulate their dimension: they are 60 - 70 nm in diameter in presence of AP180 while they are approximately 50 % bigger in AP180 depleted membrane [141, 142, 143]. Furthermore, AP180 recruits clathrin triskelia on the membrane which initiates their polymerisation [142, 143, 144], being 4 times more effective than AP2 in promoting assembly of clathrin coats [145]. However, unlike Epsin, AP180 alone is not capable of inducing membrane curvature and requires the presence AP2 to initiate clathrin-decorated buds [140].

Another particularly interesting accessory protein is Auxilin. Auxilin is involved in the dismantling of clathrin coats and thus the release of the enclosed external cargo into the cell [84, 146, 147]. It is not recruited during the triskelia polymerisation and their formation in lattice but only called upon during the bud scission from the membrane [148, 149]. To this end, it recruits heat shock protein 70 (Hsp70, also present on the clathrin triskelia) to disassemble the coats [150, 151]. Furthermore, it forms a protein layer between the hosted vesicle and the clathrin coat by binding to the terminal domain of the CHCs [152, 153].

Actually, the above-mentioned proteins are all related to clear biomechanical processes (membrane bending, size regulation, bud scission) and eventually may impact the clathrin

coat mechanics in a similar manner than AP2. Earlier, I showed that the stiffness of purified clathrin coats (containing multiple different accessory proteins) was identical to that of reconstituted ones that contained only CHCs and CLCs but considerably softer than reconstituted coats to which AP2 was added. This suggests that while AP2 stiffens the structure, the general contribution of accessory proteins is null. If the system can be considered as linear, mechanically, an idea that is supported by the fact that the stiffness of CCVs is the sum of the one from T-CCVs and enclosed vesicles, it potentially infers that some accessory proteins, *a contrario*, may soften considerably the coats to compensate. Here I have investigated reconstituted clathrin cages (CHC+CLCs) to which Epsin, AP180 and Auxilin were bound at 1:1 ratio (protein:CHCs) to mimic the *in vivo* concentration [142, 152], see Figure 5.4. The protocol to bind the proteins on the coats was identical to

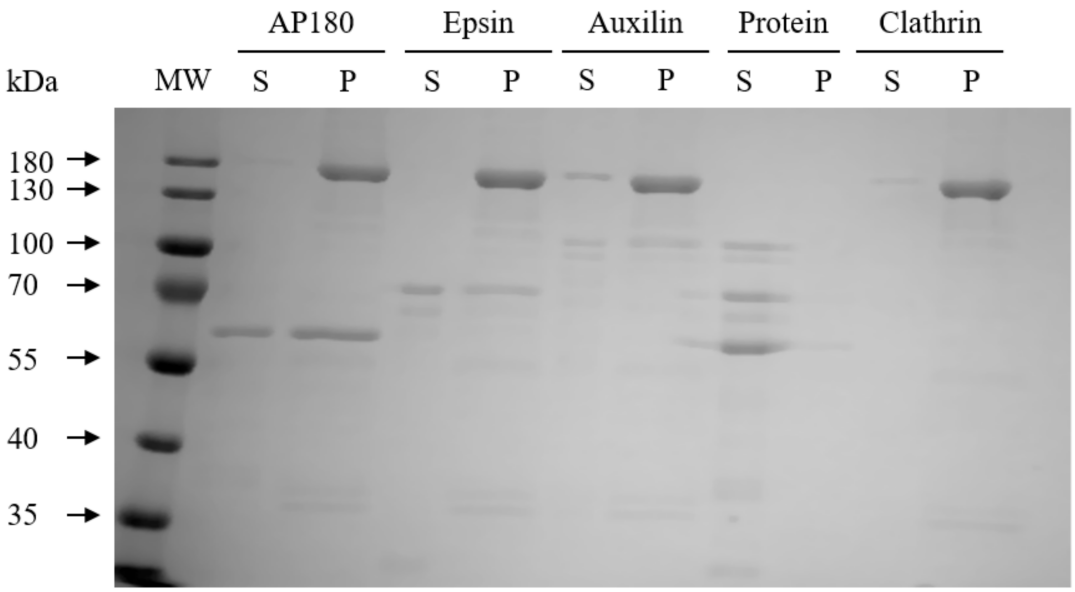

Figure 5.4: SDS-PAGE identification of accessory proteins (Dannhauser's group). *From left to right: Marker. AP180-S: supernatant fraction showing AP180 and no clathrin. AP180-P: Pelleted fraction showing both AP180 and clathrin. Epsin-S: supernatant fraction showing Epsin and no clathrin. Epsin-P: Pelleted fraction showing both Epsin and clathrin. Auxilin-S: supernatant fraction showing Auxilin and no clathrin. Auxilin-P: Pelleted fraction showing both Auxilin and clathrin. Protein-S: supernatant fraction showing all accessory proteins and no clathrin. Protein-P: pellet fraction showing no clathrin proteins nor accessory proteins. Clathrin-S: supernatant fraction of the native clathrin coat. Clathrin-P: Pelleted fraction of a native clathrin coat. The dark upper band shows the heavy chains and the two lower bands both types of light chains.*

the one used to bind AP2 onto reconstituted cages.

Figure 5.5 and Figure 5.6 show the result of the mechanical mapping on the various CHC+CLC cages. The largest effect was seen for Epsin, but even this stiffens the composite structure by only 46 %, $0.032 \pm 0.007\,\mathrm{N/m}$ ($n = 18$), while the addition of AP180 or Auxilin does not significantly alter the original mechanical properties, 36 % increase, $0.030 \pm 0.008\,\mathrm{N/m}$ ($n = 13$), and 32 % increase, $0.029 \pm 0.014\,\mathrm{N/m}$ ($n = 22$) respectively. The Student's t test reveals that only the CHC+CLC cages with Epsin are statistically different from the CHC+CLC cages, see Table 5.2.

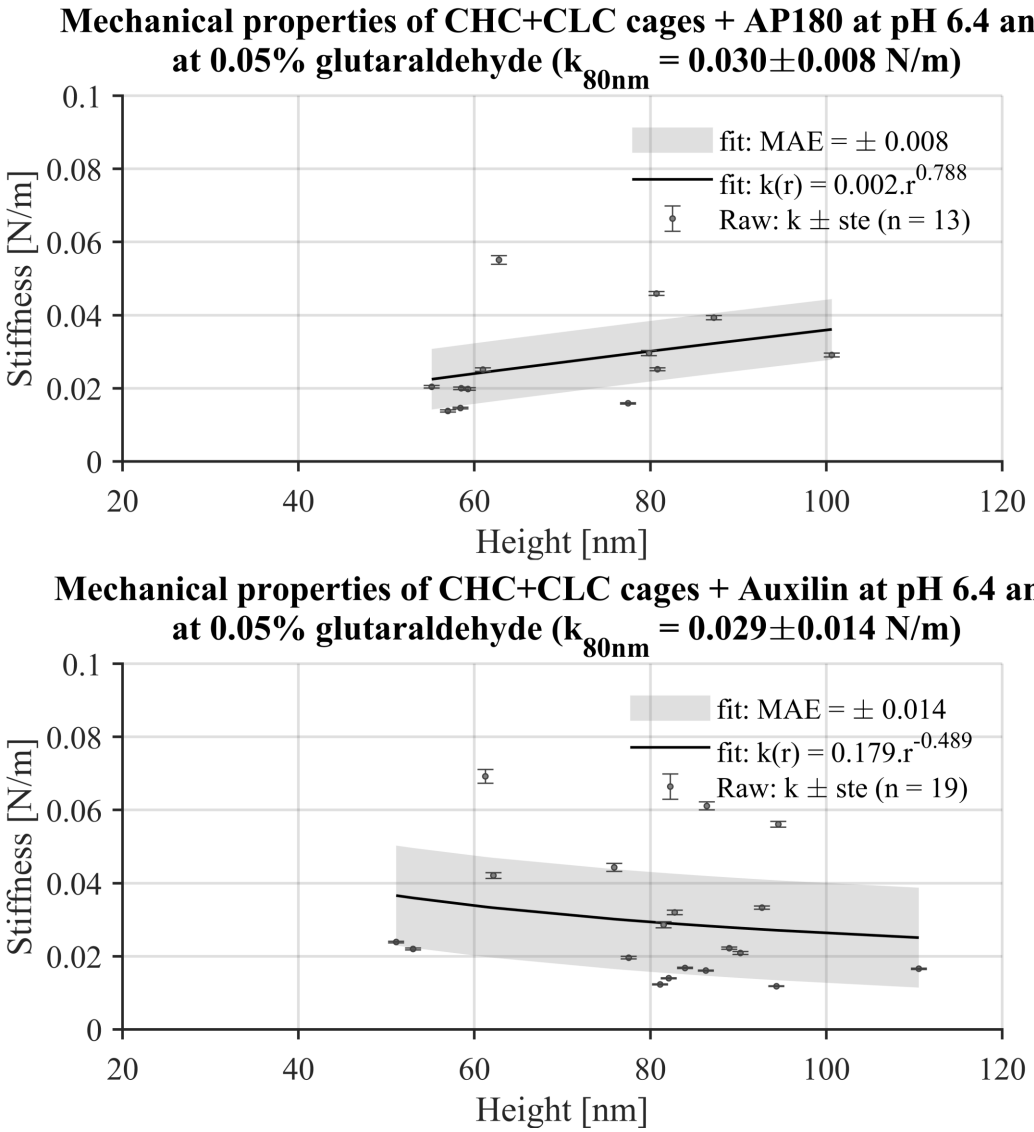

Figure 5.5: Effect of accessory proteins on CHC+CLC cages. 35 % ($n_{total} = 20$, *adjusted* $\chi^2 = 0.82$), 18 % ($n_{total} = 22$, *adjusted* $\chi^2 = 0.84$) *of the raw stiffness from AP180, Auxilin respectively were rejected. The cages were, mean* ± *s.e.m,* $70.53 \pm 3.41\,\mathrm{nm}$, $79.47 \pm 3.17\,\mathrm{nm}$ *in height for cages with AP180, Auxilin respectively.*

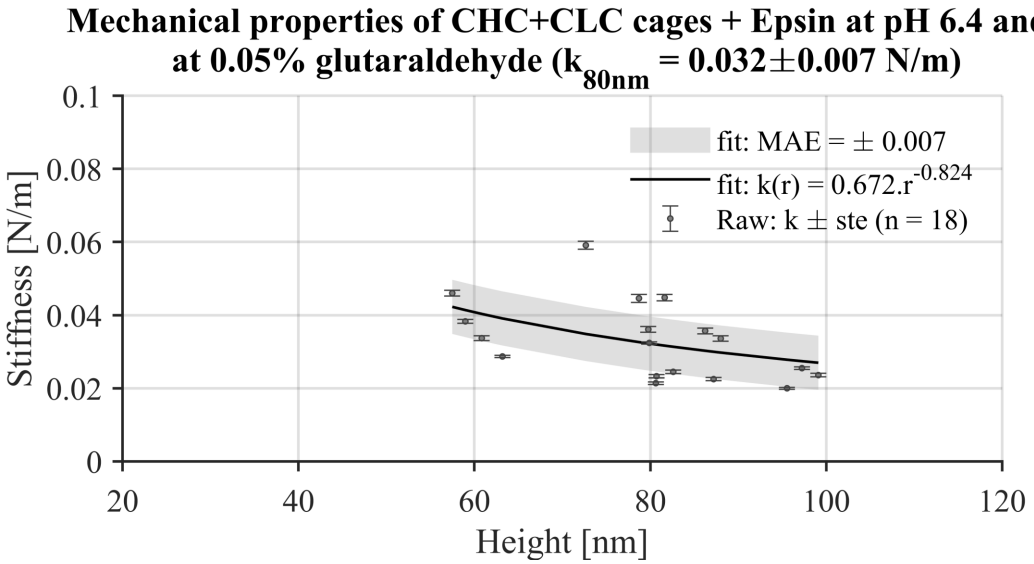

Figure 5.6: Effect of accessory proteins on CHC+CLC cages. 14 % ($n_{total} = 22$, *adjusted* $\chi^2 = 0.68$*) of the raw stiffness from Epsin were rejected. The cages were, mean ± s.e.m,* 78.33 ± 2.54 nm *in height for cages with Epsin.*

Table 5.2: Statistical analysis of the stiffness measurements. *The probabilities were calculated after performing a Student's t test assuming equal variance on the fitted mean stiffness after log-transformation (*$5e-2$ *level), see Appendix I.*

Samples compared	p **value**
CHC+CLC *versus* CHC+CLC + AP180	$9.69e-2$
CHC+CLC *versus* CHC+CLC + Auxilin	$7.52e-2$
CHC+CLC *versus* CHC+CLC + Epsin	$5.40e-4$

An overall conclusion is that the accessory proteins added to the reconstituted cages after self-assembly do not particularly affect their mechanical properties, as compared to AP2. This is interesting as Auxilin forms an additional layer within the cage by binding to the heavy chains. The thickness of the coat effectively increases and according to the shell theory it should influence the stiffness accordingly. Indeed, assuming that Auxilin has a similar thickness as clathrin then I expected the stiffness to increase by a factor of 4 ($k \propto t^2$) instead of 1.32 as seen in my measurements. In addition, while it had been shown that Auxilin changes the clathrin triskelion geometry [152, 153] and also binds to the terminal domain as well as the distal domain of the CHCs, thus closer to the triskelion knee than the other adaptor proteins investigated, this only has a mild effect on their mechanics. AP180, which resembles AP2, does neither affect significantly the cages properties nor their dimensions (the cages were found 10 % smaller than the others). However, Epsin

appears to stiffen a little the coat by 40 %, reaching almost the stiffness of clathrin coats hosting vesicles, which may help to further induce membrane curvature on top of Epsin ability to bend the membrane in absence of clathrin [139].

Nonetheless, it is too early at this stage to give real biological outcomes that can be related to a state *in vivo* of the clathrin coats. Actually, due to the large MAEs and the many possible protein combinations much more measurements are required to come to a clear conclusion. Indeed, the fact that AP180 and Epsin were added after self-assembly is non-biological and my previous investigation regarding AP2 is a clear example that dynamics are important. Indeed, AP2 inhibits the light chains softening only if it is mixed in the pool of CHCs and CLCs prior to promote assembly. Epsin and AP180 more likely follow the same trend. Especially AP180 which is supposed to regulate the size of CCVs, aspect which was hardly visible in my measurement (AP180 cages were only 10 % smaller instead of 50 % as previously found [141, 142, 143]).

Furthermore, the three proteins investigated in this study bind to AP2 [154, 155]. The last thus may trigger a change in their functions if bound and perhaps their ability to affect the mechanical properties of the coats.

Finally, since the clathrin coat is found to be dynamically regulated it is not excluded that the effect of a given protein cannot be enhanced during a specific event of the life cycle of clathrin: binding of Auxilin, scission of the buds, ATPase of the coats etc.

5.4 Measuring the impact of calcium concentration on the mechanical properties of reconstituted clathrin coats

My previous measurements suggest that the clathrin coat properties may be regulated all along its life cycle to achieve specific tasks. I hypothesised that the coat is initially stiff to induce membrane bending and then it gets softer later to facilitate its disassembly by the protein Auxilin and its cochaperon Hsc70. However, a question remains on how this is done *in vivo*.

Previous work on clathrin light chains by Näthke et al. [118] enlightened the fact that CLCs have a specific calcium binding site that can potentially affect the nodes of the clathrin coat. Indeed, the authors found that a concentration of 3 mM Ca^{2+} causes local structural modifications of the light chains. Calcium appears thus as a promising agent to regulate the light chains mechanical properties and thus the clathrin coat mechanics. To test this

hypothesis I investigated reconstituted clathrin cages in an environment that was rich in calcium ions: 0.1 mM and 0.5 mM of Ca^{2+} added in buffer G.

Figure 5.7 shows the relationship between the stiffness of the cages and their dimensions when the cages are measured in different ionic conditions. The reconstituted cages in 0.1 mM Ca^{2+} are 0.018 ± 0.010 N/m ($n = 26$). At higher concentration, the cages are 0.021 ± 0.004 N/m ($n = 27$). Table 5.3 resumes the p values from the Student's t test and shows that there is no difference between the CHC+CLC cages in medium with increasing Ca^{2+} concentration from a statistic point of view.

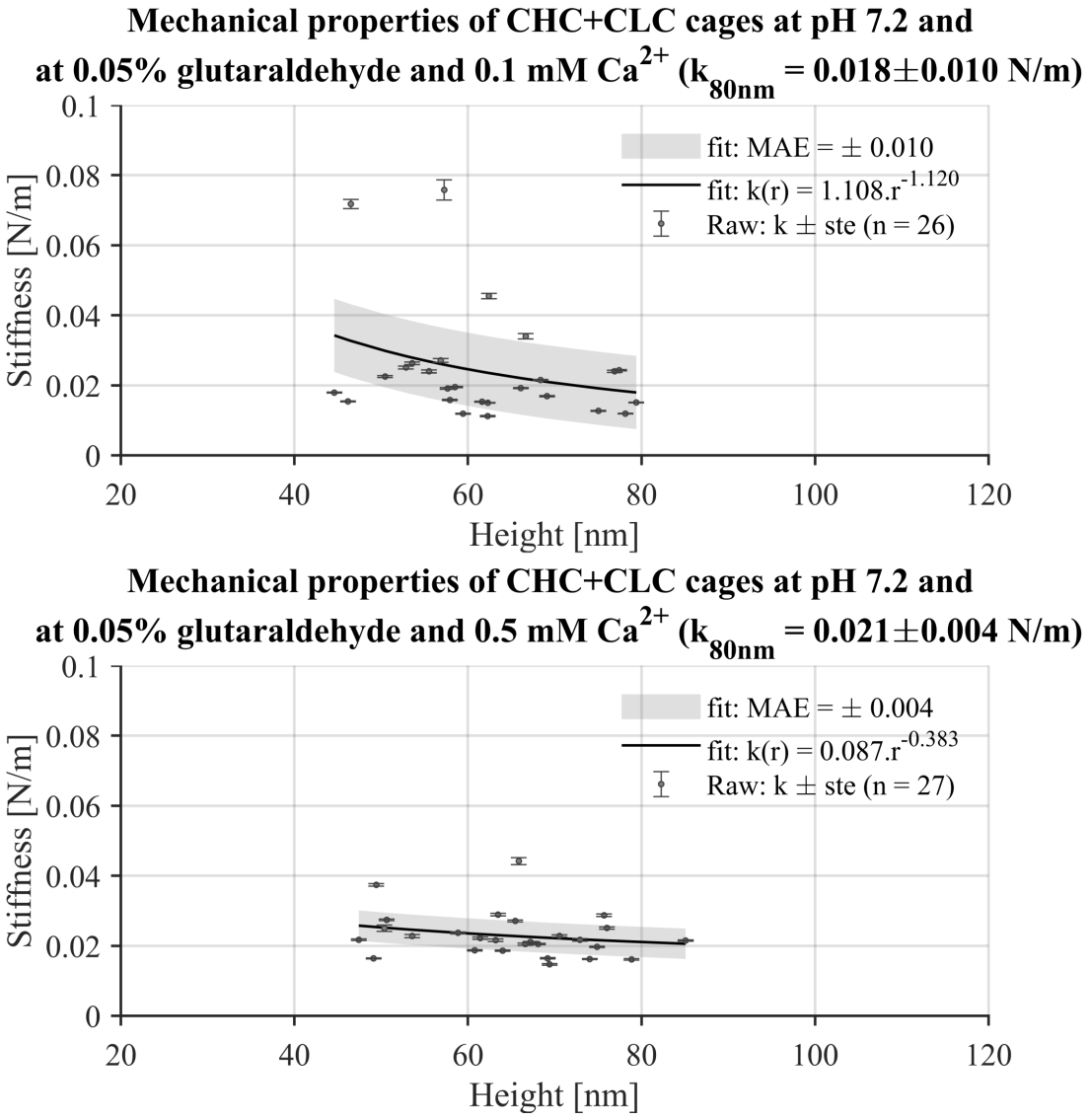

Figure 5.7: Calcium effect on the coats mechanics. *3 % of the CHC+CLC cages in 0.1 mM of Ca^{2+} raw stiffness were rejected ($n_{total} = 27$), adjusted $\chi^2 = 0.68$. 3 % of the CHC+CLC cages in 0.5 mM of Ca^{2+} raw stiffness were rejected ($n_{total} = 28$), adjusted $\chi^2 = 0.85$.*

Table 5.3: Statistical analysis of the stiffness measurements. *The probabilities were calculated after performing a Student's t test assuming equal variance on the fitted mean stiffness after log-transformation ($5e-2$ level), see Appendix I.*

Samples compared	p **value**
CHC+CLC *versus* CHC+CLC + 0.1 mM Ca^{2+}	$4.54e-1$
CHC+CLC *versus* CHC+CLC + 0.5 mM Ca^{2+}	$9.03e-1$

I recall that the reconstituted cages in buffer G are initially $0.024 \pm 0.019\,\mathrm{N/m}$ stiff. The addition of 0.1 mM Ca^{2+} in the buffer seems to have softened the coats by 25 %. However, increasing the calcium concentration by a factor of 5 did not decrease further the stiffness of the cages. Actually, the cages at 0.5 mM Ca^{2+} appear now 17 % stiffer than the ones at 0.1 mM Ca^{2+} but still 12 % softer than the initial cages. Therefore, calcium mildly softens the cages, a behaviour which may enhance the efficiency of their disassembly as already suggested by Näthke et al. [118]. However, the MAEs are too high to clearly differentiate the mechanicals properties from clathrin in presence of calcium and much more measurements would be required to come to a clear conclusion. Also, it may be possible that smaller calcium concentration may trigger already a much significant softening of the cages.

Appendix I: Stiffness distribution

The stiffness data are log-normal distributed in most cases (data not shown), which indicates that after log-transformation they present a normal distribution. Figure 5.8 to Figure 5.11 show the log-transformed stiffness (in [mN/m]) distributions from the various clathrin assemblies. The number of bins per histogram was chosen according to Sturges's rule [110]. The histograms were tested for normality and for each test, the mean log-transformed stiffness, μ, and its standard deviation, σ, were extracted.

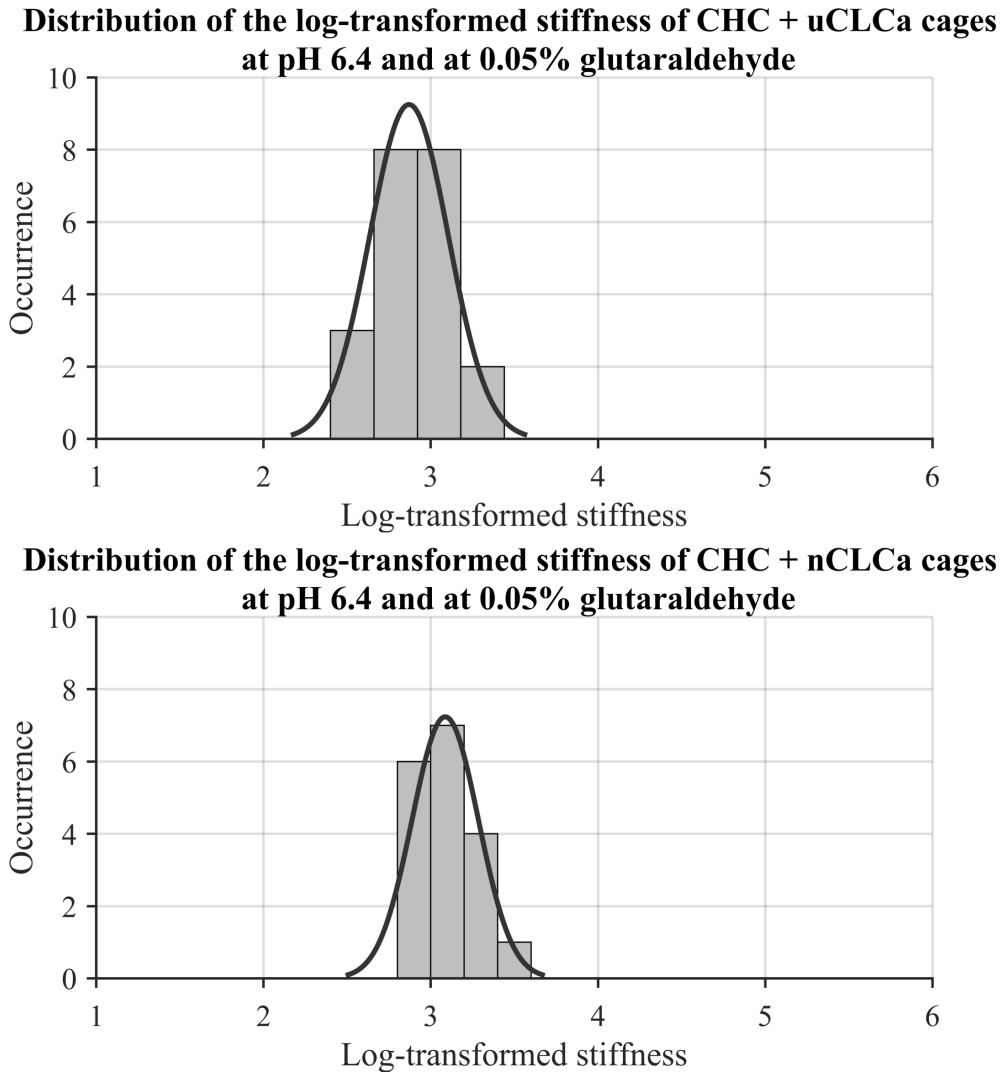

Figure 5.8: Distribution of reconstituted clathrin coat from non neuronal and neuronal CLCa stiffness. *Probability density parameters:* $\mu = 2.87$ *and* $\sigma = 0.24$*;* $\mu = 3.08$ *and* $\sigma = 0.20$ *for the CHC+uCLCa cages and CHC+nCLCa cages respectively.*

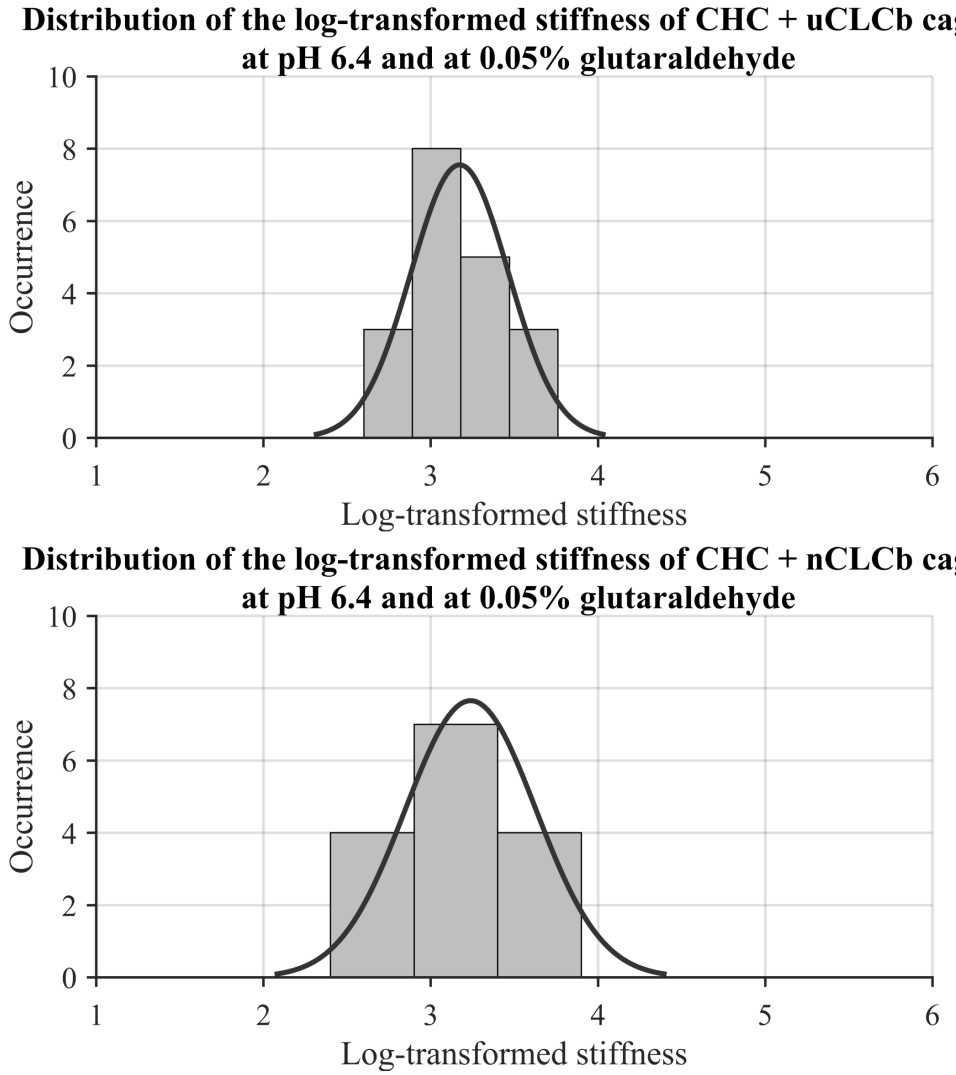

Figure 5.9: Distribution of reconstituted clathrin coat from non neuronal and neuronal CLCb stiffness. *Probability density parameters:* $\mu = 3.17$ *and* $\sigma = 0.29$*;* $\mu = 3.24$ *and* $\sigma = 0.39$ *for the CHC+uCLCb cages and CHC+nCLCb cages respectively.*

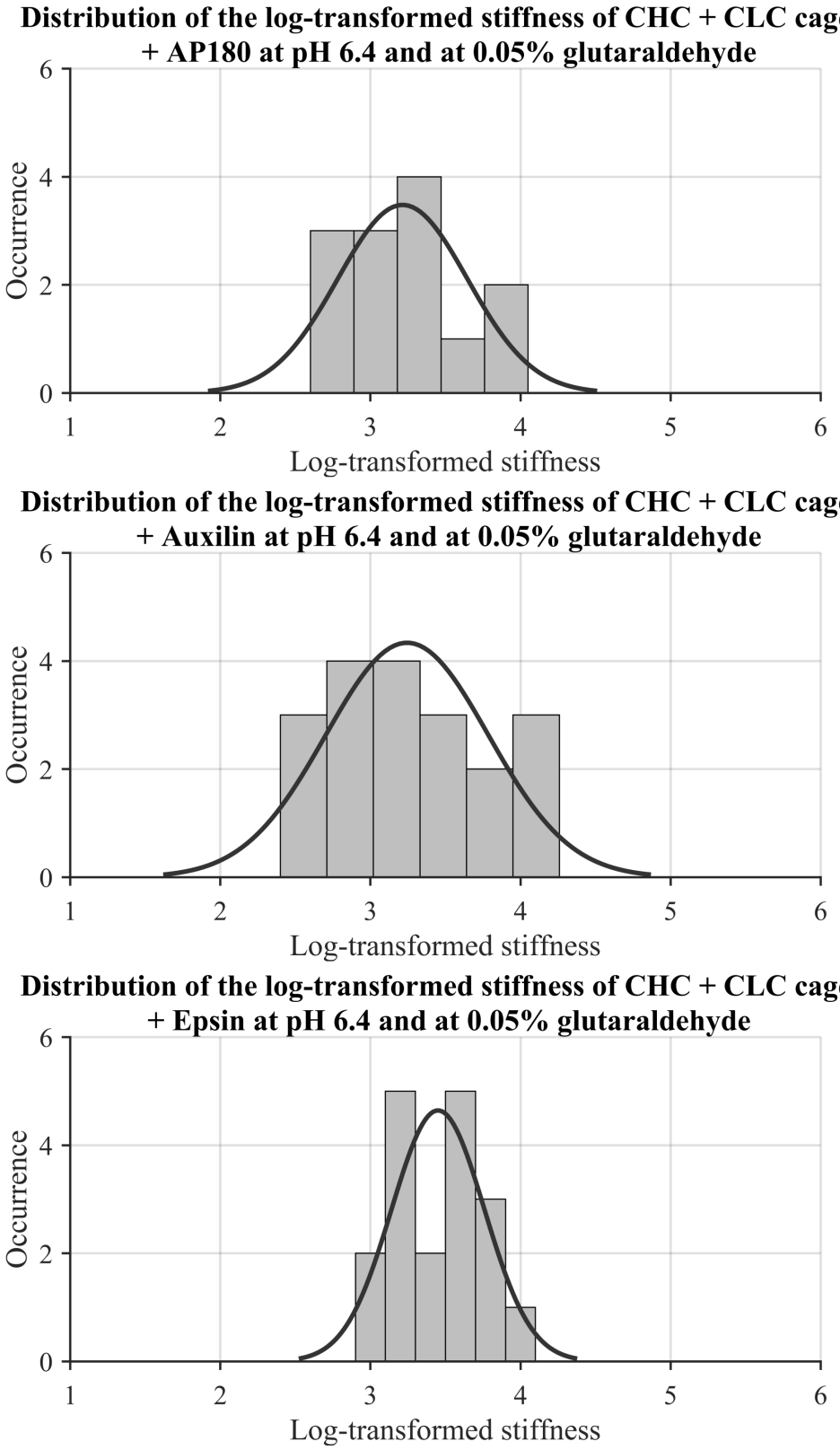

Figure 5.10: Distribution of CHC+CLC cages stiffness on which accessory proteins were added. *Probability density parameters:* $\mu = 3.21$ *and* $\sigma = 0.43$*;* $\mu = 3.24$ *and* $\sigma = 0.54$*;* $\mu = 3.45$ *and* $\sigma = 0.31$ *for the CHC+CLC cages with AP180, Auxilin and Epsin respectively.*

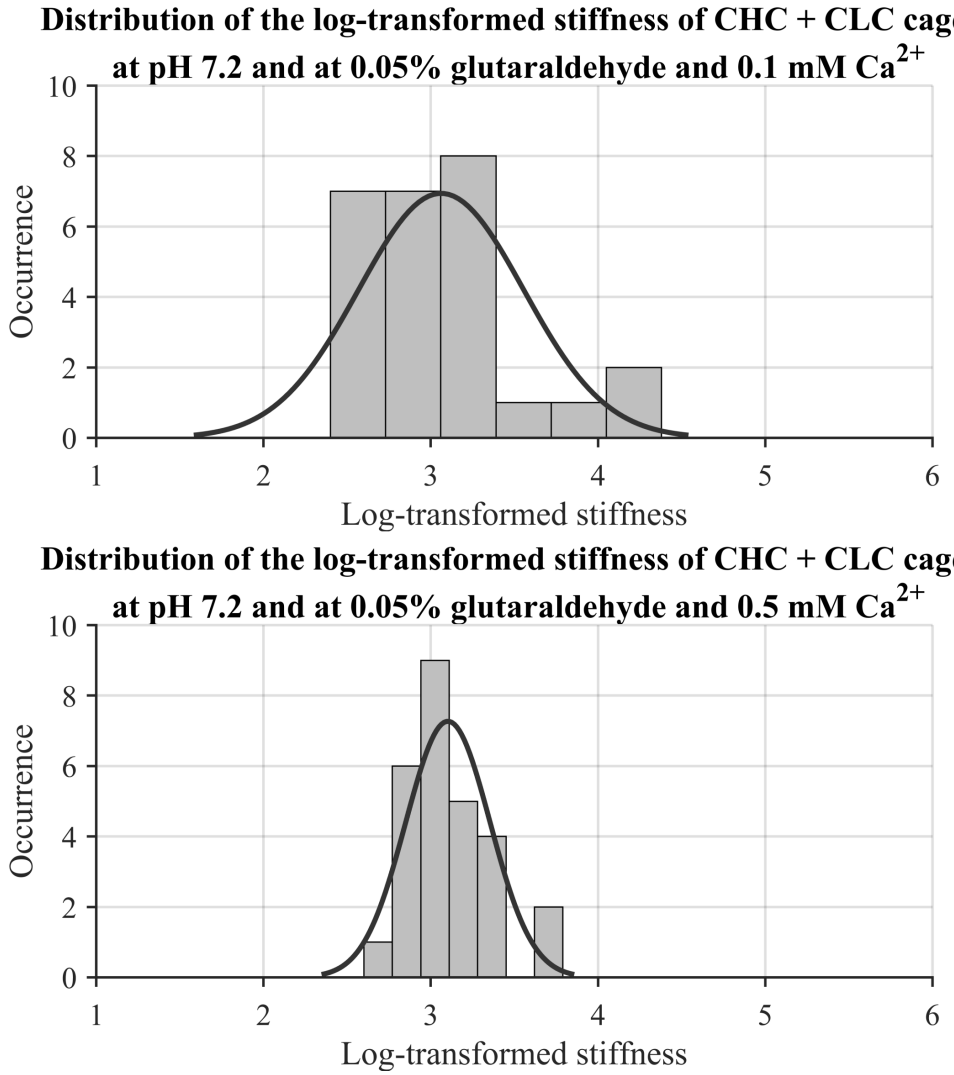

Figure 5.11: Distribution of CHC+CLC cages stiffness in different calcium concentration. *Probability density parameters:* $\mu = 3.06$ *and* $\sigma = 0.49$*;* $\mu = 3.10$ *and* $\sigma = 0.25$ *for the CHC+CLC cages with* 0.1 *and* 0.5 *mM of* Ca^{2+} *respectively.*

6

Dynamic force spectroscopy reveals structural non-uniformities in isolated nuclei

6.1 Abstract

The nucleus sees its size and shape modified during growth, differentiation and migration of the cell while experiencing forces from the cell itself and the surrounding environment. Even though there is evidence that these stimuli are used as signals to control the expression of genes, it remains largely unclear how forces are transduced through the nucleus. In order to gain a better understanding, I performed sinusoidal nanoindentation experiments between 1 Hz and 700 Hz to measure the compliance of chromatin within single nuclei of various mammalian cell-lines. I found that *i*) the quantitative response varies with more than one order of magnitude and *ii*) that it scales with the nucleus size. This fact indicates that the chromatin density itself is not a critical parameter for its functioning. The qualitative response was identical for different cell-lines: predominantly elastic and following a power law with an exponent that increases around 100 Hz. All the investigated nuclei were found to be softer and more viscous in their peripheral region. The corresponding looser, less cross-linked organisation of the chromatin, may play a key role in enhancing gene transcription in this most active region of the nucleus.

6.2 Introduction

In different cell types the nucleus can have strikingly different appearances indicating that it is not merely a static gene transcription machinery only controlled by chemical signals. Although the nucleus is often pictured as a large spherical organelle, both its size and shape can be highly variable. An extreme case is the neutrophil of which the nucleus has a shape consisting of multiple lobes [156]. Also, during the cell differentiation the nucleus can be subjected to large changes in shape and size [18]. When cells migrate through small openings their nuclei undergo considerable deformations that allow the cell to squeeze through [157, 158]. For the highly motile neutrophils it is easy to argue that their segmented nuclei are an adaptation that allows them to move through narrow gaps in tissue; form follows function. On the scale of the whole cell, a similar reasoning is used to explain why the reduced stiffness of cancer cells, as compared to their healthy counterparts, increases their invasive potential [159]. The ability of melanoma cancer cells to migrate through small pores could indeed be reduced by artificially stiffening their nuclei [160]. Although the nuclei of cancer cells often have various morphologies [161] the ambiguity whether also their stiffness is consistently decreased to improve their invasiveness persists.

The nuclear lamina plays a key role in regulating the shape of the nucleus [19, 162]. Located right under the nuclear envelope, it forms a dense fibrillar network of approximately 30 to 100 nm thick of lamin proteins. The presence of lamins is not limited to the nuclear lamina as they can be found throughout the chromatin inside the nucleus [19]. Because the nuclear lamina is physically connected to the cytoskeleton, the shape of the nucleus will depend on the forces generated by the cell [163, 164], which therefore strongly relies on the mechanical interactions of the cell with its environment [20]. Besides changing the shape of the nuclei, the mechanical signals play a role in regulating gene expression [20, 21, 22]; function follows form. It has been shown that lamins can bind DNA which may directly modulate the expression of genes [165, 166]. An additional mechanism to affect gene transcription could be the deformation of chromatin itself.

Rates of gene transcription vary in the different regions of the nucleus. The highest rate has been found in the outer layer of the nucleus, from about half the radius outward [167]. This indicates the presence of distinct functional regions within the chromatin. Historically, the chromatin is organised in heterochromatin and euchromatin, regions defined by their different staining in electron microscopy observations. Heterochromatin is stained

much more densely and it was originally thought that there is no gene transcription in this region because of its high density. Yet, work done by Dechat et al. [168] showed that gene transcription still occurs but is repressed by RNAi [168]. Heterochromatin is found in discrete regions throughout the nucleus but is more abundant at the periphery of the nucleus closely associated with the nuclear lamina, where it correlates with transcriptionally inert areas at the outer edge of the nucleus [169]. The majority of the chromatin appears as euchromatin, less densely stained in electron microscopy, and associated with transcriptionally active regions. However, the observed spatial differences in transcription point to yet unknown differences in organisation. It is safe to believe that transcription is enhanced or inhibited because of functional differences within the euchromatin. Since chromatin is a very dense fibrillar network, any change that alters its cross-linking will also greatly impact its mechanical response.

The mechanics of whole cells have been thoroughly studied and generally show a viscoelastic behaviour that is not constant through the cell [170]. Basically, the measured stiffness depends on how fast, time-scale, and how much, length-scale, the cell is deformed [171]. However, such a well defined picture is still lacking for the nucleus, partially because of its small dimension along with difficulties to separate its response from that of the cell in whole-cell studies. Nevertheless, research has indicated that the nuclear lamina plays an important role [38, 172]. Measurements with optical tweezers on nuclei that lack a lamina has shown that the chromatin has an elastic response (deformation $< 0.1\,\mu m$) [173]. On the other hand, micropipette experiments, which can induce deformations up to the μm range, revealed that the chromatin exhibits viscoelastic and even plastic properties [174].

In this work, I set out to quantify the viscoelastic response of the nucleus with the aim to identify spatial differences in the chromatin structure. To locally measure the mechanical response, I adapted an AFM micro-rheology method that was previously implemented to investigate the dynamic response of cells [175, 176]. In the experiments, single nuclei were squeezed between a tipless cantilever and the substrate and exposed to low amplitude sinusoids from 1 Hz to 700 Hz. Their effective stiffness was obtained for each of the measurement frequencies. To identify the distinct regions of the nucleus, I repeated the measurements at different indentation depths that were mapped to different nuclear regions with finite element analysis (FEA). Finally, I applied the above-mentioned dynamic indentations on nuclei that were isolated from multiple cell lines to be able to distinguish typical and conserved features in the mechanical response of nuclei.

6.3 Methods

The nuclei preparation was done at the University of Kent (Canterbury, United-Kingdom) by Dr. Toseland's group while I conducted the AFM measurements at Heriot-Watt University. To easily associate each work that has been done by a specific group, the following method section is divided in two subsections. It should be noted that the biochemical sample preparation described below is directly taken from my article [177] for the sake of clarity.

If not mentioned otherwise, all chemicals came from Sigma Aldrich (St. Louis, USA).

6.3.1 Biochemical sample preparation (Toseland's group)

- **Nuclei isolation**

HeLa, MCF-7, IMR-5 and HEK293 Cell lines were cultured at 37 °C and 5 % CO_2, in Gibco MEM Alpha medium with GlutaMAX (no nucleosides), supplemented with 10 % heat-inactivated Fetal Bovine Serum (Thermo scientific, Waltham, USA), 100 units/mL penicillin and 100 µg/mL streptomycin (Thermo scientific, Waltham, USA).

The nuclei isolation protocol was adapted from the Collas Lab protocol [178]. Cells, plated at 90 % confluency, were trypsinised in 0.05 % trypsin/EDTA (Invitrogen, Carlsbad, USA) and harvested by centrifugation at 415 g, at 4 °C. Cells were washed once with ice-cold phosphate-buffered saline (PBS), re-suspended in ice-cold Hypotonic Buffer (10 mM Hepes pH 7.5, 2 mM $MgCl_2$, 25 mM KCl supplemented with 1 mM phenymethylsulfonyl fluoride (PMSF), 1 mM dithiothreitol (DTT) and 1 x Halt Protease Inhibitor Cocktail (Thermo Fisher Scientific, Waltham, USA)) and harvested by centrifugation at 15 g, at 4 °C. Cells were then re-suspended in ice-cold hypotonic buffer and incubated for 1 h on ice. Cells were then homogenised on ice with a glass Dounce homogeniser (Wheaton, Millville, USA) by performing 100-150 strokes, until 90 % lysis was achieved. Cell lysis was assessed on the TC20 Automated Cell Counter (Bio-Rad, Hercules, USA). Cell lysate was supplemented with 125 µL of 2 M sucrose solution per mL of lysate and mixed well by inversion. The lysate was centrifuged at 4 °C at 184 g using a swinging bucket rotor. The pellet, which corresponded to isolated nuclei, was further cleaned by re-suspension in ice-cold Hypotonic Buffer plus 250 mM sucrose and further centrifugation at 4 °C at 184 g. The nuclei pellet was re-suspended in freezing medium (Hypotonic Buffer plus 70 % glycerol) before storage at −80 °C.

- **Immunofluorescence and imaging**

Purified defrosted nuclei were immobilised on Poly-D-lysine (MW 70,000-150,000) coated 13 mm glass coverslips (ThermoFisher, Waltham, USA). Immobilised nuclei were stained for 10 min at 37 °C with 1 µg/mm Hoechst 33342 (ThermoFisher, Waltham, USA) in Hypotonic Buffer. Stained nuclei were fixed in 4 % (w/v) paraformaldehyde (PFA) and residual PFA was quenched with 50 mM ammonium chloride. Nuclei were permeabilised and simultaneously blocked with 0.1 % (v/v) Triton X-100 and 2 % (w/v) BSA in Tris-buffered saline (TBS). Nuclei were then immunostained against the endogenous lamin B with the rabbit anti-Lamin B1 polyclonal antibody (Abcam, Cambridge, UK) and subsequently the donkey anti-rabbit Alexa Fluor 555-conjugated antibody (1:500, Abcam, Cambridge, UK), both diluted in 2 % (w/v) BSA in TBS. Coverslips were mounted on microscope slides with Mowiol (10 % (w/v) Mowiol 4-88, 25 % (w/v) glycerol, 0.2 M Tris-HCl, pH 8.5), supplemented with 2.5 % (w/v) of the anti-fading reagent DABCO. Nuclei were visualised using an Olympus IX71 microscope with a PlanApo 100xOTIRFM-SP 1.49 NA objective mounted on a PIFOC z-axis focus drive (Physik Instrumente, Karlsruhe, Germany), and illuminated with an automated 300 W Xenon light source (Sutter, Novato, USA) with appropriate filters (Chroma, Bellows Falls, VT). Images were acquired using a QuantEM (Photometrics, Tucson, USA) EMCCD camera, controlled by the Metamorph software (Molecular Devices, San José, USA). The whole volume of the nuclei was imaged by acquiring z-sections with a spacing of 200 nm. Images presented here correspond to a middle section of the nucleus. Images were deconvolved with the Autoquant X software applying blind deconvolution and analysed by *ImageJ*. The nuclei diameter and lamina thickness was calculated by plotting x and y intensity profiles across the nuclei. Point-to-point distances were then measured across the peaks and nuclear body. The quoted values were calculated from the average of the x and y values.

- **Immunoblot analysis**

Nuclei lysates were prepared by direct lysis of 4.10^6 freshly defrosted nuclei in NuPAGE sample buffer, followed by 5 min sonication. The total protein concentration of the nuclei fraction was determined by a Bradford Assay following the manufacturer's instructions. Nuclei were heat-denaturated and resolved by SDS-PAGE on an 8 % acrylamide gel. Proteins were transferred to 0.45 µm PVDF membrane using semi dry Power Blot Cassette (Thermo scientific, Waltham, USA). The membrane was blocked for 2 h at room temperature with 5 % (w/v) skimmed dried milk, 0.1 % (v/v) TWEEN-20 in TBS and then probed

against lamin B by incubation with the rabbit anti-Lamin B1 polyclonal antibody (Abcam, Cambridge, UK) and subsequently a goat anti-rabbit antibody coupled to horseradish peroxidase (Abcam, Cambridge, UK). The bands were visualised using the ECL Western Blotting Detection Reagents (Invitrogen, Carlsbad, USA) and the images were taken using Syngene GBox system. Images were processed in *ImageJ*.

6.3.2 AFM, modelling and data analysis (my contribution)

- **AFM sample preparation**

The nuclei were defrosted and diluted 100 times in hypotonic buffer. Then, a volume of 100 µL was deposited onto a 25 mm coverslip which was mounted in the AFM liquid cell. The solution was left 5 min for adsorption. The surface was rinsed with the same buffer used for the dilution to remove any unbound nuclei. During fluorescence imaging, 1 µL of a 10^4 times diluted BODIPY 500/510 C4, C9 stock suspension (Thermofisher, Waltham, USA; 2 mM in dimethyl sulfoxide) was added to label the nuclear membrane.

- **Optical microscopy**

The bright field and fluorescence optical images were recorded with an inverted microscope located beneath the AFM. A detailed description of this combined instrument can be found in [109]. I used an oil immersion objective (Nikon, Minato, Japan; 100 × 1.49 NA) to measure the dimensions of the nuclei from brightfield imaging while I employed a water immersion one (Nikon, Minato, Japan; 60 × 1.27 NA) for the fluorescence imaging. The water immersion objective was important to have a constant focus quality throughout the nucleus which facilitated their 3D reconstruction from the fluorescence z-stacks. I used an EM-CCD camera (Luca S-659, Andor technology, Belfast, UK) to record the images. The magnification achieved was 97.5 nm/pixel for brightfield and 166 nm/pixel for fluorescence, calibrated with a reference grid surface.

- **3D image reconstruction from fluorescence microscopy images**

The adhesive contact radius and the deformation prior to indent the nucleus were measured optically. To this end, HeLa nuclei were fluorescently labelled (BODIPY 500/510 C4, C9 stock suspension, Thermofisher, Waltham, USA) and a z-stack containing 150 images spaced by 166 nm was recorded for each individual nucleus. Fluorescence excitation was performed with a 488 nm laser (Nichia, Anan, Japan). The objective scanner (PIFOC, Physik Instrumente, Karlsruhe, Germany) of the inverted optical microscope was controlled by a custom routine developed in LabVIEW (National instruments, Austin, USA)

that also triggered the image acquisition on the camera with a 50 ms exposure time.
I used *ImageJ* and the DeconvolutionLab plugin [178] to process the z-stacks using a 3D deconvolution and a point spread function derived from the Born and Wolf model [179]. The figures shown are the maximum intensity of the projection of the deconvolved z-stacks. The adhesion radius was estimated by plotting a circle around the nucleus to obtain the intersection with the substrate.

- **Contact mechanics model**

The indentation, δ, of a sphere that is compressed by two planes is described by the double contact Hertz model [180] following:

$$\delta(F) = 2 \cdot \left(\frac{3 \cdot F \cdot (1 - \nu^2)}{4 \cdot E \cdot \sqrt{R_n}} \right)^{\frac{2}{3}} \tag{6.1}$$

where R_n is the radius of the nucleus, E its Young's modulus and ν its Poisson's ratio.
This model is further modified to include the adhesion observed in the optical images. The resulting model is derived by Alcaraz et al. [179] and is written as:

$$\delta(F) = 2 \cdot \left(\frac{3 \cdot F \cdot (1 - \nu^2)}{4 \cdot E \cdot \sqrt{R_n}} \right)^{\frac{2}{3}} + \left(\frac{3 \cdot (1 - \nu^2) \cdot \left(F + 6 \cdot \gamma \cdot \pi \cdot R_n + \sqrt{12 \cdot \gamma \cdot \pi \cdot R_n \cdot F + (6 \cdot \gamma \cdot \pi \cdot R_n)^2} \right)}{4 \cdot E \cdot \sqrt{R_n}} \right)^{\frac{2}{3}} - \left(\frac{9 \cdot \gamma \cdot \pi \cdot (1 - \nu^2)}{E} \right)^{\frac{2}{3}} \cdot R_n^{\frac{1}{3}} \tag{6.2}$$

where γ is the surface adhesion energy and depends on the adhesive contact radius, R_C, according to:

$$\gamma(R_C) = \frac{R_C^3 \cdot E}{R_n^2 \cdot \pi \cdot 9 \cdot (1 - \nu^2)} \tag{6.3}$$

$$R_C(b) = \sqrt{R_n \cdot b} \tag{6.4}$$

where b is the initial deformation which is induced by the adhesion of the nucleus on the substrate. It is written as $b = 2 \cdot R_n \cdot (1 - r)$ where R_n is measured in the optical images while r is the height/width ratio, see the subsequent section.

- **Atomic force microscopy**

I performed all the dynamic nanoindentation experiments on an MFP-3D AFM (Asylum Research, Santa Barbara, USA). I used triangular tipless MLCT-O10 cantilevers (Bruker, Billerica, USA) that resonate around 22 kHz in liquid. Their force constants were calibrated

with the built-in thermal noise method, $0.069 \pm 0.003\,\mathrm{N/m}$ (mean $\pm$ s.e.m, $n = 11$).

- **AFM micro-rheology**

Before any experiment, I measured the dimensions of the nucleus of interest. To this end, I first recorded a brightfield image to extract its average width defined as the mean of the short and long axis. Then, the height was deduced with AFM by performing two force spectroscopy curves: one on the apex of the nucleus and one on the substrate. The difference in piezo extension gave me the height. To overcome the $10\,\mu\mathrm{m}$ z-scanner range when the nucleus was higher, I manually readjusted the height of the AFM head.

During the measurement itself, the cantilever was lowered until it reached the desired indentation depth. Then, after a dwell of 1 s to reduce the creep of the material, the cantilever was brought into oscillation. The last was defined by a discrete chirp with an effective amplitude of 25 nm and frequencies increasing from 1 to 700 Hz in 7.5 s. More specifically, the frequencies investigated were [1; 3; 10; 30; 60; 100; 200; 250; 350; 400; 500; 600; 700] Hz, during [5.0000; 1.6667; 0.500; 0.1667; 0.0833; 0.0500; 0.0250; 0.0200; 0.0143; 0.0125; 0.0100; 0.0083; 0.0071] s respectively. This ensured at least 5 periods of each frequency which facilitated the analysis by reducing the background noise during the Fourier analysis. Finally, the cantilever was moved back to its original position. In practise, to achieve a constant amplitude of the chirp over the complete bandwidth I had to drive the cantilever at an amplitude that progressively grew with respect to the frequency, [25.00; 25.00; 25.00; 26.65; 32.00; 42.50; 75.00; 110.50; 135.00; 150.00; 200.00; 250.00; 325.00] nm. This was done to overcome the non-linear response of the Asylum MFP-3D z-scanner.

For the analysis, the deflection curves of the cantilever were converted into the complex stiffness of the nucleus with respect to the frequency of excitation. The complex stiffness considers the viscous and elastic property of the sample and is latter used with Eq.(6.2) and Eq.(6.4) to deduce the apparent Young's modulus, E^*. Nevertheless, to accurately extract the mechanics of the nucleus, I had to correct the deflection measured from the drag of the surrounding liquid which unfortunately adds to the deflection of the cantilever cantilever at higher frequencies.

- **Stiffness of the nucleus and phase shift**

The program to analyse the data was written in MATLAB (Mathworks, Natick, USA). The deflection and piezo scanner position signals were Fourier transformed, $\hat{d}(f)$ and $\hat{z}(f)$ respectively, using a rectangular-window to extract their modulus and their argument. Then, the apparent stiffness, $K(f_i)$, with respect to the frequency of oscillation f_i, was

calculated according to:

$$K(f_i) = \frac{|\hat{F}(f_i)|}{\delta(f_i)} = \frac{k_c \cdot |\hat{d}(f_i)|}{|\hat{z}(f_i)| - |\hat{d}(f_i)|} \tag{6.5}$$

where k_c is the cantilever spring constant, $\delta(f_i)$ the sample deformation in response of the exerted load, $F(f_i)$. The circumflex corresponds to the Fourier transformation.
The phase shift, $\Delta\theta(f_i)$, between z and d was deduced from:

$$\Delta\theta(f_i) = arg(\hat{d}(f_i)) - arg(\hat{z}(f_i)) \tag{6.6}$$

where arg is the argument of the complex signal.

- **Cantilever drag correction**

As mentioned above, the apparent stiffness of the cantilever and the phase shift calculated with Eq.(6.5) and Eq.(6.6) respectively needed to be corrected from the effect of the drag, which induces a higher K and $\Delta\theta$. To this end, I used Eq.(4) from the work of Alcaraz et al. [179] to isolate the response of the nucleus. In a nutshell, the dynamic oscillations were performed at multiple positions away from the substrate free from the nuclei. The deflection of the cantilever and the phase shift between the drive and response signal resulted only from the hydrodynamic drag and the instrument electronics. They were parametrised at each frequency and at each cantilever-substrate distance, see Appendix I. Then, the derived values at a distance which corresponds to the height of the investigated nucleus minus the indentation depth was subtracted from the measured deflection.

- **Calculating E^*, E' and E"**

Since the nucleus presents a viscoelastic response, the calculated apparent stiffness calculated also contains the unknown contribution of the viscosity and the elasticity. Yet, the exact ratio can be estimated after converting the measured stiffness into an apparent Young's modulus, E^*, also referred as dynamic modulus. At first, I deduced the initial contact radius with Eq.(6.4) prior to perform the dynamic indentation. Then after applying the drag correction I acquired the proper force and indentation amplitudes during the measurements. The apparent Young's modulus was numerically calculated after incorporating Eq.(6.4) into Eq.(6.2) and decomposed into the elastic modulus, E', and the viscous modulus, E":

$$E^*(f_i) = E'(f_i) + j \cdot E"(f_i) \tag{6.7}$$

with $E'(f_i) = E^*(f_i) \cdot \cos\left(\Delta\theta_{corrected}(f_i)\right)$ and $E''(f_i) = E^*(f_i) \cdot \sin\left(\Delta\theta_{corrected}(f_i)\right)$. Ultimately, I also calculated the loss tangent which is defined as:

$$LossTangent(f_i) = \frac{E''(f_i)}{E'(f_i)} = tan\left(\Delta\theta_{corrected}(f_i)\right) \tag{6.8}$$

- **Fitting of E^* with a power law**

On a double logarithmic scale the dynamic modulus presents two distinct linear regions, above and below 100 Hz. Each region can be described by a power law function of the form $E^*(f) \propto f^{\alpha}$, where α is the power law exponent and f the frequency. After logarithmic transformation, this equation is written as $log\left(E^*(f)\right) \propto \alpha \cdot log(f)$. Thus, the fitting routine can be simplified and reduced to a simple linear fit, instead of a non-linear regression, to extract the power law coefficient of each region.

- **Finite element analysis of nucleus deformation**

All models were developed with Comsol Multiphysic 5.2a (Comsol, Stockholm, Sweden). To mimic the nucleus geometry, I modelled a continuous sphere with a 5.5 µm radius (average values measured) lying on a fixed plane. Its mechanical properties were: a 2 kPa Young's modulus and a Poisson's ratio of 0.4 to be in line with the AFM experiments. To best match the initial contact area due to adhesion seen with optical microscopy, I applied a load over the lower boundary of the sphere which was adjusted until a contact radius of 4.5 µm was found. Eventually, the tipless cantilever, modelled by a 10° tilted plate, was lowered in discrete steps to compress the sphere. The force field was implemented by contact penalty method [107].

In the case of the computations in which the Young's modulus is not homogeneous within the sphere I developed 2D axisymmetric models to reduce the required computation time. In these models, the plate was not titled but parallel to the surface (as I found the tilt effect of the cantilever can be neglected) and the initial deformation was not included. The variable Young's modulus was implemented by a linear function with negative slope from 0.3 kPa at the outer region to 10 kPa at the centre. A linear decrease is the simplest assumption but this does not exclude that a non-linear function would give a better match. I described the lamin layer by a 100 nm thick coating with a Young's modulus of 200 kPa. It resulted in a bulk modulus of 24 mN/m, as previously reported [173]. The mechanical response of this thin coat is dictated by in-plane stretching and not by bending. The exact thickness of the lamin layer is then not critical as long as the bulk modulus is coherent.

6.4 Results and discussion

6.4.1 Contact mechanics

During the experiments, the nucleus was effectively compressed between the supporting cover glass on one side and the tipless AFM cantilever on the other, Figure 6.1. Although a simple analysis of the resulting force spectroscopy curve would allow me to convert the measured stiffness of the nucleus into its elastic modulus, I first had to better understand the geometrical constrains between the nucleus and both surfaces to accurately select the contact model that best describes the experimental conditions. Indeed, if the nucleus would behave like a simple homogeneous sphere bare from any initial deformation and solely compressed between 2 parallel plates, basic Hertzian contact mechanics could be used to extract its mechanical properties. However, if the system is more complex, the above-mentioned model would lead to severe deviations of the measured mechanics.
Previously, AFM has been combined with confocal microscopy to observe the shape of whole cells while they were deformed with a tipless cantilever [181]. Here, I used the previously described combined fluorescence microscope with AFM [109] to visualise the morphology of deformed nuclei during the measurements. The nuclear membrane was labelled with a membrane dye and a stack of images was recorded with the fluorescence microscope. The images were then combined into a 3D representation of the nucleus which was used to estimate the experimental conditions, thus, the appropriate contact mechanics model to use.

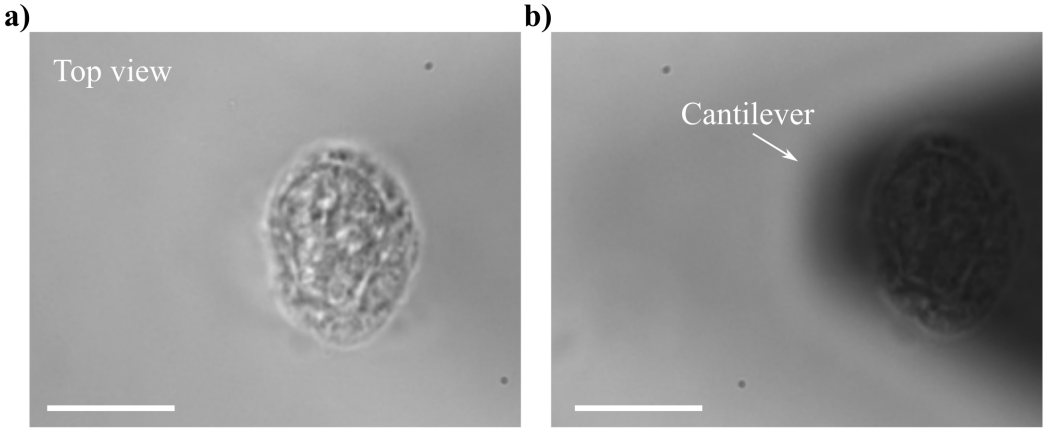

Figure 6.1: Defining the adhesive contact during the deformation of nuclei. *Top-view microscopy images of a single nucleus resting on the cover glass before and after lowering the AFM cantilever, (a) and (b) respectively. Scale bars:* 10 µm.

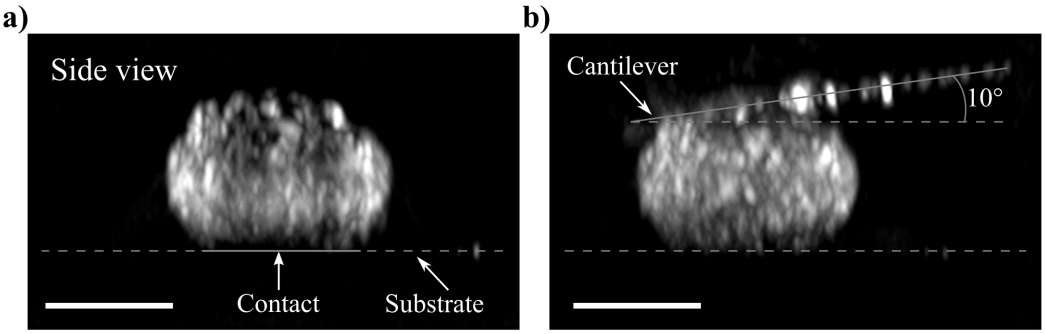

Figure 6.2: Defining the adhesive contact with fluorescence. *Side-view projections generated from a z-stack of fluorescence microscopy images before and after lowering the AFM cantilever, (a) and (b) respectively. Scale bars:* 10 µm.

Figure 6.2 shows that the nucleus was already deformed before any mechanical measurements as its bottom is flattened but also that the tipless cantilever is tilted by 10° with respect to the substrate. As a result, I concluded that Hertz's model is obviously not sufficient to properly describe the compression of nuclei.

- **Adhesive contact estimation**

The 3D representation of the nucleus reconstructed from the fluorescence images were also used to estimate the adhesive contact between the nucleus and the cover glass. I found that the radius of this adhesive contact ranged from 3 and up to 6 µm.

Nonetheless, labelling the nuclei to measure the initial contact may influence their mechanical response to stimuli. To overcome this limitation, I developed an alternative strategy to obtain the adhesive contact. Figure 6.2 shows that the adhesion of the nuclei onto the substrate induced a reduction in height, assuming that the nuclei are spherical. Thus, it is possible to estimate the adhesive contact radius from this aspect ratio. To this end, I combined optical microscopy to assess the lateral dimensions of the nucleus with AFM to measure its height. Then, I derived the initial deformation, b, from the ratio, r, of the vertical and lateral dimension, $b = 2 \cdot R_n \cdot (1 - r)$ with R_n the nucleus radius. To appraise the goodness of this new strategy I compared the deformations measured with and without fluorescent labelling, see Figure 6.3. The calculated values were in good agreement with the experimentally measured ones (within 15 %) and allowed me to estimate the initial deformation by only measuring the dimensions of the nuclei with optical microscopy, which is non-invasive. This removed the need to perform force spectroscopy curves on top of the nuclei and thus possible cantilever contamination or adhesion of the nuclei on the cantilever, which happened many time and forced me to bin directly the cantilever.

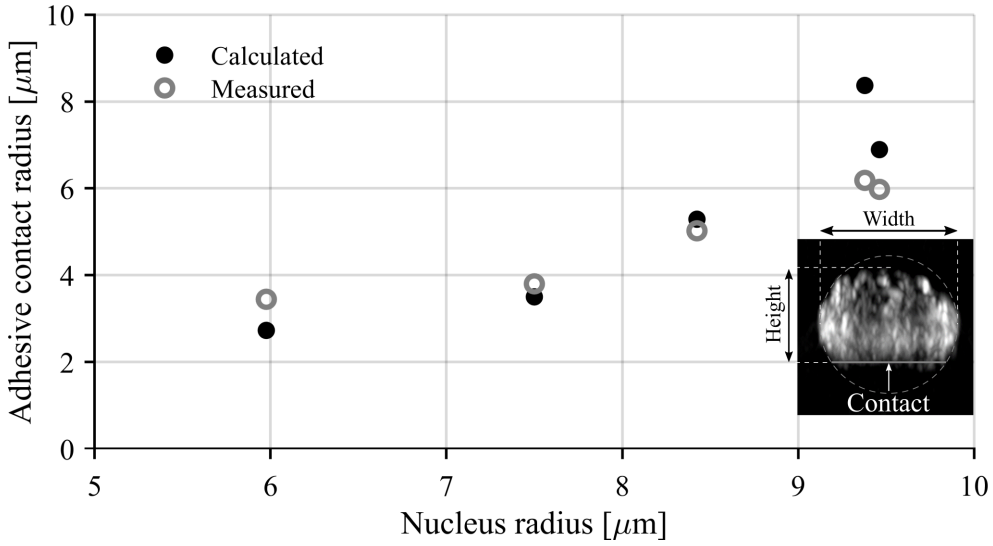

Figure 6.3: Defining the contact radius between nucleus and substrate. *The adhesive contact radii of five nuclei of different sizes as measured from fluorescence side-view projections are described well by the height/width ratio calculation. Inset: principle of the height/width ratio calculation.*

Table 6.1: Dimensions of the nuclei studied in this research. *The dimensions are mean ± s.e.m. The height was measured with AFM while the width was estimated from optical microscopy top-view images.*

Cell line	Height [μm]	Width [μm]	Height/width	n
Hela	10.91 ± 0.59	12.73 ± 0.54	0.86 ± 0.03	23
IMR5	6.19 ± 0.35	8.32 ± 0.16	0.77 ± 0.02	21
HEK	8.31 ± 0.26	10.06 ± 0.18	0.83 ± 0.03	29
MCF7	15.95 ± 0.66	17.99 ± 0.51	0.88 ± 0.03	20

The above-mentioned strategy was used for all subsequent analysis to estimate the dimensions of the nuclei, therefore their initial contact area, Table 6.1.

- **Effect of the tilt of the cantilever**

The other aspect to take into account was the contact area between the cantilever and the nucleus, which depends on the tilting angle. At first, I set out to estimate this area by using different fluorescence side-view projections recorded at different compression forces. Unfortunately, this resulted in unclear blurry reconstructions as the AFM cantilever was insufficiently defined during the fluorescence measurements. Furthermore, it was very challenging to keep the cantilever position constant during the image acquisition (data not shown). I decided to find an alternative method.

Because the cantilever was tilted by 10° with respect to the substrate, the total load from the cantilever gains a lateral component that influences the measured mechanics. To address the impact of this lateral force, I modelled a nucleus with an initial adhesive contact area and being compressed by either a parallel or a 10° tilted plate. The FEA resulted in a small discrepancy of approximately 10% between the two plate geometries in the computed force spectroscopy curves, as shown in Figure 6.4. Thus, the tilting of the tipless cantilever does not have a large impact on the measured mechanics, which is in line with earlier experiments [179]. I compared the FEA computed force curves with the widely used Hertz theoretical model, which accounts neither for the adhesive contact nor for the tilt of the cantilever. As expected, the variation between both models is considerable, approximately 40%, which indicates that the initial deformation of the nucleus has more impact on the measured stiffness than the tilting of the cantilever. Recently, a modified Hertz model that takes into account the adhesive contact area of spherical particles was analytically derived [182]. For comparison, I included the model in Figure 6.4. Even if it still predicts a response that is approximately 25% softer than the FEA, I chose this model to quantify the nuclei mechanics in the subsequent experiments for the sake of reproducibility by eventual follow-up experiments.

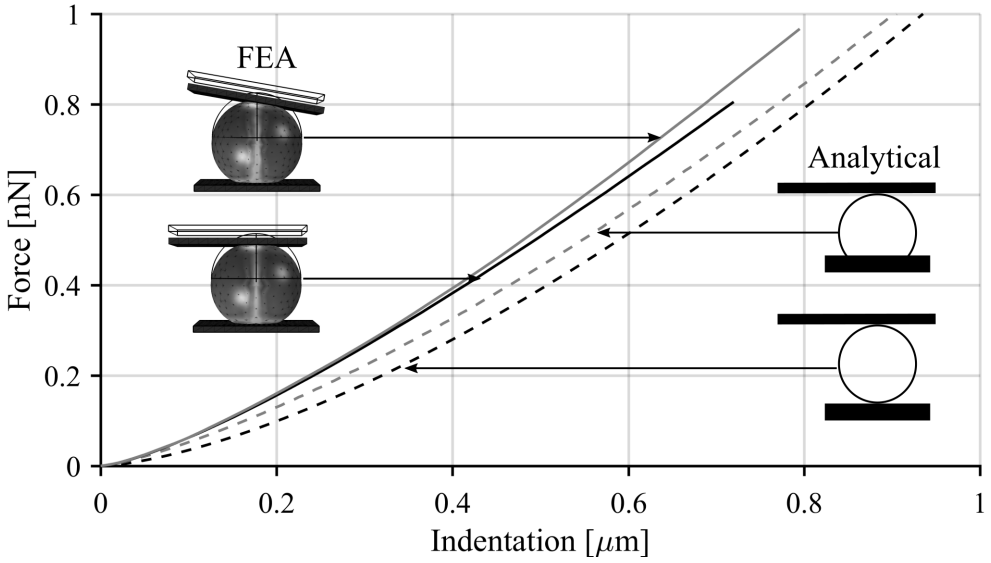

Figure 6.4: FEA simulation of the initial adhesion and the cantilever angle effects. *I computed the compression of a* 2 kPa *sphere with adhesive contact by a horizontal (black solid line) and* 10° *tilted plate (grey solid line). For comparison, I added two analytical solutions according to the Hertzian theory (black dashed) and an extension of this model that takes into account the adhesive contact [180] (grey dashed).*

6.4.2 Viscoelasticity is not homogeneous through the nucleus

- **Measurement principle**

After having established the experimental contact conditions and thus the appropriate mechanical model to apply, I performed micro-rheology measurements, also called dynamic nanoindentation, to separate the viscous properties from the elastic properties of the nuclei. Figure 6.5 shows the measurement principle: when the tip reached the desired indentation depth the piezo-element holding the tipless cantilever was oscillated with a sequence of sinusoids. As a result, the deflection of the cantilever with respect to the oscillatory motion of the piezo-element reflects directly the viscoelastic properties of the nucleus. Prior further investigation, I controlled whether successive dynamic oscillations on a nucleus would affect the mechanical properties measured due to memory effects, see Figure 6.6. Since the measured amplitude remained similar in all control experiments it confirmed that the nucleus does not exhibit memory effects and that I could perform multiple successive measurements without altering the nuclei behaviour.
Hereafter, I defined the measured modulus as the apparent Young's modulus, E^*, which is the sum of the elastic, E', and viscous ,E", moduli.

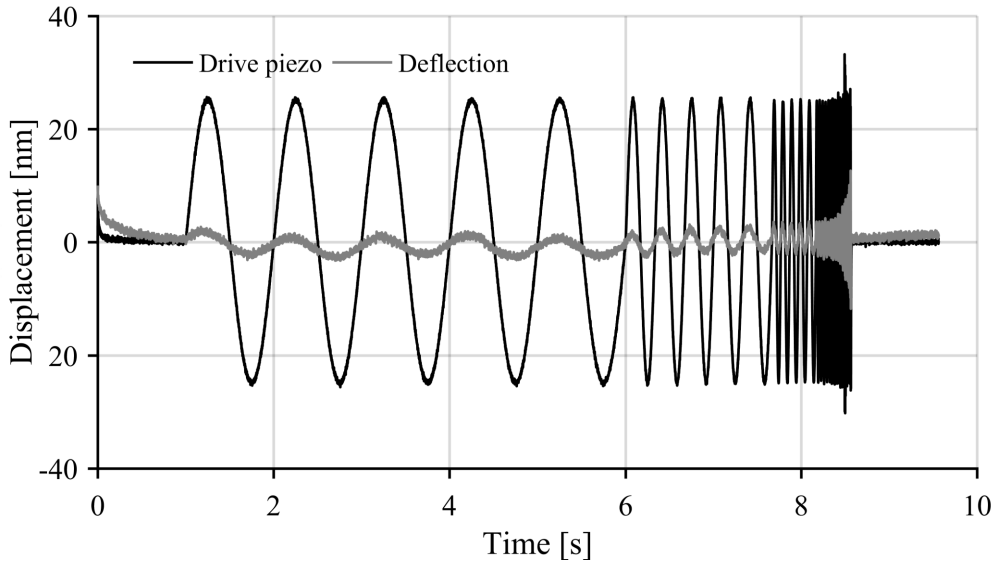

Figure 6.5: Dynamic nanoindentation principle. *After reaching the desired indentation depth, the piezo-element supporting the cantilever base was oscillated with successive sinusoids of increasing frequencies but constant amplitude (black). In return, the cantilever will follow this oscillation but with a reduced amplitude (grey). This damping is caused by the compliance of the nucleus and the drag of the surrounding buffer.*

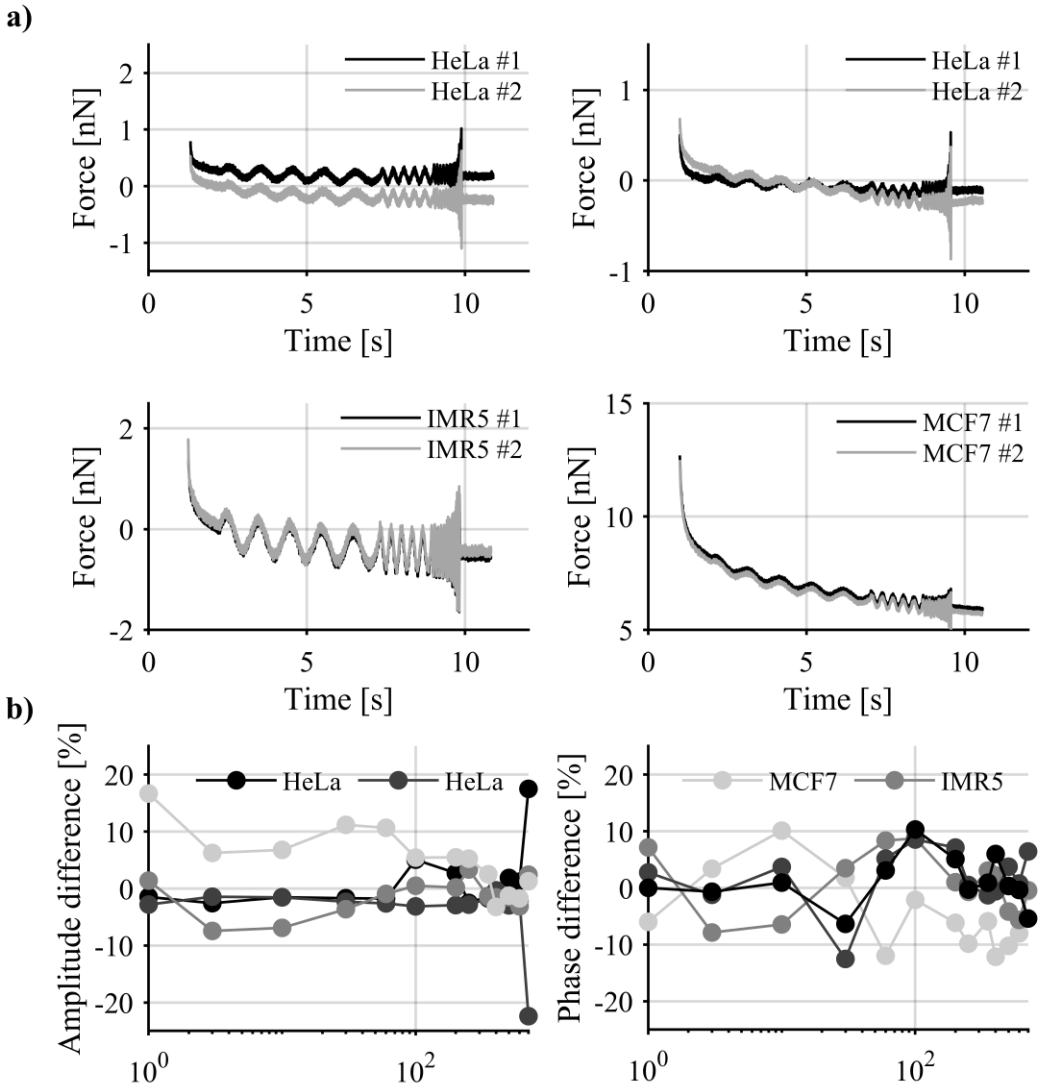

Figure 6.6: Memory effect experiments. *(a) First frequency sequence (grey) and second one (black) for 4 different nucleus from three different cell lines, HeLa, IMR5 and MCF7. (b) The differences are mostly below* 10 % *and do not show a systematic trend.*

- **Viscoelastic measurement**

First, I focus on the viscoelastic properties of HeLa nuclei at low frequencies (1 Hz) which is a common velocity in typical AFM force spectroscopy experiment. As compared to a cell, the nucleus has a more homogeneous structure mainly described by its nuclear envelope and its chromatin contents. Thus, one may expect that its mechanical properties should be relatively constant at increasing deformations as compared to cells that show a response that is length-scale dependent [171]. To test this, I performed the dynamic nanoindentation experiments at different indentation depths to identify the mechanics of the nucleus regions. By changing the exerted force from 1 to 15 nN I indented the nuclei by 0.5 to 2.6 µm.

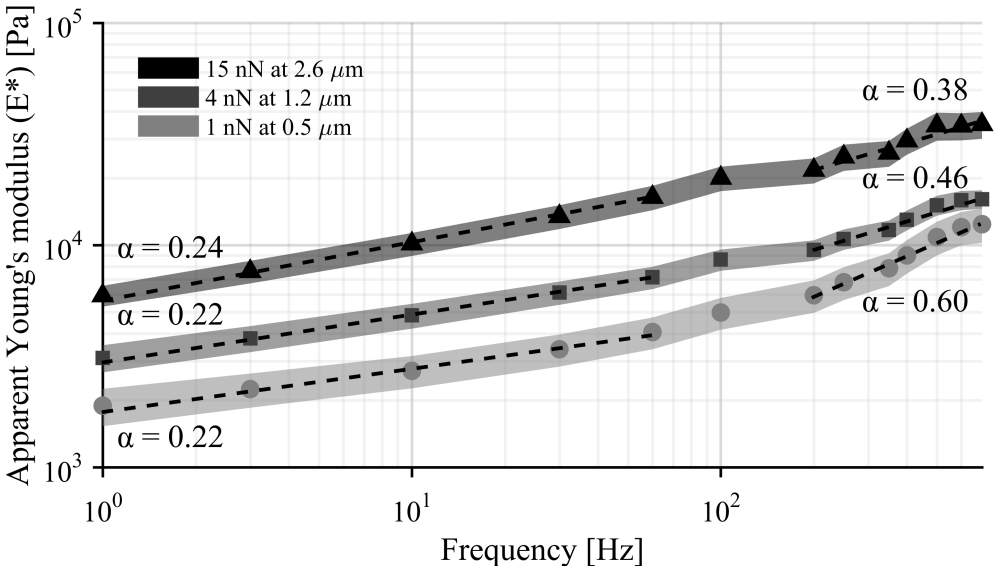

Figure 6.7: Viscoelastic response of HeLa nuclei. *The apparent Young's modulus increases with respect to the frequency of oscillation and indentation depth and can be described by two distinct power laws, below and above* 100 Hz *(dashed black lines). The power law coefficients, α, are included. The data shown is the mean ± s.e.m of the log transformed data (shaded area).*

Figure 6.7 shows that the apparent Young's modulus of the nucleus at 1 Hz is however not constant but increases at larger deformations: it grows nearly a 3-fold from 2 kPa at 0.5 µm to 6 kPa at 2.6 µm indentation depth. This aspect suggests the presence of spatial differences in the arrangement of the nucleus.

When the nucleus mechanics is measured at higher frequencies, its apparent modulus grows accordingly, as shown in Figure 6.7. In an interesting manner, this increase also depends on the indentation depth. Indeed, the slope of the curves is not constant but increases with the frequency at low indentation depth, whereas at high deformations it is almost constant. Furthermore, the dynamic modulus presents two distinct linear regions, above and below 100 Hz, which is consistent with earlier reports [183, 184]. In Figure 6.7, the curves are plotted on a double logarithmic scale to facilitate the reading. Then, a constant slope indicates that the nucleus behaviour can be described by a power law function with a constant exponent, α, such as: $E^*(f) \propto f^\alpha$, where f is the frequency. At low deformation, 0.5 µm, the power law exponent goes from 0.22 below 100 Hz to 0.60 above 100 Hz, a 172 % increase, while remaining nearly constant around 0.30 at both 1.2 µm and 2.6 µm indentation depths (109 % and 64 % increase respectively). A high α value indicates that the nucleus is more sensitive to changes in the deformation rate.

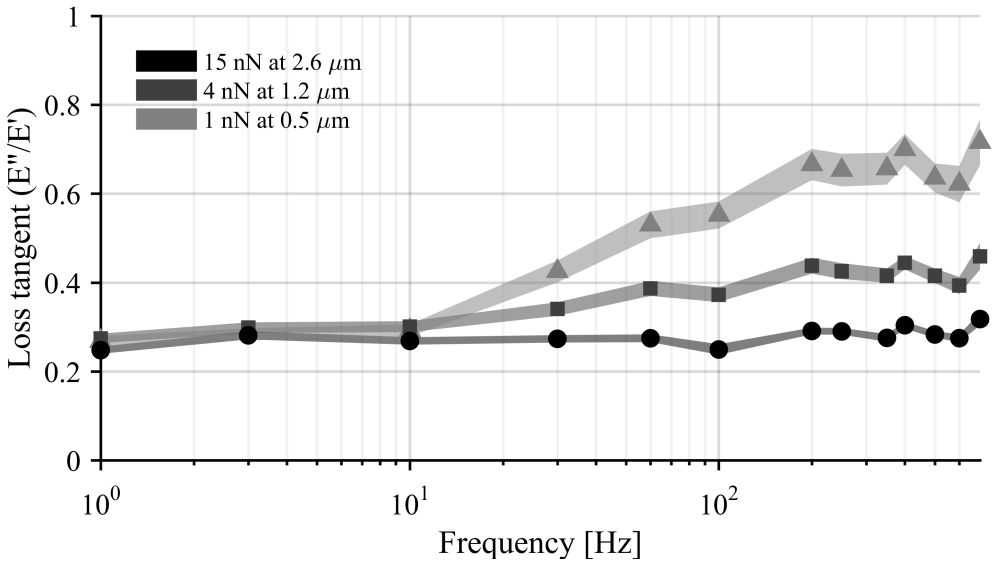

Figure 6.8: Viscous contribution of HeLa nuclei. *The apparent Young's modulus can be decomposed in its viscous and elastic components which are used to calculate the loss tangent. The data is shown as the mean ± s.e.m of the log transformed data (shaded area).*

In order to assess the impact of the viscous properties in the measured dynamic response, I calculated the loss tangent which is the ratio between viscous and elastic components of the apparent Young's modulus, see Figure 6.8. At large deformation the loss tangent equals 0.3 which indicates that the viscous contribution is small. Furthermore, it remains low along the full frequency range. On the other hand, at low indentation depth, it increases up to 0.7 at higher frequencies showing a stronger viscous response. The change in viscosity at different deformation further supports the presence of spatial variation within the nucleus. To test my hypothesis that a variation in the organisation of the nucleus causes the observed mechanical response, I modelled with FEA the nucleus as a continuous spherical body of which the elastic modulus is a function of the distance to its centre, see Figure 6.9. First, I confirmed that a constant Young's modulus did not match the experimental behaviour, even after adding an extra stiff layer to mimic the presence of the nuclear lamina. Then, I computed the next simplest assumption which is that the Young's modulus increases linearly towards the centre of the nucleus, described by a linear function with negative slope from 0.3 kPa at the outer region to 10 kPa at the centre. The computed Young's moduli followed the same trend than the experiments and confirmed my initial hypothesis (the exact function to perfectly match the AFM data was not determined). This also suggests that the chromatin is less dense packed and/or contains less cross-links towards the outside.

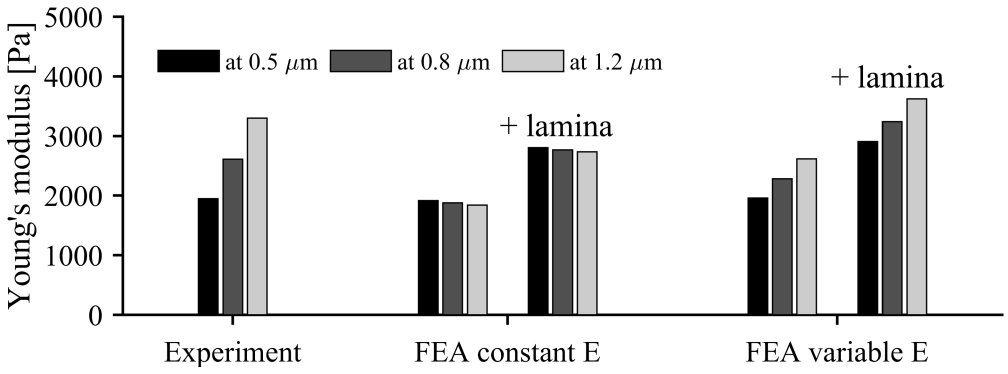

Figure 6.9: Using FEA to model the spatial differences. *For comparison, the experimental data at* 1 Hz *is added.*

6.4.3 The elasticity of the nucleus scales with its size

So far I used HeLa nuclei as my model system, however, nuclei from different cell types have diverse morphologies, which may have a large effect on their mechanical properties. Earlier work showed that all major lamin subtypes are determinants for nuclear shape [159, 185]. As a result, I compared nuclei from 4 different cell lines, HeLa, IMR5, HEK and MCF7 which lamins B were stained to screen if they play a role in regulating the size of the nuclei, therefore their mechanics, see Figure 6.10.

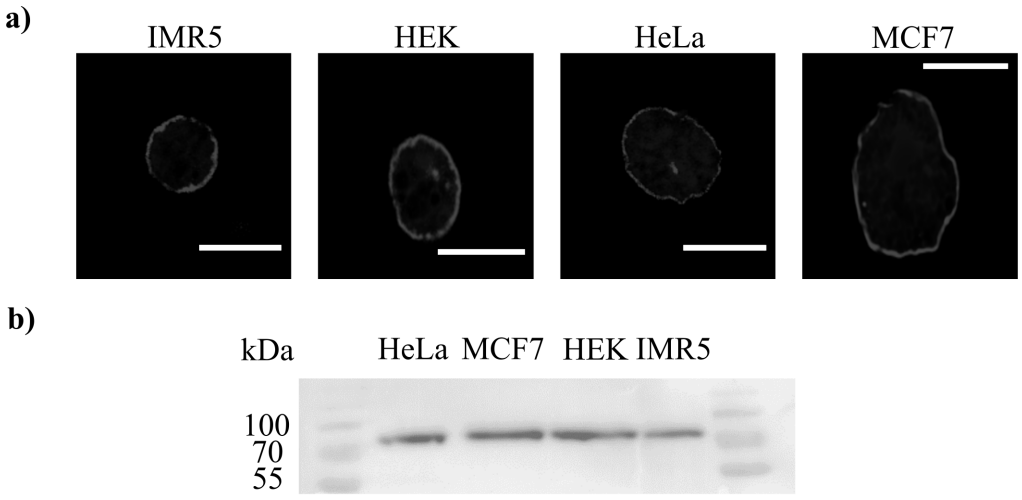

Figure 6.10: Comparing the shape and composition of various nuclei (Toseland's group). *(a) Example images from immunofluorescence staining against Lamin B with Hoechst staining for DNA in isolated IMR5, HEK, HeLa and MCF7 nuclei. Scale bars* = 10 µm. *(b) Western blot showing the presence of lamin B in the nuclear extracts. The samples were normalised to total protein content in the nuclear extract.*

Table 6.2: Lamina quantity in the nuclei. *The values shown are the mean ± s.e.m. The lamina quantity, defined as the ratio between the nucleus volume and the volume of the lamina shell, is almost the same in all the nuclei.*

Cell line	Lamina thickness [μm]	Nucleus diameter [μm]	Lamina quantity	n
IMR5	0.99 ± 0.05	8.9 ± 0.2	1.42	18
HeLa	0.62 ± 0.04	11.4 ± 0.4	1.18	33
HEK	0.85 ± 0.04	11.6 ± 0.4	1.26	20
MCF7	0.68 ± 0.02	15.6 ± 0.3	1.14	20

The values of the lamina thickness for each cell line are contained in Table 6.2 and shows that the quantity of lamina inside each nucleus is approximately identical, 1.25 ± 0.11 (mean ± std), but organised as a thicker layer for smaller nuclei. A thicker lamina may enable greater compression of the chromatin to generate a higher packing density, as would be required in smaller nuclei, assuming the same chromatin content between small and large nuclei. Despite the difference in nuclear size, the quantity of chromatin inside, at least based on karyotype, will be approximately identical in the different mammalian cell lines tested here. Therefore, the larger MCF7 nuclei would have their chromatin less densely packed which should result in a lower Young's modulus. To test this, I compared the stiffness of nuclei obtained from the four different cell lines, Figure 6.11.

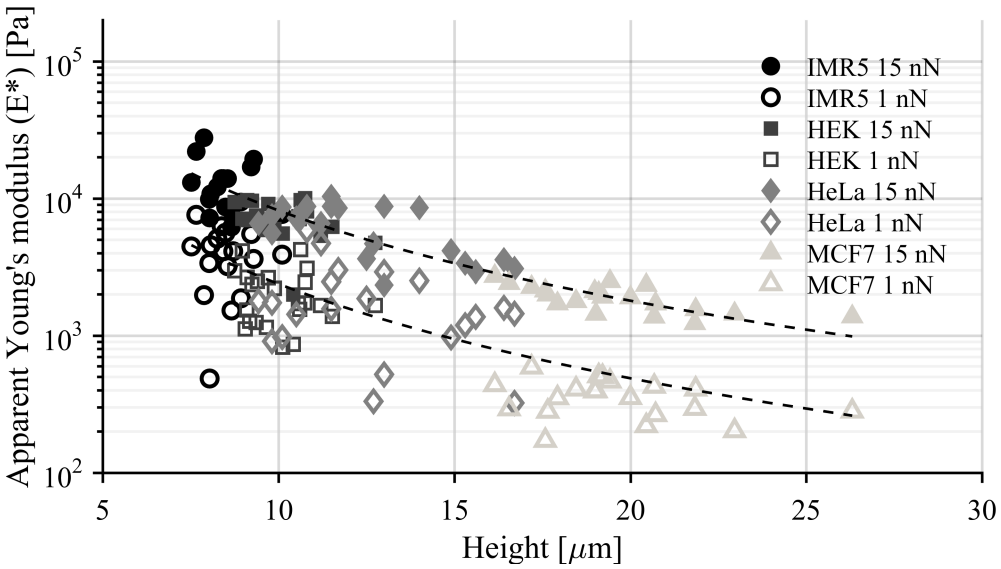

Figure 6.11: Apparent Young's modulus measured at 1 Hz. *E^* scales with the inverse of the nucleus squared radius as shown by the fit: $log\left(E^*(r)\right) \propto \alpha \cdot log(r)$ with $\alpha \pm$ ste equals* -2.21 ± 0.05 *($\chi^2 = 0.65$) and* -2.16 ± 0.01 *($\chi^2 = 0.84$) at* 1 nN *and* 15 nN *respectively.*

The quantitative response, *i.e.*, the apparent Young's modulus at a given deformation and frequency, varies with more than one order of magnitude but scales almost perfectly with the reciprocal of the radius squares of the investigated nuclei. Although the chromatin packing density, seen through the dimensions of the nuclei, has a large effect on the response, the difference at small and high indentation depths is preserved, which suggests that the observed chromatin softening towards the outside is not due to spatial differences in density.

The qualitative response of all nuclei types can be estimated by comparing the slopes of the apparent Young's modulus *versus* frequency above and below 100 Hz. Figure 6.12 shows that the behaviour of the different nuclei was nearly identical and unrelated to their size. Similar to what was shown in Figure 6.3, the nuclei modulus increased with the frequency while the contribution of the viscosity is small and only plays a larger role at small deformations and higher frequencies. The individual responses of the nuclei can be found in Appendix II.

All the measurements were performed on nuclei that were stored at −80 °C. To ensure that the storage temperature did not affect the mechanical properties of the nuclei I also performed measurements on HeLa nuclei that were freshly prepared. These nuclei, 'HeLa fresh' were larger than the HeLa ones by 35 %, 17.2 ± 0.39 µm (mean ± s.e.m, n = 16). Furthermore, to emphasise the relationship between nucleus dimension and

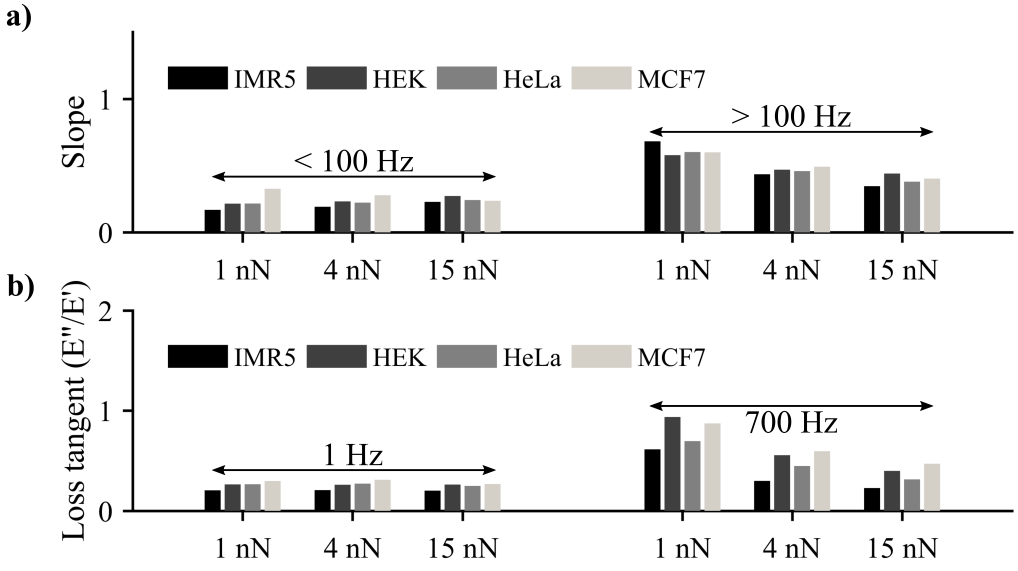

Figure 6.12: Further mechanical properties of nuclei from different cell lines. *All nuclei show (a) a slope of the modulus vs. frequency response and (b) a loss tangent that only increase when probed at small deformations and at high frequency.*

apparent Young's modulus, I have measured HeLa nuclei that were subjected to hypotonic conditions to induce osmotic swelling. Under these conditions, the nuclei were 20.7 ± 0.61 µm (mean ± s.e.m, $n = 10$), thus 63 % bigger than the HeLa nuclei. The measurements showed that although the process of freezing induces shrinkage of the nuclei, the mechanical properties are fully consistent, see Figure 6.13.

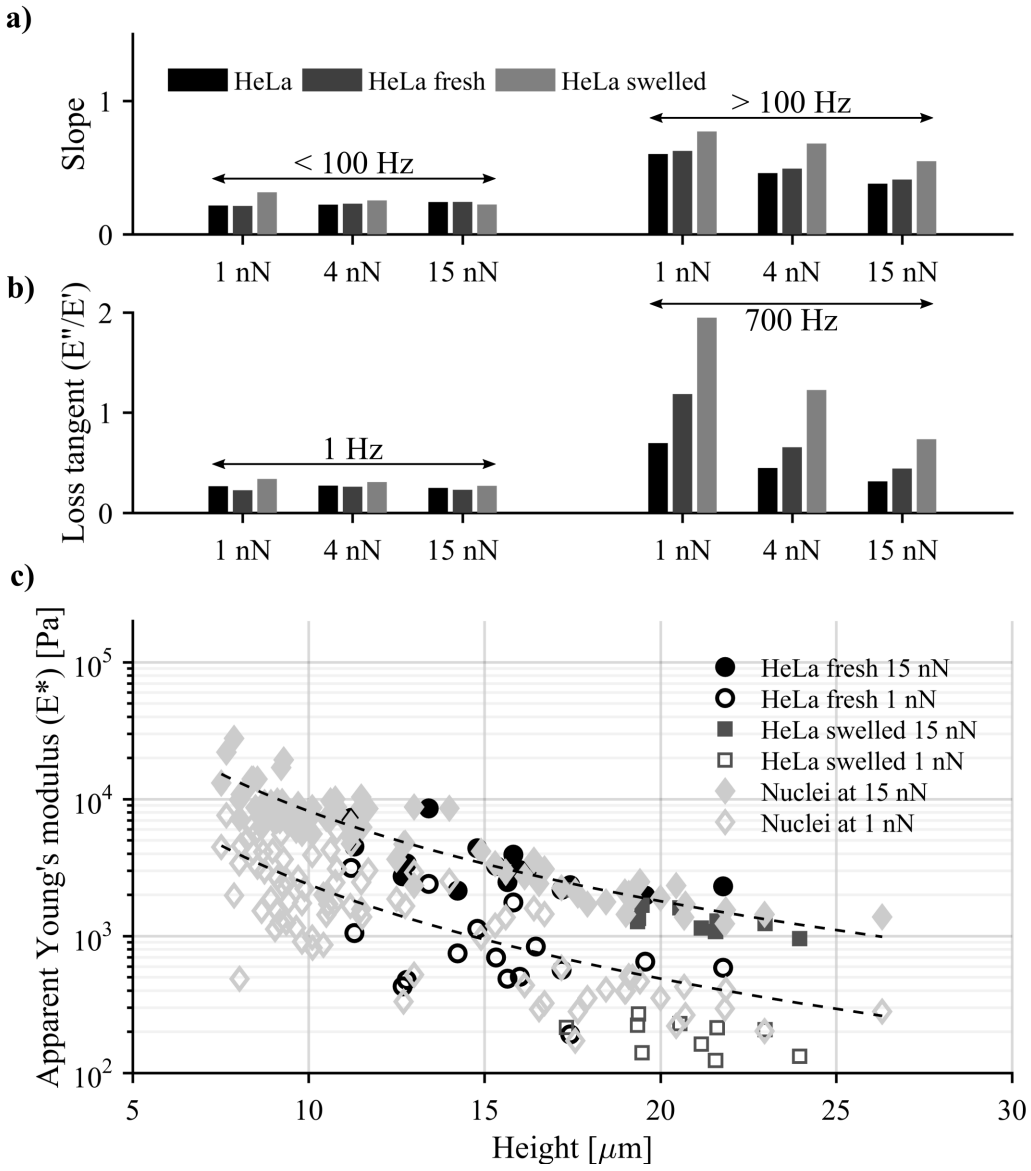

Figure 6.13: Mechanical response of HeLa stored under different conditions. *(a) At low frequencies, the difference between the HeLa samples is very small. However, at high frequencies, the swelled nuclei have the highest slope. (b) Variations in the loss tangent are noticeable at high frequencies. (c) The response of 'HeLa fresh' (black) and 'HeLa swelled' (in grey) reveal a size-dependent behaviour similar to that of the nuclei of the different cell lines, the larger, the softer. To facilitate the comparison, the dynamic moduli from the HeLa, IMR5, HEK and MCF7 nuclei are added in bright grey.*

6.5 Conclusion

In this experimental work, I have defined the viscoelastic properties of isolated nuclei. By varying the deformation in combination with finite element analysis I identified mechanical inhomogeneities in the chromatin. Such a detailed understanding of the viscous and elastic properties at different indentation depths is novel and will help to understand nucleus deformations that are observed in migrating and differentiating cells. Furthermore, my results pave the way to employ the nucleus as a calibrated intrinsic force sensor for cell and tissue mechanical measurements. By observing the fluctuations in shape and knowing the mechanical response of the nucleus the responsible forces can be reconstructed.

My results also shed more light on what structural features of chromatin define its ability to be transcriptionally active. The apparent Young's modulus for nuclei of different cell lines varies by more than one order of magnitude. The dimension, controlled by the nuclear lamina, is the main parameter that determines the elastic response of the nuclei via its compaction. Because of this large variation it is unlikely that gene expression is regulated by simple mechanical compaction of chromatin.

A feature that all nuclei, small and large, share is that they are softer and more viscous towards their outside. If this softening would be solely caused by a reduced density then it is expected that especially in the smaller, thus more compressed, nuclei this difference would disappear, which it does not. It is therefore unlikely that the looser chromatin structure that I consistently observed at the outside of the nuclei is a result of a lower density. Instead I speculate that the degree of cross-linking determines the measured elasticity gradient and is an important feature to regulate transcription. In the nuclear core the cross-linking is higher, which results in higher stiffness but also limits gene expression. Towards the outside of the nucleus the cross-linking is reduced which facilitates gene expression in this region, which has also been observed [167], and results in a lower elastic modulus and an increased viscosity.

Appendix I: Drag coefficients and correction

All functions cited are MATLAB built-in functions.

Estimation of the drag forces

According to Alcaraz et al. [179], the drag forces exerted on a cantilever can be written as:

$$F_{drag}(h,t) = c_a(h) \cdot v(t) \tag{6.9}$$

with $c_a(h)$ the drag coefficient with respect to the distance cantilever-substrate, h, and v the relative velocity of the cantilever with the surrounding liquid.
It should be noted that for $v = \dot{z(t)}$, Eq.(6.9) has a similar notation than Eq.(2.15) in chapter 2. To estimate the drag coefficients, I first derived the mechanical transfer function, $H_a(f_i)$, with respect to the frequency of oscillation, f_i [179]:

$$H_a(f_i) = \frac{k_c \cdot \hat{d}(f_i)}{\hat{z}(f_i)} \tag{6.10}$$

with k_c the cantilever spring constant, $\hat{z}(f_i)$ and $\hat{d}(f_i)$ the Fourier transformation results at a frequency f_i of the z-piezo signal, z, and deflection signal, d, respectively. The circumflex corresponds to the Fourier transformation. The signals were transformed using the *FFT* function. The corresponding drag transfer function is written as [179]:

$$H_d(f_i) = \frac{k_c \cdot H_a(f_i)}{k_c - H_a(f_i)} \tag{6.11}$$

The drag transfer function is then a complex number due to the Fourier transformation of the signals. It was further separated into an in-phase, $H_d'(f_i)$, and an out-of-phase, $H_d''(f_i)$, component: $H_d(f_i) = H_d'(f_i) + j \cdot H_d''(f_i) = real\left(H_d(f_i)\right) + j \cdot imag\left(H_d(f_i)\right)$, using the *real* and *imag* functions. The drag coefficient was extracted from the slope of the linear fit of the $H_d''(f_i)$ function *versus* f_i [179] using the *polyfit* function, an example being given in Figure 6.14. Experimentally, I performed multiple dynamic oscillations, as previously described, at different distances from the substrate and measured the z-piezo and deflection signals needed for the calculation of the coefficients. Furthermore, I repeated the measurements and the calculation after performing the oscillations on top of a random nucleus to assess the impact of the sample on the measured drag, see Table 6.3.

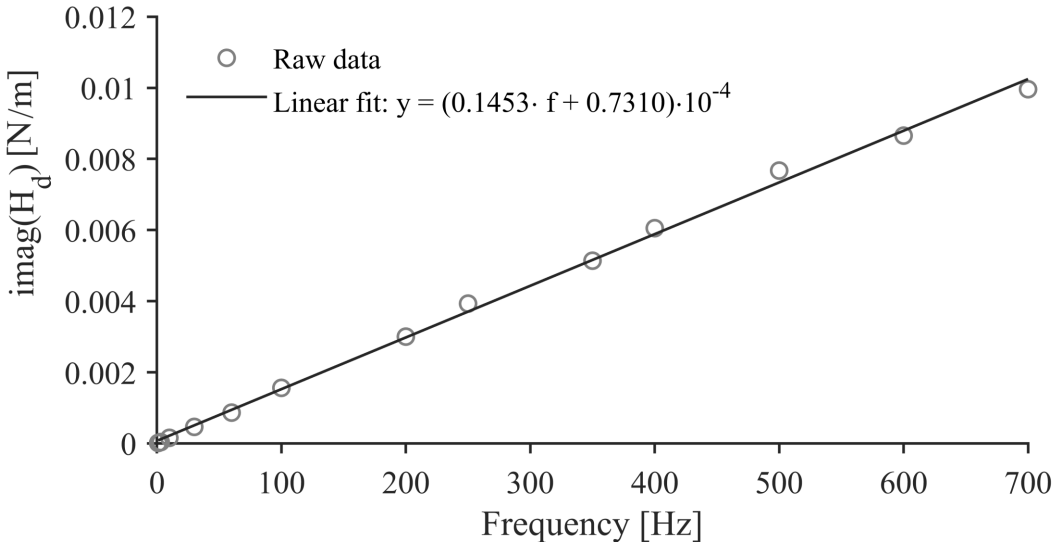

Figure 6.14: Drag coefficient calculation. *An example of the imaginary part fitting of the drag transfer function. The measurements were taken* $30\,\mu\text{m}$ *away from the surface. The drag coefficient found was* $b(h = 30\,\mu\text{m}) = 1.45e-5 \pm 2.42e-7\,\text{N.s/m}$ *(value* $\pm$ *ste).*

Table 6.3: Drag coefficients. *The coefficients were estimated from the slope of the linear fit. The* χ^2 *is also shown as goodness of fit parameter. Left: measurements above the bare substrate. Right: measurements above a nucleus. The distance is always given as the distance to the surface.*

Substrate				**Nucleus**			
Distance [μm]	c_a [N.s/m]	**ste** [N.s/m]	χ^2	**Distance** [μm]	c_a [N.s/m]	**ste** [N.s/m]	χ^2
0.5	$2.05e-4$	$1.41e-5$	0.95	11.2	$2.15e-5$	$6.18e-7$	0.98
1	$7.28e-5$	$3.23e-6$	0.98	11.5	$2.12e-5$	$5.78e-7$	0.98
4	$4.22e-5$	$1.89e-6$	0.98	11.7	$2.10e-5$	$5.55e-7$	0.98
6	$3.33e-5$	$1.06e-6$	0.99	12.0	$2.07e-5$	$5.14e-7$	0.98
8	$2.65e-5$	$9.68e-7$	0.98	12.5	$2.05e-5$	$5.97e-7$	0.98
10	$2.25e-5$	$8.00e-7$	0.99	13.0	$2.01e-5$	$4.86e-7$	0.99
12	$2.02e-5$	$7.11e-7$	0.99	14.0	$1.93e-5$	$4.75e-7$	0.99
14	$1.90e-5$	$4.96e-7$	0.99	16.0	$1.82e-5$	$3.38e-7$	1.00
16	$1.80e-5$	$3.75e-7$	0.99				
20	$1.63e-5$	$3.72e-7$	0.99				
21	$1.63e-5$	$4.34e-7$	0.99				
22	$1.55e-5$	$3.18e-7$	0.99				
24	$1.50e-5$	$3.59e-7$	0.99				
27	$1.47e-5$	$4.06e-7$	1.00				
30	$1.45e-5$	$2.42e-7$	1.00				

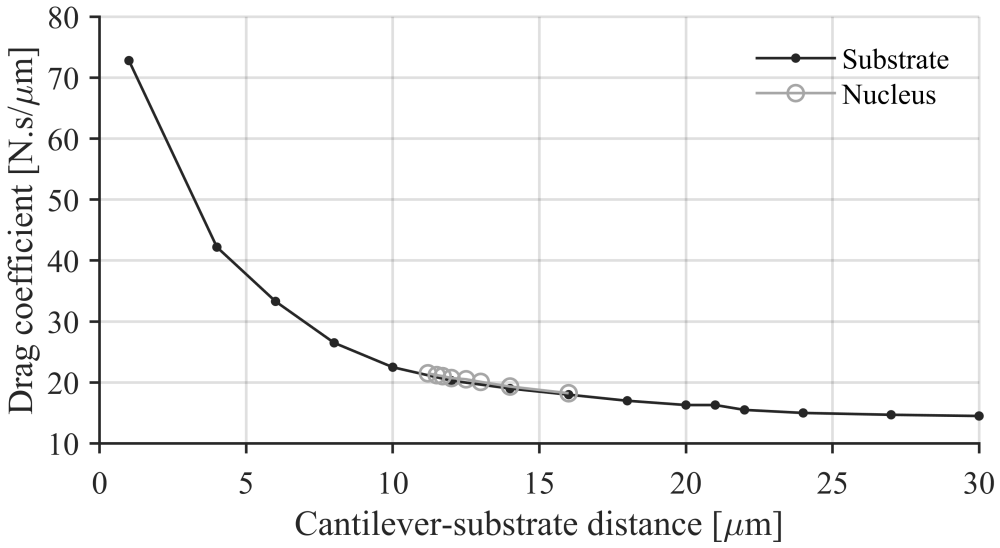

Figure 6.15: Drag coefficient during the experiment. *The coefficients were obtained by performing the dynamic oscillations at increasing cantilever-substrate separations, black. Experiments on top of a nucleus, gray, show that it does not impact the drag forces measured. The drag coefficient decreases when the cantilever is further away from the substrate, as expected [179]. The standard errors are displayed in Table 6.3 but not shown to facilitate the comparison between measurements on bare substrate and on nuclei.*

This step allowed me to estimate that the nucleus has only a small effect on the drag forces felt by the cantilever, see Figure 6.15. The corrections needed can then be parametrised from the drag measurements from the substrate only. It should be noted that here the drag coefficients include also the effect of the electronics lags.

Correction from the drag forces

To effectively correct the measurements on nuclei for the drag, I parametrised its effect with respect to the cantilever-substrate distance. To do so, I performed dynamic oscillations at various cantilever-substrate distances. For each distance and frequency, I calculated the phase shift between driving and deflection signals as well as the ratio:

$$\frac{K_{drag}(h, f_i)}{k_c} = \frac{|\hat{d}_{drag}(h, f_i)|}{|\hat{z}_{drag}(h, f_i)| - |\hat{d}_{drag}(h, f_i)|} \tag{6.12}$$

with $K_{drag}(f_i)$ the apparent stiffness measured because of the drag forces normalised with the spring constant of the cantilever. Since no nuclei were present on the substrate, these values were only the effect of the viscous behaviour of the liquid and the electronics.

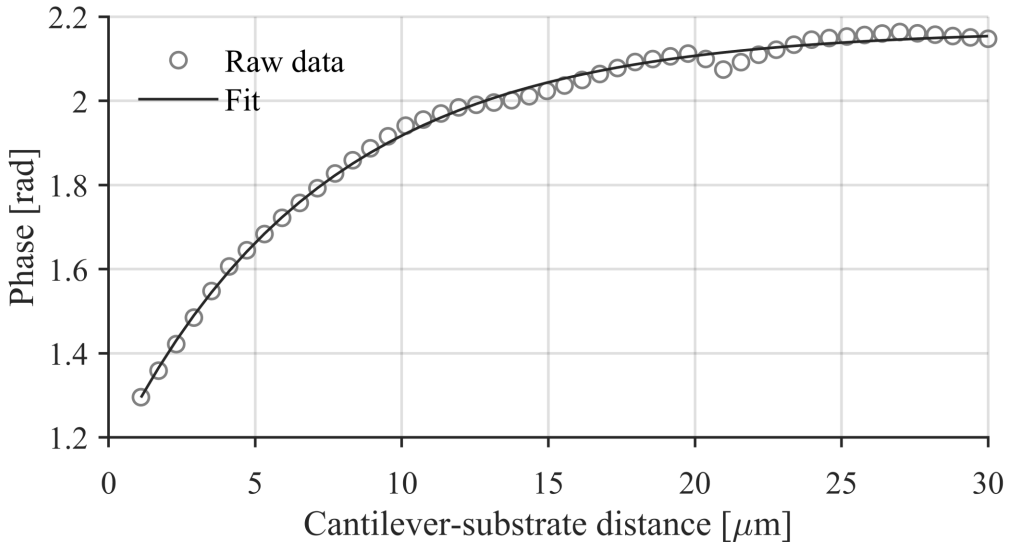

Figure 6.16: Phase shift fitting. *An example of the phase shift fitting for a frequency of oscillation of* 700 Hz*. The fit, in black, gave an adjusted* $\chi^2 > 0.99$*.*

Then, the phase shift and the normalised apparent stiffness *versus* f_i curves were parametrised with respect to the cantilever-substrate distance, h, using a generic function $y(h) = A + B \cdot \exp(C \cdot h) + D \cdot \exp(E \cdot h)$ where A,B,C,D, E are unknown parameters. The latter were estimated with the robust bisquare option from the non linear regression function *nlinfit* and iterative least square minimisation. The initial guesses for the parameters were $[0.1; -0.1; 100; -0.1; 100]$ and $[0.1; 0.1; 5 \cdot 10^5; 0.1; 5 \cdot 10^4]$ for the phase shift and normalised apparent stiffness curves respectively. I computed the adjusted χ^2 value for each fit. Figure 6.16 shows an example of the fitting result of the phase shift with the generic function. Table 6.4 resumes the fitting parameters found and goodness of fits. The fits were rather difficult at low frequencies, adjusted $\chi^2 \ll 0.99$, especially in the case of the phase shift. However, they were robust enough in the majority of the cases, adjusted $\chi^2 > 0.99$ in 65 % cases, and for the sake of reproducibility, I kept all fitting results.
Alcaraz et al. [179] estimated that a mechanical transfer function, $H(f_i)$, can be written as the ratio between the Fourier transformation of the force measured, $\hat{F}$, and the indentation, δ, such as $H(f_i) = \hat{F}(f_i)/\delta(f_i)$, with respect to the frequency of oscillation, f_i. The mechanical transfer function of the nuclei, $H_n(f_i)$ equals then:

$$H_n(f_i) = H(f_i) - H_{drag}(f_i) \tag{6.13}$$

with $H(f_i)$ the uncorrected transfer function measured and $H_{drag}(f_i)$ the effect from the drag forces.

Table 6.4: Drag parametrisation. *The coefficients were estimated using a robust bisquare option of the non linear regression. The adjusted χ^2 is also shown as goodness of fit parameter.*

Phase shift $\Delta\theta_{drag}(f_i)$

Frequency [Hz]	**A** [rad]	**B** [rad]	**C** [m^{-1}]	**D** [rad]	**E** [m^{-1}]	χ^2
1	1.74	−1.53	67788.22	−1.53	67748.23	0.43
3	2.80	−0.85	−3024.43	−0.85	−3387.80	0.33
10	1.56	−0.04	133736.25	−0.04	133664.64	0.17
30	2.42	−0.83	−2381.25	−0.07	153955.41	0.12
60	1.65	−0.08	159478.88	−0.08	159562.32	0.86
100	18.53	−16.95	252.21	−0.37	679738.22	0.84
200	2.02	−0.19	362838.04	−0.43	44583.73	0.99
250	2.63	−0.77	4059.67	−0.47	124388.01	0.99
350	2.27	−0.45	193047.02	−0.56	19935.43	0.99
400	2.06	−0.69	78597.05	−0.15	509603.12	0.99
500	2.00	−0.43	128749.04	−0.43	128752.51	0.99
600	3.46	−0.91	163776.58	−1.48	2262.96	0.99
700	2.42	−0.37	12742.82	−0.93	164320.21	0.99

Normalised apparent stiffness $K_{drag}(f_i)/k_c$

Frequency [Hz]	**A** [rad]	**B** [rad]	**C** [m^{-1}]	**D** [rad]	**E** [m^{-1}]	χ^2
1	−0.00	−0.00	2146500.31	0.00	46069.73	0.73
3	0.44	0.00	27334159.30	−0.44	−190.30	0.64
10	0.06	−0.03	−4880.42	−0.02	−4858.19	0.67
30	−0.06	0.07	2331.21	0.04	288422.97	0.99
60	−0.08	0.10	3231.45	0.09	285915.59	0.99
100	−0.19	0.17	289619.35	0.23	2198.65	0.99
200	−0.01	0.34	311084.59	0.09	16137.71	0.99
250	−0.06	0.48	305684.05	0.15	7877.71	0.99
350	0.05	0.68	330237.10	0.10	32447.33	0.99
400	−0.41	0.85	318609.02	0.56	3101.35	0.99
500	0.12	1.48	417272.80	0.20	74511.21	0.99
600	0.16	1.81	438628.44	0.23	87213.75	0.99
700	0.23	0.51	147081.14	2.80	549218.25	0.99

During the data analysis, I extracted separately the phase shift, $\Delta\theta(f_i)$, and the apparent stiffness, $K(f_i)$, of the overall behaviour of the cantilever (thus it included the effect of drag but also the effect of the nucleus):

$$K(f_i) = \frac{|\hat{F}(f_i)|}{\delta(f_i)} = k_c \cdot \frac{|\hat{d}(f_i)|}{|\hat{z}(f_i)| - |\hat{d}(f_i)|} \tag{6.14}$$

These values were mapped to polar coordinates. To make the correction simple, they were transformed into Cartesian coordinates:

$$x = K(f_i) \cdot cos\big(\Delta\theta(f_i)\big) \tag{6.15}$$

$$y = K(f_i) \cdot sin\big(\Delta\theta(f_i)\big) \tag{6.16}$$

using the *pol2cart* function.

In parallel, I calculated the corresponding phase shift and the normalised apparent stiffness from the drag, thanks to the parametrisation of the drag effect with respect to the frequency and cantilever-substrate distance, at the distance cantilever-substrate defined as the nucleus height minus the indentation depth, and transformed them as well into Cartesian coordinates, x_{drag} and y_{drag}.

The corrected values, in polar coordinates, were defined as:

$$x_{corrected} = x - x_{drag} \tag{6.17}$$

$$y_{corrected} = y - y_{drag} \tag{6.18}$$

and transformed back into polar coordinates with *cart2pol*, giving the values $\Delta\theta_{corrected}(f_i)$ and $K_{corrected}(f_i) = |\hat{F}_{corrected}(f_i)|/\delta_{corrected}(f_i)$ corrected from the effect of drag and electronics lags.

Then, I assumed that while the forces during the experiments were not constant, the indentation depth at which they were conducted was. Thus:

$$\delta_{corrected}(f_i) = \delta(f_i) \tag{6.19}$$

and

$$F_{corrected}(f_i) = K_{corrected}(f_i) \cdot \delta(f_i) \tag{6.20}$$

$F_{corrected}(f_i)$ and $\Delta\theta_{corrected}(f_i)$ were used to calculate the dynamic modulus of the nuclei.

Appendix II: Individual elastic and viscous responses

The following figures show the nuclei response of each cell line (mean ± s.e.m of the log transformed data (shaded area)). I recall that the elastic modulus, $E'(f_i)$, and the viscous modulus, $E"(f_i)$, are given by $E'(f_i) = E^*(f_i) \cdot \cos\left(\Delta\theta_{corrected}(f_i)\right)$ and $E"(f_i) = E^*(f_i) \cdot \sin\left(\Delta\theta_{corrected}(f_i)\right)$. See section 6.3 for more details.

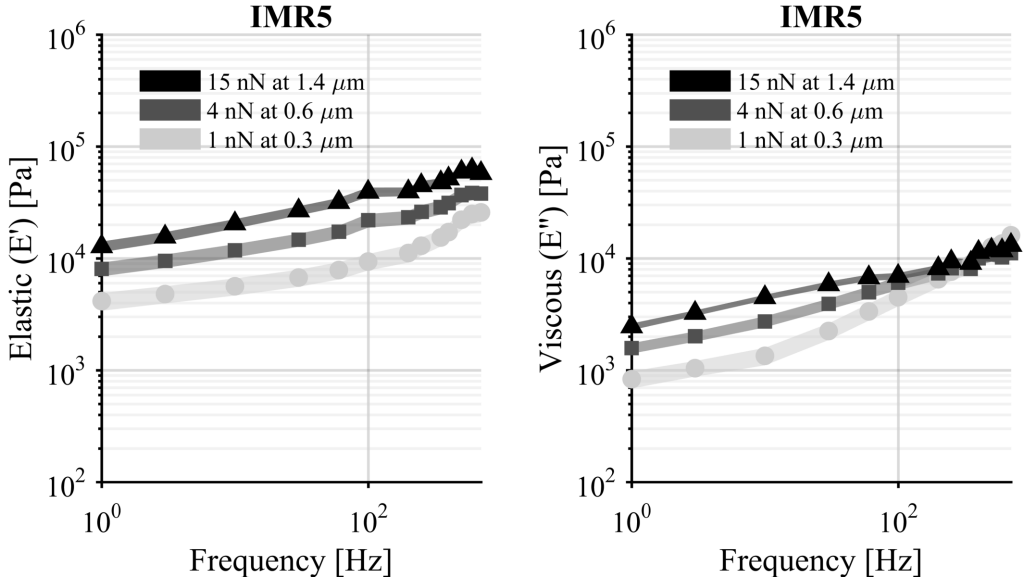

Figure 6.17: The elastic (E') and viscous ($E"$) response of the IMR5 nuclei. *These were the smallest nuclei probed and showed the stiffest response.*

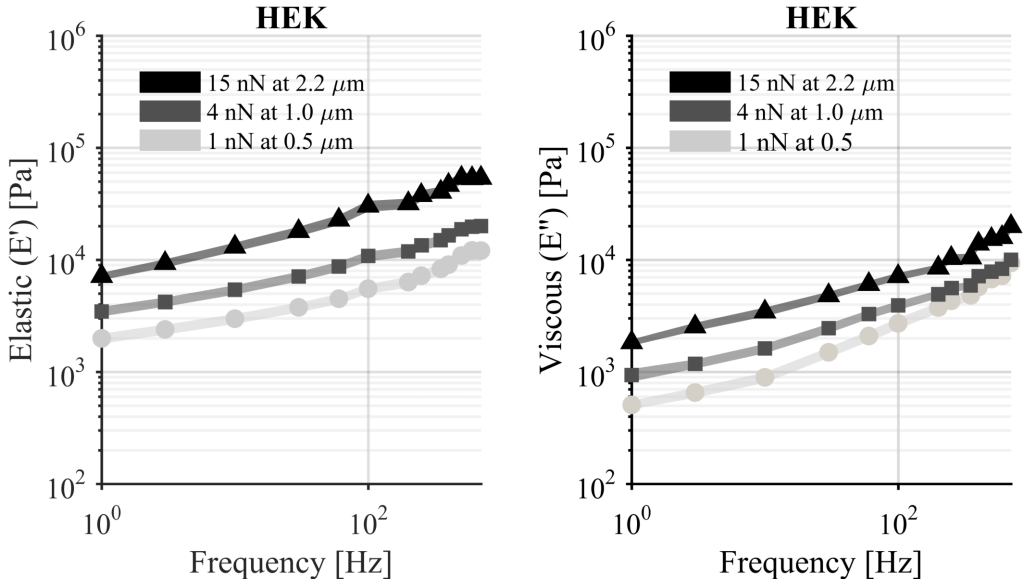

Figure 6.18: The elastic (E') and viscous ($E"$) response of the HEK nuclei.

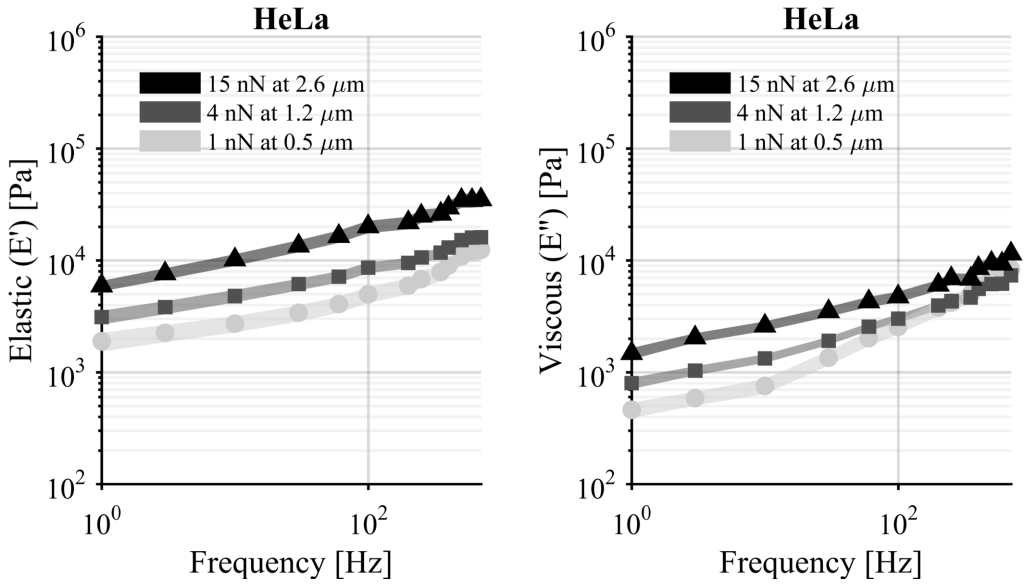

Figure 6.19: The elastic (E′) and viscous (E”) response of the HeLa nuclei.

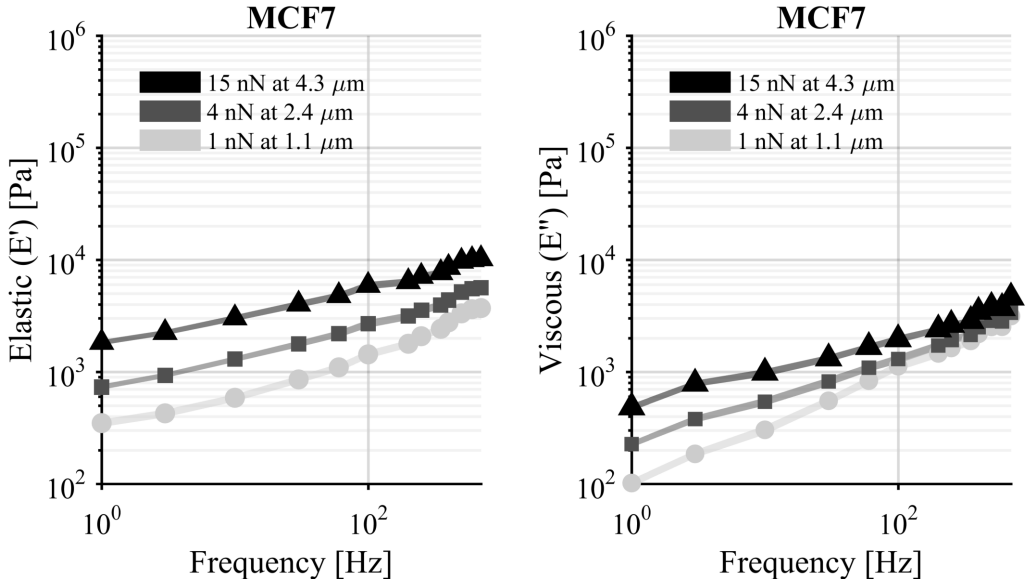

Figure 6.20: The elastic (E′) and viscous (E”) response of the MCF7 nuclei. *These were the biggest nuclei probed and showed the softest response.*

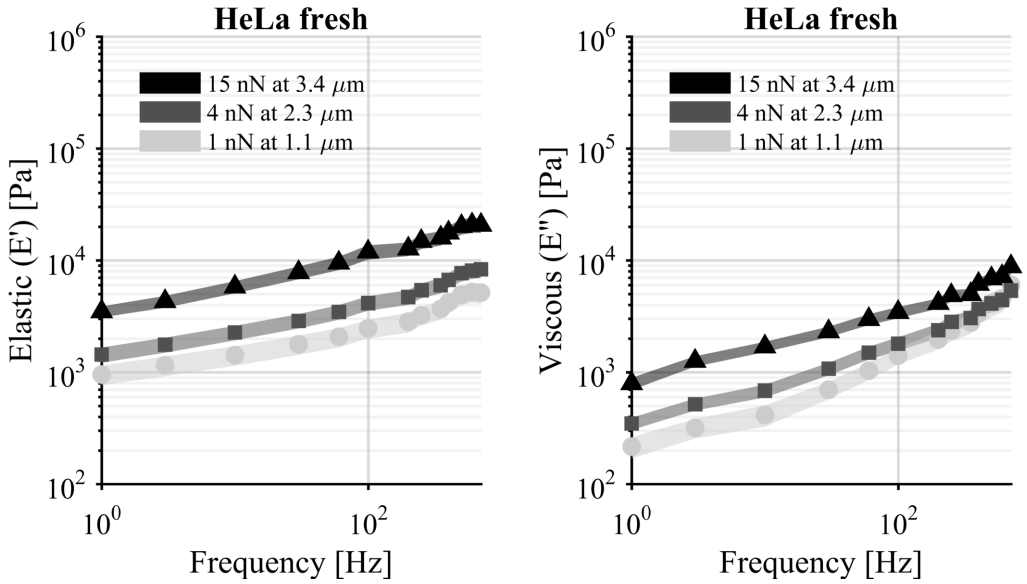

Figure 6.21: Frequency dependent elastic response of fresh HeLa nuclei. *HeLa fresh nuclei were directly investigated after isolation to avoid storage at* −80 °C.

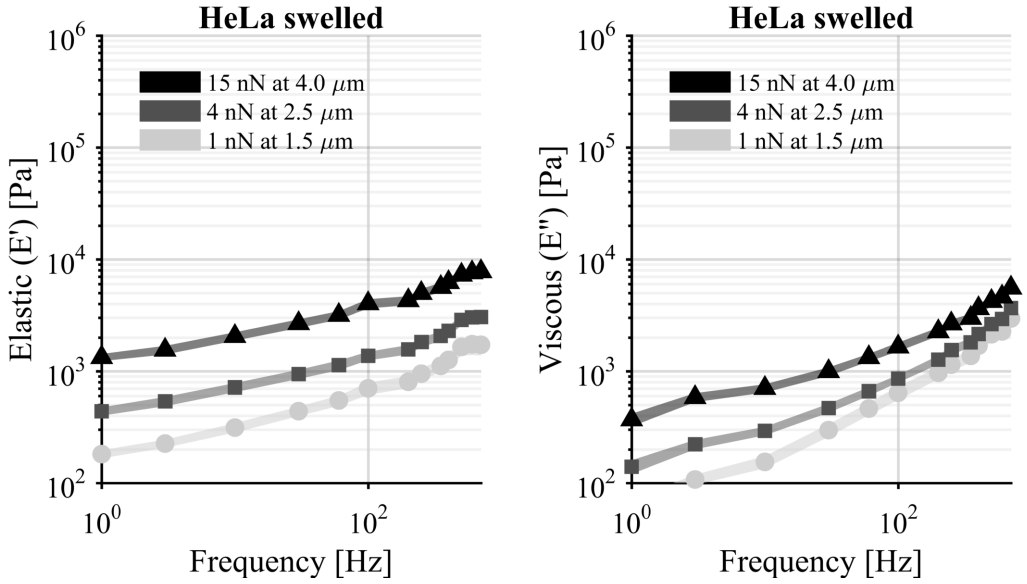

Figure 6.22: Frequency dependent elastic response of swelled HeLa nuclei. *HeLa swelled nuclei were HeLa nuclei, previously stored at* −80 °C, *which were subjected to hypotonic conditions to induce osmotic swelling.*

Bibliography

[1] G. Elgozy. *L'esprit des mots ou l'antidictionnaire*. Denoël, 1981.

[2] National Center for Biotechnology Information. U. S. National Library of Medicine . https://www.ncbi.nlm.nih.gov/pubmed/, 2018. [Online; accessed 14-April-2018].

[3] G. Binnig, C. F. Quate, and C. Gerber. Atomic Force Microscope. *Phys. Rev. Lett.*, 56(9):930–933, March 1986.

[4] S. W. Schneider, K. C. Sritharan, J. P. Geibel, H. Oberleithner, and B. P. Jena. Surface dynamics in living acinar cells imaged by atomic force microscopy: Identification of plasma membrane structures involved in exocytosis. *Proceedings of the National Academy of Sciences of the United States of America*, 94(1):316–321, January 1997.

[5] B. Jena. *Methods in nano cell biology. Preface*, volume 90. Elsevier, February 2008.

[6] M. L. Casem. Endocytosis. In *Case studies in cell biology*, pages 217–240. Academic Press, Boston, 2016.

[7] J. Rosenbluth and S. L. Wissig. The distribution of exogenous ferritin in toad sprinal ganglia and the mechanism of its uptake by neurons. *The Journal of Cell Biology*, 23(2):307–325, November 1964.

[8] B. M. Pearse. Clathrin: a unique protein associated with intracellular transfer of membrane by coated vesicles. *Proceedings of the National Academy of Sciences of the United States of America*, 73(4):1255–1259, April 1976.

[9] T. Kirchhausen and S. C. Harrison. Protein organization in clathrin trimers. *Cell*, 23(3):755–761, March 1981.

[10] M. L. Ferguson, K. Prasad, H. Boukari, D. L. Sackett, S. Krueger, E. M. Lafer, and

R. Nossal. Clathrin triskelia show evidence of molecular flexibility. *Biophysical Journal*, 95(4):1945–1955, August 2008.

[11] A. Fotin, Y. Cheng, P. Sliz, N. Grigorieff, S. C. Harrison, T. Kirchhausen, and T. Walz. Molecular model for a complete clathrin lattice from electron cryomicroscopy. *Nature*, 432:573, October 2004.

[12] M. Ehrlich, W. Boll, A. van Oijen, R. Hariharan, K. Chandran, M. L. Nibert, and T. Kirchhausen. Endocytosis by random initiation and stabilization of clathrin-coated pits. *Cell*, 118(5):591–605, September 2004.

[13] P. N. Dannhauser, M. Platen, H. Böning, H. Ungewickell, I. A. T. Schaap, and E. J. Ungewickell. Effect of clathrin light chains on the stiffness of clathrin lattices and membrane budding. *Traffic*, 16(5):519–533, April 2015.

[14] A. Bado, S. Levasseur, S. Attoub, S. Kermorgant, J. Laigneau, M. Bortoluzzi, L. Moizo, T. Lehy, M. Guerre-Millo, Y. Le Marchand-Brustel, and M. J. M. Lewin. The stomach is a source of leptin. *Nature*, 394:790, August 1998.

[15] R. Nossal. Energetics of clathrin basket assembly. *Traffic*, 2(2):138–147, May 2002.

[16] P. N. Dannhauser and E. J. Ungewickell. Reconstitution of clathrin-coated bud and vesicle formation with minimal components. *Nature Cell Biology*, 14:634, April 2012.

[17] M. Mettlen and G. Danuser. Imaging and modeling the dynamics of clathrin-mediated endocytosis. *Cold Spring Harbor perspectives in biology*, 6(12):a017038–a017038, 2014.

[18] A. J. S. Ribeiro, P. Khanna, A. Sukumar, C. Dong, and K. N. Dahl. Nuclear stiffening inhibits migration of invasive melanoma cells. *Cellular and Molecular Bioengineering*, 7(4):544–551, December 2014.

[19] D. Egecioglu and J. H. Brickner. Gene positioning and expression. *Nucleus and gene expression*, 23(3):338–345, June 2011.

[20] M. L. Gardel, J. H. Shin, F. C. MacKintosh, L. Mahadevan, P. Matsudaira, and D. A. Weitz. Elastic behavior of cross-linked and bundled actin networks. *Science*, 304(5675):1301, May 2004.

[21] K. N. Dahl, A. J. S. Ribeiro, and J. Lammerding. Nuclear shape, mechanics, and mechanotransduction. *Circulation Research*, 102(11):1307–1318, May 2008.

[22] M. Le Berre, J. Aubertin, and M. Piel. *Fine control of nuclear confinement identifies a threshold deformation leading to lamina rupture and induction of specific genes*, volume 4. The Royal Society of Chemistry, October 2012.

[23] A. A. Michelson and E. W. Morley. On the relative motion of the Earth and the luminiferous ether. *American Journal of Science*, Series 3 Vol. 34(203):333–345, November 1887.

[24] J. H. Scofield. Frequency domain description of a lock-in amplifier. *American Journal of Physics*, 62(2):129–133, February 1994.

[25] J. V. Lauritsen and M. Reichling. Atomic resolution non-contact atomic force microscopy of clean metal oxide surfaces. *Journal of Physics: Condensed Matter*, 22(26):263001, 2010.

[26] Y. Namai, K. Fukui, and Y. Iwasawa. Atom-resolved non-contact Atomic Force Microscopic observations of CeO2(111) surfaces with different oxidation states: surface structure and behavior of surface oxygen atoms. *The Journal of Physical Chemistry B*, 107(42):11666–11673, October 2003.

[27] G. G. Stokes. On the change of refrangibility of light. *Phil Trans R Soc*, 142: 463–562, 1852.

[28] K. N Fish. Total Internal Reflection Fluorescence (TIRF) microscopy. *Current protocols in cytometry / editorial board, J. Paul Robinson, managing editor . . . [et al.]*, 0 12:Unit12. 18–Unit12. 18, October 2009.

[29] R. B. Sekar and A. Periasamy. Fluorescence resonance energy transfer (FRET) microscopy imaging of live cell protein localizations. *The Journal of Cell Biology*, 160(5):629–633, March 2003.

[30] L. Riachy, D. El Arawi, R. Jaffiol, and C. Vézy. Nanometer-Scale Resolution Achieved with Nonradiative Excitation. *ACS Photonics*, 5(6):2217–2224, June 2018.

[31] E. Betzig, G. H. Patterson, R. Sougrat, O. W. Lindwasser, S. Olenych, J. S. Bonifacino, M. W. Davidson, J. Lippincott-Schwartz, and H. F. Hess. Imaging Intracellular

Fluorescent Proteins at Nanometer Resolution. *Science*, 313(5793):1642, September 2006.

[32] M. Bates, S. A. Jones, and X. Zhuang. Stochastic Optical Reconstruction Microscopy (STORM): A method for superresolution fluorescence imaging. *Cold Spring Harbor Protocols*, 2013(6):pdb.top075143, June 2013.

[33] S. W. Hell and J. Wichmann. Breaking the diffraction resolution limit by stimulated emission: stimulated-emission-depletion fluorescence microscopy. *Optics letters*, 19(11):780–782, June 1994.

[34] S. T. Hess, T. P. K. Girirajan, and M. D. Mason. Ultra-High Resolution Imaging by Fluorescence Photoactivation Localization Microscopy. *Biophysical Journal*, 91 (11):4258–4272, December 2006.

[35] H. R. Hertz. Über die Berührung fester elastischer Körper und über die Härte. *Verhandlungen des Vereins zur Beförderung des Gewerbfleißes, Berlin : Verein zur Beförderung des Gewerbefleisses*, 1882:449–463, 2006.

[36] D. J. Webb and C. M. Brown. Epi-Fluorescence Microscopy. *Methods in molecular biology (Clifton, N. J.)*, 931:29–59, 2013.

[37] I. A. T. Schaap, C. Carrasco, P. J. de Pablo, F. C. MacKintosh, and C. F. Schmidt. Elastic response, buckling, and instability of microtubules under radial indentation. *Biophysical Journal*, 91(4):1521–1531, August 2006.

[38] S. Nawaz, P. Sánchez, K. Bodensiek, S. Li, M. Simons, and I. A. T. Schaap. Cell visco-elasticity measured with AFM and optical trapping at sub-micrometer deformations. *PLOS ONE*, 7(9):e45297, September 2012.

[39] S. Bhattacharyya, Warfield. K. L., G. T. Ruthel, S. Bavari, M. J. Aman, and T. J. Hope. Ebola virus uses clathrin-mediated endocytosis as an entry pathway. *Virology*, 401 1:18–28, 2010.

[40] J. B. Pethica and W. C. Oliver. Tip surface interactions in STM and AFM. *Physica Scripta*, 1987(T19A):61, 1987.

[41] M. Kasha and G. A. Crosby. Quantum chemistry: An introduction (Kauzmann, Walter). *Journal of Chemical Education*, 34(9):A412, September 1957.

[42] B. W. Ninham and V. A. Parsegian. van der Waals forces: Special characteristics

in lipid-water systems and a general method of calculation based on the Lifshitz theory. *Biophysical Journal*, 10(7):646–663, July 1970.

[43] R. A. Buckingham. The classical equation of state of gaseous helium, neon and argon. *Proceedings of the Royal Society of London. Series A. Mathematical and Physical Sciences*, 168(933):264, October 1938.

[44] Y. F. Dufrêne, T. Ando, R. Garcia, D. Alsteens, D. Martinez-Martin, A. Engel, C. Gerber, and D. J. Müller. Imaging modes of atomic force microscopy for application in molecular and cell biology. *Nature Nanotechnology*, 12:295, April 2017.

[45] N. Jalili and K. Laxminarayana. A review of atomic force microscopy imaging systems: application to molecular metrology and biological sciences. *Mechatronics*, 14(8):907–945, October 2004.

[46] R. Garcia and R. Perez. Dynamic atomic force microscopy methods. *Surface Science Reports*, 47(6):197–301, September 2002.

[47] J. Portoles, P. Cumpson, J. Hedley, S. Allen, P. Williams, and S. Tendler. Accurate velocity measurements of AFM-cantilever vibrations by Doppler interferometry. *J. Experimental Nanoscience*, 1(1):51–62, March 2006.

[48] A. Raman, J. Melcher, and R. Tung. Cantilever dynamics in atomic force microscopy. *Nano Today*, 3(1):20–27, February 2008.

[49] O. A. Bauchau and J. I. Craig. Euler-Bernoulli beam theory. In O. A. Bauchau and J. I. Craig, editors, *Structural Analysis*, pages 173–221. Springer Netherlands, Dordrecht, 2009.

[50] H. J. Butt and M. Jaschke. Calculation of thermal noise in atomic force microscopy. *Nanotechnology*, 6(1):1, 1995.

[51] B. Voigtländer. *Frequency modulation (FM) mode in dynamic Atomic Force Microscopy—non-contact Atomic Force Microscopy*. Springer Berlin Heidelberg, Berlin, Heidelberg, 2015.

[52] C. Vančura, I. Dufour, S. M. Heinrich, F. Josse, and A. Hierlemann. Analysis of resonating microcantilevers operating in a viscous liquid environment. *Sensors and Actuators A: Physical*, 141(1):43–51, January 2008.

[53] D. Kiracofe and A. Raman. On eigenmodes, stiffness, and sensitivity of atomic force microscope cantilevers in air versus liquids. *Journal of Applied Physics*, 107 (3):033506, February 2010.

[54] C. Rankl, V. Pastushenko, F. Kienberger, C. M Stroh, and P. Hinterdorfer. Hydrodynamic damping of a magnetically oscillated cantilever close to a surface. *Proceedings of the Fifth International Conference on Scanning Probe Micrscopy, Sensors and Nanostructures*, 100(3):301–308, August 2004.

[55] M. H. Korayem and N. Ebrahimi. Nonlinear dynamics of tapping-mode atomic force microscopy in liquid. *Journal of Applied Physics*, 109(8):084301, April 2011.

[56] C. A. J. Putman, B. G. De Grooth, N. F. Van Hulst, and J. Greve. A detailed analysis of the optical beam deflection technique for use in atomic force microscopy. *Journal of Applied Physics*, 72(1):6–12, July 1992.

[57] R. Wolfson. The lock-in amplifier: A student experiment. *American Journal of Physics*, 59(6):529–572, June 1991.

[58] M. Freeman. Feedback control of intercellular signalling in development. *Nature*, 408:313, November 2000.

[59] J. Aué and J. T. M. De Hosson. Influence of atomic force microscope tip–sample interaction on the study of scaling behavior. *Applied Physics Letters*, 71(10):1347–1349, September 1997.

[60] C. Wong, P. West, K. Olson, M. Mecartney, and N. Starostina. *Tip dilation and AFM capabilities in the characterization of nanoparticles*, volume 59. JOM: the journal of the Minerals, Metals & Materials Society, May 2007.

[61] J. E. Sader, J. W. M. Chon, and P. Mulvaney. Calibration of rectangular atomic force microscope cantilevers. *Review of Scientific Instruments*, 70(10):3967–3969, September 1999.

[62] J. L. Hutter and J. Bechhoefer. Calibration of atomic force microscope tips. *Review of Scientific Instruments*, 64(7):1868–1873, July 1993.

[63] N. A. Burnham, X. Chen, C. S. Hodges, G. A. Matei, E. J. Thoreson, C. J. Roberts, M. C. Davies, and S. J. B. Tendler. Comparison of calibration methods for atomic-force microscopy cantilevers. *Nanotechnology*, 14(1):1, 2003.

[64] D. R. Baselt and J. D. Baldeschwieler. Imaging spectroscopy with the atomic force microscope. *Journal of Applied Physics*, 76(1):33–38, July 1994.

[65] M. Radmacher, J. P. Cleveland, M. Fritz, H. G. Hansma, and P. K. Hansma. Mapping interaction forces with the atomic force microscope. *Biophysical Journal*, 66(6): 2159–2165, June 1994.

[66] N. H Green, S. Allen, M. C. Davies, C. J. Roberts, S. J. B. Tendler, and P. M. Williams. Force sensing and mapping by atomic force microscopy. *TrAC Trends in Analytical Chemistry*, 21(1):65–74, January 2002.

[67] K. R. Symon. *Mechanics*. Addison-Wesley world student series edition. Addison-Wesley Publishing Company, 1970.

[68] F. Eghiaian and I. A. T. Schaap. Structural and dynamic characterization of biochemical processes by atomic force microscopy. In Gregory I. Mashanov and Christopher Batters, editors, *Single Molecule Enzymology: Methods and Protocols*, pages 71–95. Humana Press, Totowa, NJ, 2011.

[69] R. S. Gates, M. G. Reitsma, J. A. Kramar, and J. R. Pratt. Atomic Force Microscope cantilever flexural stiffness calibration: Toward a standard traceable method. *Journal of Research of the National Institute of Standards and Technology*, 116(4): 703–727, 2011.

[70] J. E. Sader. Frequency response of cantilever beams immersed in viscous fluids with applications to the atomic force microscope. *Journal of Applied Physics*, 84 (1):64–76, June 1998.

[71] J. E. Sader, J. Pacifico, C. P. Green, and P. Mulvaney. General scaling law for stiffness measurement of small bodies with applications to the atomic force microscope. *Journal of Applied Physics*, 97(12):124903, June 2005.

[72] S. M. Cook, T. E. Schäffer, K. M. Chynoweth, M. Wigtonm, R. M. Simmonds, and K. M. Lang. Practical implementation of dynamic methods for measuring atomic force microscope cantilever spring constants. *Nanotechnology*, 17(9):2135, 2006.

[73] R. Proksch, T. E. Schäffer, J. P. Cleveland, R. C. Callahan, and M. B. Viani. Finite optical spot size and position corrections in thermal spring constant calibration. *Nanotechnology*, 15(9):1344, 2004.

[74] N. P. D'Costa and J. H. Hoh. Calibration of optical lever sensitivity for atomic force microscopy. *Review of Scientific Instruments*, 66(10):5096–5097, October 1995.

[75] M. J. Higgins, R. Proksch, J. E. Sader, M. Polcik, S. Mc Endoo, J. P. Cleveland, and S. P. Jarvis. Noninvasive determination of optical lever sensitivity in atomic force microscopy. *Review of Scientific Instruments*, 77(1):013701, January 2006.

[76] A. Roters and D. Johannsmann. Distance-dependent noise measurements in scanning force microscopy. *Journal of Physics: Condensed Matter*, 8(41):7561, 1996.

[77] J. L. Hutter. Comment on tilt of Atomic Force Microscope cantilevers: Effect on spring constant and adhesion measurements. *Langmuir*, 21(6):2630–2632, March 2005.

[78] J. E. Sader, J. Lu, and P. Mulvaney. Effect of cantilever geometry on the optical lever sensitivities and thermal noise method of the atomic force microscope. *Review of Scientific Instruments*, 85(11):113702, November 2014.

[79] M. L. Meade. Advances in lock-in amplifiers. *Journal of Physics E: Scientific Instruments*, 15(4):395, 1982.

[80] Asylum research Oxford instruments. Getreal automated probe calibration, November 2013.

[81] F. M. Brodsky. Diversity of clathrin function: New tricks for an old protein. *Annual Review of Cell and Developmental Biology*, 28(1):309–336, October 2012.

[82] X. Sun, V. K. Yau, B. J. Briggs, and G. R. Whittaker. Role of clathrin-mediated endocytosis during vesicular stomatitis virus entry into host cells. *Virology*, 338 (1):53–60, July 2005.

[83] P. N. Dannhauser and E. J. Ungewickell. Reconstitution of clathrin-coated bud and vesicle formation with minimal components. *Nature Cell Biology*, 14:634, April 2012.

[84] E. Ungewickell, H. Ungewickell, S. E. H. Holstein, R. Lindner, K. Prasad, W. Barouch, B. Martini, L. E. Greene, and E. Eisenberg. Role of auxilin in uncoating clathrin-coated vesicles. *Nature*, 378:632, December 1995.

[85] W. Helfrich. *Elastic properties of lipid bilayers: Theory and possible experiments*, volume 28. Zeitschrift fur Naturforschung C, December 1973.

[86] A. J. Jin and R. Nossal. Rigidity of triskelion arms and clathrin nets. *Biophysical Journal*, 78(3):1183–1194, March 2000.

[87] M. G. J. Ford, I. G. Mills, B. J. Peter, Y. Vallis, G. J. K. Praefcke, P. R. Evans, and H. T. McMahon. Curvature of clathrin-coated pits driven by epsin. *Nature*, 419: 361, September 2002.

[88] H. T. McMahon and J. L. Gallop. Membrane curvature and mechanisms of dynamic cell membrane remodelling. *Nature*, 438:590, November 2005.

[89] B. M. Pearse. Clathrin: a unique protein associated with intracellular transfer of membrane by coated vesicles. *Proceedings of the National Academy of Sciences of the United States of America*, 73(4):1255–1259, April 1976.

[90] T. F. Roth and K. R. Porter. Yolk protein uptake in the oocyte of the mosquito aedes aegyptil. *The Journal of Cell Biology*, 20(2):313–332, February 1964.

[91] J. Zimmerberg and M. M. Kozlov. How proteins produce cellular membrane curvature. *Nature Reviews Molecular Cell Biology*, 7:9, November 2005.

[92] J. C. Stachowiak, F. M. Brodsky, and E. A. Miller. A cost–benefit analysis of the physical mechanisms of membrane curvature. *Nature Cell Biology*, 15:1019, September 2013.

[93] H. T. McMahon and E. Boucrot. Membrane curvature at a glance. *Journal of Cell Science*, 128(6):1065, March 2015.

[94] J. C. Stachowiak, E. M. Schmid, C. J. Ryan, H. S. Ann, D. Y. Sasaki, M. B. Sherman, P. L. Geissler, D. A. Fletcher, and C. C. Hayden. Membrane bending by protein–protein crowding. *Nature Cell Biology*, 14:944, August 2012.

[95] S. Li, C. Sieben, K. Ludwig, C. T. Höfer, S. Chiantia, A. Herrmann, F. Eghiaian, and I. A. T. Schaap. ph-controlled two-step uncoating of influenza virus. *Biophysical Journal*, 106(7):1447–1456, April 2014.

[96] J. D. Wilbur, P. K. Hwang, J. A. Ybe, M. Lane, B. D. Sellers, M. P. Jacobson, R. J. Fletterick, and F. M. Brodsky. Conformation switching of clathrin light chain regulates clathrin lattice assembly. *Developmental Cell*, 18(5):854–861, May 2010.

[97] E. Ungewickell and H. Ungewickell. Bovine brain clathrin light chains impede heavy

chain assembly in vitro. *Journal of Biological Chemistry*, 266(19):12710–12714, July 1991.

[98] A. Young, S. Stoilova-McPhie, A. Rothnie, Y. Vallis, P. Harvey-Smith, N. Ranson, H. Kent, F. M. Brodsky, B. M. F. Pearse, A. Roseman, and C. J. Smith. Hsc70-induced changes in clathrin-auxilin cage structure suggest a role for clathrin light chains in cage disassembly. *Traffic (Copenhagen, Denmark)*, 14(9):987–996, September 2013.

[99] S. Zaremba and J. H. Keen. Assembly polypeptides from coated vesicles mediate reassembly of unique clathrin coats. *The Journal of Cell Biology*, 97(5):1339, November 1983.

[100] A. J. Jin, K. Prasad, P. D. Smith, E. M. Lafer, and R. Nossal. Measuring the elasticity of clathrin-coated vesicles via atomic force microscopy. *Biophysical Journal*, 90 (9):3333–3344, May 2006.

[101] B. M. F. Peaese. On the structural and functional components of coated vesicles. *Journal of Molecular Biology*, 126(4):803–812, December 1978.

[102] J. H. Keen, M. C. Willingham, and I. H. Pastan. Clathrin-coated vesicles: Isolation, dissociation and factor-dependent reassociation of clathrin baskets. *Cell*, 16(2): 303–312, February 1979.

[103] S. Ahle, A. Mann, U. Eichelsbacher, and E. J. Ungewickell. Structural relationships between clathrin assembly proteins from the Golgi and the plasma membrane. *The EMBO Journal*, 7(4):919–929, April 1988.

[104] F. K. Winkler and K. K. Stanley. Clathrin heavy chain, light chain interactions. *The EMBO Journal*, 2(8):1393–1400, 1983.

[105] I. A. T. Schaap, F. Eghiaian, A. des Georges, and C. Veigel. Effect of envelope proteins on the mechanical properties of influenza virus. *The Journal of Biological Chemistry*, 287(49):41078–41088, November 2012.

[106] I. L. Ivanovska, P. J. de Pablo, B. Ibarra, G. Sgalari, F. C. MacKintosh, J. L. Carrascosa, C. F. Schmidt, and G. J. L. Wuite. Bacteriophage capsids: Tough nanoshells with complex elastic properties. *Proceedings of the National Academy of Sciences of the United States of America*, 101(20):7600–7605, May 2004.

[107] P. Wriggers, T. Vu Van, and E. Stein. Finite element formulation of large deformation impact-contact problems with friction. *Computers & Structures*, 37(3):319–331, January 1990.

[108] L. D. Landau. *Theory of elasticity*. Course of theoretical physics ; 7. Pergamon, London, 1959.

[109] A. Ortega-Esteban, K. Bodensiek, C. San Martín, M. Suomalainen, U. F. Greber, P. J. de Pablo, and I. A. T. Schaap. Fluorescence tracking of genome release during mechanical unpacking of single viruses. *ACS Nano*, 9(11):10571–10579, November 2015.

[110] H. A. Sturges. The Choice of a Class Interval. *Journal of the American Statistical Association*, 21(153):65–66, March 1926.

[111] E. J. Ungewickell and D. Branton. Assembly units of clathrin coats. *Nature*, 289: 420, January 1981.

[112] S. Li, F. Eghiaian, C. Sieben, A. Herrmann, and I. A. T. Schaap. Bending and puncturing the influenza lipid envelope. *Biophysical Journal*, 100(3):637–645, February 2011.

[113] M. Marchetti, G. J. L. Wuite, and W. H. Roos. Atomic force microscopy observation and characterization of single virions and virus-like particles by nano-indentation. *Antiviral strategies, Virus structure and expression*, 18:82–88, June 2016.

[114] R. A. Crowther and B. M. Pearse. Assembly and packing of clathrin into coats. *The Journal of Cell Biology*, 91(3):790, December 1981.

[115] A. Fotin, Y. Cheng, P. Sliz, N. Grigorieff, S. C. Harrison, T. Kirchhausen, and T. Walz. Molecular model for a complete clathrin lattice from electron cryomicroscopy. *Nature*, 432:573, October 2004.

[116] A. Hoffmann, P. N. Dannhauser, S. Groos, L. Hinrichsen, U. Curth, and E. J. Ungewickell. A comparison of gfp tagged clathrin light chains with fluorochromated light chains in vivo and in vitro. *Traffic*, 11(9):1129–1140, August 2010.

[117] B. T. Kelly, S. C. Graham, N. Liska, P. N. Dannhauser, S. Höning, E. J. Ungewickell, and D. J. Owen. AP2 controls clathrin polymerization with a membrane-activated switch. *Science*, 345(6195):459, July 2014.

[118] I. Näthke, B. Hill, P. Parham, and F. M. Brodsky. The calcium-binding site of clathrin light chains. *Journal of Biological Chemistry*, 265, November 1990.

[119] D. E. Wakeham, L. Abi-Rached, M. C. Towler, J. D. Wilbur, P. Parham, and F. M. Brodsky. Clathrin heavy and light chain isoforms originated by independent mechanisms of gene duplication during chordate evolution. *Proceedings of the National Academy of Sciences of the United States of America*, 102(20):7209–7214, May 2005.

[120] E. J. Ungewickell. Biochemical and immunological studies on clathrin light chains and their binding sites on clathrin triskelions. *The EMBO Journal*, 2(8):1401–1408, 1983.

[121] F. K. Winkler and K. K. Stanley. Clathrin heavy chain, light chain interactions. *The EMBO Journal*, 2(8):1393–1400, 1983.

[122] C. Chen and F. M. Brodsky. Huntingtin-interacting protein 1 (Hip1) and Hip1-related protein (Hip1r) bind the conserved sequence of clathrin light chains and thereby influence clathrin assembly in vitro and actin distribution in vivo. *Journal of Biological Chemistry*, 280(7):6109–6117, February 2005.

[123] A. P. Jackson, H. Seow, N. Holmes, K. Drickamer, and P. Parham. Clathrin light chains contain brain-specific insertion sequences and a region of homology with intermediate filaments. *Nature*, 326:154, March 1987.

[124] T. Kirchhausen, S. C. Harrison, P. Parham, and F. M. Brodsky. Location and distribution of the light chains in clathrin trimers. *Proceedings of the National Academy of Sciences of the United States of America*, 80(9):2481–2485, May 1983.

[125] M. A. Senetar, S. J. Foster, and R. O. McCann. Intrasteric inhibition mediates the interaction of the I/LWEQ module proteins Talin1, Talin2, Hip1, and Hip12 with actin. *Biochemistry*, 43(49):15418–15428, December 2004.

[126] J. D. Wilbur, C. Chen, V. Manalo, P. K. Hwang, R. J. Fletterick, and F. M. Brodsky. Actin binding by Hip1 (Huntingtin-interacting protein 1) and Hip1r (Hip1-related protein) is regulated by clathrin light chain. *Journal of Biological Chemistry*, 283 (47):32870–32879, November 2008.

[127] B. L. Hill, K. Drickamer, F. M. Brodsky, and P. Parham. Identification of the

phosphorylation sites of clathrin light chain LCb. *Journal of Biological Chemistry*, 263(12):5499–5501, April 1988.

[128] C. DeLuca-Flaherty, D. B. McKay, P. Parham, and B. L. Hill. Uncoating protein (hsc70) binds a conformationally labile domain of clathrin light chain LCa to stimulate ATP hydrolysis. *Cell*, 62(5):875–887, September 1990.

[129] S. Wu, S. R. Majeed, T. M. Evans, M. D. Camus, N. M. L. Wong, Y. Schollmeier, M. Park, J. R. Muppidi, A. Reboldi, P. Parham, J. G. Cyster, and F. M. Brodsky. Clathrin light chains' role in selective endocytosis influences antibody isotype switching. *Proceedings of the National Academy of Sciences*, 113(35):9816, August 2016.

[130] D. H. Wong, M. J. Ignatius, G. Parosky, P. Parham, J. Q. Trojanowski, and F. M. Brodsky. Neuron-specific expression of high-molecular-weight clathrin light chain. *The Journal of Neuroscience*, 10(9):3025, September 1990.

[131] B. T. Kelly, S. C. Graham, N. Liska, P. N. Dannhauser, S. Höning, E. J. Ungewickell, and D. J. Owen. AP2 controls clathrin polymerization with a membrane-activated switch. *Science (New York, N. Y.)*, 345(6195):459–463, July 2014.

[132] L. M. Traub. Sorting it out: AP-2 and alternate clathrin adaptors in endocytic cargo selection. *The Journal of Cell Biology*, 163(2):203–208, October 2003.

[133] M. S. Robinson. Adaptable adaptors for coated vesicles. *Trends in Cell Biology*, 14 (4):167–174, April 2004.

[134] M. Lakadamyali, M. J. Rust, and X. Zhuang. Ligands for clathrin-mediated endocytosis are differentially sorted into distinct populations of early endosomes. *Cell*, 124(5):997–1009, March 2006.

[135] C. Chen and X. Zhuang. Epsin 1 is a cargo-specific adaptor for the clathrin-mediated endocytosis of the influenza virus. *Proceedings of the National Academy of Sciences of the United States of America*, 105(33):11790–11795, August 2008.

[136] H. Chen, S. Fre, V. I. Slepnev, M. Capua, K. Takei, M. H. Butler, P. Di Fiore, and P. De Camilli. Epsin is an EH-domain-binding protein implicated in clathrin-mediated endocytosis. *Nature*, 394:793, August 1998.

[137] M. T. Drake, M. A. Downs, and L. M. Traub. Epsin binds to clathrin by associat-

ing directly with the clathrin-terminal domain: Evidence for cooperative binding through two discrete sites. *Journal of Biological Chemistry*, 275(9):6479–6489, March 2000.

[138] T. Itoh, S. Koshiba, T. Kigawa, A. Kikuchi, S. Yokoyama, and T. Takenawa. Role of the ENTH domain in phosphatidylinositol-4,5-bisphosphate binding and endocytosis. *Science*, 291(5506):1047, February 2001.

[139] M. G. J. Ford, I. G. Mills, B. J. Peter, Y. Vallis, G. J. K. Praefcke, P. R. Evans, and H. T. McMahon. Curvature of clathrin-coated pits driven by epsin. *Nature*, 419: 361, September 2002.

[140] M. G. J. Ford, B. M. F. Pearse, M. K. Higgins, Y. Vallis, D. J. Owen, A. Gibson, C. R. Hopkins, P. R. Evans, and H. T. McMahon. Simultaneous binding of PtdIns(4,5)P_2 and clathrin by AP180 in the nucleation of clathrin lattices on membranes. *Science*, 291(5506):1051, February 2001.

[141] S. Ahle and E. J. Ungewickell. Purification and properties of a new clathrin assembly protein. *The EMBO Journal*, 5(12):3143–3149, December 1986.

[142] K. Prasad and R. E. Lippoldt. Molecular characterization of the AP180 coated vesicle assembly protein. *Biochemistry*, 27(16):6098–6104, August 1988.

[143] W. Ye and E. M. Lafer. Bacterially expressed F1-20/AP3 assembles clathrin into cages with a narrow size distribution: Implications for the regulation of quantal size during neurotransmission. *Journal of Neuroscience Research*, 41(1):15–26, October 2004.

[144] W. Ye and E. M. Lafer. Clathrin binding and assembly activities of expressed domains of the synapse-specific clathrin assembly protein AP-3. *Journal of Biological Chemistry*, 270(18):10933–10939, May 1995.

[145] R. Lindner and E. J. Ungewickell. Clathrin-associated proteins of bovine brain coated vesicles. An analysis of their number and assembly-promoting activity. *Journal of Biological Chemistry*, 267(23):16567–16573, August 1992.

[146] S. K. Lemmon. Clathrin uncoating: Auxilin comes to life. *Current Biology*, 11(2): R49–R52, January 2001.

[147] W. E. Gall, M. A. Higginbotham, C. Chen, M. F. Ingram, D. M. Cyr, and T. R.

Graham. The auxilin-like phosphoprotein Swa2p is required for clathrin function in yeast. *Current Biology*, 10(21):1349–1358, November 2000.

[148] R. H. Massol, W. Boll, A. M. Griffin, and T. Kirchhausen. A burst of auxilin recruitment determines the onset of clathrin-coated vesicle uncoating. *Proceedings of the National Academy of Sciences*, 103(27):10265, July 2006.

[149] D. Lee, X. Wu, E. Eisenberg, and L. E. Greene. Recruitment dynamics of GAK and auxilin to clathrin-coated pits during endocytosis. *Journal of Cell Science*, 119 (17):3502, September 2006.

[150] K. Prasad, W. Barouch, L. Greene, and E. Eisenberg. A protein cofactor is required for uncoating of clathrin baskets by uncoating ATPase. *Journal of Biological Chemistry*, 268(32):23758–23761, November 1993.

[151] S. E. H. Holstein, H. Ungewickell, and E. J. Ungewickell. Mechanism of clathrin basket dissociation: separate functions of protein domains of the DnaJ homologue auxilin. *The Journal of Cell Biology*, 135(4):925–937, November 1996.

[152] A. Fotin, Y. Cheng, N. Grigorieff, T. Walz, S. C. Harrison, and T. Kirchhausen. Structure of an auxilin-bound clathrin coat and its implications for the mechanism of uncoating. *Nature*, 432:649, October 2004.

[153] Y. Xing, T. Böcking, M. Wolf, N. Grigorieff, T. Kirchhausen, and S. C. Harrison. Structure of clathrin coat with bound Hsc70 and auxilin: mechanism of Hsc70-facilitated disassembly. *The EMBO Journal*, 29(3):655, February 2010.

[154] U. Scheele, C. Kalthoff, and E. J. Ungewickell. Multiple interactions of auxilin 1 with clathrin and the AP-2 adaptor complex. *Journal of Biological Chemistry*, 276 (39):36131–36138, September 2001.

[155] B. Doray and S. Kornfeld. γ cubunit of the AP-1 adaptor complex binds clathrin: Implications for cooperative binding in coated vesicle assembly. *Molecular Biology of the Cell*, 12(7):1925–1935, July 2001.

[156] P. Friedl, K. Wolf, and J. Lammerding. Nuclear mechanics during cell migration. *Cell structure and dynamics*, 23(1):55–64, February 2011.

[157] R. D. Goldman, Y. Gruenbaum, R. D. Moir, D. K. Shumaker, and T. P. Spann.

Nuclear lamins: building blocks of nuclear architecture. *Genes & development*, 16 (5):533–547, 2002.

[158] H-R. Thiam, P. Vargas, N. Carpi, C. L. Crespo, M. Raab, E.l Terriac, M. C. King, J. Jacobelli, A. S. Alberts, T. Stradal, A-M. Lennon-Dumenil, and M. Piel. Perinuclear Arp2/3-driven actin polymerization enables nuclear deformation to facilitate cell migration through complex environments. *Nature Communications*, 7:10997, March 2016.

[159] J. Lammerding, L. G. Fong, J. Y. Ji, K. Reue, C. L. Stewart, S. G. Young, and R. T. Lee. Lamins A and C but Not Lamin B1 Regulate Nuclear Mechanics. *Journal of Biological Chemistry*, 281(35):25768–25780, September 2006.

[160] D. Zink, A. H. Fischer, and J. A. Nickerson. Nuclear structure in cancer cells. *Nature Reviews Cancer*, 4:677, September 2004.

[161] P. Meister, B. D. Towbin, B. L. Pike, A. Ponti, and S. M. Gasser. The spatial dynamics of tissue-specific promoters during C. elegans development. *Genes & Development*, 24(8):766–782, April 2010.

[162] T. Cremer and M. Cremer. Chromosome Territories. *Cold Spring Harbor Perspectives in Biology*, 2(3):a003889–a003889, March 2010.

[163] E. Deniaud and W. A. Bickmore. Transcription and the nuclear periphery: edge of darkness? *Chromosomes and expression mechanisms*, 19(2):187–191, April 2009.

[164] T. A. Volpe, C. Kidner, I. M. Hall, G. Teng, S. I. S. Grewal, and R. A. Martienssen. Regulation of heterochromatic silencing and histone H3 Lysine-9 Methylation by RNAi. *Science*, 297(5588):1833, September 2002.

[165] M. Versaevel, T. Grevesse, and S. Gabriele. Spatial coordination between cell and nuclear shape within micropatterned endothelial cells. *Nature Communications*, 3: 671, February 2012.

[166] A. J. Engler, S. Sen, H. L. Sweeney, and D. E. Discher. Matrix elasticity directs Stem cell lineage specification. *Cell*, 126(4):677–689, August 2006.

[167] N. Jain, K. V. Iyer, A. Kumar, and G. V. Shivashankar. Cell geometric constraints induce modular gene-expression patterns via redistribution of HDAC3 regulated by

actomyosin contractility. *Proceedings of the National Academy of Sciences*, 110 (28):11349, July 2013.

[168] T. Dechat, K. Pfleghaar, K. Sengupta, T. Shimi, D. K. Shumaker, L. Solimando, and R. D. Goldman. Nuclear lamins: major factors in the structural organization and function of the nucleus and chromatin. *Genes & Development*, 22(7):832–853, April 2008.

[169] V. Stierlé, J. Couprie, C. Östlund, I. Krimm, S. Zinn-Justin, P. Hossenlopp, H. J. Worman, J. Courvalin, and I. Duband-Goulet. The carboxyl-terminal region common to lamins A and C contains a DNA binding domain. *Biochemistry*, 42(17): 4819–4828, May 2003.

[170] K. V. Iyer, S. Pulford, A. Mogilner, and G. V. Shivashankar. Mechanical activation of cells induces chromatin remodeling preceding MKL nuclear transport. *Biophysical Journal*, 103(7):1416–1428, October 2012.

[171] S. M. Schreiner, P. K. Koo, Y. Zhao, S. G. J. Mochrie, and M. C. King. The tethering of chromatin to the nuclear envelope supports nuclear mechanics. *Nature Communications*, 6:7159, June 2015.

[172] B. D. Hoffman and J. C. Crocker. Cell mechanics: dissecting the physical responses of cells to force. *Annual Review of Biomedical Engineering*, 11(1):259–288, July 2009.

[173] K. N. Dahl, S. M. Kahn, K. L. Wilson, and D. E. Discher. The nuclear envelope lamina network has elasticity and a compressibility limit suggestive of a molecular shock absorber. *Journal of Cell Science*, 117(20):4779, September 2004.

[174] J. Lammerding, P. C. Schulze, T. Takahashi, S. Kozlov, T. Sullivan, R. D. Kamm, C. L. Stewart, and R. T. Lee. Lamin A/C deficiency causes defective nuclear mechanics and mechanotransduction. *The Journal of Clinical Investigation*, 113 (3):370–378, February 2004.

[175] K. N. Dahl, A. J. Engler, J. D. Pajerowski, and D. E. Discher. Power-law rheology of isolated nuclei with deformation mapping of nuclear substructures. *Biophysical Journal*, 89(4):2855–2864, October 2005.

[176] G. Gerlitz and M. Bustin. The role of chromatin structure in cell migration. *Trends in Cell Biology*, 21(1):6–11, January 2011.

[177] M. Lherbette, A. dos Santos, Y. Hari-Gupta, C. P. Fili, N.and Toseland, and I. A. T. Schaap. Atomic Force Microscopy micro-rheology reveals large structural inhomogeneities in single cell-nuclei. *Scientific Reports*, 7:8116, 2017.

[178] D. Sage, L. Donati, F. Soulez, D. Fortun, G. Schmit, A. Seitz, R. Guiet, C. Vonesch, and M. Unser. DeconvolutionLab2: An open-source software for deconvolution microscopy. *Image Processing for Biologists*, 115:28–41, February 2017.

[179] J. Alcaraz, L. Buscemi, M. Puig-de Morales, J. Colchero, A. Baró, and D. Navajas. Correction of microrheological measurements of soft samples with Atomic Force Microscopy for the hydrodynamic drag on the cantilever. *Langmuir*, 18(3):716–721, February 2002.

[180] M. Glaubitz, N. Medvedev, D. Pussak, L. Hartmann, S. Schmidt, C. A. Helm, and M. Delcea. A novel contact model for AFM indentation experiments on soft spherical cell-like particles. *Soft Matter*, 10(35):6732–6741, 2014.

[181] A. Mazumder, T. Roopa, A. Basu, L. Mahadevan, and G. V. Shivashankar. Dynamics of chromatin decondensation reveals the structural integrity of a mechanically prestressed nucleus. *Biophysical Journal*, 95(6):3028–3035, September 2008.

[182] A. Palmer, J. Xu, and D. Wirtz. High-frequency viscoelasticity of crosslinked actin filament networks measured by diffusing wave spectroscopy. *Rheologica Acta*, 37 (2):97–106, April 1998.

[183] B. D. Hoffman, G. Massiera, K. M. Van Citters, and J. C. Crocker. The consensus mechanics of cultured mammalian cells. *Proceedings of the National Academy of Sciences*, 103(27):10259, July 2006.

[184] L. Deng, X. Trepat, J. P. Butler, E. Millet, K. G. Morgan, D. A. Weitz, and J. J. Fredberg. Fast and slow dynamics of the cytoskeleton. *Nature Materials*, 5:636, July 2006.

[185] C. Coffinier, H. Jung, C. Nobumori, S. Chang, Y. Tu, R. H. Barnes, Y. Yoshinaga, P. J. de Jong, L. Vergnes, K. Reue, L. G. Fong, S. G. Young, and T. M. Magin. Deficiencies in lamin B1 and lamin B2 cause neurodevelopmental defects and distinct nuclear shape abnormalities in neurons. *Molecular Biology of the Cell*, 22 (23):4683–4693, October 2011.